MEASUREMENT OF HIGH MASS MUON PAIRS PRODUCED IN HADRONIC COLLISIONS AND A DETERMINATION OF THE PION STRUCTURE FUNCTION

Catherine Newman

March, 1979

FERMILAB
LIBRARY

PAB1888

THE UNIVERSITY OF CHICAGO

MEASUREMENT OF HIGH MASS MUON PAIRS PRODUCED IN HADRONIC COLLISIONS AND A DETERMINATION OF THE PION STRUCTURE FUNCTION

A DISSERTATION SUBMITTED TO
THE FACULTY OF THE DIVISION OF THE PHYSICAL SCIENCES
IN CANDIDACY FOR THE DEGREE OF
DOCTOR OF PHILOSOPHY

DEPARTMENT OF PHYSICS

BY

CATHERINE B. NEWMAN

CHICAGO, ILLINOIS

JUNE, 1979

ACKNOWLEDGMENTS

High energy physics experiments are only possible through the efforts of many people and I thank all who supplied their talents for this research. It is a pleasure to thank my collaborators: Kirk McDonald, Jim Pilcher, Eli Rosenberg, Gary Sanders, Stew Smith, Jon Thaler, Kelby Anderson, Rick Coleman, Gary Hogan and Kari Karhi. Each of them has contributed to my education as well as to the success of this experiment. Excellent technical support was provided by the Enrico Fermi Institute and Princeton University. I thank the Engineering Services Department of the EFI, including Dick Armstrong, Cliff Brill, Robert Ryan and Rich Northrup for their work on the design and construction of the experiment. The EFI Electronics Shop was also most helpful - Bob Norton deserves special mention. The Fermilab Neutrino Department assisted throughout the data collection period.

Jim Pilcher was my research advisor and I thank him for sharing some of his extensive knowledge of experimental physics. I thank Eli Rosenberg, Kirk McDonald and Gary Hogan for useful conversations. I especially thank Kelby Anderson who provided a beautiful computer graphics package and much helpful advice throughout this work.

TABLE OF CONTENTS

	Page
ACKNOWLEDGMENTS	ii
LIST OF TABLES.	iv
LIST OF ILLUSTRATIONS	v
ABSTRACT.	xi
Chapter	
I. INTRODUCTION	1
The Quark-Parton Model	
The Quark-Antiquark Annihilation Model	
The Experiment	
II. THE DETECTOR	10
Beam Line	
Beam Definition	
Target and Interaction Counters	
Hadron Absorber	
J Hodoscope	
Multiwire Proportional Chambers	
The Magnet	
Spark Chambers	
F Hodoscope	
Downstream Steel Absorber and P Hodoscope	
Fast Electronics	
The Mass Box	
Data Acquisition	
III. DATA ANALYSIS.	27
Reconstruction Program	
Mass Calculation and Event Selection	
Monte Carlo Calculation	
Normalizaton	
IV. RESULTS.	49
General Features of the Data	
Comparison of the Data with the Quark-Antiquark Annihilation Model	
Structure Functions	
Conclusions	
REFERENCES.	81

LIST OF TABLES

Table		Page
1.	Quark quantum numbers.	86
2.	Average beam composition	87
3.	Target information	88
4.	MWPC efficiencies and resolutions.	89
5.	Spark chamber efficiencies and resolutions . . .	90
6.	Reconstruction efficiency.	91
7.	Effect of software trigger requirement	92
8.	Values used for Monte Carlo calculation.	93
9.	Čerenkov counter efficiencies and accidental probabilities	93
10.	Normalization factors.	94
11.	J/ψ and ψ' cross sections.	95
12.	Feynman x distribution fits.	96
13.	The cross section $d\sigma/dMdx_F$ for π^- induced μ pairs.	97
14.	Transverse momentum distribution fits.	98
15.	Mean transverse momentum	99
16.	Helicity angular distribution fits	100
17.	Pion structure function fits	101
18.	Nucleon structure function fits.	102

LIST OF ILLUSTRATIONS

Figure		Page
1.	Diagram of inelastic lepton-proton scattering	104
2.	Processes for the study of form factors in the timelike region	106
3.	The Drell Yan process for lepton pair production	108
4.	The Chicago cyclotron magnet spectrometer as configured for this experiment.	110
5.	Diagram of the Neutrino beam line.	112
6.	Detector elements for beam particle identification	114
7.	Arrangement of counters in the J hodoscope . . .	116
8.	Configuration of the proportional chambers . . .	118
9.	Arrangement of counters in the P hodoscope . . .	120
10.	Logic diagram of the trigger electronics	122
11.	Difference between upstream and downstream reconstructed impact parameters for beam particles.	124
12.	Difference between upstream and downstream reconstructed y intercepts for beam particles.	126
13.	Difference between upstream and downstream reconstructed y slopes for beam particles.	128
14.	Momentum distribution for beam particles	130
15.	Plot of the number of good events divided by the number of beam particles as a function of run number	132

Figure Page

16. Momentum distribution for events with mass greater than 2 GeV/c^2 which satisfy the software trigger requirement 134

17. Momentum distributions after beam momentum limits are imposed. 136

18. Vertex χ^2 probability distribution 138

19. Scatter plot of the reconstructed x vertex vs. y vertex 140

20. Scatter plot of the reconstructed vertex position vs. momentum. 142

21. Momentum distribution after all event selection criteria have been applied 144

22. Mass spectra for π^- induced μ pair events 146

23. The detector efficiency as a function of mass, Feynman x and transverse momentum. . . . 148

24. Detector efficiency vs. cos θ^* 150

25. Detector efficiency vs. ϕ^* 152

26. Effect of resolution smearing on the Feynman x distribution 154

27. Effect of resolution smearing on the transverse momentum spectrum 156

28. Muon pair mass spectrum for protons incident on a carbon target. 158

29. Muon pair mass spectrum for π^+ incident on a carbon target 160

30. Muon pair mass spectra for K^+ and $\bar{p}$ incident on a carbon target. 162

31. Muon pair mass spectrum for π^- incident on a carbon target 164

32. Muon pair mass spectrum for π^- incident on a copper target 166

33. Muon pair mass spectrum for π^- incident on a tungsten alloy target 168

Figure | Page

34. Mass spectrum for π^- induced μ pairs (per nucleon) 170

35. Mass spectrum for π^- induced μ pairs with masses between 2.5 and 4.5 GeV/c^2 172

36. $Ed\sigma/dx_F$ per nucleon for π^- induced μ pairs with p_T less than 1 GeV/c and mass less than 4 GeV/c^2 174

37. $Ed\sigma/dx_F$ per nucleon for π^- induced μ pairs with mass greater than 4 GeV/c^2 176

38. $Ed\sigma/dx_F$ per nucleon for π^- induced μ pairs with p_T greater than 1 GeV/c and mass less than 4 GeV/c^2 178

39. $Ed\sigma/dx_F$ per nucleon for π^- induced μ pairs with p_T greater than 1 GeV/c and mass greater than 4 GeV/c^2 180

40. $Ed\sigma/dx_F$ per nucleon for π^+ induced μ pairs with mass less than 3.5 GeV/c^2 182

41. $Ed\sigma/dx_F$ per nucleon for π^+ induced μ pairs with mass greater than 3.5 GeV/c^2 184

42. $Ed\sigma/dx_F$ per nucleon for proton induced μ pairs with mass less than 3.5 GeV/c^2 186

43. $Ed\sigma/dx_F$ per nucleon for proton induced μ pairs with mass greater than 3.5 GeV/c^2 188

44. $Ed\sigma/dx_F$ per nucleon for K^+ and $\bar{p}$ induced J/ψ events 190

45. $1/p_T\, d\sigma/dp_T$ (per nucleon) for π^- induced μ pairs with x_F less than 0.3 and mass less than 4 GeV/c^2 192

46. $1/p_T\, d\sigma/dp_T$ (per nucleon) for π^- induced μ pairs with mass greater than 4 GeV/c^2 194

47. $1/p_T\, d\sigma/dp_T$ (per nucleon) for π^- induced μ pairs with x_F greater than 0.3 and mass less than 4 GeV/c^2 196

48. $1/p_T\, d\sigma/dp_T$ (per nucleon) for π^- induced μ pairs with x_F greater than 0.3 and mass greater than 4 GeV/c^2 198

Figure Page

49. $1/p_T d\sigma/dp_T$ (per nucleon) for π^+ induced μ pairs with mass less than 3.5 GeV/c^2 200

50. $1/p_T d\sigma/dp_T$ (per nucleon) for π^+ induced μ pairs with mass greater than 3.5 GeV/c^2. . . . 202

51. $1/p_T d\sigma/dp_T$ (per nucleon) for proton induced μ pairs with mass less than 3.5 GeV/c^2 204

52. $1/p_T d\sigma/dp_T$ (per nucleon) for proton induced μ pairs with mass greater than 3.5 GeV/c^2. . . 206

53. $1/p_T d\sigma/dp_T$ (per nucleon) for K^+ and $\bar{p}$ induced J/ψ events 208

54. Mean transverse momentum vs. mass for pion and proton induced μ pairs. 210

55. Mean transverse momentum vs. x_F for pion induced μ pairs. 212

56. Total cross section vs. atomic mass number for five mass intervals. 214

57. A dependence power α vs. mass for π^- induced μ pairs. 216

58. A dependence power α vs. mass for proton induced μ pairs. 218

59. A dependence power α vs. p_T for π^- induced μ pairs. 220

60. A dependence power α vs. x_F for π^- induced μ pairs. 222

61. Ratio of π^- induced μ pair cross section to proton induced μ pair cross section. 224

62. The ratio of π^+ induced μ pair cross section to π^- induced μ pair cross section as a function of mass 226

63. Polar angular distribution for μ pair events in three mass regions 228

64. Reference directions for measuring the angle θ^* 230

Figure Page

65. Polar angle distributions for μ pairs with mass below the J/ψ for the s, t, and u channel systems. 232

66. Polar angle distributions for μ pairs at the J/ψ mass for the s, t, and u channel systems. 234

67. Polar angle distributions for μ pairs with mass above the J/ψ for the s, t, and u channel systems. 236

68. Polar angle distributions for μ pairs with mass above the J/ψ and p_T less than 1 GeV/c. 238

69. Polar angle distributions for μ pairs with mass above the J/ψ and p_T greater than 1 GeV/c. 240

70. Azimuthal angle distribution for μ pair events in three mass regions 242

71. Azimuthal angle distributions of μ pairs with mass below the J/ψ for the s, t, and u channel systems. 244

72. Azimuthal angle distributions for μ pairs at the J/ψ mass for the s, t, and u channel systems. 246

73. Azimuthal angle distributions for μ pairs with mass greater than 3.5 GeV/c^2 for the s, t and u channel systems. 248

74. Scaling plot for proton induced μ pairs. 250

75. Scaling plot for π^- induced μ pairs. 252

76. The ratio of the π^+ induced μ pair cross section to the π^- induced μ pair cross section as a function of $M/\sqrt{s}$ for continuum μ pairs. 254

77. Distribution of events in the x_1, x_2 plane . . . 256

78. The nucleon function $g^N(x_2)$. 258

Figure Page

79. νW_2 vs. x for lepton-deuterium scattering at high q^2 260

80. The momentum distribution for a valence quark in the charged pion. 262

81. The pion valence quark probability function 264

82. Mass spectrum for π^- induced μ pairs with mass between 4.0 and 8.75 GeV/c^2 266

83. The x_F distributions for π^- induced μ pairs with mass between 4.0 and 8.75 GeV/c^2. 268

84. Mass plot for π^- induced μ pairs with mass betweem 0.3 and 8.75 GeV/c^2 and x_F greater than 0.1 270

85. The ratio of the π^+ induced μ pair cross section to the π^- induced μ pair cross section as a function of mass. 272

86. Diagrams for deep inelastic lepton proton scattering 274

87. Diagrams for QCD corrections to the Drell Yan mechanism. 276

ABSTRACT

Results are presented from an experiment which detected muon pairs produced in collisions of 225 GeV hadrons with nuclear targets. The use of a large acceptance detector permits the observation of high mass muon pairs over a wider kinematic region than that of any previously reported experiment. Cross sections for high mass muon pair production by positive and negative pions have been measured for the first time.

The data provide the first conclusive evidence for the quark-antiquark annihilation model. The observed spin alignment of the μ pairs and the dependence of the cross section on beam particle type are in excellent agreement with predictions of the model. Finally, the data taken with a negative pion beam are used to determine the momentum distribution for valence quarks in the pion.

CHAPTER I

INTRODUCTION

Scattering processes have been used to study the structure of matter since the early twentieth century, when Rutherford (1906) and Geiger and Marsden (1909,1913) measured the scattering of alpha particles off thin foils. The experiments led Rutherford to propose that the positive charge in atoms was concentrated in a very small volume. The cross section for the elastic electromagnetic scattering of spinless charged particles off nuclei of charge Z is given in the Born approximation by:

$$\frac{d\sigma}{dq^2} = \frac{4\pi\alpha^2 Z^2}{q^4} |F(q^2)|^2$$

where q^2 is the momentum transfer squared and $F(q^2)$ is a form factor, equal to the Fourier transform of the nuclear charge distribution. The value $F(q^2) = 1$ corresponds to a point charge and the above expression reduces to Rutherford's formula in this case. With Rutherford's momentum transfers, which were on the order of a few MeV/c, the nucleus looked like a point. From the Uncertainty Principle, the smallest distance measurable by a 10 MeV/c particle is about 20 fm. Larger momentum transfers are required to probe smaller distances.

The first information about nuclear form factors was obtained from a series of experiments performed at Stanford 1953-1961.[1] Hofstadter and his collaborators measured the scattering of 400 - 600 MeV electrons by nuclear targets. The maximum momentum transfer was about 700 MeV/c so distances smaller than 1 fm could be "seen". The experiment was performed with hydrogen and deuterium targets in 1956, providing the first measurement of nucleon form factors.

More recently, inelastic lepton-proton scattering experiments[2,3] have provided interesting information about nucleon structure. The inelastic collision is described by the energy transfer $\nu = E' - E$ as well as q^2; see Figure 1. The cross section is expressed in terms of two structure functions W_1 and W_2 :

$$\frac{d^2\sigma}{dq_\gamma^2 d\nu} = \frac{E'}{E}\frac{4\pi\alpha^2}{q_\gamma^4}\left[W_2(q_\gamma^2,\nu)\cos^2\frac{\theta}{2} + 2W_1(q_\gamma^2,\nu)\sin^2\frac{\theta}{2}\right]$$

Experimenters at the Stanford Linear Accelerator Center (SLAC) found that for $\nu > 3$ GeV, the structure functions showed extremely weak q^2 dependence. This suggested the presence of pointlike objects in the nucleon, just as the constant form factor of Rutherford scattering suggested a pointlike nucleus within the atom. Moreover, at large values of ν and q^2, νW_2 depended only on the ratio ν/q^2.[4] This remarkable result suggested that the leptons were undergoing elastic collisions since q^2 and ν are proportional in elastic scattering. Thus for large values of ν and q^2, the deep inelastic lepton scattering data were

interpreted as elastic collisions between leptons and pointlike constituents within hadrons. These constituents were called partons.

In scattering experiments, the momentum transfer is spacelike. Several processes may be used to study form factors in the timelike region (Figure 2), including $p\bar{p} \to e^+e^-$, $e^+e^- \to$hadrons, and massive lepton pair production in hadron collisions. This thesis reports results from an experiment on the latter type of reaction, namely the production of muon pairs by pions and protons on nuclear targets.

In 1970, Drell and Yan[5] asserted that nonresonant muon pairs should be produced predominantly by virtual photons from parton-antiparton annihilation (see Figure 3). This leads to several specific predictions which can be checked experimentally. If the dimuons are produced via the Drell-Yan mechanism, dimuon data can be used to determine hadron structure functions.

In this chapter, the quark-parton model will be described briefly. Then the quark-antiquark annihilation model will be described and some of its predicitions discussed. Finally, the experimental objectives will be listed.

The Quark-Parton Model

In 1964,[6] Gell-Mann and Zweig proposed that hadrons were composed of fractionally charged pointlike particles which

Gell-Mann called "quarks". Originally three quarks were suggested. The current estimate is at least five, and more are likely. The quark quantum numbers are listed in Table 1. With these quantum number assignments, a proton is a uud state while a neutron is ddu. A π^+ is $u\bar{d}$ and a π^- is $\bar{u}d$. In addition to the quantum numbers listed, the quarks are believed to have a degree of freedom called "color". The existence of particles made up of three quarks of the same type (e.g., Ω^- = sss) indicated that the spin 1/2 quarks could not obey Fermi statistics. The introduction of the color quantum number solved this problem. Each type of quark comes in three colors.

The quark model allowed many hadron states to be classified in an attractively simple way, but when experimental searches failed to find evidence for fractionally charged particles, quarks were believed to be only hypothetical. Then the results from deep inelastic lepton scattering experiments led to the development of the parton model by Feynman, Bjorken and others.[7] Eventually partons were identified with quarks.[8] Now the word "parton" generally refers to a quark or a gluon. Gluons are pointlike spin one particles which "hold quarks together" in hadrons. The rapidly developing theory of quantum chromodynamics[9] (QCD) is an attempt to explain strong interactions by coupling quarks and gluons through the color charge. QCD has been used successfully to calculate the violations of scaling observed in deep inelastic scattering.[10]

Some of the implications of QCD relevant to this thesis are discussed in Chapter IV.

The quarks which give hadrons their observed quantum numbers, such as charge and strangeness, are known as valence quarks. In addition to these quarks, each hadron is believed to contain a "sea" of virtual quark-antiquark pairs. The momentum of a hadron is divided among the valence quarks, sea quarks and gluons. The momentum distribution of the sea quarks is expected to fall much more steeply than that for valence quarks, i.e., the sea quarks are concentrated at low momentum. In the quark-antiquark annihilation model, the annihilating quarks may be sea or valence quarks.

The Quark - Antiquark Annihilation Model

The cross section for lepton pair production in the Drell-Yan (quark-antiquark annihilation) model is:

$$\frac{d^2\sigma}{dM\,dx_F} = \frac{8\pi\alpha^2}{9M^3}\frac{1}{\sqrt{x_F^2+4M^2/s}}\sum_i e_i^2\left[x_1 f_i^A(x_1)\,x_2 f_{\bar{i}}^B(x_2) + x_1 f_{\bar{i}}^A(x_1)\,x_2 f_i^B(x_2)\right] \qquad (1)$$

where m is the invariant mass of the lepton pair, x_F is the Feynman x ($x_F = 2P_{\parallel}^{*}/\sqrt{s}$), $x_{1,2} = (\pm x_F + \sqrt{x_F^2+4m^2/s})/2$ are the momentum fractions of the annihilating quarks in the projectile and target hadrons, e_i is the charge of the i type quark and $f_i^A(x)$ is the probability of finding a quark of flavor i in hadron A with momentum fraction x. The structure functions of deep inelastic scattering are simple functions of these f's.

From equation (1) it is clear that one prediction of the Drell-Yan model is that $m^3 d\sigma/dm$ should be a function only of m^2/s, i.e., the data should show a form of scaling similar to that observed in deep inelastic lepton scattering.

A second test of the model involves comparing lepton pair production using a π^+ beam to production from a π^- beam. Because the sea quark distributions fall much more steeply with x_1 and x_2 than the valence quark distributions, quarks in the sea will not contribute to μ pair production if x_1 and x_2 are sufficiently large. This corresponds to considering high mass muon pairs since $x_1 x_2 = m^2/s$. A nucleon contains no valence antiquarks so for π-N collisions, the only valence antiquark available for annihilation is that of the pion. Thus in the high mass limit, the sum in equation (1) has only one nonzero term:

$$\frac{d^2\sigma}{dM\,dx_F} = \frac{8\pi\alpha^2}{9M^3}\frac{1}{\sqrt{x_F^2+4M^2/s}}\left\{\frac{1}{9}x_1\bar{d}^{\pi^+}(x_1)\,x_2 d^N(x_2)\right\} \qquad \text{for } \pi^+$$

$$\frac{d^2\sigma}{dM\,dx_F} = \frac{8\pi\alpha^2}{9M^3}\frac{1}{\sqrt{x_F^2+4M^2/s}}\left\{\frac{4}{9}x_1\bar{u}^{\pi^-}(x_1)\,x_2 u^N(x_2)\right\} \qquad \text{for } \pi^-$$

where the N superscript stands for nucleon. The charge e_i has been set to -2/3 for the $\bar{u}$ in the π^- and 1/3 for the $\bar{d}$ in the π^+. From isospin and charge conjugation invariance, it is expected that $\bar{u}^{\pi^-} = \bar{d}^{\pi^+} = d^{\pi^-} = u^{\pi^+}$. Also $u^n = d^p$ and $u^p = d^n$ where the superscripts refer to neutrons and protons. If an isoscalar target is used, there are equal numbers of u and d quarks available for annihilation. Then $u^N = 1/2\, u^n +$

$1/2\ u^p$ and $d^N = 1/2\ d^n + 1/2\ d^p$. Since $u^n = d^p$ and $d^n = u^p$, $u^N = d^N$ for an isoscalar target. Thus the Drell Yan model predicts:

$$\frac{\sigma(\pi^+ C \to \mu^+\mu^- X)}{\sigma(\pi^- C \to \mu^+\mu^- X)} \longrightarrow \frac{\frac{1}{9}}{\frac{4}{9}} = \frac{1}{4}$$

The ratio should approach 1/4 if the mass is high enough so that sea quarks do not contribute and if an isoscalar target is used. If the muon pairs are produced via a strong interaction mechanism, the π^+/π^- cross section ratio would be equal to one; this is another consequence of the isoscalar target.

Measurement of the decay angular distribution of the muon pair provides another test of the Drell Yan model. If the μ pairs come from an intermediate state with J = 1, then the maximum power of $\cos\theta^*$ that can appear in the angular distribution is 2. In particular, the model predicts:

$$\frac{d\sigma}{d\Omega} \sim 1 + \cos^2\theta^* \qquad (2)$$

where θ^* is the angle between one of the muons and the annihilating quarks in the muon pair rest frame. Equation (2) can be derived as follows:

The angular distribution of a hadronically produced lepton pair to lowest order in the electromagnetic interaction is given by:[11]

$$W(\theta^*,\phi^*) = \frac{1-\beta^2\{\rho_{00}\cos^2\theta^* + \rho_{11}\sin^2\theta^* - \rho_{1-1}\sin^2\theta^*\cos 2\phi^* - \sqrt{2}\,\mathrm{Re}\,\rho_{10}\sin 2\theta^*\cos\phi^*\}}{4\pi\,(1-\frac{1}{3}\beta^2)} \qquad (3)$$

where θ^* and ϕ^* are the polar and azimuthal angles of one of the leptons, ρ_{ij} are the density matrix elements for the

virtual photon produced and β is the lepton velocity in the dilepton center of mass system. The value of β is $(1-4m_\mu^2/M_{\mu\mu}^2)$ and β is thus 0.99 for M = 2 GeV/c^2, the lowest mass considered by this experiment. Setting β = 1 and integrating over ϕ^* gives:

$$W(\theta^*) \propto 1 - \rho_{00}\cos^2\theta^* - \rho_{11}\sin^2\theta^*$$

The timelike virtual photon from the annihilation of massless spin 1/2 quarks is transversely polarized[5] so ρ_{11} = 1/2 and $\rho_{00} = 1 - 2\rho_{11} = 0$. Then:

$$W(\theta^*) \propto 1+\cos^2\theta^*$$

If the quarks are not massless, this result is modified to:[12]

$$W(\theta^*) \propto 1 + \frac{M_{\mu\mu}^2 - 4m_q^2}{M_{\mu\mu}^2 + 4m_q^2}\cos^2\theta^*$$

where m_q is the quark mass.

The Experiment

This thesis discusses a measurement of muon pairs produced in hadron collisions. In particular, data are presented for muon pair production using π^+ and π^- beams on an isoscalar target. The detector had large enough acceptance to effectively measure the angular distribution of high mass muon pairs. The data are in the region:

$$2.0 < M_{\mu\mu} < 11.0 \text{ GeV}/c^2$$

$$-0.05 < x_F < 1.0$$

$$0.0 < p_T < 5.0 \text{ GeV}/c$$

$$-1.0 < \cos\theta^* < 1.0$$

The features of dimuon production are measured over a wide kinematic area and one can test the hypothesis that the muon pairs come from quark-antiquark annihilation.

Chapter II describes the experimental set-up. The data analysis is discussed in Chapter III. Chapter IV reports the results, including comparisons with the predictions of the Drell Yan model and a determination of the pion structure function.

CHAPTER II

THE DETECTOR

The experiment was performed at the Fermi National Accelerator Laboratory in Batavia, Illinois. An unseparated secondary hadron beam in the Neutrino area was focussed on a target in the Muon Lab. The detector used the Chicago Cyclotron Magnet (CCM) facility. Figure 4 is a drawing of the detector. A hadron beam strikes a nuclear target in the front of the Muon Lab. The spectrometer detects dimuons. Particle trajectories are measured with proportional chambers before the Chicago Cyclotron magnet. After bending by the magnet, trajectories are measured by wire spark chambers.

For future reference in this section, it is useful to define a right handed coordinate system with the origin at the center of the CCM, Z along the beam direction and positive Y pointing up, perpendicular to the floor. The various elements of the detector are described in detail below.

Beam Line

Protons are accelerated to 400 GeV by the main ring accelerator at FNAL. They are then extracted and split into

three beam lines. Figure 5 shows the arrangement of magnets in the Neutrino beam line for this experiment. The extracted proton beam was steered onto a 14 inch aluminum target. The secondary beam was then focussed with a series of magnets ("quad triplet train"). Particles at an angle of 0.87 mrad proceeded to another series of magnets, finally arriving at the Muon Lab with momentum 225 GeV/c, plus or minus 5%. The beam spot on the target in the Muon Lab was 2 cm x 3 cm.

The beam intensity in the Muon Lab was 10^6 - 10^7 particles delivered in a 1.0 second spill with 10^{12} - 10^{13} protons per pulse incident on the production target. Because of the radio frequency acceleration in the main ring, the particles were grouped in "RF buckets" less than 2 nsec wide with ~ 19 nsec between buckets. Thus at an intensity of 10^7 particles per pulse, 12% of the buckets would contain more than one particle if all buckets were equally populated.

In the 914 meters from the production target to the Muon Lab, 7% of the 225 GeV/c pions decayed and 27% of the kaons decayed into muons. This caused both a small muon component in the beam and a "halo" of muons around the beam. Scintillation counters were used to veto these muons as described below.

The negative beam was essentially all pions (< 1% kaons). The positive beam was a mixture of protons and pions with a small kaon component. During the data collection using positive beam, a block of polyethylene 1 - 2 meters in length was placed in the beam. Since more protons were absorbed than pions, the polyethylene increased the percentage of pions in the beam from 14% to about 30%. The number of protons on the production target was increased to compensate for the reduction of total flux caused by the polyethylene absorber. Muons were not absorbed by the polyethylene so the muon component of the beam was slightly larger when the polyethylene was used. This was not a problem as beam muons were vetoed by a scintillation counter, as discussed below.

Beam Definition

Figure 6 shows the detector elements used to define and identify beam particles. The beam particle signal was defined by several scintillation counters. Four gas Čerenkov counters were used to separate pions, kaons, and protons. This section describes the beam definition detectors.

Scintillation Counters

The first beam defining counter, called T1, was a 3" x 3" hodoscope located at the front of beam line magnet enclosure 104, as shown in Figure 6. T1 consisted of eight

horizontal counters of 1/8" scintillator. At the downstream end of enclosure 104 was a second hodoscope, T2, consisting of eight vertical counters and one horizontal counter. All counters were 1/8" scintillator and the total size was 2" x 2". A 2" x 1 1/2" counter, T4, was placed at the front of the Muon Lab about two meters upstream of the target. During some of the data taking, the pulse height in this counter was used to veto triggers with more than one beam particle in an RF bucket.

Vetoes

Scintillation counters were also used to veto halo and beam muons. In enclosure 104, three sets of "jaw" counters detected halo particles. Each pair of jaws consisted of two pieces of scintillator 12.2 cm x 19.6 cm with a semicircular hole of radius 4.4 cm cut in the middle. The counters overlapped 1.2 cm so the beam passed through an elliptical hole 6.4 cm by 8.8 cm between each set of scintillators. A signal V_J was sent to the logic if any of the jaw counters was struck.

At the front of the Muon Lab, halo particles were veoted by a wall of scintillation counters surrounding the T4 counter. The wall was made up of four counters 0.3 m wide and 1.2 m tall on each side of the beam, and counters 0.3 m wide and 0.6 m high above and below the beam. A signal in any of these counters, V_M , inhibited the trigger. V_M counted at the level of 10 - 20% of the beam.

Finally, a 3" counter, V_μ , was placed in the beam twenty meters downstream of the target following three meters of steel. Events with beam muons were vetoed by this counter. Since the counter followed the CCM, it was centered on the deflected beam position. V_μ counted at the level of 6% of the beam for positive beam and 2% for negative beam. The percentage of muons in the beam was greater for positive beam because of the presence of the polyethylene absorber.

Čerenkov Counters

Gas Čerenkov counters were used to identify positive beam particles. For the first half of the positive beam running, three counters were used. Detectors for the Čerenkov light were located in enclosures 102, 103, and 104 (called C2, C3, and C4 respectively). The beam pipe upstream of each Čerenkov counter was filled with helium below atmospheric pressure. Čerenkov light was focussed by a spherical mirror onto an RCA C31000M photomultiplier tube. The counter lengths were 115 m, 49 m, and 69 m for C2, C3 and C4 respectively. The C2 and C4 pressures were set just below kaon threshold; thus these counted pions only. C3 was set to count pions and kaons. The pion definition required all Čerenkov counters on while a proton had all Čerenkov counters off.

With only three Čerenkov counters, the kaon sample ($\overline{C2}\cdot C3\cdot\overline{C4}$) is contaminated by protons accompanied by

accidental counts in C3. For the second half of the positive beam running, a fourth Čerenkov counter, C5, was used to improve the separation of kaons. C5 was 26 m long with the counter located in the upstream end of the Muon Lab. The C5 pressure was set so C5 counted pions and kaons. Then the definitons were:

$$\pi = C2 \cdot C3 \cdot C4 \cdot C5$$

$$K = \overline{C2} \cdot C3 \cdot \overline{C4} \cdot C5$$

$$p = \overline{C2} \cdot \overline{C3} \cdot \overline{C4} \cdot \overline{C5}$$

Table 2 gives the average beam composition. Čerenkov counter efficiencies and particle misidentification probabilities are discussed with the data normalization in Chapter III.

Target and Interaction Counters

The experiment used three different targets made of carbon, copper, and a tungsten alloy. Table 3 gives the lengths and densities of the three targets. Carbon was chosen as the isoscalar material easiest to work with and most readily available. The carbon target was used during all of the positive beam running and some of the negative beam running to allow a measurement of the π^+/π^- cross section ratio as explained in the introduction.

The carbon target consisted of three 4" blocks of high density carbon with 1/4" thick scintillation counters between the blocks. These counters were connected to analogue to digital converters (ADC's) and pulse height

information was written on the data tapes. This information was used during the data analysis to determine the block in which the interaction had taken place.

Another interaction counter, TI6, was located 25 cm downstream of the third carbon block. During the data taking with the carbon target, an ADC was connected to this counter. The trigger then required that at least two particles pass through this counter, as determined by the ADC pulse height.

About two thirds of the negative beam running time was spent taking data with the copper and tungsten targets. Because they were shorter than the carbon target, the interaction counters were not needed to localize the interaction point. Thus higher intensity beams could be used and the sensitivity of the experiment correspondingly increased without a serious loss of mass resolution.

Hadron Absorber

Three meters of steel were placed 1.7 meters downstream of the target. Muons passed through this material while hadrons were absorbed. In addition, 16.5 cm of borax, located close to the downstream end of the steel was used to absorb neutrons. Multiple scattering in the absorber gave muons a transverse momentum change (Δp_T) of about 140 MeV/c. Typically, a 30 GeV muon will be multiple scattered transversely 1.3 cm and lose about 4.8 GeV of its energy in the absorber.

J Hodoscope

The J hodoscope is shown in Figure 7. It consisted of two planes of scintillator - 24 vertical (x) counters and 16 horizontal (y) counters. The trigger required a particle on each side of the J hodoscope, both horizontally and vertically; that is, it required two particles in diagonally opposite quadrants. In addition, J hodoscope information was used for an on-line fast mass calculation as described below.

Multiwire Proportional Chambers

Particle trajectories upstream of the CCM were measured by multiwire proportional chambers. The configuration is shown in Figure 8. A total of fourteen planes were used. Six were on loan from the CERN-Heidelberg collaboration[13] and eight were built at the Enrico Fermi Institute for muon scattering experiment 98 at FNAL.[14]

Three planes were placed directly after the J hodoscope. The first and second planes, 82 cm x 58 cm, measured particles' y coordinates on the left and right sides of the beam respectively. These planes were separated by a 2 cm vertical dead strip and each covered about half of the x acceptance. The third plane, 166 cm x 58 cm measured the x coordinate. It was followed by two pairs of planes, 1 m x 1 m, placed side by side in pairs. One pair was tilted at an angle of 45° and the wires of the remaining pair were placed at -45° with respect to the vertical.

These "u" and "v" planes were used to correlate x and y track projections measured by the other chambers, and to measure tracks which passed through the central dead region of the CERN chambers.

The tilted planes were followed by another chamber on loan from CERN. This module also consisted of an x plane (218 cm x 77 cm) and two y half-planes (108 cm x 77 cm) separated by a 2 cm dead strip. Following the large CERN chamber were four more planes 1 m x 1 m. The first two of this set were x planes and the back two were y planes. Both pairs overlapped 4 cm in the center. The y pair was used along with the tilted planes to measure y tracks which would otherwise be lost to the central dead region of the CERN chambers. These dead strips did not seriously affect the acceptance for high mass muon pairs because such pairs generally had large opening angles.

Because the proportional chambers were arranged so that separate chambers overlapped in the center, it was possible for particles to pass through the chamber frames. This was not a problem, as the only particles of interest were muons which do not interact strongly. Muons going through the center of the detector generally had high momentum so multiple scattering in the frames was small. The average transverse momentum kick was about 7 MeV/c per frame. This is to be compared with Δp_T for the CCM which is about 1 GeV/c. On the average, a 50 GeV muon would be multiple scattered only about 0.02 mm for each frame passed through.

This is more than 50 times smaller than the wire spacing of the proportional chambers, so the momentum resolution is not affected.

The proportional chambers from CERN were read out by shift register scanners[15] using electronics built at Princeton University. The 1 m x 1 m MWPC's were operated as described in reference 14.

Plane efficiencies and resolutions are listed in Table 4. Efficiencies were calculated from the number of times a plane had a hit on a track which passed through its active area. The 1 m x 1 m MWPC's had wire spacings of 1.6 mm. The wire spacing was 2 mm for the CERN proportional chambers. The observed spatial resolution was consistent with that expected from the wire spacing.

The Magnet

The magnet from the University of Chicago Cyclotron was used for momentum analysis. This magnet has a radius of 2.16 m and a gap height of 1.27 m. For this experiment, the field is well approximated by a hard edge configuration with B = 6.95 kG out to a radius of 2.59 m and B = 0 beyond. This magnetic field corresponds to a transverse momentum kick of 1.1 GeV/c.

Spark Chambers

Particle trajectories downstream of the magnet were measured by twelve planes of wire spark chambers 2 m high

and 4 m wide. Planes were arranged in three modules of four planes each. Two planes of each module had vertical wires and the other two had wires tilted at an angle of arctangent 1/8 to the vertical. These chambers were constructed at the Enrico Fermi Institute for the muon scattering experiment; details of their construction are in reference 16. Some modifications were made to these chambers in anticipation of higher particle fluxes. The spark gaps were replaced by hydrogen thyratron pulsers.[17] Also, a gas recirculation system[18] was used to purify and reuse the spark chamber gas. This increased the flow rate of gas to 2 standard cubic feet per hour per chamber without a corresponding increase in cost. The efficiencies and resolutions for the spark chambers are summarized in Table 5.

F Hodoscope

Immediately following the last spark chamber was a large scintillation counter hodoscope, called F. This array consisted of 56 pieces of 1/4" thick NE102 scintillator arranged in two rows of 28 vertical strips. The counters were 7" wide and 40" tall with 1/8" overlap between counters. Light was collected by adiabatic lucite light guides and detected by RCA 8575 photomultiplier tubes. Phototube voltages were set 100 volts above the beginning of plateaus as measured with a muon beam.

The trigger required at least one hit in each of the two rows of the F bank. In addition, the struck counters

were required to be separated by at least one counter in the horizontal direction. Signals from the F counters were also used in the fast mass calculation.

Downstream Steel Absorber and P Hodoscope

Final muon identification was provided by a second steel absorber and another scintillation counter hodoscope. Steel from the University of Rochester cyclotron, averaging 2.3 m in thickness, filtered out hadrons not absorbed in the steel following the target.

The arrangement of counters in the P hodoscope is shown in Figure 9. The P hodoscope requirement in the trigger could be satisfied by various hit configurations. Three possibilities were: a hit in region A and a hit in C, an A hit with a D hit, or a B hit with a D hit. The fourth possibility was a B hit with a C hit with the additional requirement that the struck counters be separated by at least one counter in the horizontal direction.

Fast Electronics

Signals from the various scintillation counters were used to trigger the detector on high mass muon pairs. The trigger required the following: one beam particle, two hits in diagonally opposite quadrants of the J hodoscope, one hit in the top half and one in the bottom half of the F hodoscope with at least one counter separating the struck counters in the horizontal direction, and similarly for the

P hodoscope. For most of the running, a specially constructed module ("mass box") was used to suppress dimuons with masses below about 2 GeV/c^2.

A diagram of the fast logic is shown in Figure 10. Here T1, T2, and T4 are the beam defining counters already described and TI refers to the target interaction counters. V_μ is the beam muon veto counter, V_M represents a signal in the halo muon veto wall, and V_J is the signal from the jaw veto counters. Then define:

$$B'' = (T1)\cdot T2\cdot T4$$

$$V2 = V_\mu + V_M + V_J + (T4\geq 2)$$

$$B = B''\cdot \overline{V2}$$

$$BI = B\cdot (TI)$$

Quantities in parentheses were not present during the running with higher intensity beams.

The proportional chambers placed time constraints on the logic which required the construction of intermediate levels or "pretriggers". The CERN chambers had 200 nsec delay lines and thus required a gate for their latches within that time. These chambers were equipped with a prompt reset so the gate did not have to be the final trigger. The 1 m x 1 m MWPC's had a 500 nsec delay built into them but they had no reset feature. Thus the final trigger decision had to be made within 500 nsec.

The gate for the CERN MWPC's was called "pretrigger 1" defined by:

$$\text{pretrig1} = T4\cdot (TI)\cdot JXU\cdot JXD\cdot JYU\cdot JYD\cdot FT\cdot FB\cdot \overline{V1}$$

The T2 signal coming from enclosure 1Ø4 was too late for pretrigger 1. Most of the J and F hodoscope logic was also too late but one hit above and one hit below the median plane were required in the F hodoscope and in each plane (x and y) of the J hodoscope. Then in the notation above, FT(B) means a hit in the top (bottom) half of the F hodoscope. JXU(D) means a hit in the upper (lower) half of the vertical counter J hodoscope plane.

The CERN chamber latches were set by a pulse from pretrigger 1. A delayed pulse from pretrigger 1 reset the CERN chambers unless vetoed by a real event trigger. Pretrigger 1 could also be vetoed by a signal from either V_M or V_μ.

The next level of logic was called pretrigger 2. Pretrigger 2 was used to gate the CAMAC latches. It was also used by the mass box as a gate for the F hodoscope latches. The definition was:

$$\text{pretrig 2} = \text{pretrig 1} \cdot [\text{ULDR1} + \text{URDL1}] \cdot \overline{(\text{V3})}$$

Here ULDR1 stands for "up-left, down-right", i.e., at least one hit in each of two diagonally opposing quadrants of the J hodoscope. The signal V3 was related to the total number of J counters struck. During some of the high intensity running, events with more than 14 hits in the J hodoscope were vetoed. Such events would not be reconstructed successfully by the analysis program anyway and their loss is corrected for as described in Chapter III. Inspection of

these events using a computer display program indicated that less than 10% of these events were good dimuon triggers.

The final trigger was:

event = BI·J·F·pretrig2·P·mass box

This signal was fanned out and used to load the shift registers for the 1 m x 1 m MWPC's , to trigger the spark chambers, and to inhibit the prompt reset of the CERN chambers. The event trigger started a dead time gate 10 - 20 msec long. This time allowed the computer to finish reading out the event and the spark chambers to recover after being pulsed. This dead time was one of the ingredients of "gate 2". This gate was used to gate the CAMAC scalers and also as a veto on pretrigger 1. Thus during the dead time, the scalers were gated off and no triggers were accepted.

The Mass Box

For most of the data taking, the trigger used a specially built electronics module to do a fast calculation of the muon pair invariant mass. The mass is given by;

$$M^2_{\mu\mu} = 2P_1 P_2 (1-\cos\theta_{12})$$

where P_i is the momentum of the ith muon and θ_{12} is the opening angle between the muons. The "mass box" computed the muon momenta using the counter hits in the J and F hodoscope banks. An "up-down" requirement was imposed throughout the trigger; that is, the trigger required one hit above and below the median plane in the J, F, and P

hodoscope banks. Since the magnet did not affect the particle paths in the vertical plane, the "up-down" requirement allowed the mass box to match a muon trajectory in the front of the detector to its counterpart downstream of the magnet, providing a determination of the momentum. The hits in the J counter planes (both x and y) were used to compute the opening angle between the two muons. In case of ambiguities which arose if more than two tracks were present, the upstream and downstream tracks were paired to give the highest possible mass. The mass box took 100 nsec to calculate the muon pair invariant mass from the counter input. Details of the design and operation of the mass box may be found in reference 19.

Data Acquisition

The data were read out by an XDS Sigma III computer via CAMAC. The event trigger initiated the data acquisition and also started a gate signal which vetoed triggers during the readout of the event. This gate was stopped when a reset pulse arrived from the computer and the dead time had elapsed. The dead time was set to 10 - 20 msec depending on the running conditions. During running with high intensity beams, the spark chambers needed more time to recover. The Sigma III required about 12 msec to read out an event.

The data acquisition rate was 10 - 20 events per one second spill. At the end of each spill, the computer wrote one record on magnetic tape for each event read out during

the spill. All scintillation counter signals were discriminated and latched. Coincidences between B and various Čerenkov counter hit combinations were summed using CAMAC scalers. The sums were written on tape and used later to normalize the data. Pulse height information from ADC's on the target interaction counters, the beam defining counter T4, and the Čerenkov counters was also recorded.

In addition to recording data, the Sigma III was used extensively during the experiment to check detector performance. A system of on-line displays allowed the experimenters to view a diagram of the spectrometer showing counter and wire hits as well as hodoscope counter hit distributions, ADC pulse height spectra and wire chamber hit distributions. CAMAC scaler sums were printed out periodically. Besides the scaler sums required to normalize the data, quantities such as singles rates in the hodoscope planes were scaled to monitor the running conditions. The CRT displays and frequent printed summaries enabled any equipment problems to be detected very quickly.

CHAPTER III

DATA ANALYSIS

The primary data tapes, written during the experiment, were analyzed later in several stages. The main reconstruction program found tracks in the MWPC's and in the spark chambers. These track segments on either side of the magnet were linked by matching impact parameters in the horizontal plane and slopes and intercepts in the vertical plane. The change of slope in the horizontal plane provided the momentum measurement.

All track information was written to a "secondary tape" along with a copy of each raw data record. Then "tertiary tapes" were created containing only compressed track information for events with two or more muons. In this way, 170 primary tapes were reduced to 10 tertiary tapes. Various summary tapes were made beyond the tertiary tape level. A tape containing only "good events" created after the final cuts on the data were decided, was particularly useful.

This chapter discusses the data analysis. The first section describes the track reconstruction program. The second section explains the calculation of kinematic quantities and the event selection procedure. The third

section discusses the Monte Carlo calculation and the fourth section describes the normalization of the data.

Reconstruction Program

The off-line reconstruction program proceeded in four steps. First, tracks were found in the MWPC's upstream of the magnet. Second, tracks were found in the spark chambers downstream of the magnet. The third step was the linking of upstream tracks to downstream tracks. Finally, muon momenta and other kinematic quantities were computed.

The program used a coordinate system with the origin at the center of the CCM. The z axis was chosen to go through the center of the CERN chambers with positive z downstream of the CCM. The y direction was perpendicular to the floor with increasing y pointing up. Positive x pointed west. With this choice of axes, the angle of the beam in the lab was 3.4 mr in the x-z plane and -6.9 mr in the y-z plane.

Upstream Track Finder

The MWPC configuration (see Figure 8) and the trigger both suggested separate track searches in the right and left halves of the upstream detectors. X and y track projections were found separately. There were three x planes and three y planes on each side. The track search was begun by pairing each hit on one side in the small CERN chamber with each hit (on the same side) in the large CERN chamber. The two-point track thus constructed was extrapolated back to

the target region. If the extrapolated track fell within a box 0.6 m x 0.6 m x 1.75 m centered on the target, the third plane on the side (one of the 1 m x 1 m MWPC's) was searched for a hit along the trial track. If a hit was found within 7.5 mm of the projected track, a least squares fit was performed. The χ^2 probability for this fit was required to be greater than 0.001. If, in addition, the track extrapolated to within 12.5 mm of a struck J hodoscope counter, the track slope and intercept were saved and the three chamber hits used were removed from further consideration.

Because of inefficiencies in the MWPC's as well as the central dead region in the CERN y planes, the above procedure was supplemented with a two-point track finder. Hits not used in three point tracks were paired in all combinations. Also, a special track search used the last two overlapping y planes to find tracks that passed through the dead region of the CERN chambers. All two point tracks were required to extrapolate to the target and to point to struck J hodoscope counters, as above.

The tilted planes were then used to match the x and y track projections. Each x track was paired with each y track on the same side. A y track formed from hits in the last two y planes was allowed to pair with an x track on either side. The x and y tracks were projected into the tilted planes and the program looked for hits within 3.25 mm of the projected track position. If one or more hits were

found, an overall fit was performed tying together the x and y track segments. Each of these "globally fit" upstream tracks was required to have a χ^2 less than 8 per degree of freedom and to point to a Jx counter and a Jy counter which intersected.

Downstream Track Finder

The procedure used to find tracks in the upstream chambers was not practical for the downstream chambers. The large number of spark chamber planes (12) made methods which considered all combinations of hits far too complicated. The search could not be begun in a subset of the spark chambers because of plane inefficiencies. All subsets would have to be tried and this would be too time consuming. Instead the impact parameter of each upstream track already found was used to initiate a "waddle" track search.

In a cylindrically symmetric magnetic field, the ingoing and outgoing impact parameters of a particle are equal. So the downstream track finder began by projecting the first spark on each x plane to a z position roughly in the center of the chambers along a line joining the spark to the trial impact parameter. If the sparks lined up, a cluster would be formed when the sparks were projected to one z plane. For each upstream impact parameter, the program searched for such clusters. To decrease the time spent searching, a spark was not considered if it did not lie on a line joining the trial impact parameter to a struck

F hodoscope counter. This prevented the program from spending a lot of time reconstructing tracks not in time with the scintillation counter hits.

When a cluster was found, a track was fit. These track candidates - projections in the xz plane - were used to find y track segments. Every x plane had a plane with tilted wires (u or v) on the opposite side of the chamber gap. An x spark combined with a u or v spark gave a measurement of the y coordinate. So after an x track candidate was found, the x sparks were paired with their matching tilted wire sparks to initiate a y track search. When both an x and a y track candidate had been found, the program did an overall fit, just as was done for the "globally fit" tracks upstream. Finally, a track was accepted if it pointed to hit counters in both the F and P arrays.

Linking

The linking program paired tracks upstream of the CCM with their matches downstream of the magnet. This was done by forming the link chi square:

$$\chi^2_{LINK} = \frac{(\Delta b)^2}{\sigma_b^2} + \frac{(\Delta yslp)^2}{\sigma^2_{yslp}} + \frac{(\Delta yint)^2}{\sigma^2_{yint}}$$

where Δb is the difference between upstream and downstream impact parameters, Δ yslp is the difference in y slopes and Δ yint is the difference in y intercepts. The σ's for the contributions to the χ^2 were determined from distributions of

the data. The values used were: σ_b = 3.75 mm, σ_{ySLP} = 5 mr and σ_{yINT} = 35.4 mm. The link chi square was required to be less than 30 for a link.

Note that the y intercept difference was allowed to be much larger than the impact parameter difference. Because the u and v wires in the spark chambers were at such small angles to the x wires, the measurement of the y coordinate downstream of the CCM was not very precise. This was not a problem as y information was used only to help the linking and was not needed for the momentum determination.

For each downstream track, the program first tried to find a match among the globally fit upstream tracks. If no such track was a good link, the program tried to match the downstream track to unassociated upstream track pieces in x and y. Finally, globally fit upstream tracks which failed to link were broken up and their x and y pieces were allowed to link separately. Figures 11, 12, and 13 show the difference between upstream and downstream impact parameter, y intercept, and y slope for beam tracks. The corresponding distributions for the data were broader. This is because muons produced in the target had lower momenta than beam particles and were thus multiple scattered more in passing through the spectrometer.

Momentum Calculation

For a particle passing through an axially symmetric hard edge magnetic field,

$$P = (\sqrt{R^2 - b^2}\ \cot\frac{\Delta\theta}{2} + b) * 2.9978E-4 * B$$

where P = momentum in GeV/c in the plane perpendicular to the field - the xz plane for this experiment

B = magnetic field (kG)

b = impact parameter (cm)

R = magnetic field radius (cm)

$\Delta\theta$ = difference between upstream and downstream angles (from the z axis, in the xz plane) For very small angles, this is equal to the difference between the upstream and downstream track x slopes.

Because the last four proportional chambers, including two x planes, were in the fringe field of the CCM, the above simple prescription was modified to improve the momentum resolution. The momentum was calculated as above; then the expected deflections for the proportional chamber hits in the back chambers were calculated. The hits were moved and the track refit. During this refit, the upstream and downstream pieces were fit simultaneously with the impact parameters forced to be equal. The resulting momentum distribution for beam particles is shown in Figure 14.

Finally, muon momenta were corrected for energy lost in the steel absorber. This was done using an empirical fit to numbers calculated by Theriot.[80] The calculation included the

effects of collision losses, pair production, bremmstrahlung, and nuclear interactions.

Reconstruction Efficiency

Typically, about 85% of the events written to tape were reconstructed as muon pairs, though this number was as high as 95% for some sections of data taking. Events not reconstructed by the program were either bad triggers or reconstruction failures. Bad triggers were caused by single muons accompanied by accidental hits in the counters or halo or beam muons.

To determine the fraction of good triggers which reconstructed successfully, a computer program was used to display events on a CRT. Chamber and counter hits were shown together with any reconstructed tracks. If two tracks could be seen in the spark chambers which pointed to struck F and P counters, the event was called a "good trigger". A sample of events from each set of running conditions was scanned. The fraction of good triggers which reconstructed successfully is shown in Table 6 for each target and beam sign. Losses due to chamber inefficiencies have been removed from these numbers because such losses are included in the Monte Carlo calculation of the spectrometer acceptance, as described later in this chapter. These reconstruction efficiency corrections were applied when the data were normalized.

Every event on tape was not scanned and intermittent detector problems or changing beam conditions could have caused the reconstruction efficiency to vary with time. To check for this, the number of good events reconstructed per incident beam particle is plotted in Figure 15 as a function of run number. If each rate is fitted to a constant, one obtains a χ^2 per degree of freedom of 1 when 10-15% systematic errors are combined with the statistical errors shown in Figure 15.

Mass Calculation and Event Selection

The Mass Fit

The invariant mass of a muon pair is given by:

$$M^2_{\mu\mu} = 2m^2_\mu + 2(E_1 E_2 - P_1 P_2 \cos\theta_{12})$$

where m_μ is the muon mass, E_1, E_2 are the muon energies, P_1, P_2 are the momenta of the muons and θ_{12} is the opening angle between them. The opening angle was measured after the muons had passed through the 3 meter steel absorber. Thus, the measured opening angle is not the true opening angle at the target because of multiple scattering. To get the best estimate for the slope of each muon track, it is assumed that the two muons come from a common vertex located at the center of the target along the beam direction. Then the joint probability distribution for the projected multiple scattering angle θ_x and the displacement x is used:[21]

$$P(x,\theta_x) \propto \exp\left\{-\frac{4}{A}\left(\frac{\theta_x^2}{z} - \frac{3x\theta_x}{z^2} + \frac{3x^2}{z^3}\right)\right\}$$

where z = length of the absorber, $A = (.021)^2 / P_i P_f X_o$ with X_o the radiation length of iron and $P_{i(f)}$ the momentum before (after) passing through the steel. A χ^2 is associated with the probability distribution: $P \propto e^{-1/2 \chi^2}$ and the best fit slope for each track is obtained by minimizing the χ^2. It is assumed that the multiple scattering of the two muons is uncorrelated and that scattering in the x projection is uncorrelated with scattering in the y projection. From eight observed quantities - the x and y slopes and intercepts for two tracks - the best fit slopes were calculated, as well as the position of the vertex assuming both tracks came from the same point. The probability associated with the hypothesis that both tracks come from a common vertex in the target proved to be one of the most useful quantities for rejecting background events, as described below.

Event Selection

After muon tracks were reconstructed and momenta calculated, the data were subjected to various tests to eliminate background events. The same tests were included in the Monte Carlo calculation to correct for the loss of any good events.

The first requirement applied to the data was a software version of the trigger. An event was rejected if the counters to which the muon tracks pointed did not satisfy the conditions of the trigger, including the

hardware mass threshold. Thus this requirement removed false triggers caused by accidentals in the counters. Dimuons with masses below 2 GeV/c^2 were also eliminated at this point. These lower mass μ pairs have been studied elsewhere.[22]

The fraction of events which survived these cuts ranged from about 3% to 18% depending on the setting of the hardware mass threshold; see Table 7.

Background events were also caused by halo and beam muons in accidental coincidence with muons arising from decays of hadrons produced in the target. These sources lead to an excess of muons with the same charge as the beam, which must be eliminated. Figure 16 shows the momentum distributions for muons with the same charge as the beam (upper plot) and for muons with charge opposite to the beam (lower plot). The trigger and mass requirements described above have been applied. An excess of muons with the same charge as the beam ("same sign muons") is clearly seen. The comparison of these two plots is used to evaluate the effectiveness of the event selection criteria. For good dimuon events, the two plots should look the same, aside from small differences due to acceptance.

To eliminate events which contained beam associated muons not vetoed by the hardware, the following requirements were imposed: The momentum of each track was required to be less than 175 GeV/c and the sum of the muon momenta had to be less than 225 GeV/c - the beam momentum. In addition,

both tracks, when projected to the beam muon veto counter, were required to lie outside an area 200 mm x 120 mm centered on the veto counter. These requirements removed 15% of the events. The resulting momentum distributions are shown in Figure 17. An excess of same sign muons is still present. The excess corresponds to an inefficiency in the beam halo veto counters of about 1%. Next the vertex was evaluated. If the two muon tracks passed all the above requirements, the vertex χ^2 described above was formed. This is χ^2 for the hypothesis that the two tracks come from a common vertex located in the target. The vertex position, vertex χ^2, and best fit slopes were calculated. The vertex χ^2 probability is plotted in Figure 18. This quantity was required to be greater than 0.03. Next the reconstructed x-y position of the vertex was required to be within 70 mm of the beam center. Figure 19 shows a scatter plot of the reconstructed vertex positions with the cut indicated.

The final requirement was designed to eliminate halo muons, i.e., muons far from the beam with high momentum. Figure 20 shows a scatter plot of track momentum vs. vertex position. Muons with the same charge as the beam are used for the top plot; the bottom plot contains opposite sign muons. The cut was determimed by comparing these two plots. The momentum of each muon was required to be less than 225 GeV/c - 200 GeV/c * R/70 where R is the distance from the center of the beam to the fitted vertex in mm.

If an event contained more than two muons, each oppositely charged pair was considered as above. For example, if an event contained a muon pair from the target accompanied by a halo muon, only one of the two possible oppositely charged combinations would form a vertex in the target with a good χ^2.

Figure 21 shows the momentum spectra for single muons of the same sign as the beam and opposite sign to the beam after all requirements have been imposed. There is no longer evidence for background. The curves are not expected to be identical because the acceptance is slightly different for the two charges.

A few per cent of the events reconstructed contained two muons with the same charge. These events were subject to the same cuts as the oppositely charged pairs. Like sign events which pass all cuts arise from muonic decays of two hadrons produced in the target. Such decays also produce oppositely charged μ pairs which constitute a background not eliminated by the cuts. To correct for this, the like sign events are subtracted from the oppositely charged μ pair signal. Figure 22 shows the mass spectrum for like sign events compared to the spectrum for oppositely charged pairs. The like sign signal is negligible for masses above 3 GeV/c^2.

Monte Carlo Calculation

The number of muon pairs produced in the target must be known in order to calculate cross sections. To obtain this number from the observed number of muon pairs, knowledge of the detector efficiency is needed. The spectrometer efficiency was calculated with a Monte Carlo simulation program. The program generated muon pairs and counted the number of events in which both muons survived passage through the detector. Multiple scattering and energy loss were taken into account in addition to the detailed geometry of the detector. The effect of statistical fluctuations in the energy lost in the steel hadron absorber was also included. If a generated pair was in the acceptance of the spectrometer it was subject to further tests. Each muon was required to hit enough MWPC's and spark chambers to be reconstructed by the analysis program. The probability of a hit for a given plane was determined from that plane's measured efficiency. In addition, the generated muons were required to point to J, F, and P hodoscope counters which satisfied the requirements of the trigger, including the hardware mass threshold. All counters were assumed to be 100% efficient with the exception of one of the 72 P hodoscope counters which was known to have given some trouble during part of the data collection.

Finally, the muon pairs were required to satisfy the momentum and vertex χ^2 requirements applied to the data. In

this way, a correction was made for real events lost by these cuts.

A muon pair which fulfilled all the above conditions was counted as a "success". Then the detector efficiency is defined by:

$$\epsilon = \frac{N_{success}}{N_{generated}}$$

where Ngenerated is the number of μ pairs generated.

The Monte Carlo program did not generate any extra fake tracks or wire hits. Such noise does occur in the real data and can potentially confuse the analysis program so that the reconstruction fails. It is losses of this type that the reconstruction efficiency correction covers as described earlier in this chapter.

Six variables are required to completely specify each muon pair. A useful choice for this set of variables is the muon pair invariant mass (m), Feynman x (x_F), transverse momentum (p_T), azimuthal angle (φ), and the decay angles (θ^*, ϕ^*) of one of the muons in the μ pair rest frame. The probability for detecting a muon pair depends on these variables. The angle φ, i.e., the azimuthal angle of the μ pair in the plane perpendicular to the beam, has no physical significance since the beam and target are not polarized. For this reason, the variable φ is not considered and all results represent averages over φ.

One possible way to determine the detector efficiency as a function of the five remaining variables is to generate μ pairs at fixed points in m, x_F, p_T, θ^*, ϕ^* space and

determine the fraction of generated events in which both muons pass through the entire detector. This procedure was not used as it was judged to be too time consuming. For just 5 fixed points in each variable, there are $5^5 = 3125$ points at which to determine the efficiency. Instead, μ pairs were generated at fixed values of m, x_F and p_T, but from spectra for $\cos\theta^*$ and ϕ^*. The values of m, x_F and p_T used are listed in Table 8. Two different $\cos\theta^*$ spectra were used: a $1 + \cos^2\theta^*$ distribution and a distribution flat in $\cos\theta^*$. The ϕ^* distribution used was flat. These choices were motivated by the data as discussed in Chapter IV. Thus two sets of efficiencies were calculated at the values of m, x_F, and p_T given in the table:

$$\epsilon(m, x_F, p_T;\ \text{averaged over angle}) = \frac{\#\ \text{of successes in}\ m, x_F, p_T\ \text{bin}}{\#\ \text{generated}}$$

The next step was to determine how the efficiency varied with angle. For this calculation, muon pairs were generated from spectra in mass, x_F and p_T, but at fixed angles. The mass, x_F and p_T distributions used were taken from the data. The "successes", as described above, were binned according to the values of the angles reconstructed. In this way, the resolution smearing of the detector was taken into account. Because of the resolution smearing, the reconstructed values of the angles are not the same as the generated values. So for the angle efficiencies:

$$\epsilon(\theta^*, \phi^*;\ \text{averaged over}\ m, x_F, p_T) = \frac{\#\ \text{of successes in}\ \theta^*, \phi^*\ \text{bin}}{\#\ \text{generated}}$$

The calculated acceptance was smoothly varying over the whole range of mass, x_F, p_T, θ^* and Φ^*. Some plots of the acceptance are shown in Figures 23-25. Note that the acceptance in angle varies somewhat with the choice of reference axis. Possible choices for the reference axis are discussed in Chapter IV. Linear interpolation was used to get the efficiency between the generated values.

The Monte Carlo program was also used to calculate the resolution and shifts in mass, x_F and p_T. Events were generated from distributions in mass, x_F and p_T to simulate the real data. For each event which satisfied all requirements to be detected (a "success" as defined above), the kinematic quantities were reconstructed from simulated wire hits. Plots were made of the difference between the generated value and the reconstructed value for each variable in different kinematic regions. The widths of these distributions are due to the detector resolution. The deviation of the centers of the distributions from zero ("shifts") was also studied.

In mass, the average shift is very small - about 10 MeV/c^2. The mass resolution (σ) is 170 MeV/c^2 at the J/ψ and increases with mass although the ratio σ_m/m decreases slightly with mass. The average x_F shift is about -.002. The average x_F resolution is .02. The x_F resolution is worse at larger values of x_F (about .04 at x_F =0.9) since high momentum particles are bent less by the magnet and the change in angle is therefore harder to measure.

The transverse momentum resolution (σ) is about 280 MeV/c. For p_T > 1 GeV/c, the average p_T shift is about -30 MeV/c. For small p_T though, the shifts are much higher - about 130 MeV/c. This is because p_T is always greater than zero, so the small p_T values can only be smeared to larger p_T.

The effects of resolution smearing are shown in Figures 26 and 27. In these figures, the generated x_F and p_T distributions at the J/ψ (solid lines) are compared with the reconstructed spectra (x's). The x's were obtained by binning the successes, weighted by efficiency, according to the value of x_F (Figure 26) or p_T (Figure 27) reconstructed. The reconstructed spectra would differ from the generated spectra if the reconstructed values of x_F and p_T were very different from the generated values. Also, the efficiencies used to weight the reconstructed events were based on the reconstructed (not generated) mass, x_F, and p_T. Thus variations of efficiency over the range of the resolution in mass, x_F, or p_T could distort the reconstructed spectrum. In Figure 26, the reconstructed p_T spectrum falls below the generated spectrum at low p_T. This is because the reconstructed p_T values tend to be shifted to higher p_T where the cross section is smaller. The otherwise good agreeement between the generated and reconstructed spectra in Figures 26 and 27 indicates that the resolution and shifts do not cause significant distortion and that the detector efficiency is well understood.

Normalization

Cross sections are calculated from the data using:

$$\sigma = \frac{N_{ev}}{\frac{\rho N_0 \ell}{A} B_0 (1-e^{-\ell/\lambda}) \frac{\lambda}{\ell}} \qquad (4)$$

where N_{ev} = # of events, corrected for acceptance

ρ = target density

ℓ = target length

N_0 = Avogadro's number

A = target atomic weight

B_0 = number of incident beam particles

λ = absorption length for beam particles in the target material.

The factor $(1-e^{-\ell/\lambda})\ \lambda/\ell$ accounts for attenuation of the beam in the target. Absorption lengths were calculated using measured absorption cross sections from reference 23. Target lengths and densities have been presented in Table 3.

The number of incident beam particles was scaled and written on tape with each trigger as the data were collected. For the positive beam data, sums of coincidences between B and the Čerenkov counters were used to define the number of pions, kaons, and protons. All Čerenkov counters were required to be off for a proton and all Čerenkov counters on for a pion. The requirement for a kaon was C2 and C4 off with C3 and C5 on. Table 9 shows the Čerenkov counter efficiencies and the probabiltiies for accidentals in the counters. These numbers were calculated assuming that accidentals and inefficiencies in the four Čerenkov

counters were uncorrelated. The numbers of Table 9 together with the beam composition information (Table 2) show that the kaon sample contains ~ 2% protons and 3% pions. There is negligible contamination in the pion and proton samples (<.1%).

For the negative data, all Čerenkov counters were set just below $\bar{p}$ threshold and the Čerenkov counter latch bits were used to identify antiproton events. An antiproton was defined as no more than one Čerenkov counter on for the negative beam running on carbon only. For normalization, the $\bar{p}$ component was taken to be 0.5% of the beam, as measured by Aubert, et al.[24] No Čerenkov counter information was used for normalization of the data taken with heavy targets. The beam scaler was used for B_o in equation (4).

Two corrections were applied to the number of beam particles measured by the scalers. The numbers are in Table 10. The CAMAC error correction arose because the CAMAC scalers were not reset after events with CAMAC errors. Thus these events were lost, but the beam scalers still counted. The number in the table is (1.0 - # CAMAC errors/# events). This correction ranged from 0.3% for the carbon data to about 5% for the data taken with the tungsten target.

The second correction was the "multiple particle bucket" correction. As described in Chapter II, an electronic veto on more than one beam particle per RF bucket was not present during the high intensity running with negative beam and heavy targets. Since the beam scaler

cannot count more than one particle per bucket, B will be too low. This is corrected for in the following way: The beam scaler can count only 1 particle per bucket. If B counts one for every bucket with at least one particle then:

$$B_{meas} = N_B - N_B P_o$$

where B_{meas} is the measured number of beam particles per pulse, N_B is the number of buckets per pulse and $N_B P_o$ is the number of buckets per pulse with no particles in the bucket. The parameter N_B is corrected for the experimental dead time and a duty factor which is a measure of the flatness of the spill in time. Both of these effects decrease the effective length of the spill. The experiment was live 80-85% of the time and the duty factor was about 0.7 so N_B is the number of buckets in an effective spill about .6 the length of the actual spill. To determine P_o - the probability for an empty bucket - it is assumed that the probability for n particles in a bucket follows a Poisson distribution:

$$P_n = \frac{\lambda^n e^{-\lambda}}{n!}$$

where λ is the mean number of particles per bucket:

$$\lambda = \frac{B_{True}}{N_B}$$

so $B_{meas} = N_B (1 - e^{-B_{True}/N_B})$

or $B_{True} = -N_B \ln(1 - B_{meas}/N_B)$

This prescription was used to calculate the true beam intensity from the measured intensity. The corrections to the copper and tungsten data were about 20%.

Two overall corrections were applied; see Table 10. One of the P hodoscope counters was known to be inefficient during part of the data taking. The effect on overall reconstruction efficiency was calculated with the Monte Carlo program. Finally the reconstruction efficiency corrections determined from the event display scanning are included.

The sensitivities in picobarns/nucleus-event are listed in Table 10. The extrapolation to cross sections per nucleon is discussed in Chapter IV.

CHAPTER IV

RESULTS

This chapter presents the results of the experiment. The first section describes the general features of the data. The second section compares the data with the quark-antiquark annihilation model and the third section uses the data to determine the pion quark structure function.

General Features of the Data

The normalized data were binned in mass, Feynman x, and transverse momentum. For each event, a correction was made for acceptance using the efficiencies calculated from the Monte Carlo program. The like sign events were subtracted from each bin as explained in Chapter III. Features of the resulting cross section distributions are discussed in this section. It should be noted that the errors shown in the cross section plots are statistical. Overall normalization uncertainties of 20% should also be applied for systematic effects.

Mass Dependence

Muon pair invariant mass distributions are shown in Figures 28 - 35 for the various beam and target types. In

Figures 34 and 35, the measured atomic mass number dependence (discussed below) has been used to combine the data from π^- on three different targets, in order to plot cross sections per nucleon.

All the mass spectra show a strong peak at the J/ψ resonance (3.1 GeV/c^2). A summary of the cross section results for J/ψ production is given in Table 11. The errors quoted for the $\bar{p}$ and K^+ J/ψ cross sections are dominated by uncertainties in the normalization.

Production of the $\psi'(3.7)$ is also observed in the data. The ψ' is clearly seen in Figure 35 where the π^- data from the three different targets are combined and the mass scale is expanded to show the region 2.5 - 4.5 GeV/c^2 in more detail. The cross sections for ψ' production are also given in Table 11. To determine these cross sections, the data were fit to two resonances (J/ψ and ψ') and an exponentially falling continuum. The fit, drawn in Figure 35, is in excellent agreement with the data. The J/ψ line shape used was determined by the Monte Carlo program. The ψ' line shape was taken to be the same as that of the J/ψ. The ψ' cross sections were obtained by integrating the ψ' line shape, as normalized by the fit, with the continuum and J/ψ tail subtracted.

The π^-, π^+, and p induced data show a substantial muon pair continuum. For the π^- data, the shape of the continuum

in the region 4.0 - 8.0 GeV/c^2 is reasonably represented by either a power law or an exponential:

$$\frac{d\sigma}{dM} \sim e^{-(0.99 \pm .03) M} \quad \text{or} \quad \frac{d\sigma}{dM} \sim \frac{1}{M^{5.6 \pm .05}}$$

The π^+ and p induced mass distributions fall off more rapidly with mass. This is discussed in more detail in the next section.

The π^- data sample (Figure 34) contains events out to 11 GeV/c^2 in mass. No conclusive evidence is seen for an enhancement at 9.5 GeV/c^2 . An upper limit for Υ production in 225 GeV/c π^--N collisions can be obtained by fitting the data to a power law continuum plus a Gaussian resonance centered at 9.46 GeV/c^2 with a σ of 380 MeV/c^2 (the experimental resolution in this mass region as determined by the Monte Carlo program). The limit is 1.4 pb/nucleon with 95% confidence. The ratio of signal to continuum is 0.4 ± 0.4 in a 1.0 GeV/c^2 wide mass region. For comparison, the Columbia-Fermilab-Stonybrook (CFS) collaboration[25] observes no signal for Υ production by 200 GeV protons and reports a limit for the ratio of resonance to continuum of 0.1 ± 0.1 over a 1 GeV/c^2 mass interval. The π^- induced μ pair continuum is about 100 times larger than the p induced continuum in this mass region, and could mask the resonance, depending on the production mechanism.

Feynman X Distributions

The Feynman x (x_F) of the pair is defined by:

$$x_F = p_{\parallel}^* / p_{\parallel}^*(max)$$

where * indicates measurement in the center of mass system.

For sufficiently low pair masses, $P_{\parallel}^{*}$ (max) = $\sqrt{s}$ /2, where $\sqrt{s}$ is the total center of mass energy. But if $M_{\mu\mu}$ = 8.5 GeV/c^2, for example, $P_{\parallel}^{*}$ (max) = .83 $\sqrt{s}$ /2. In the x_F distributions shown, the x_F definition takes into account the creation of a massive pair.

Plots of $Ed\sigma/dx_F$ are shown in Figures 36-44. In Figures 36-39, the x_F distribution is plotted for the π^- induced data for p_T above and below 1 GeV/c. The data have been divided into six mass intervals. For data with masses above the J/ψ mass, the x_F distribution becomes progressively flatter as the mass increases. Similar trends are seen in the π^+ induced data (Figures 40-41) and the proton induced data (Figures 42-43). For both pions and protons, the x_F distribution for J/ψ events is steeper than the x_F distribution for continuum events above and below the resonance. The π^- induced x_F distributions show the flattening with increasing mass in both p_T intervals. The x_F distributions are steeper in the higher p_T bin for each mass interval.

The x_F distributions for K^+ and $\bar{p}$ induced J/ψ events are shown in Figure 44. By comparing the plots to Figures 40 and 42, one finds that the $\bar{p}$ induced spectrum closely resembles that of protons while the distribution from K^+ induced μ pairs is closer in shape to the pion induced distribution.

Parametrizations for fits to $Ed\sigma/dx_F$ are listed in Table 12. The form $a(1-x)^b$ was used for the proton fits. The pion fits were folded about $x_F = 0.2$ as suggested by Abolins, et al.[26] In Table 13, the cross section $d\sigma/dMdx_F$ is given for π^- induced μ pairs with mass above 4 GeV/c^2.

Transverse Momentum Distributions

The transverse momentum (p_T) distributions are shown in Figures 45-53. The data have been fit to the form:

$$\frac{1}{p_T}\frac{d\sigma}{dp_T} = \frac{a}{\left(1+\frac{p_T^2}{b^2}\right)^6}$$

as suggested by Yoh, et al.[25] Parameters for the fits are given in Table 14. The parameter b varies slowly with mass and is not strongly dependent on particle type. The π^- data have been divided into two x_F regions for each mass bin. The transverse momentum distributions are slightly flatter for the low x_F data.

In Figure 54, the mean transverse momentum is plotted as a function of mass. The π^- and proton induced data from this experiment are shown as well as some results from other experiments. The lower mass π^- data are from an earlier experiment performed by this collaboration.[27] The proton data at high masses are from an experiment performed by the Columbia-Fermilab-Stonybrook (CFS) collaboration[25] in which 200 GeV protons were used and high mass muon pairs with x_F = 0 were detected. The mean p_T increases with mass up to M =

4 GeV/c^2 where it reaches a plateau. The plateau value is approximately 1.2 GeV/c for pion induced μ pairs and about 200 MeV/c lower for the proton induced data. These results are summarized in Table 15 along with values of $\langle p_T^2 \rangle$ for the various beam particle types and mass intervals.

Figure 55 shows the mean p_T plotted versus x_F for the π^- induced data. Within uncertainties of ~100 MeV/c, no dependence of $\langle p_T \rangle$ on x_F is observed. Thus the difference in $\langle p_T \rangle$ between pions and protons is not due to a variation of $\langle p_T \rangle$ with x_F.

Dependence on Atomic Mass Number

Previous measurements[27,28] have shown that the cross sections for μ pair production from different nuclear targets are consistent with a power law:

$$\sigma(A) = \sigma_0 A^{\alpha}$$

where A is the atomic mass number of the target nucleus and α is a parameter which may depend on the kinematic region considered. The π^- induced data from C, Cu, and W targets were fit to this form and the behavior of α was investigated as a function of mass, p_T and x_F. For the fits, the statistical error associated with each cross section measurement was combined in quadrature with a 12% systematic error. A good χ^2 was obtained for each determination of α. Figure 56 shows the cross section σ plotted vs. A for five mass intervals. The fits for α as a function of x_F and p_T are of similar quality.

The variation of α with mass is shown in Figure 57 for π^- induced μ pairs. Most of the lower mass data points are taken from reference 27; reference 29 has furnished a value of α for J/ψ events. The power α rises with mass up to masses around 3.5 GeV/c^2. For masses greater than 4 GeV/c^2, the data are consistent with α constant at 1.12 $\pm$ .05.

For comparison, Figure 58 shows α plotted versus mass for proton induced μ pair data. The data for masses above 5 GeV/c^2 are from reference 30. As in the π^- induced data, α rises with mass for masses below 4 GeV/c^2. The higher mass points are consistent with α constant at 1.02.

Figures 59 and 60 show the transverse momentum and x_F dependence of α for three different mass regions: the continuum below the J/ψ resonance ($2.0<M<2.7$ GeV/c^2), the J/ψ ($2.7<M<3.5$ GeV/c^2) and the continuum above the J/ψ ($M>4$ GeV/c^2). A systematic rise of α with p_T is seen in the J/ψ interval. Similar results have been reported for other inclusive hadron production.[31] In particular, Antipov et al.[29] report an increase of α with p_T for π^- induced J/ψ events. No significant variation of α with x_F is seen in any mass interval.

Comparison of the Data with the Quark-Antiquark Annihilation Model

As discussed in Chapter I, several specific predictions arise if the muon pairs are assumed to come from virtual

photons produced by quark-antiquark annihilation. This section shows how the data compare with the predictions.

Cross Section Ratios

In the Drell Yan model, the cross section for lepton pair production is:

$$\frac{d^2\sigma}{dM\,dx_F} = \frac{8\pi\alpha^2}{9M^3}\frac{1}{\sqrt{x_F^2+4M^2/s}}\sum_i e_i^2\left[x_1 f_i^A(x_1)\,x_2 f_i^B(x_2) + x_1 f_i^A(x_1)\,x_2 f_i^B(x_2)\right] \qquad (1)$$

where $x_{1,2}$ are the momentum fractions of the annihilating quarks in the projectile and target hadrons and $xf_i^A(x)$ is the momentum spectrum for quarks of flavor i in hadron A. Transverse momentum is neglected in this equation and a factor of 1/3 for color is included.

If the two interacting hadrons are both nucleons, there are no valence antiquarks available for annihilation. Then the antiquarks must come from the $q\bar{q}$ sea. Since the probability density distributions for quarks in the sea fall steeply with x_1 and x_2, the cross section for pN $\rightarrow \mu^+\mu^- X$ should fall rapidly with mass at fixed x_F.

If a pion beam is used, the projectile hadron contains a valence antiquark. Valence quarks are more likely to carry large momentum than sea quarks. Thus the mass spectrum for pion induced μ pairs should fall more slowly with mass than the proton induced μ pair mass spectrum. This effect was mentioned in the preceding section (see Figures 28 and 34).

Figure 61 shows the ratio of the pion induced μ pair cross section to the proton induced cross section. Cross sections with c.m. rapidity in the range $0.0<y<0.4$ are used so that proton induced data from another experiment[25] can be included for the higher mass points. The cross section ratio rises steeply with $m/\sqrt{s}$ as predicted by the model.

Another test of the quark-antiquark annihilation model is provided by the ratio of the π^+ induced μ pair production cross section to the π^- induced μ pair production cross section. If x_1 is sufficiently large (greater than 0.2), it is expected that the pion sea may be neglected in equation (1) and for π -N collisions:

$$\frac{d^2\sigma^{\pi N}}{dM\,dx_F} = \frac{8\pi\alpha^2}{9M^3}\frac{1}{\sqrt{x_F^2+4M^2/s}}\left\{\frac{4}{9}x_1\bar{u}^{\pi}(x_1)x_2u^N(x_2)+\frac{1}{9}x_1d^{\pi}(x_1)x_2\bar{d}^N(x_2)\right\}$$

The appropriate quark charges (e_i) have been inserted. Setting $x_1\bar{u}^{\pi^-}(x_1) = f^{\pi}(x_1)$ and using $\bar{u}^{\pi^-} = \bar{d}^{\pi^+} = d^{\pi^-} = u^{\pi^+}$ (from G parity invariance), one finds:

$$\frac{d^2\sigma}{dM\,dx_F} = \frac{8\pi\alpha^2}{9M^3}\frac{1}{\sqrt{x_F^2+4M^2/s}}f^{\pi}(x_1)\left\{\frac{4}{9}x_2u^N(x_2)+\frac{1}{9}x_2\bar{d}^N(x_2)\right\} \text{ for } \pi^- \qquad (5a)$$

$$\frac{d^2\sigma}{dM\,dx_F} = \frac{8\pi\alpha^2}{9M^3}\frac{1}{\sqrt{x_F^2+4M^2/s}}f^{\pi}(x_1)\left\{\frac{4}{9}x_2\bar{u}^N(x_2)+\frac{1}{9}x_2d^N(x_2)\right\} \text{ for } \pi^+ \qquad (5b)$$

As noted in Chapter I, $u^N = d^N$ for an isoscalar target. Thus equations (5a) and (5b) show that the ratio of the π^+ induced cross section to π^- induced cross section will be 1/4 if the $\bar{u}^N$ and $\bar{d}^N$ terms are negligible. The nucleon contains $\bar{u}$ and $\bar{d}$ quarks only in the sea and thus terms involving $\bar{u}^N$

and $\bar{d}^N$ are negligible for high x_2 . The prediction is :

$$\frac{\sigma(\pi^+ C \to \mu^+\mu^- X)}{\sigma(\pi^- C \to \mu^+\mu^- X)} \xrightarrow[\text{mass}]{\text{high}} \frac{1}{4}$$

Figure 62 shows the measured π^+/π^- cross section ratio as a function of mass. The ratio is close to one for the J/ψ. A value of one would be expected if the J/ψ were produced strongly because the isoscalar target makes the reaction charge symmetric. For masses above the J/ψ , the ratio decreases toward 1/4 as predicted. From equations (5a) and (5b), it can be seen that the approach to 1/4 of the π^+/π^- ratio is determined by the nucleon sea quark distribution. If x_2 goes to zero, then $\bar{u}^N = u^N$ and the ratio is one. As the mass increases, the contribution of the sea to the cross section decreases and the ratio approaches 1/4. This point is discussed more fully later in this chapter.

Helicity Angular Distributions

As shown in Chapter I, the Drell Yan model predicts that in the μ pair rest frame:

$$\frac{d\sigma}{d\Omega} \sim 1 + \cos^2\theta^* \qquad (2)$$

for the annihilation of massless quarks. The above equation requires that θ^* be measured relative to the quark momentum direction. If the μ pair is produced with some nonzero transverse momentum, then the quark momentum direction is not known. Collins and Soper[32] have suggested the direction halfway between the beam and the reverse of the target vector as an estimate of the quark momentum direction. With

this choice of reference axis, the angular distributions for three different mass regions were calculated. The mass intervals used were below the J/ψ ($2.0<m<2.7$), the J/ψ ($2.7<m<3.5$) and above the J/ψ ($m>3.5$ GeV/c^2). The results are shown in Figure 63, along with fits to the form $1 + \lambda \cos^2\theta^*$. Values of λ obtained are summarized in Table 16.

The J/ψ angular distribution is consistent with being flat. The continuum both above and below the J/ψ shows definite spin alignment. The angular distributions have been corrected for detector acceptance, but the efficiency as a function of angle is not strongly mass dependent. Thus the change of the angular distribution with mass is not due to changes in acceptance.

The angular distributions were also calculated using other possible estimates for the quark momentum direction. These are shown in Figure 64, together with the Collins-Soper direction described above. The s channel system uses the recoil direction, the t channel the beam direction, and the u channel the target particle direction. If the μ pair has no transverse momentum, all of the directions shown in Figure 64 are equivalent. In Figures 65-67, the s, t, and u channel helicity angular distributions are plotted. These have been fit to the form $1 + \lambda \cos^2\theta^*$ and values of λ are included in Table 16. Results similar to those presented in Figure 60 are seen. In particular, the angular distribution for the J/ψ is much flatter than that of the continuum, for all choices of reference axis. Thus, two different

production mechanisms are suggested by the change in angular distribution with mass and this conclusion is independent of the choice of reference direction.

Recently, it has been suggested that muon pairs of large transverse momentum ($p_T > 1$ GeV/c) may be produced by QCD processes.[33] Such processes could lead to an angular distribution different from the $1 + \cos^2\theta^*$ prediction of the Drell Yan model. Figures 68 and 69 show the angular distribution for the continuum above the J/ψ plotted in two different p_T regions for the four choices of reference axis described above. There is evidence for spin alignment in both p_T intervals. As might be expected, the four angular distributions look more alike in the low p_T region, since in the limit of zero p_T all reference axes are the same. For $p_T < 1.0$ all choices of reference axis give a value of λ consistent with 1.0 except the s channel. The s channel helicity angle uses the recoil direction as a reference axis. When p_T is small, the p_T measurement is not very precise due to the detector resolution. The recoil direction is more sensitive to p_T effects than the beam or target direction. Also, the μ pair cross section falls with both x_F and p_T so the cross section is largest when these variables are small. But if x_F and p_T are small, the recoil is nearly motionless and thus the recoil direction will not be well defined in the dimuon center of mass frame.[34] For this reason, the s channel helicity may be less meaningful than the other choices when p_T is small.

If the virtual photon from quark-antiquark annihilation is not in a pure spin state, the off-diagonal elements of the photon spin density matrix will be nonzero. Then according to equation (3), the data would show some dependence on the azimuthal angle ϕ^*. The ϕ^* angle is measured from an x axis defined as normal to the plane containing the beam, target and recoil vectors. The z axis should be the quark momentum direction; it is approximated by any of the four vectors in Figure 64 as explained above. Then ϕ^* is the azimuthal angle in the x,y plane with the y axis chosen to make a right handed coordinate system.

Since background events are not negligible in the mass region below the J/ψ, a background subtraction must be performed. To simulate uncorrelated μ pairs of opposite sign which arise from decays, muons in real data events were paired with muons of the opposite charge in the following event. The resulting uncorrelated μ pairs which passed all cuts were normalized to the observed like sign μ pair signal and subtracted from the ϕ^* distributions. The like sign events themselves were not used to estimate the background because the detector acceptance in ϕ^* for like sign pairs is not the same as that for opposite sign pairs.

The resulting ϕ^* distributions are shown in Figures 70-73 for the J/ψ ($2.7<m<3.5$ GeV/c^2) and the continuum regions above and below the J/ψ. In Figure 70 the Collins-Soper direction was used for the z axis. No evidence is seen for variation with ϕ^* in any mass interval. In Figures

71-73 the distributions are shown for the other three choices of z axis. Some peaking of the ϕ^* distribution is seen in the t channel plot in the lowest mass interval. The other distributions are consistent with being flat.

Scaling

If equation (1) is integrated over x_F, one arrives at the scaling prediction, i.e., $m^3 d\sigma/dm$ is a function only of m^2/s. This experiment has data at only one value of s and thus data from other experiments are required to check the scaling prediction.[25,35-37] Figure 74 shows $m^3 d\sigma/dm$ for proton induced μ pairs plotted versus m^2/s. Data with beam momentum greater than 200 GeV/c are consistent with the scaling prediction. The scaling plot for π^- induced μ pair data is shown in Figure 75. The data[26,35,38,39] do not all lie on one curve so the scaling prediction is not supported. However, it should be noted that the data from several of the experiments included in Figure 75 are at masses below the J/ψ. In this lower mass region, resonance production and other non-Drell Yan processes may contribute. Also, both the $\langle p_T \rangle$ and the A dependence are changing in the mass region below 4 GeV/c^2. A better test of the scaling prediction will be possible when more high mass data at different values of s become available.

Structure Functions

As the data support the quark-antiquark annihilation model, information about hadron structure functions can be extracted from the measured μ pair cross sections. The procedure is described in this section. Using the definitions $x_{1,2} = (\pm x_F + \sqrt{x_F^2 + 4m^2/s})/2$, equation (5a) can be transformed to:

$$\frac{d^2\sigma}{dx_1 dx_2} = \frac{4\pi\alpha^2 s}{9M^4} x_1 \bar{u}^{\pi}(x_1) \{\tfrac{4}{9} x_2 u^N(x_2) + \tfrac{1}{9} x_2 \bar{d}^N(x_2)\}$$

or

$$\frac{d^2\sigma}{dx_1 dx_2} = \frac{4\pi\alpha^2 s}{9M^4} f^{\pi}(x_1) g^N(x_2) \qquad (6)$$

where $g^N(x_2) = \frac{4}{9} x_2 u^N(x_2) + \frac{1}{9} x_2 \bar{d}^N(x_2)$.

There are not enough high mass μ pair events to determine the structure functions from the π^+ data, so the discussion is restricted to π^--N collisions. Since $m^2/s = x_1 x_2$, equation (6) shows that the cross section distribution in x_1 and x_2 factors into a function of x_1 times a function of x_2. Using equation (6), the factorization hypothesis can be tested and the functions $f^{\pi}(x_1)$ and $g^N(x_2)$ deduced.

Factorization

To use equation (6), data with $4<m<8.75$ GeV/c^2 are binned in a rectangular grid of x_1 and x_2. The mass limits are chosen to avoid resonances. Data below 4 GeV/c^2 contain the J/ψ and ψ'. Above 8.75 GeV/c^2, the Υ and Υ' are not resolved but are expected to be present in the data at some level. From the Monte Carlo program, the mass resolution

(σ) at 9.5 GeV/c^2 is determined to be 380 MeV/c^2 so the choice of mass upper limit is 2σ from the Υ peak value.

The distribution of events in the x_1, x_2 plane is shown in Figure 77. Lines of constant x_F ($x_F = x_1 - x_2$) and curves of constant mass are also shown. The range of x_1 used is .25 to 1.0. The x_2 range is .05 to .28. The x_1 range is divided into 14 bins and the x_2 range is divided into 9 bins. Altogether 85 populated bins which lie entirely within the boundaries are used in the fit. The remaining 41 bins are eliminated by the mass cuts. For each event, x_1 and x_2 are calculated. The event is then entered into the appropriate x_1, x_2 bin with a weight equal to:

$$\text{WEIGHT} = \frac{m^4 * \text{cross section normalization factor (pb/event)}}{\text{detector efficiency}}$$

Thus a table of $m^4 d\sigma/dx_1 dx_2$ is generated. Data from C, Cu and W targets were used for the structure function fit. The extrapolation to per nucleon cross sections used the measured A dependence (α =1.12).

Next, the table is fit to a function of x_1 times a function of x_2 . The values of the functions at the center of each x bin are the fit parameters so no assumptions about the functions' shapes are necessary. The χ^2 for the fit is 65 for 61 degrees of freedom, so the factorization hypothesis is supported.

Normalization and the Nucleon Function

To deduce the pion structure function, the shape determined from the factorization test must be suitably normalized. Only the normalization of the product $f^{\pi}(x_1)g^{N}(x_2)$ is measured directly. The scale is fixed by normalizing the target nucleon structure function to a calculation based on deep inelastic lepton scattering data. The nucleon function cannot be normalized directly to data from these other experiments because a different linear combination of quark distribution functions is measured. Instead, individual nucleon quark distribution functions are needed so that the specific combination measured in this experiment can be calculated and compared with the data.

Several authors[40-42] have extracted the individual nucleon quark distribution functions using fits to deep inelastic lepton scattering data with the q^2 dependence calculated from QCD. In addition, a nucleon sea quark distribution has been determined by the CFS collaboration.[43] Over the interval $.05<x_2<.28$, the function $g^{N}(x_2)$ is normalized to $\frac{4}{9}x_2u^{N}+\frac{1}{9}x_2\bar{d}^{N}$ where the u valence quark distribution is taken from Buras and Gaemers[40] with $q^2 = -m^2$ and the u and d sea distributions are taken from reference 43. The data used for the structure function calculation are from three targets. Only the carbon target is isoscalar. Thus $u^{N} = a_n u^{n} + a_p u^{p}$ where the a's are the fractions of neutrons or protons in the target nucleus. In Figure 78, the normalized nucleon structure function is shown, together with the results of

the calculation. The shape of the calculation is in good agreement with the data. For comparison, Figure 78 also shows the expected functions if the sea distributions, as well as the valence quark distribution functions are taken from references 40 and 41. Both of these curves are somewhat flatter than that obtained with the CFS sea distribution. In addition, the normalization is 15-20% smaller.

It should be noted that the data from deep inelastic lepton scattering experiments, on which the fits of references 40 and 41 depend, are very sparse in the low x ($x<.3$), high q^2 ($q^2>15$) region. This means that the fits are not well constrained in the kinematic region relevant to this experiment. Figure 79 shows measurements of νW_2 from deep inelastic lepton scattering experiments,[44] together with curves calculated from the parametrizations of Buras and Gaemers and the nucleon sea quark distribution of CFS. The νW_2 data are consistent with the sea distributions of both reference 40 and reference 43. The conclusion is that the structure function normalization cannot be determined from lepton pair experiments to better than about 20% with currently available deep inelastic scattering data.

The Pion Structure Function

The pion quark distribution function is shown in Figure 80. It has been fit to the forms $x_1\bar{u}^{\pi}(x_1) = a\sqrt{x_1}(1-x_1)^b$ and $x_1\bar{u}^{\pi}(x_1) = a(1-x\ )^b$. The square root form is used so that

the quark probability function $\bar{u}^{\pi}(x_1)$ may be extrapolated to $x_1 = 0$. Several authors have suggested that the pion structure function should approach zero like $\sqrt{x}$.[45] The parameters for these and other fits described below are summarized in Table 17. Theoretical predictions for the exponent b are in the range 0 - 2.0.[46-47] The errors quoted in Table 17 and shown in Figures 78 and 80 are purely statistical. An overall normalization uncertainty of 20% should also be applied to allow for systematic effects. In particular, the cross section normalization (per nucleon) is sensitive to the power α which characterizes the A dependence.

Using the values for a and b from fit 1 in Table 17 and including normalization uncertainties, one finds:

$$\int_{.25}^{1.0} x\bar{u}^{\pi}(x)\,dx = 0.14 \pm .03 \qquad \int_{.25}^{1.0} \bar{u}^{\pi}(x)\,dx = 0.31 \pm .07$$

If the fit is used to extrapolate the results to $x_1 = 0$, the integrals are 0.20 ± 0.05 and 1.11 ± 0.27, respectively for $0<x_1<1$. The first integral is the fraction of the pion momentum carried by the $\bar{u}$ valence quark in the pion. Since both pion valence quarks are assumed to have the same distribution function, the first integral indicates that about 40% of the pion momentum is carried by valence quarks. This is close to the estimate of several authors.[47]

The second integral provides a check of a sum rule. This integral is expected to be 1 since a pion contains one

$\bar{u}$ valence quark. The value is consistent with 1, but is dependent on the unobserved low x behavior of $\bar{u}^{\pi}(x)$.[48]

All Drell Yan cross section formulae written so far have included a factor 1/3 for color. Equation (6), for example, is:

$$\frac{d^2\sigma}{dx_1 dx_2} = \frac{4\pi\alpha^2 s}{3m^4}\,\frac{1}{3}\,f^{\pi}(x_1)\,g^{N}(x_2) \qquad (6)$$

where the factor of 1/3 is now shown explicitly. The factor enters if one assumes that a quark can only annihilate an antiquark of its own color. If there are three colors, this requirement decreases the cross section by 1/3. The question then arises as to whether or not the presence of the 1/3 color factor can be confirmed on the basis of the pion structure function normalization. If the factor of 1/3 for color is not present in equation (6), then the pion quark distribution will be smaller by a factor of 1/3. The integrals given above for the measured x region become:

$$\int_{.25}^{1.0} x\,\tilde{\bar{u}}^{\pi}(x)\,dx = .05 \pm .01 \qquad \int_{.25}^{1.0} \tilde{\bar{u}}^{\pi}(x)\,dx = .10 \pm .02$$

where $\tilde{\bar{u}}^{\pi}(x) = 1/3\ \bar{u}^{\pi}(x)$. Using this alternative normalization and the function of x already obtained gives a result for the fraction of momentum carried by valence quarks of 13%. The unmeasured region accounts for about 1/3 of this integral. A value of 13% seems somewhat low, but this number is not solidly predicted. However $\int_0^1 \bar{u}(x)dx$ must be equal to 1. Figure 81 shows $\bar{u}^{\pi}$ and $\tilde{\bar{u}}^{\pi}$. For $\bar{u}^{\pi}$, the fit drawn is $a(1-x)^b/\sqrt{x}$ with a and b from fit 1 in Table 17.

For $\tilde{\bar{u}}^{\pi}$, a straight line is drawn in the region $0<x_1<.25$. The slope is chosen so that the integral of $\tilde{\bar{u}}^{\pi}$ from 0 to 1 will be 1.0. Firm conclusions are difficult since so much of the integral of $\bar{u}^{\pi}$ comes from the low x region where there are no data. The color free case cannot be excluded.

To investigate the sensitivity of the results to transverse momentum and mass dependence, the structure function fit has been performed in different kinematic regions. The results are summarized in Tables 17 and 18. The variation of the pion structure function is described by the parameters from the fit to the form $a\sqrt{x_1}(1-x_1)^b$. To gauge the sensitivity of the nucleon function to mass and p_T effects, the χ^2 for the fit of $g^N(x_2)$ to curve A of Figure 78 is given (Table 18).

The mass intervals $4.0<m<6.0$ GeV/c^2 and $5.0<m<8.75$ GeV/c^2 were used. In the lower interval, the mean mass is 4.7 GeV/c^2 while that in the upper interval is 6.0 GeV/c^2. No significant variation in either the pion or nucleon structure function was observed with mass. To further investigate the possibility of some m^2 dependence for the pion quark function, the cross section $d\sigma/dx_1dx_2$ was fit to the form $a\sqrt{x_1}(1-x_1)^b(1-x_2)^c(1+d(0.3-x)\ln(m^2/0.09))$. This form is motivated by the scale breaking observed in deep inelastic lepton scattering experiments. A value for d of -0.05 ± 0.09 was obtained, so again no evidence is seen for mass dependence. Note that since $x_1x_2 = m^2/s$, this expression cannot be written in the form $f(x_1)g(x_2)$. For

this reason, the fitting procedure described earlier could not be used. Instead, the above four parameter form was assumed and a conventional fitting program was used to determine the parameters a, b, c and d. This alternative fitting procedure was also used to check the results of the more complicated but functional form independent method. The two methods were in excellent agreement.

The structure function fit was also performed in two p_T regions: $p_T < 1.0$ GeV/c and $p_T > 1.0$ GeV/c. The pion function is the same in both cases within statistics. The nucleon function is slightly flatter in the higher p_T region. Some simple methods of including transverse momentum are discussed later in this chapter.

A Monte Carlo program was used to check the fitting procedure and estimate the effect of Fermi motion. Events were generated from the distribution $m^4 d\sigma/dx_1 dx_2 \sim (1-x_1)^1 (1-x_2)^3$. They were then binned and processed with the same fitting program used for the data. The generated distributions were successfully reproduced by the fitting program within statistical errors. This test was done with the number of events generated comparable to the number in the actual data sample (~1500), as well as with a very large Monte Carlo sample. Addition of Fermi motion increased the power for the pion quark distribution function by 0.02.[49] The nucleon structure function was more sensitive to Fermi motion; the power increased by about 0.9.

Effect of Transverse Momentum

Some simple methods of including the observed transverse momentum have been tried. There is no unique way to incorporate p_T since its origin is unknown. For the prescriptions described here, it is assumed that the measured μ pair p_T arises from the intrinsic p_T of the annihilating quarks. Then only the vector sum of the two quark transverse momenta is known.

Transverse momentum can affect the structure functions in two ways. First, the calculation of x_1 and x_2 changes. Both x_1 and x_2 are shifted to lower values. The second effect is that the quark distribution functions are smeared by a transverse momentum probability spectrum. The p_T distributions for the quarks in pions and nucleons are not known. The methods considered here ignore this aspect of the problem and deal only with the shifts of x_1 and x_2.

The μ pair energy is given by:

$$E_{\mu\mu}^2 = p_{\mu\mu}^2 + m_{\mu\mu}^2 = p_L^2 + p_T^2 + m^2$$

Also $E_{\mu\mu}^2 = (E_1 + E_2)^2$ where E_1 and E_2 are the energies of the annihilating quarks. For massless quarks, $E_i^2 = p_{Li}^2 + p_{Ti}^2$. Using the relations $x_F = 2p_L/\sqrt{s}$, $x_i = 2p_{Li}/\sqrt{s}$, one finds:

$$\frac{4M^2}{s} + \frac{4p_T^2}{s} + x_F^2 = \left(\sqrt{x_1^2 + \frac{4p_{T1}^2}{s}} + \sqrt{x_2^2 + \frac{4p_{T2}^2}{s}}\right)^2 \qquad (7)$$

Since $x_2 = x_1 - x_F$, equation (7) can be solved for x_1 in terms of m, x_F, p_T, p_{T1} and p_{T2}. The result is:

$$x_1 = \frac{x_F}{2}\left\{1 + \frac{p_{T1}^2 - p_{T2}^2}{M^2 + p_T^2}\right\} + \frac{\alpha}{2}\sqrt{1 - \frac{2(p_{T1}^2 + p_{T2}^2)}{M^2 + p_T^2} + \frac{(p_{T1}^2 - p_{T2}^2)^2}{(M^2 + p_T^2)^2}}$$

where $\alpha = \sqrt{4m^2/s + 4p_T^2/s + x_F^2}$. If $p_{T1} = p_{T2} = p_T = 0$, this expression reduces to $x_1 = x_F/2 + \sqrt{(x_F^2 + 4m^2/s)}/2$ as before.

Two methods of estimating p_{T1} and p_{T2} were tried. In one method, the quarks were assumed to have fixed $p_T = 1$ GeV/c for the pion quark and 0.75 GeV/c for the nucleon quark.[50] The angle between the two p_T vectors was chosen to produce the observed transverse momentum for the μ pair. For μ pairs with $p_T > 1.75$ GeV/c, the quark p_T vectors were assumed to be aligned. Then the observed p_T was split such that the nucleon and pion quark transverse momenta were in the ratio 0.75 to 1. For the second method, the μ pair p was split in this way for all events.

The results of the inclusion of p_T according to these two prescriptions are given in Tables 17 and 18. The shape of the pion structure function is not affected. As expected, given the results of the structure function fit in two p_T regions, the nucleon function is more sensitive to transverse momentum effects. The nucleon structure function is flatter when the p_T is included as described above.

Note that including p_T decreases the magnitude of the pion function slightly. This is because when p_T is included, the values of x_1 and x_2 decrease for each event. Since the cross section falls steeply with mass and the normalization of the nucleon function is fixed, the pion function must decrease.

Cross Sections from Structure Functions

From equations (5a) and (5b), it is clear that if the hadron structure functions are known, cross section distributions in mass and x_F may be calculated and compared with data. For the π^- induced data, this amounts to a consistency check since the data were used to determine the structure functions. Figure 82 shows the mass spectrum of the π^- induced data between 4.0 and 8.75 GeV/c^2. In Figure 83, the x_F distribution is shown for four mass intervals. The curves calculated from the structure functions of Figures 78 and 80 are in good agreement with the data.

In Figure 84, data from an earlier experiment[51] are plotted together with the data from this experiment so that the dimuon mass spectrum from 0.3 to 8.75 GeV/c^2 may be compared with the calculation based on the measured structure functions. The Drell Yan model cannot account for all continuum μ pairs produced below the J/ψ.

It is interesting to use equations (5a) and (5b) to calculate the π^+ and π^- induced μ pair cross sections and compare the ratio with the data plotted in Figure 62. In order to compute the ratio, the pion quark distribution function and two different linear combinations of nucleon quark distribution functions are needed. These are defined by:

$$G^{\pi^+} = \frac{4}{9} x_2 \bar{u}^N(x_2) + \frac{1}{9} x_2 d^N(x_2) \qquad G^{\pi^-} = \frac{4}{9} x_2 u^N(x_2) + \frac{1}{9} x_2 \bar{d}^N(x_2)$$

G^{π^+} and G^{π^-} are not measured in this experiment. Thus some

outside determination of the nucleon quark distributions is required.

In Figure 85, the ratio $\sigma(\pi^+ C \rightarrow \mu^+\mu^- X)/\sigma(\pi^- C \rightarrow \mu^+\mu^- X)$ is plotted. Two contributions to the ratio are included in addition to that calculated from equations (5a) and (5b). Because the plot includes data down to 2 GeV/c^2 in mass, the pion sea quarks may contribute to the cross section. Then equations (5a) and (5b) become:

$$\frac{d^2\sigma}{dM\,dx_F} = \frac{8\pi\alpha^2}{9M^3}\frac{1}{\sqrt{x_F^2+4M^2/s}}\left[f^{\pi}(x_1)G^{\pi^+}(x_2) + f_s^{\pi}(x_1)x_2\left\{\tfrac{4}{9}u^N + \tfrac{4}{9}\bar{u}^N + \tfrac{1}{9}d^N + \tfrac{1}{9}\bar{d}^N + \tfrac{1}{9}s^N + \tfrac{1}{9}\bar{s}^N\right\}\right] \quad (\pi^+)$$

$$\frac{d^2\sigma}{dM\,dx_F} = \frac{8\pi\alpha^2}{9M^3}\frac{1}{\sqrt{x_F^2+4M^2/s}}\left[f^{\pi}(x_1)G^{\pi^-}(x_2) + f_s^{\pi}(x_1)x_2\left\{\tfrac{4}{9}u^N + \tfrac{4}{9}\bar{u}^N + \tfrac{1}{9}d^N + \tfrac{1}{9}\bar{d}^N + \tfrac{1}{9}s^N + \tfrac{1}{9}\bar{s}^N\right\}\right] \quad (\pi^-)$$

The pion sea quark distribution ($f_s^{\pi}(x_1)$) has not been measured. It is estimated[48] to be $0.1(1-x)^5$. With this estimate, the pion sea has a negligible effect on the ratio for masses above the J/ψ. Below the J/ψ, the pion sea contributes less than 5% to the ratio.

The effect of resonances is taken into account by using the observed value of 0.9 for the cross section ratio at the J/ψ and assuming the same value for the ψ'. The relative amounts of resonance and continuum as a function of mass are determined from the fit to the data shown in Figure 35. Thus:

R(drawn) = R(calculated)*fraction of continuum
+ 0.9*fraction of resonance

The two curves in Figure 85 used different parametrizations of the nucleon sea quark distribution. The solid curve used the CFS sea distribution[43] and the dashed

curve used the sea distribution of Buras and Gaemers.[40] In both cases, the valence quark distributions were taken from Buras and Gaemers and the pion quark function used was that determined by this experiment. But, as mentioned in the preceding section, the ratio is insensitive to $\bar{u}^{\pi}$; it is determined mainly by the nucleon sea quark distribution. Figure 85 indicates that the data are better described by the nucleon sea quark distribution of CFS than that of Buras and Gaemers. This was also the case in Figure 78 where the nucleon function determined from this experiment was in good agreement with a calculation which used the CFS sea. The CFS experiment measures the nucleon sea quark distribution more directly than the deep inelastic lepton scattering experiments. Also, the CFS data are at q^2 values closer to this experiment ($25<q^2<150$ GeV^2), though their measured x range ($0.2<x<0.5$) is higher than the x_2 range of this experiment. The agreement of the solid curve with the data in Figure 85 as well as Figure 78 suggests that the CFS nucleon sea quark distribution may be successfully extrapolated below x = 0.2.

A Few Words About QCD

This chapter has interpreted the experimental data within the framework of the quark-antiquark annihilation model. The data were seen to be in reasonable agreement with several predictions of the model and the model was used to determine the momentum distribution for valence quarks in

the charged pion. However, the "naive" Drell Yan model has certain limitations.[52]

The transverse momentum distribution of muon pairs produced in hadron collisions is a feature of the data not explained by the quark-antiquark annihilation model. When equation (1) was introduced, it was stated that the quark transverse momenta were being neglected. The transverse momentum carried by quarks and antiquarks in hadrons was assumed to be small. Yet experimentally, the muon pairs are observed to have fairly large transverse momentum - about 1.2 GeV/c for pion induced μ pairs above the J/ψ. The quarks are expected to have some transverse momentum from being confined within a hadron. From the Uncertainty Principle, the estimate is about 300 MeV/c. If, in addition, the motion of the quarks in the hadron is considered, the estimate becomes $\sim$ 600 MeV/c.[53] These estimates cannot easily account for the observed μ pair p_T if it is assumed to come from the transverse momentum of the annihilating quarks.

A second possible difficulty with the Drell Yan model involves scale breaking in the structure functions. The structure functions written throughout this chapter were assumed to depend only on x, not explicitly on m^2. Some simple tests showed no evidence for mass dependence in the pion structure function. But deep inelastic lepton scattering experiments have shown that hadron structure functions depend on q^2 as well as the dimensionless scaling

variable $x = q^2/2m\nu$.[54] Figure 86 shows the lowest order diagrams which are believed to contribute to deep inelastic scattering. The first diagram was shown in Chapter I. The other two diagrams contain gluons and the strong coupling constant α_s. These are QCD diagrams. In the QCD picture,[55] a quark may radiate a gluon, losing energy. Thus the QCD diagrams give relatively more low energy quarks. The expectation from QCD is that at high q^2, where the QCD diagrams contribute more, the quark distribution functions become more strongly peaked at low x. This has been observed experimentally.[54]

This leads to a third objection to the naive quark-antiquark annihilation model. Diagrams like those of Figure 86 have not been considered. The two lowest order QCD diagrams for dilepton production are shown in Figure 87. Currently, these three problems - large transverse momentum, scaling violations, and contribution of other diagrams- are all believed to be interconnected.[56,57] The connection between QCD diagrams and scale breaking in structure functions has been mentioned above. In addition, the QCD diagrams can generate lepton pairs with large transverse momentum since there is a gluon or quark jet to recoil from the virtual photon.

Politzer[56] has conjectured that the Drell Yan model is completely consistent with QCD as long as q^2 dependent structure functions are used. The idea is that the QCD diagrams to all orders in α_s generate the q^2 dependence of

structure functions. Then QCD diagrams are included automatically if scale breaking structure functions are used. The conjecture also states that the structure functions measured in high mass lepton pair experiments are the same as those of deep inelastic lepton scattering with $m^2 = |q^2|$. For this QCD model, the conjecture has been proven to order α_s^2 for leading logarithmically divergent contributions in each order.

Many people are currently working on QCD calculations[58] and trying to compare the results with experimental data, particularly transverse momentum distributions. There are some difficulties. The calculated QCD cross sections diverge like p_T^{-2} for small p_T.[59] Another problem is the effect of the intrinsic p_T associated with confinement. This contribution to the transverse momentum is not understood. It is expected to be very important in the small p_T region (< 1 GeV/c) and it will smear the p_T distribution at larger values of p_T.[60] Both of these problems make the QCD calculations difficult to compare with data if p_T is small. In addition, the QCD calculations require knowledge of quark and gluon momentum distributions. The gluon momentum distribution is not well known. Before this experiment, the pion structure function had not been determined so most of the published results of QCD calculations of p_T distributions are for proton collisions. For these reasons, no QCD calculations are presented with the results of this experiment. As the determinations of

quark and gluon distribution functions become more reliable and understanding of the intrinsic quark p_T improves, comparison of the QCD calculations with experimental data may become more meaningful.

Conclusions

This thesis has presented the results of an experiment which studied muon pairs produced in hadron collisions. Detailed measurements were made of the μ pair production cross section as a function of invariant mass, Feynman x, transverse momentum, and decay angle. The data have been compared with expectations of the quark-antiquark annihilation model. Several predictions of the model have been strikingly supported including the dependence of μ pair production on incident beam particle type and the form of the μ pair decay angular distributions. The data have been used within the framework of the quark-antiquark annihilation model to determine the momentum distribution for valence quarks in the charged pion. The resulting pion structure function is within the range of theoretical predictions of both normalization and shape. A nucleon structure function obtained is in good agreement with expectations based on earlier experiments.

Data from several other μ pair experiments using pion beams will be available soon. They should extend the work of this experiment in several ways. Detectors with acceptance for high mass events with negative Feynman x will

be able to determine the pion structure function for $x < 0.25$ and may provide information about the momentum distribution for the pion sea quarks. The scaling prediction, not well satisfied by existing data on pion induced μ pair production, will be more stringently tested as more high mass data at different values of s become available. Data at different values of s may also make possible a determination of the m^2 dependence of the pion structure function.

Dilepton experiments have become an important complement to deep inelastic lepton scattering experiments for the study of hadron structure through the electromagnetic interaction. Eventually, both types of experiment may also contribute to an understanding of the strong interaction based on quantum chromodynamics.

REFERENCES

1. R. Hofstadter, Ann. Rev. Nucl. Sci. 7, 231 (1957); F. Bumiller et al., Phys. Rev. 124, 1623 (1961).

2. E. D. Bloom et al., Report to the Fourteenth International Conference on High Energy Physics, Vienna, 1968; S. Stein et al., Phys. Rev. D12, 1884 (1975).

3. H. L. Anderson et al., Phys. Rev. Lett. 37, 4 (1976) and Phys. Rev. Lett. 38, 1450 (1977).

4. This scaling behavior was predicted by Bjorken; see J. D. Bjorken, Phys. Rev. 179, 1547 (1969).

5. S. D. Drell and T.-M. Yan, Phys. Rev. Lett. 25, 316 (1970) and Ann. Phys. 66, 578 (1971).

6. M. Gell-Mann, Phys. Lett. 8, 214 (1964); G. Zweig, CERN report 8419/Th412 (1964).

7. R. P. Feynman, "The Behavior of Hadron Collisions at Extreme Energies," in High Energy Collisions, Third International Conference at State University of New York, Stony Brook 1969 (Gordon and Breach, 1969), p. 237; J. D. Bjorken and E. A. Paschos, Phys. Rev. 185, 1975 (1969).

8. Quarks and partons are discussed extensively in R. P. Feynman, Photon-Hadron Interactions (Benjamin, 1972).

9. For a recent review of QCD, see R. D. Field, CALT-68-683, invited talk given at the XIX International Conference on High Energy Physics, Tokyo, Japan, 1978, and references contained therein.

10. D. J. Gross and F. Wilczek, Phys. Rev. D9, 980 (1974); H. Georgi and H. D. Politzer, Phys. Rev. D9, 416 (1974).

11. R. C. Oakes, Nuovo Cimento 44A, 440 (1966).

12. K. Vasavada, Phys. Rev. D16, 146 (1977).

13. P. Schilly et al., Nucl. Instr. and Meth. 91, 221 (1971) and H. Cunitz et al., Nucl. Instr. and Meth. 91, 211 (1971).

14. K. B. Burns et al., Nucl. Instr. and Meth. 106, 171 (1973).

15. T. A. Nunnamaker, Nucl. Instr. and Meth. 106, 557 (1973).

16. T. A. Nunnamaker and D. B. Turner, Nucl. Instr. and Meth. 113, 445 (1973).

17. E. G. & G. HY-13

18. E. F. McLaughlin and R. V. Shafer, Nucl. Instr. and Meth. 70, 343 (1973).

19. G. E. Hogan, submitted to Nucl. Instr. and Meth.

20. D. Theriot, FERMILAB-TM-229, March, 1970.

21. B. Rossi, High Energy Particles (Prentice-Hall, 1952), p. 71.

22. G. G. Henry, Ph.D. thesis, University of Chicago, 1978, (unpublished); K. J. Anderson et al., to be published in Phys. Rev.

23. S. P. Denisov et al., Nucl. Phys. B61, 62 (1973).

24. B. Aubert et al., FERMILAB-Conf-75/31-EXP 7300.001, submitted to the International Colloquium of the CNRS on Neutrino Physics at High Energy, Paris, 1975.

25. J. K. Yoh et al., Phys. Rev. Lett. 41, 684 (1978).

26. M. A. Abolins et al., Preprint submitted to XIX International Conference on High Energy Physics, Tokyo, Japan, 1978 (unpublished).

27. J. G. Branson et al., Phys. Rev. Lett. 38, 1334 (1977).

28. M. Binkley et al., Phys. Rev. Lett. 37, 571 (1976).

29. Yu. M. Antipov et al., Phys. Lett. 76B, 235 (1978).

30. L. M. Lederman, XIX International Conference on High Energy Physics, Tokyo, Japan, 1978 (unpublished).

31. J. W. Cronin et al., Phys. Rev. D11, 3105 (1975), and references contained therein; U. Becker et al., Phys. Rev. Lett. 37, 1731 (1977); L. Kluberg et al., Phys. Rev. Lett. 38, 670 (1977).

32. J. C. Collins and D. E. Soper, Phys. Rev. D16, 2219 (1977).

33. J. Kogut, Phys. Lett. 65B, 377 (1976); H. D. Politzer, Nucl. Phys. B129, 301 (1977); J. Kogut and J. Shigemitsu, Phys. Lett. 71B, 165 (1977); C. S. Lam and T.-M. Yan, Phys. Lett. 71B, 173 (1977); H. Fritzsch and P. Minkowski, Phys. Lett. 73B, 80 (1978); G. Altarelli, G. Parisi and R. Petronzio, Phys. Lett. 76B, 351 (1978) and Phys. Lett. 76B, 356 (1978); E. L. Berger, "Massive Lepton Pair Production in Hadronic Collisions," in New Results in High Energy Physics - 1978, Vanderbilt Conference (AIP, 1978), p. 178; F. Halzen and D. M. Scott, University of Wisconsin preprint COO-881-21 (1978).

34. Problems with the s channel helicity are mentioned by E. L. Berger, J. T. Donohue and S. Wolfram, Phys. Rev. D17, 858 (1978). See also C. S. Lam and Wu-Ki Tung, Phys. Rev. D18, 2447 (1978).

35. M. J. Corden et al., Phys. Lett. 76B, 226 (1978).

36. L. M. Lederman and B. G. Pope, Phys. Lett. 66B, 486 (1977).

37. D. Antreasyan et al., Phys Rev. Lett. 39, 906 (1977).

38. J. Alspector et al., Preprint submitted to XIX International Conference on High Energy Physics, Tokyo, Japan, 1978.

39. S. V. Golovkin et al., Preprint submitted to XIX International Conference on High Energy Physics, Tokyo, Japan, 1978.

40. A. J. Buras and K. J. F. Gaemers, Nucl. Phys. B132, 249 (1978).

41. G. C. Fox, Nucl. Phys. B131, 107 (1977), and private communication.

42. I. Hinchliffe and C. H. Llewellyn-Smith, Nucl. Phys. B128, 93 (1977); M. Gluck and E. Reya, Nucl. Phys. B130, 76 (1977).

43. D. M. Kaplan, et al., Phys. Rev. Lett. 40, 435 (1978).

44. The data in Figure 79 are from Leon Myrianthopoulos (private communication).

45. See for example, P. V. Landshoff and J. C. Polkinghorne, Nucl. Phys. B19, 432 (1970); J. Kuti and V. F. Weisskopf, Phys. Rev. D4, 3418 (1971).

46. Many of the predictions use the Drell-Yan-West relation (S. D. Drell and T.-M. Yan, Phys. Rev. Lett. 24, 181 (1970); G. B. West, Phys. Rev. Lett. 24, 1206 (1970)) which states that if the elastic form factor behaves like $(1/q^2)^p$ at large q^2 then νW_2 will go as $(1-x)^{2p-1}$ as x approaches 1. Brodsky and Farrar (Phys. Rev. Lett. 31, 1153 (1973)) used quark counting rules to conclude that $F_{el}(q^2) \sim (q^2)^{1-n}$ where n is the number of quarks. Recent measurements of C. J. Bebek et al. (Phys. Rev. D17, 1693 (1978)) indicate that $F^{\pi}_{el}(q^2) \sim 1/q^2$ in agreement with Brodsky and Farrar. Then the Drell-Yan-West relation would predict $\nu W_2^{\pi} \sim (1-x)^1$.

47. G. R. Farrar, Nucl. Phys. B77, 429 (1974); G. Altarelli, N. Cabibbo, L. Maiani, and R. Petronzio, Nucl Phys. B92, 413 (1975); A. Donnachie and P. V. Landshoff, Nucl. Phys. B112, 233 (1976); R. D. Field and R. P. Feynman, Phys. Rev. D15, 2590 (1977); G. R. Farrar and D. R. Jackson, Phys. Rev. Lett. 35, 1416 (1975).

48. The contribution of the pion sea (neglected in equation (6)) may be estimated by assuming it has the form $f^{\pi}_s(x) = 0.1(1-x)^5$ as suggested by G. R. Farrar, Nucl. Phys. B77, 429 (1974) and R. D. Field and R. P. Feynman, Phys. Rev. D15, 2590 (1977). If the pion sea is included parametrized this way, the normalization of the pion valence quark distribution function decreases by about 4%.

49. The momentum distribution for particles in the nucleus was taken from R. D. Amado and R. M. Woloshyn, Phys. Rev. Lett. 36, 1435 (1978).

50. These values are obtained by assuming that the observed mean p_T for dimuons produced in πN and pN collisions comes from two quark p_T vectors of fixed magnitude with a random angle between them.

51. J. G. Branson, Ph.D. thesis, Princeton University, 1977 (unpublished).

52. For a recent review of the Drell Yan model with QCD, see E. L. Berger, "Massive Lepton Pair Production in Hadronic Collsions," in New Results in High Energy Physics - 1978, Vanderbilt Conference (AIP, 1978), p. 178.

53. E. L. Berger (Ref. 52) gives this estimate. Altarelli, Parisi and Petronzio (Ref. 33, p. 356) arrive at a similar number.

54. D. J. Fox et al., Phys. Rev. Lett. 33, 1504 (1974); C. Chang et al., Phys. Rev. Lett. 35, 901 (1975). See also Ref. 3.

55. H. D. Politzer, Phys. Rep. 14C, 129 (1974). See also Ref. 10.

56. H. D. Politzer, Nucl. Phys. B129, 301 (1977).

57. I. Hinchliffe and C. H. Llewellyn-Smith, Phys. Lett. 66B, 281 (1977); C. T. Sachrajda, Phys. Lett. 73B, 185 (1978); K. Kajantie and R. Raitio, Nucl. Phys. B139, 72 (1978).

58. see references 33, 40, 41, 42, 56, and 57.

59. See, for example, F. Halzen and D. M. Scott (Ref. 33); E. L. Berger (Ref. 52); K. Kajantie and R. Raitio (Ref. 57).

60. R. D. Field has called this "the primordial smerge", (seminar given at the Enrico Fermi Institute, 1978). See also F. Halzen and D. M. Scott (Ref. 33); E. L. Berger (Ref. 52).

TABLE 1

QUARK QUANTUM NUMBERS

Flavor	u	d	s	c	b
Spin	1/2	1/2	1/2	1/2	1/2
Baryon Number	1/3	1/3	1/3	1/3	1/3
Charge	2/3	-1/3	-1/3	2/3	-1/3
I_3	1/2	-1/2	0	0	0
Strangeness	0	0	-1	0	0
Charm	0	0	0	1	0
Beauty[a]	0	0	0	0	1

[a]Also called "bottom".

TABLE 2

AVERAGE BEAM COMPOSITION

Positive Beam	Pions	.309
	Kaons	.013
	Protons	.678
Negative Beam	Pions and Kaons	.995
	Antiprotons	.005

TABLE 3

TARGET INFORMATION

Type	Length (cm)	Density (g/cm^3)
Carbon	31.16	2.2
Copper	15.24	8.96
Tungsten[a]	10.6	17.08

[a]Mallory 1000 = 89.9% tungsten, 4.04% copper, 6.06% nickel.

TABLE 4

MWPC EFFICIENCIES AND RESOLUTIONS

Plane	Type	Efficiency	Resolution (σ, mm)
1	y	.97	.58
2	y	.97	.58
3	x	.96	.58
4	u	.96	.46
5	u	.96	.46
6	v	.94	.46
7	v	.97	.46
8	x	.94	.58
9	y	.96	.58
10	y	.96	.58
11	x	.86	.46
12	x	.96	.46
13	y	.86	.46
14	y	.95	.46

TABLE 5

SPARK CHAMBER EFFICIENCIES AND RESOLUTIONS

Plane	Type	Efficiency	Resolution (σ, mm)
15	u	.950	.25
16	x	.965	.35
17	x	.883	.38
18	v	.826	.28
19	u	.959	.43
20	x	.970	.33
21	x	.987	.38
22	v	.982	.45
23	u	.897	.25
24	x	.904	.30
25	x	.960	.33
26	v	.754	.28

TABLE 6

RECONSTRUCTION EFFICIENCY FROM SCANNING

Data Sample	Reconstruction Efficiency
positive beam, carbon target	.94
negative beam, carbon target	.94
negative beam, copper target	.90
negative beam, tungsten target	.92

TABLE 7

EFFECT OF SOFTWARE TRIGGER REQUIREMENT

Beam Sign	Target	Mass Threshold (GeV/c^2)	% of events with $M > 2$ GeV/c^2 which satisfy software trigger requirements
+	C	no threshold	2.6
+	C	0.72	2.7
-	C	0.72	4.5
-	Cu	1.6	6.9
-	W	2.8	17.8

TABLE 8

VALUES USED FOR MONTE CARLO CALCULATION

Mass (GeV/c^2)	2.0	2.5	3.0	3.5	4.0	6.0	8.0	10.0
x_F	-0.05	0.0	0.1	0.2	0.3	0.4	0.6	0.8
p_T (GeV/c)	0.0	0.5	1.0	3.0	5.0			

TABLE 9

CERENKOV COUNTER EFFICIENCIES AND ACCIDENTAL PROBABILITIES

Counter	Efficiency	Accidental Probability
C2	.935	.091
C3	.997	.019
C4	.984	.006
C5	.984	.014

TABLE 10

NORMALIZATION FACTORS

	CARBON					COPPER	TUNGSTEN
	p	π^+	K^+	$\bar{p}$	π^-	π^-	π^-
Corrections to B							
CAMAC Errors	.997	.997	.997	.996	.996	.982	.955
Multiple particle/bucket	1.000	1.000	1.000	1.000	1.000	1.202	1.228
B (uncorrected)	3.22×10^{11}	1.45×10^{11}	6.11×10^{9}	1.64×10^{9}	3.28×10^{11}	3.07×10^{11}	4.17×10^{11}
B (corrected)	3.21×10^{11}	1.45×10^{11}	6.09×10^{9}	1.63×10^{9}	3.27×10^{11}	3.63×10^{11}	4.89×10^{11}
Overall Corrections							
P14 Inefficiency	1.045	1.045	1.045	1.000	1.000	1.09	1.00
Reconstruction Efficiency	1.064	1.064	1.064	1.064	1.064	1.10	1.09
Final Factors (pb/nucleus-event)	1.50	3.01	68.5	290	1.28	3.75	5.60

TABLE 11

J/ψ AND $\psi'(3.7)$ CROSS SECTIONS

CARBON TARGET ($x_F > 0$)

Beam	$B\sigma(J/\psi)$ nb/nucleus	$B\sigma(\psi')/B\sigma(J/\psi)$
π^-	88 ± 12	0.021 ± 0.006
π^+	82 ± 12	0.017 ± 0.009
p	53 ± 7	0.016 ± 0.009
K^+	49 ± 15	---
$\bar{p}$	85 ± 40	---

TABLE 12

FEYNMAN X DISTRIBUTION FITS

Fit $\frac{Ed\sigma}{dx_F}$ to $a(1-x_F)^b$

	Mass Interval (GeV/c^2)	a(GeV-nb)	b
	$\pi^- N \rightarrow \mu^+\mu^- X$[a]		
	2.0-2.7	8.29 ±.23	1.12 ±.04
	J/ψ	23.8 ±.23	1.46 ±.014
p_T<1.0	3.5-4.0	0.87 ±.03	0.87 ±.05
	4.0-6.0	0.48 ±.02	0.66 ±.05
	6.0-8.0	0.069±.01	0.52 ±.13
all p_T	8.0-	0.058±.013	0.33 ±.18
	2.0-2.7	6.79 ±.40	1.96 ±.11
	J/ψ	32.5 ±.43	1.95 ±.02
p_T>1.0	3.5-4.0	1.37 ±.08	1.53 ±.08
	4.0-6.0	0.68 ±.04	1.05 ±.06
	6.0-8.0	0.093±.015	0.81 ±.16
	$\pi^+ N \rightarrow \mu^+\mu^- X$[a]		
	2.0-2.7	13.8 ±1.4	1.42 ±.18
all p_T	J/ψ	70.2 ±1.9	1.73 ±.04
	3.5-4.0	1.45±0.23	1.00 ±.20
	4.0-	0.43±0.09	0.52 ±.17
	$pN \rightarrow \mu^+\mu^- X$		
	2.0-2.7	18.0 ±1.4	2.98 ±.18
all p_T	J/ψ	73.3 ±1.7	3.39 ±.05
	3.5-4.0	1.52±0.25	2.40 ±.33
	4.0-	0.33±0.08	1.02 ±.30
	$K^+ N \rightarrow \mu^+\mu^- X$		
all p_T	J/ψ	34.6 ±5.6	1.74 ±.30
	$\bar{p}N \rightarrow \mu^+\mu^- X$		
all p_T	J/ψ	111 ± 27	3.00 ±.53

[a]Fits for pion induced μ pairs have been folded about $x_F = 0.2$ (See Ref. 26).

TABLE 13

THE CROSS SECTION $d\sigma/dMdx_F$ FOR π^- INDUCED μ PAIRS

	Mass (GeV/c^2)								
Bin L.E.	4.00	4.50	5.00	5.50	6.00	7.00	8.00	9.00	10.00
<M>	4.22	4.74	5.23	5.73	6.37	7.43	8.42	9.44	10.51
$<x_F>$									
0.056	0.152E+00	0.886E-01	0.570E-01	0.294E-01	0.748E-02	0.144E-01	0.133E-01	0.224E-02	0.192E-02
	±0.258E-01	0.181E-01	0.169E-01	0.947E-02	0.370E-02	0.601E-02	0.133E-01	0.225E-02	0.192E-02
0.154	0.165E+00	0.537E-01	0.409E-01	0.233E-01	0.140E-01	0.850E-02	0.611E-02	0.491E-02	0.203E-02
	±0.185E-01	0.104E-01	0.966E-02	0.706E-02	0.415E-02	0.356E-02	0.285E-02	0.492E-02	0.204E-02
0.251	0.146E+00	0.790E-01	0.573E-01	0.327E-01	0.154E-01	0.142E-01	0.182E-02	0.452E-02	0.176E-02
	±0.137E-01	0.102E-01	0.883E-02	0.695E-02	0.328E-02	0.435E-02	0.140E-02	0.264E-02	0.136E-02
0.354	0.131E+00	0.654E-01	0.430E-01	0.352E-01	0.128E-01	0.710E-02	0.283E-02	0.468E-02	0.000E+01
	±0.107E-01	0.796E-02	0.672E-02	0.591E-02	0.261E-02	0.200E-02	0.143E-02	0.211E-02	0.000E+01
0.449	0.121E+00	0.721E-01	0.383E-01	0.225E-01	0.179E-01	0.854E-02	0.417E-02	0.379E-02	0.213E-02
	±0.996E-02	0.740E-02	0.556E-02	0.427E-02	0.274E-02	0.209E-02	0.190E-02	0.171E-02	0.151E-02
x_F 0.547	0.755E-01	0.518E-01	0.232E-01	0.136E-01	0.792E-02	0.463E-02	0.565E-02	0.283E-02	0.828E-03
	±0.717E-02	0.613E-02	0.415E-02	0.316E-02	0.170E-02	0.136E-02	0.163E-02	0.118E-02	0.829E-03
0.647	0.657E-01	0.354E-01	0.264E-01	0.132E-01	0.604E-02	0.301E-02	0.342E-02	0.758E-03	0.945E-03
	±0.646E-02	0.480E-02	0.411E-02	0.287E-02	0.136E-02	0.101E-02	0.130E-02	0.759E-03	0.946E-03
0.745	0.369E-01	0.194E-01	0.227E-01	0.919E-02	0.434E-02	0.188E-02	0.252E-02	0.230E-02	0.000E+01
	±0.480E-02	0.350E-02	0.417E-02	0.242E-02	0.118E-02	0.805E-03	0.106E-02	0.230E-02	0.000E+01
0.844	0.150E-01	0.974E-02	0.524E-02	0.197E-02	0.133E-02	0.514E-03	0.000E+01	0.000E+01	0.000E+01
	±0.304E-02	0.260E-02	0.170E-02	0.115E-02	0.672E-03	0.514E-03	0.000E+01	0.000E+01	0.000E+01
0.926	0.189E-02	0.199E-02	0.194E-02	0.000E+01	0.551E-03	0.000E+01	0.000E+01	0.000E+01	0.000E+01
	±0.189E-02	0.121E-02	0.138E-02	0.000E+01	0.417E-03	0.000E+01	0.000E+01	0.000E+01	0.000E+01

The first line of each table entry is the cross section in $nb/GeV/c^2$ per nucleon. The second line is the error associated with the cross section measurement. The extrapolation to cross sections per nucleon used the measured A dependence (α=1.12). The quoted errors are from the statistics of the data and the calculated efficiencies; no systematic uncertainties are included.

The average mass in each mass bin is given as well as the bin lower edges. The upper edge of the last mass bin is 11.0 GeV/c^2. Note that x_F in this table is $2P_{\parallel}^{*}/\sqrt{s}$. All x_F bins are 0.1 wide. The lower edge of the first x_F bin is x_F=0.0.

TABLE 14

TRANSVERSE MOMENTUM DISTRIBUTION FITS

Fit $\frac{1}{p_T}\frac{d\sigma}{dp_T}$ to $\frac{a}{(1+\frac{p_T^2}{b^2})^6}$

	Mass Interval (GeV/c²)	a(pb/GeV²/c²)	b(GeV²/c²)
	$\pi^- N \to \mu^+\mu^- X$		
	2.0-2.7	2106 ± 112	2.07 ±.04
	J/ψ	3743 ± 48	2.59 ±.014
$x_F<0.3$	3.5-4.0	137.8 ± 8.4	2.67 ±.07
	4.0-6.0	55.7 ± 5.3	2.79 ±.12
	6.0-8.0	4.78 ± 1.99	3.19 ±.93
all x_F	8.0-	2.03 ± 0.46	3.50 ±.37
	2.0-2.7	1362 ± 41	1.91 ±.02
	J/ψ	2175 ± 20	2.52 ±.01
$x_F>0.3$	3.5-4.0	116.8 ± 4.4	2.50 ±.04
	4.0-6.0	72.8 ± 3.3	2.58 ±.05
	6.0-8.0	6.84 ± .73	3.05 ±.13
	$\pi^+ N \to \mu^+\mu^- X$		
	2.0-2.7	2972 ± 299	1.87 ±.09
all x_F	J/ψ	8185 ± 241	2.42 ±.03
	3.5-4.0	187 ± 32	2.62 ±.22
	4.0-	76.8 ± 18.5	2.34 ±.27
	$pN \to \mu^+\mu^- X$		
	2.0-2.7	3474 ± 634	1.80 ±.12
all x_F	J/ψ	6871 ± 197	2.39 ±.03
	3.5-4.0	161 ± 27	2.38 ±.21
	4.0-	59.1 ± 16.9	2.17 ±.29
	$K^+ N \to \mu^+\mu^- X$		
all x_F	J/ψ	4468 ± 841	2.51 ±.20
	$\bar{p}N \to \mu^+\mu^- X$		
all x_F	J/ψ	9370 ± 3088	2.60 ±.39

TABLE 15

MEAN TRANSVERSE MOMENTUM AND MEAN TRANSVERSE MOMENTUM SQUARED VERSUS MUON PAIR MASS AND BEAM PARTICLE TYPE

Mass (GeV/c^2)	Beam Particle Type p	$\bar{p}$	π^+	π^-
		$\langle p_T \rangle$ (GeV/c)		
2.0 - 2.7	.79±.10	1.17±.34	.82±.10	.82±.10
J/ψ	.97±.10	.88±.13	1.01±.10	1.05±.10
3.5 - 4.5	1.00±.13	1.26±.49	1.05±.12	1.10±.10
4.5 - 6.5	.87±.21	---	1.16±.25	1.25±.10
6.5 - 8.5	---	---	1.08±.45	1.17±.12
8.5 - 12.0	---	---	---	1.17±.16
		$\langle p_T^2 \rangle$ (GeV^2/c^2)		
2.0 - 2.7	.81±.10	1.80±.50	.87±.10	.89±.10
J/ψ	1.25±.10	1.02±.14	1.33±.10	1.47±.10
3.5 - 4.5	1.42±.15	1.70±.70	1.47±.14	1.64±.10
4.5 - 6.5	.91±.20	---	1.63±.34	2.06±.11
6.5 - 8.5	---	---	1.56±.65	1.79±.15
8.5 - 12.0	---	---	---	1.57±.20

TABLE 16

HELICITY ANGULAR DISTRIBUTION FITS

Angle	Flat χ^2/DOF	$1+\cos^2\theta^*$ χ^2/DOF	$1+\lambda\cos^2\theta^*$ λ	χ^2/DOF
		$2.0 < M_{\mu\mu} < 2.7$ GeV/c^2		
s channel	77.5/9	15.7/9	1.10±.16	15.3/8
t channel	67.4/9	15.7/9	.71±.11	8.8/8
u channel	102.5/9	34.2/9	1.72±.22	22.4/8
Collins-Soper	79.7/9	25.6/9	1.14±.17	25.0/8
		J/ψ		
s channel	19.0/9	240.0/9	.03±.06	18.7/8
t channel	36.7/9	101.0/9	.33±.06	2.2/8
u channel	12.3/9	131.0/9	.09±.07	10.7/8
Collins-Soper	7.0/9	212.0/9	-.10±.07	4.7/8
		$M_{\mu\mu} > 3.5$ GeV/c^2, all p_T		
s channel	32.3/9	104.0/9	.05±.10	32.0/8
t channel	49.7/9	11.1/9	.82±.15	9.8/8
u channel	47.8/9	17.7/9	1.31±.26	16.2/8
Collins-Soper	44.6/9	6.6/9	1.30±.23	4.9/8
		$M_{\mu\mu} > 3.5$ GeV/c^2, $p_T > 1$ GeV/c		
s channel	11.7/7	25.4/7	.16±.19	11.0/6
t channel	30.4/9	15.8/9	.65±.17	12.4/8
u channel	29.4/7	13.7/7	1.42±.39	12.5/6
Collins-Soper	36.4/9	11.2/9	1.47±.32	8.8/8
		$M_{\mu\mu} > 3.5$ GeV/c^2, $p_T < 1$ GeV/c		
s channel	13.1/7	11.9/7	.50±.22	7.4/6
t channel	26.0/9	3.3/9	1.05±.24	3.3/8
u channel	28.2/9	12.6/9	1.11±.31	12.5/8
Collins-Soper	31.6/9	12.6/9	1.17±.29	12.2/8

TABLE 17

PION STRUCTURE FUNCTION FITS

	Fit	a	b
$4.0 < M < 8.75$, all p_T	$a\sqrt{x_1}\,(1-x_1)^b$	0.90±.06	1.27±.06
$4.0 < M < 6.0$, all p_T	$a\sqrt{x_1}\,(1-x_1)^b$	0.93±.07	1.30±.07
$5.0 < M < 8.75$, all p_T	$a\sqrt{x_1}\,(1-x_1)^b$	0.81±.10	1.23±.11
$4.0 < M < 8.75$, $p_T<1$	$a\sqrt{x_1}\,(1-x_1)^b$		1.17±.08
$4.0 < M < 8.75$, $p_T>1$	$a\sqrt{x_1}\,(1-x_1)^b$		1.21±.09
$4.0 < M < 8.75$, all p_T p_T method 1*	$a\sqrt{x_1}\,(1-x_1)^b$	0.61±.05	1.17±.09
$4.0 < M < 8.75$, all p_T p_T method 2**	$a\sqrt{x_1}\,(1-x_1)^b$	0.85±.06	1.30±.06
$4.0 < M < 8.75$, all p_T	$a(1-x_1)^b$	0.52±.03	1.01±.05

*For p_T method 1, p_T (π quark) = 1.0 GeV/c and p_T (N quark) = 0.75 GeV/c. If $p_{T\mu\mu} > 1.75$ GeV/c, p_T (N quark) = 0.75 p_T (π quark).

**For p_T method 2, p_T (N quark) = 0.75 p_T (π quark).

TABLE 18

NUCLEON STRUCTURE FUNCTION FITS

	χ^2/DOF for Fit to Normalization Curve of Fig. 78.
$4.0 < M < 8.75$, all p_T	5.1/8
$4.0 < M < 6.0$, all p_T	6.6/8
$5.0 < M < 8.75$, all p_T	0.5/6
$4.0 < M < 8.75$, $p_T<1.0$	10.4/8
$4.0 < M < 8.75$, $p_T>1.0$	7.5/8
$4.0 < M < 8.75$, all p_T p_T method 1*	12.0/8
$4.0 < M < 8.75$, all p_T p_T method 2**	2.0/8

*For p_T method 1, p_T (π quark) = 1.0 GeV/c and p_T (N quark) = 0.75 GeV/c. If $p_{T\mu\mu} > 1.75$ GeV/c, p_T (N quark) = 0.75 p_T (π quark).

**For p_T method 2, p_T (N quark) = 0.75 p_T (π quark).

Fig. 1.--Inelastic lepton-proton scattering. The incident lepton with initial energy E is scattered through an angle θ. The final lepton energy is E'. Momentum q and energy ν are transferred to the proton.

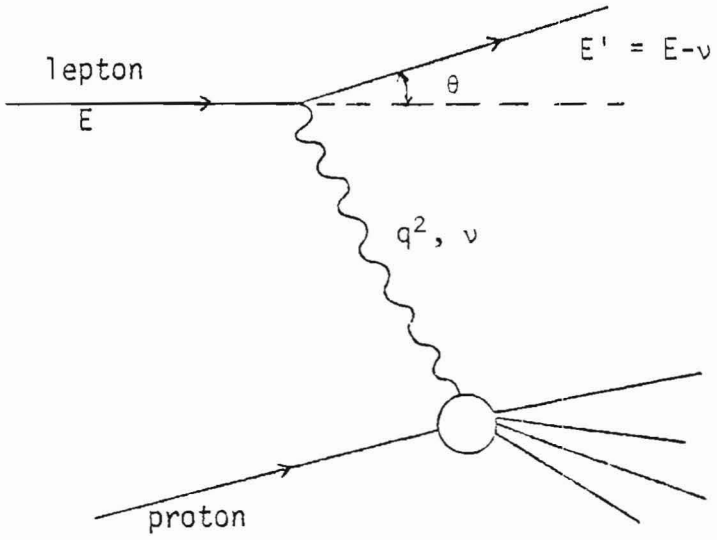
lepton
E
E' = E-ν
θ
q², ν
proton

Fig. 2.--Processes for the study of form factors in the timelike region. (a) $p\bar{p} \rightarrow e^+e^-$; (b) $e^+e^- \rightarrow$ hadrons; (c) Massive lepton pair production in hadron collisions.

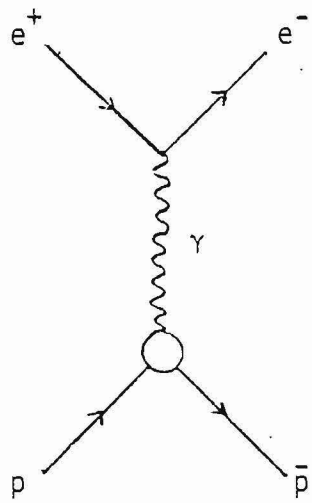
e+
e-
γ
p
p̄

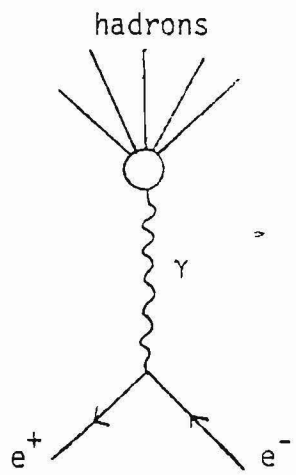
hadrons
γ
e+
e-

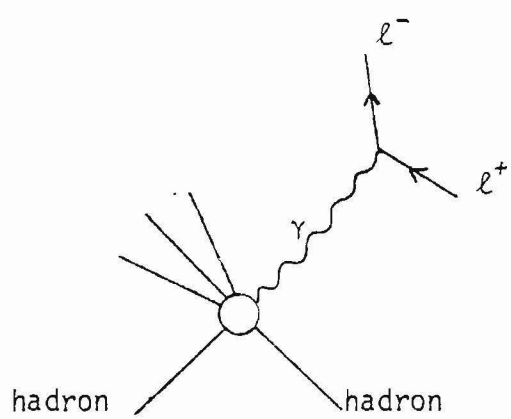
ℓ-
ℓ+
γ
hadron
hadron

Fig. 3.--The Drell Yan process for lepton pair production via quark-antiquark annihilation.

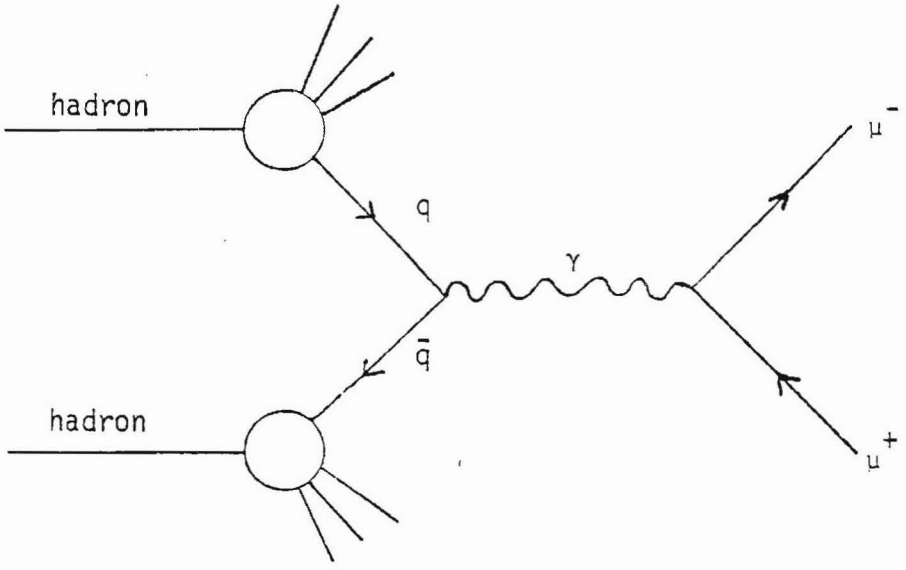
hadron
q
γ
$\bar{q}$
hadron
μ^-
μ^+

Fig. 4.--The Chicago cyclotron magnet spectrometer as configured for this experiment.

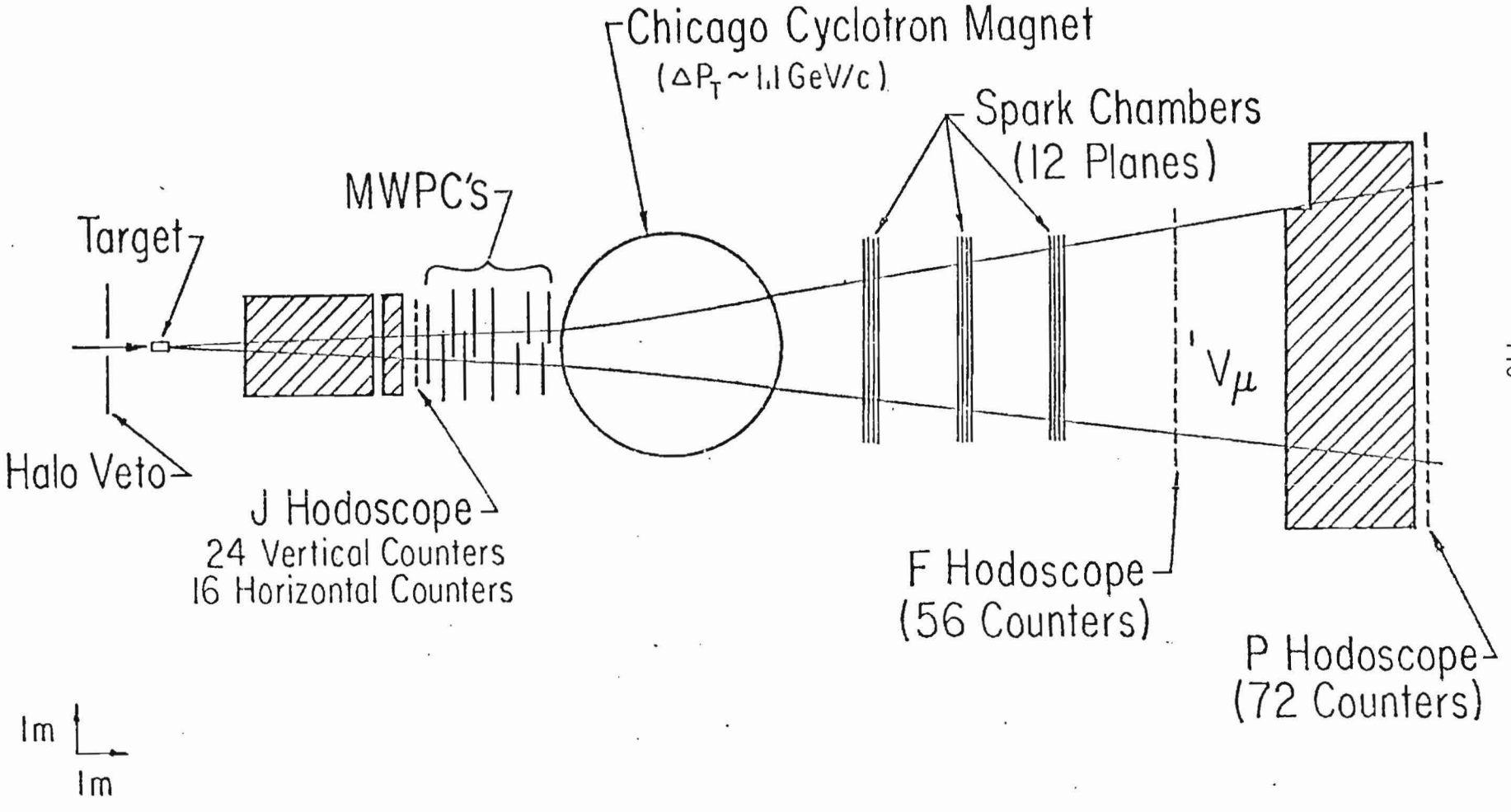
Chicago Cyclotron Magnet
($\Delta P_T \sim 1.1$ GeV/c)
Spark Chambers
(12 Planes)
MWPC's
Target
V_μ
Halo Veto
J Hodoscope
24 Vertical Counters
16 Horizontal Counters
F Hodoscope
(56 Counters)
P Hodoscope
(72 Counters)
1m
1m

Fig. 5.--Diagram of the Neutrino beam line.

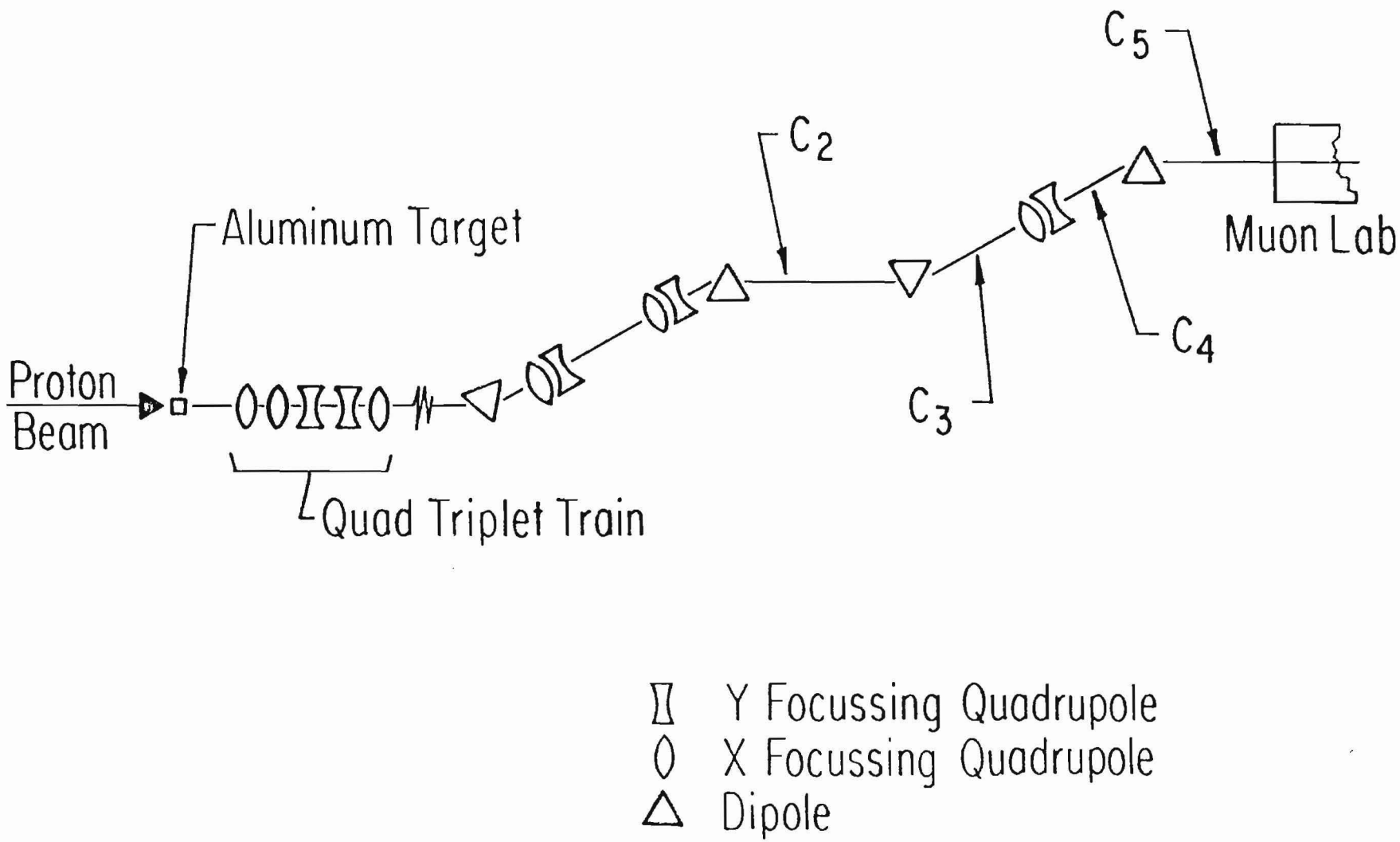
Proton
Beam
Aluminum Target
Quad Triplet Train
C2
C3
C4
C5
Muon Lab
Y Focussing Quadrupole
X Focussing Quadrupole
Dipole

Fig. 6.--Detector elements for beam particle identification.

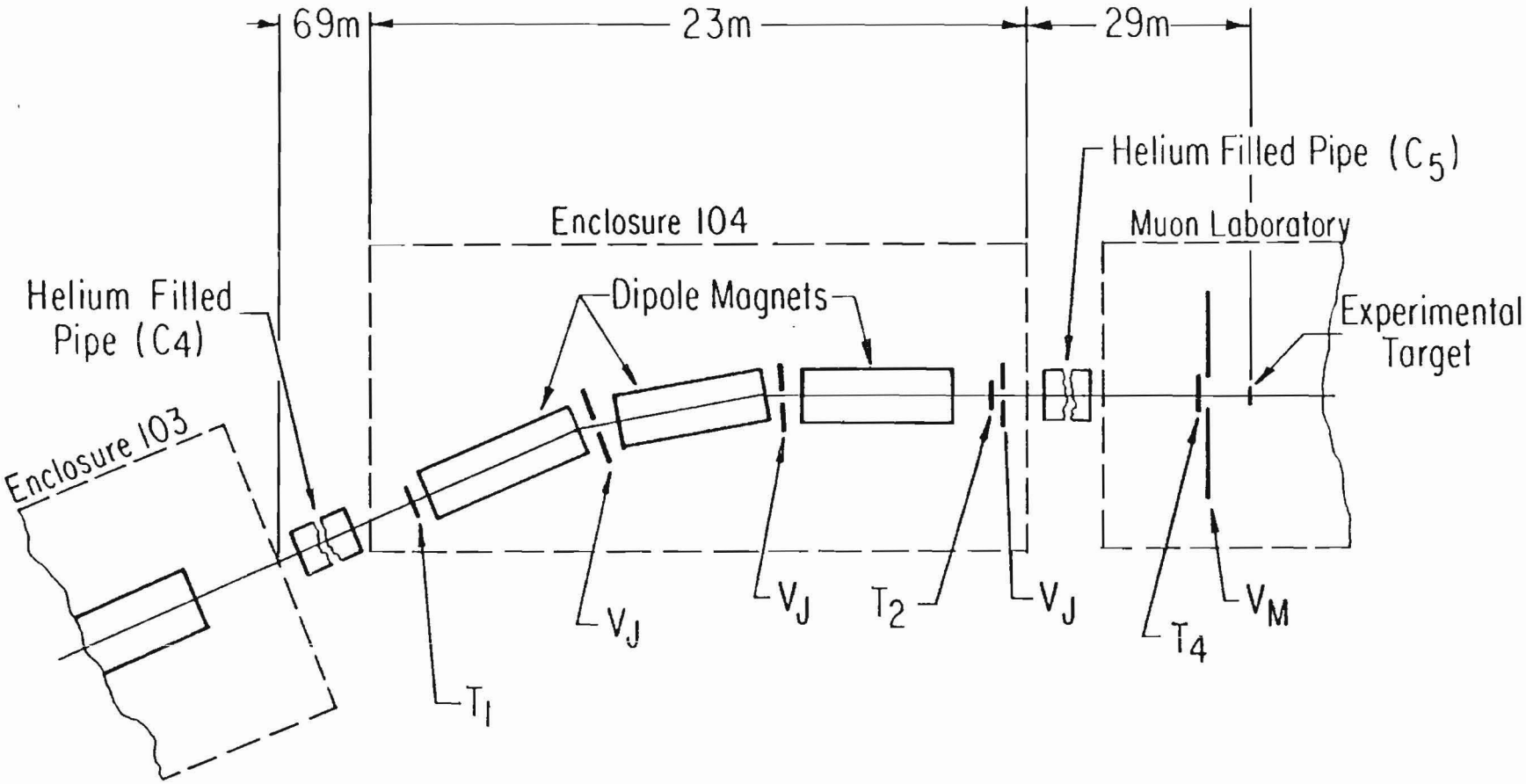

T Beam Defining Scintillation Counter
V_J "Jaw" Veto Counter
V_M Halo Veto Wall
C Čerenkov Counter

Fig. 7.--Arrangement of counters in the J hodoscope (looking along the beam direction). (a) The Jx plane; (b) The Jy plane.

(a)

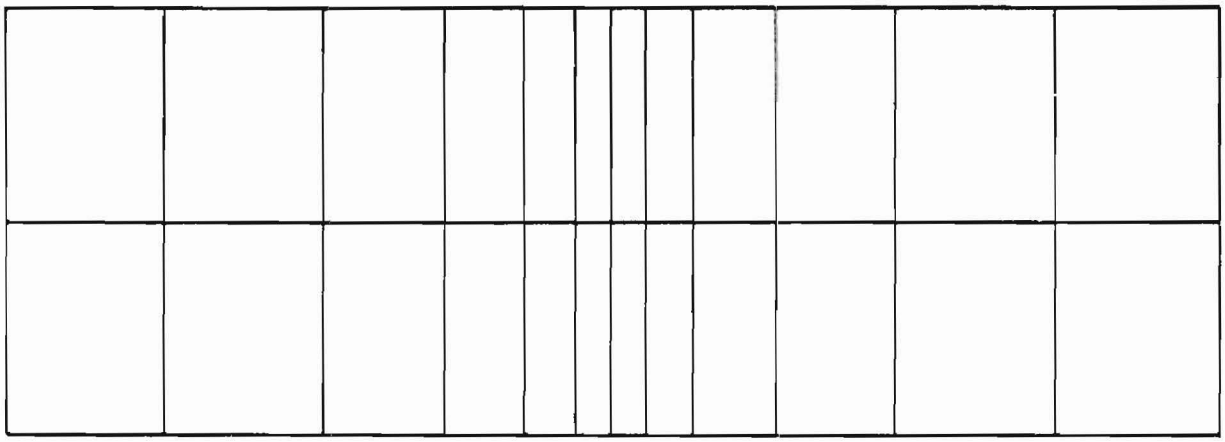

(b)

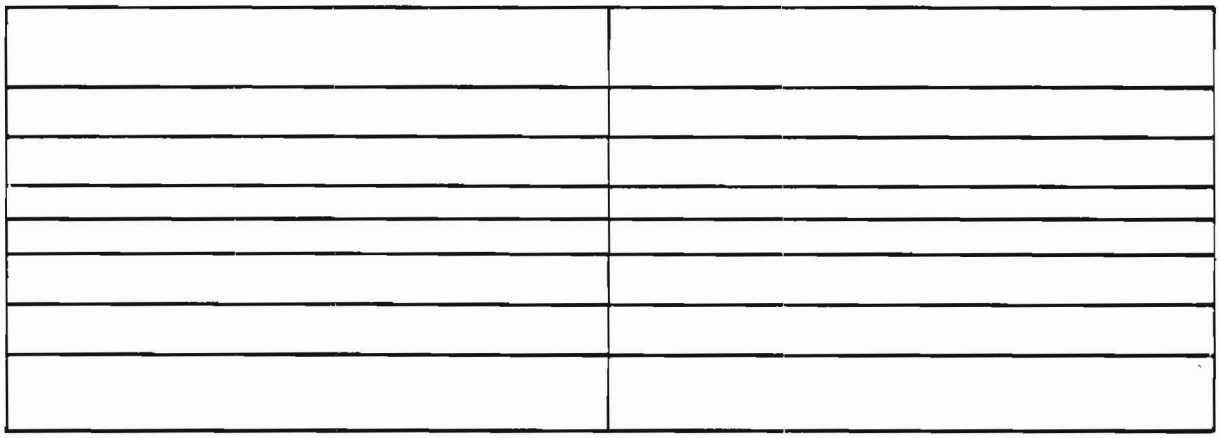

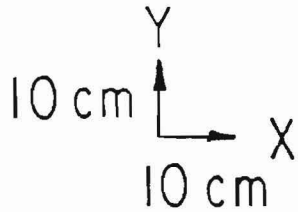

Fig. 8.--MWPC configuration. (a) Plan view; (b) Front view of the tilted planes.

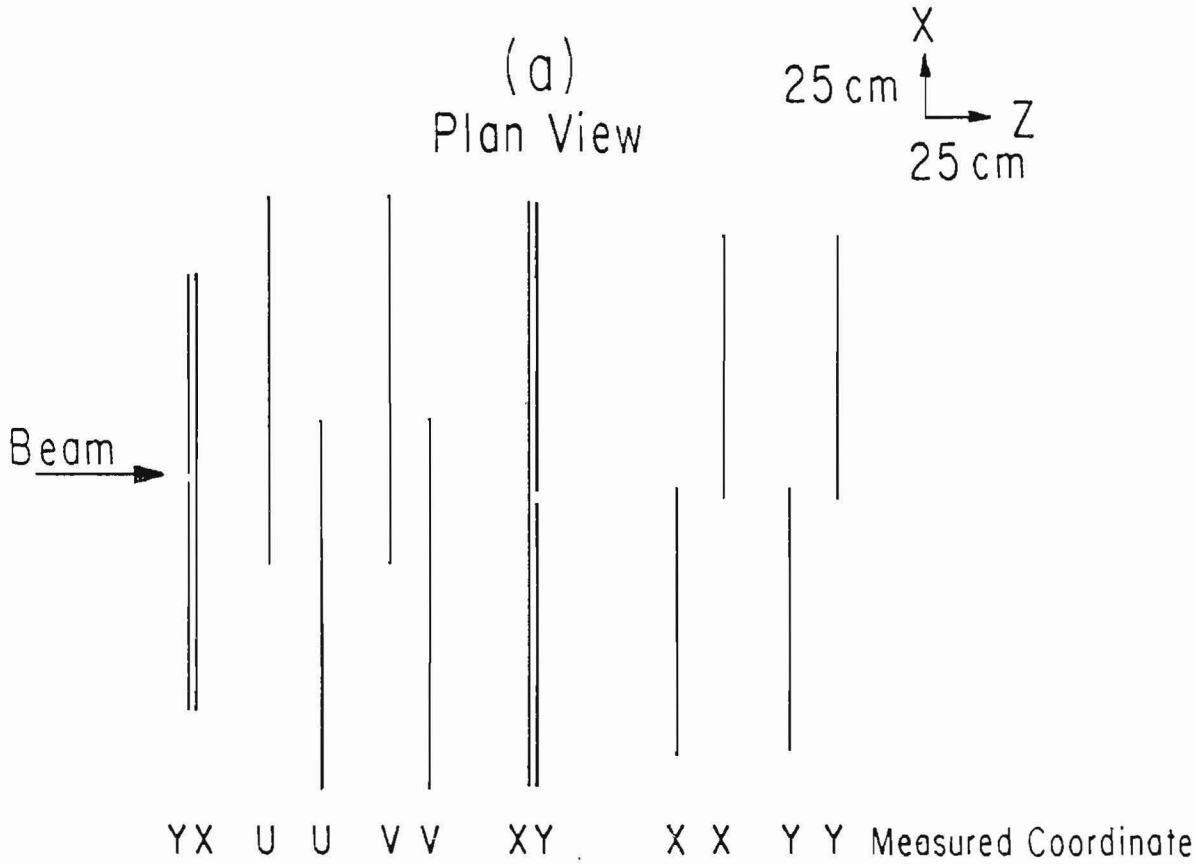
(a)
Plan View
X
25 cm
Z
25 cm
Beam
YX U U V V XY X X Y Y Measured Coordinate

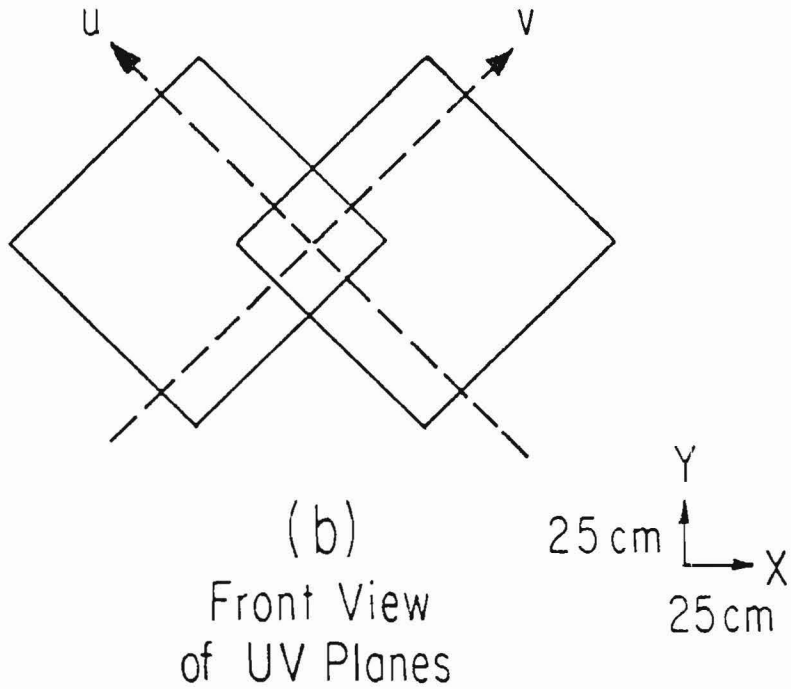
U
V
(b)
Front View
of UV Planes
Y
25 cm
X
25cm

Fig. 9.--Arrangement of counters for the P hodoscope (viewed along the beam direction).

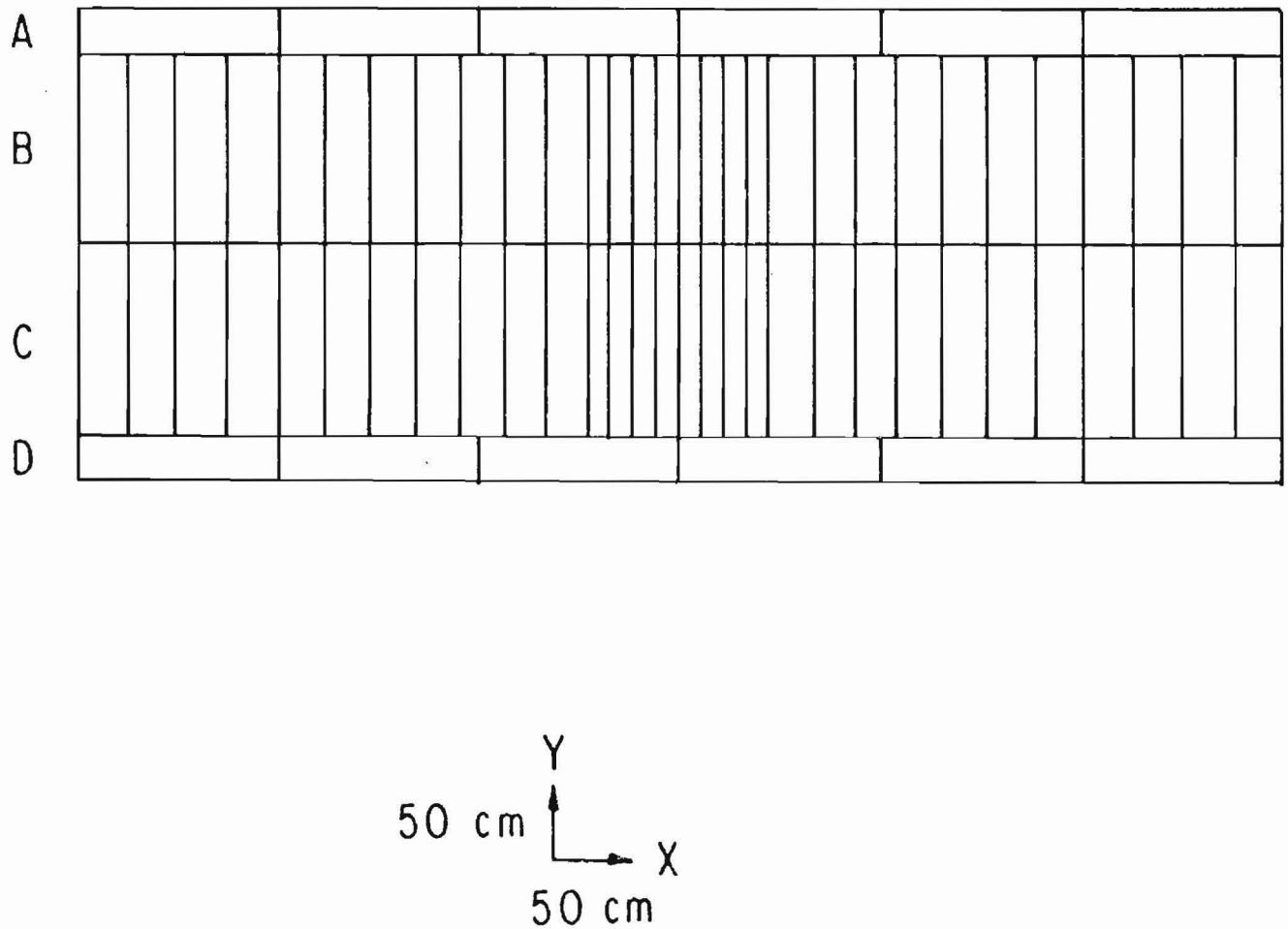
A
B
C
D
Y
50 cm
X
50 cm

Fig. 10.--Logic diagram of the trigger electronics.

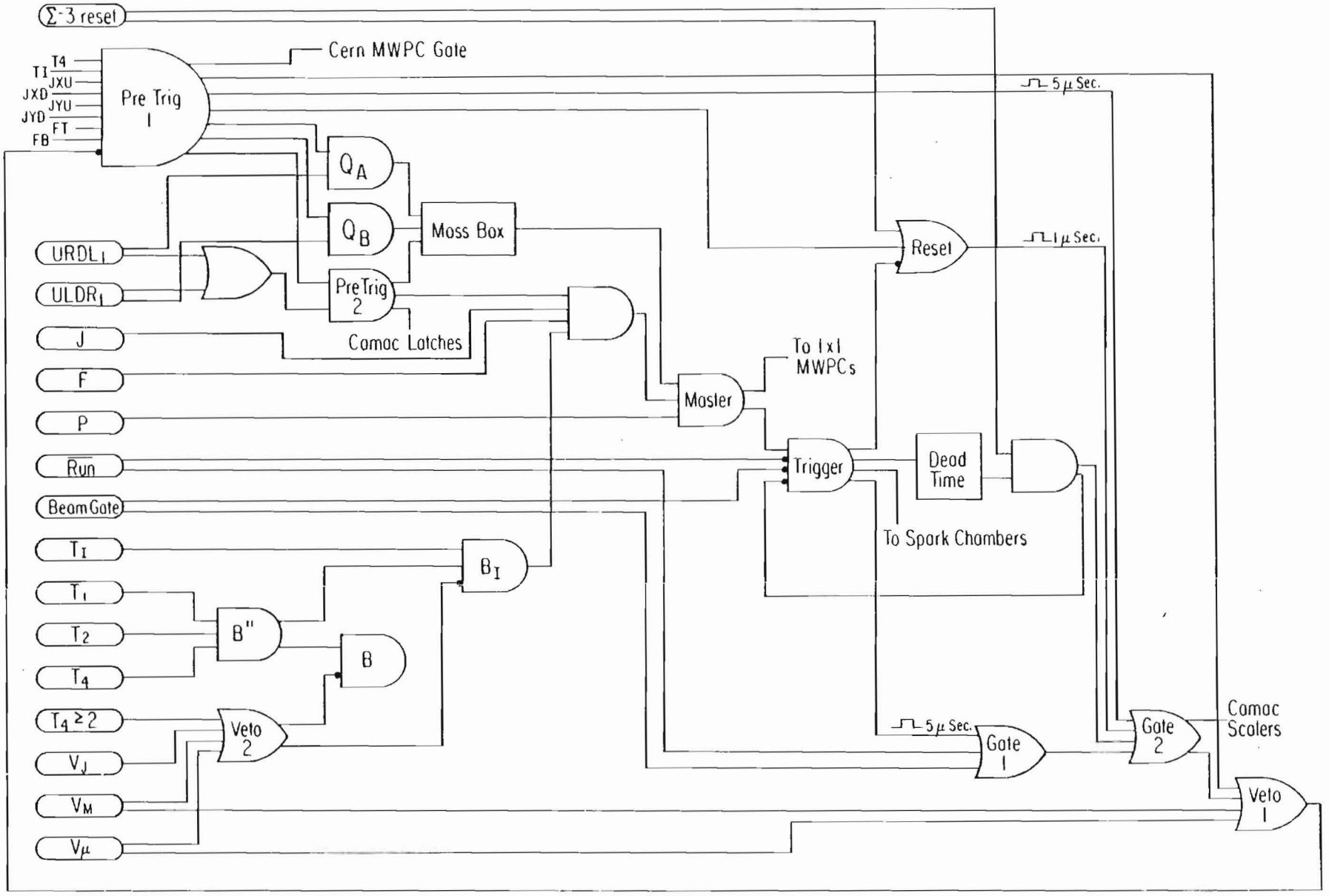
Σ-3 reset
Cern MWPC Gate
T4
TI
JXU
JXD
JYU
JYD
FT
FB
Pre Trig 1
5 μ Sec.
QA
QB
Moss Box
Reset
1 μ Sec.
URDL1
ULDR1
PreTrig 2
Camac Latches
J
F
P
Master
To 1x1 MWPCs
Run
Trigger
Dead Time
Beam Gate
To Spark Chambers
TI
BI
T1
T2
T4
B''
B
T4 ≥ 2
Veto 2
5 μ Sec.
Gate 1
Gate 2
Camac Scalers
VJ
VM
Vμ
Veto 1

Fig. 11.--Difference between upstream and downstream reconstructed impact parameters for beam particles.

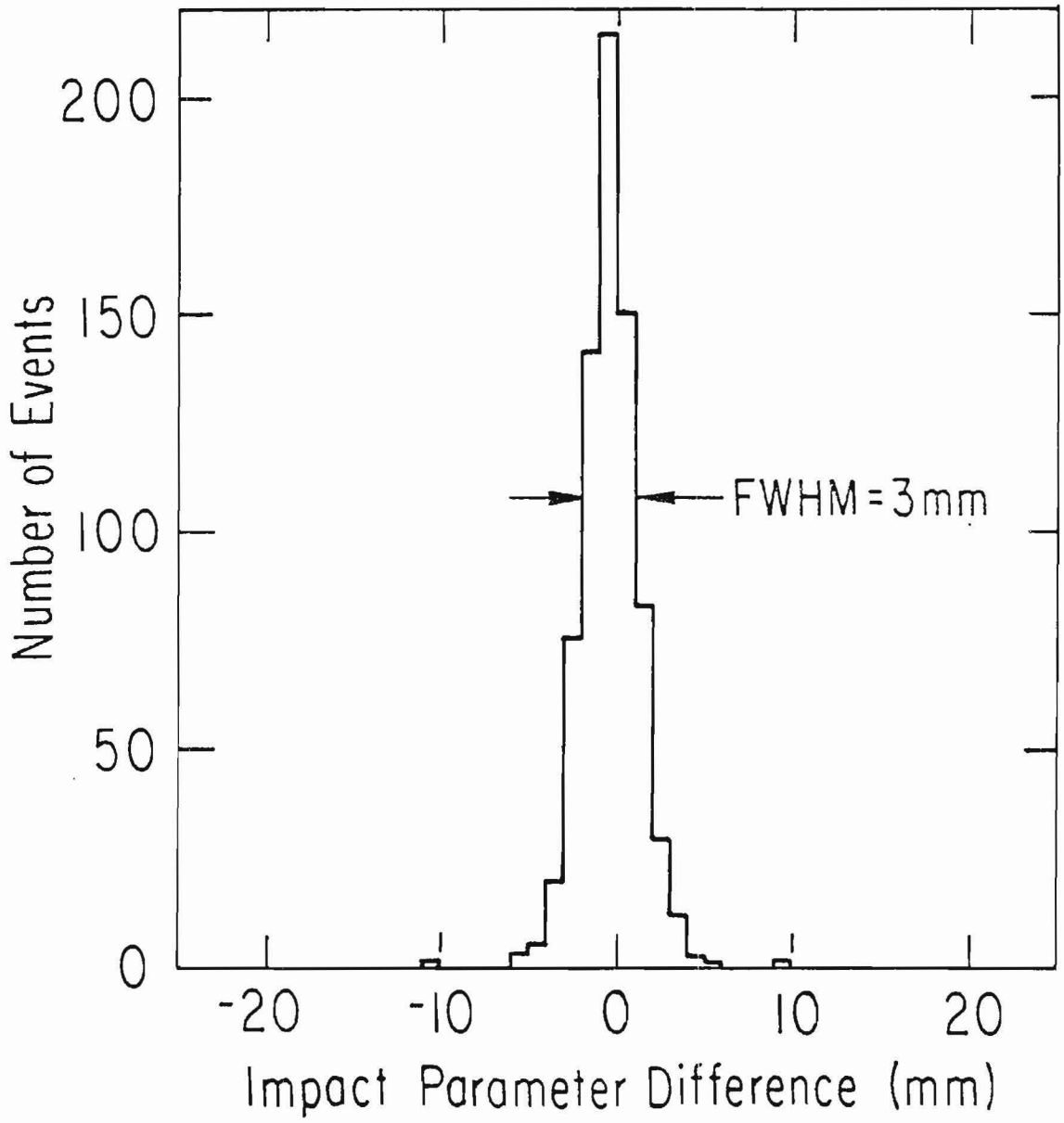
200
150
100
50
0
Number of Events
FWHM = 3mm
-20
-10
0
10
20
Impact Parameter Difference (mm)

Fig. 12.--Difference between upstream and downstream reconstructed y intercepts for beam particles.

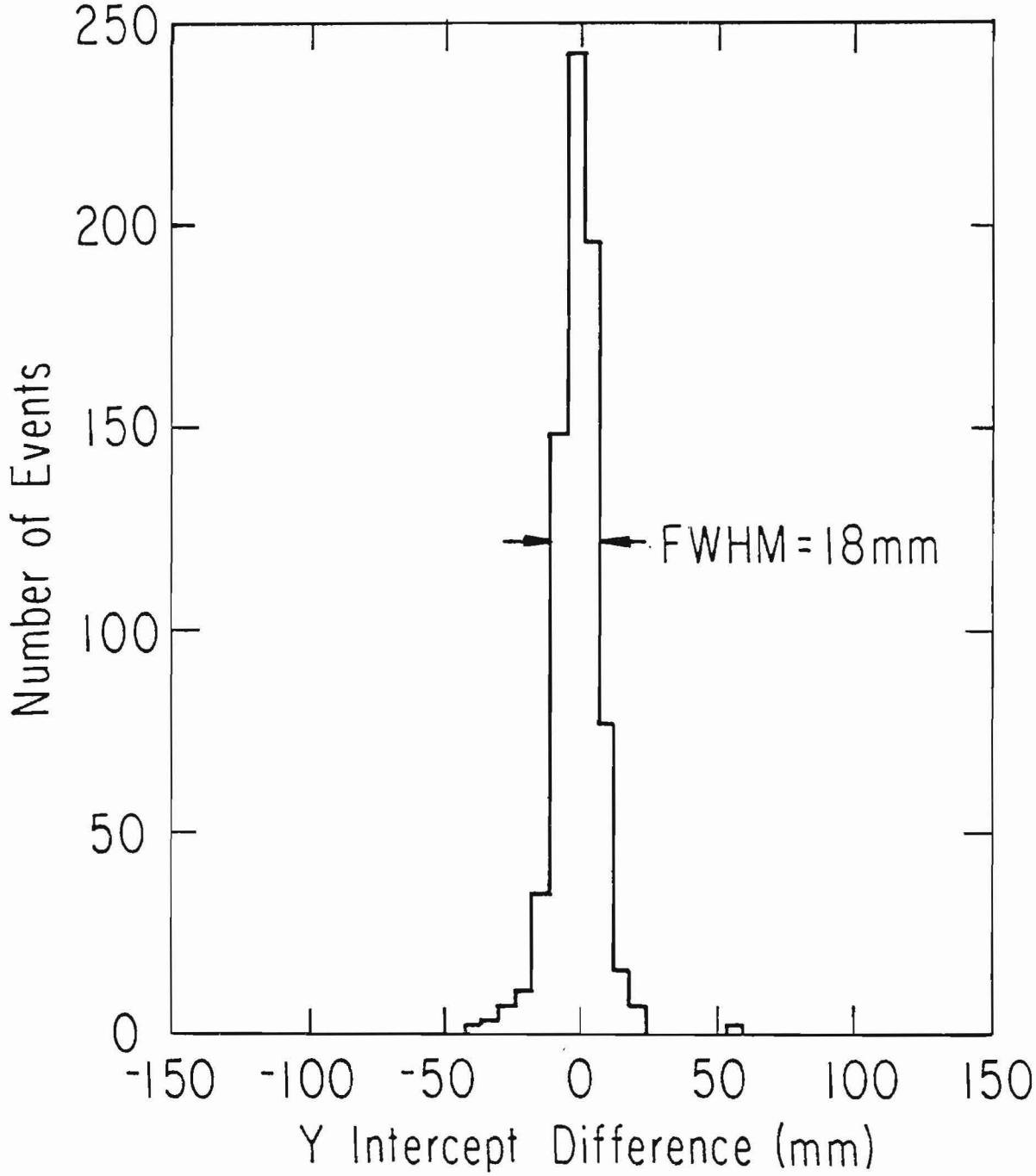
250
200
150
100
50
0
Number of Events
FWHM = 18mm
-150
-100
-50
0
50
100
150
Y Intercept Difference (mm)

Fig. 13.--Difference between upstream and downstream reconstructed y slopes for beam particles.

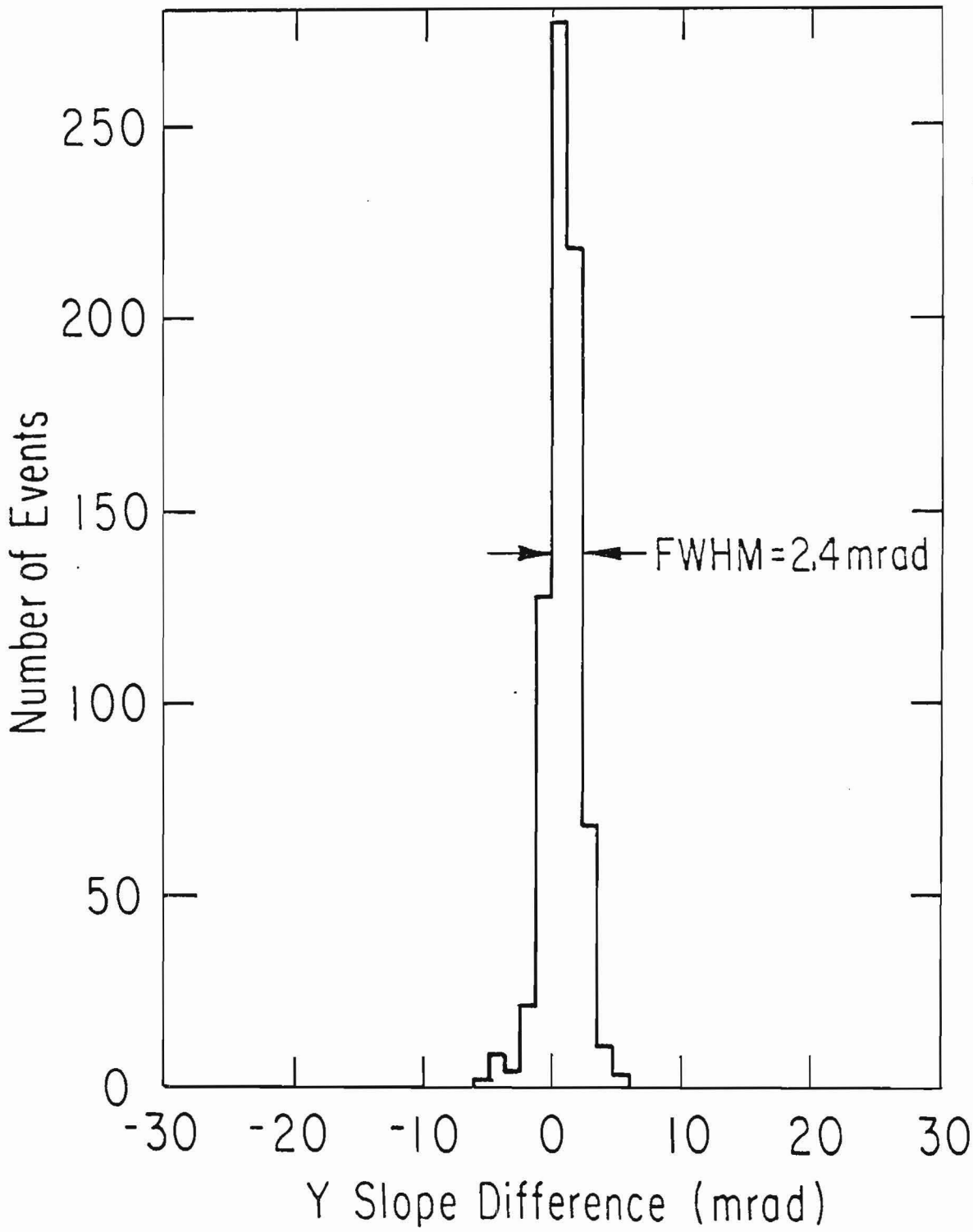
250
200
150
100
50
0
Number of Events
FWHM=2.4 mrad
-30
-20
-10
0
10
20
30
Y Slope Difference (mrad)

Fig. 14.--Momentum distribution for beam particles.

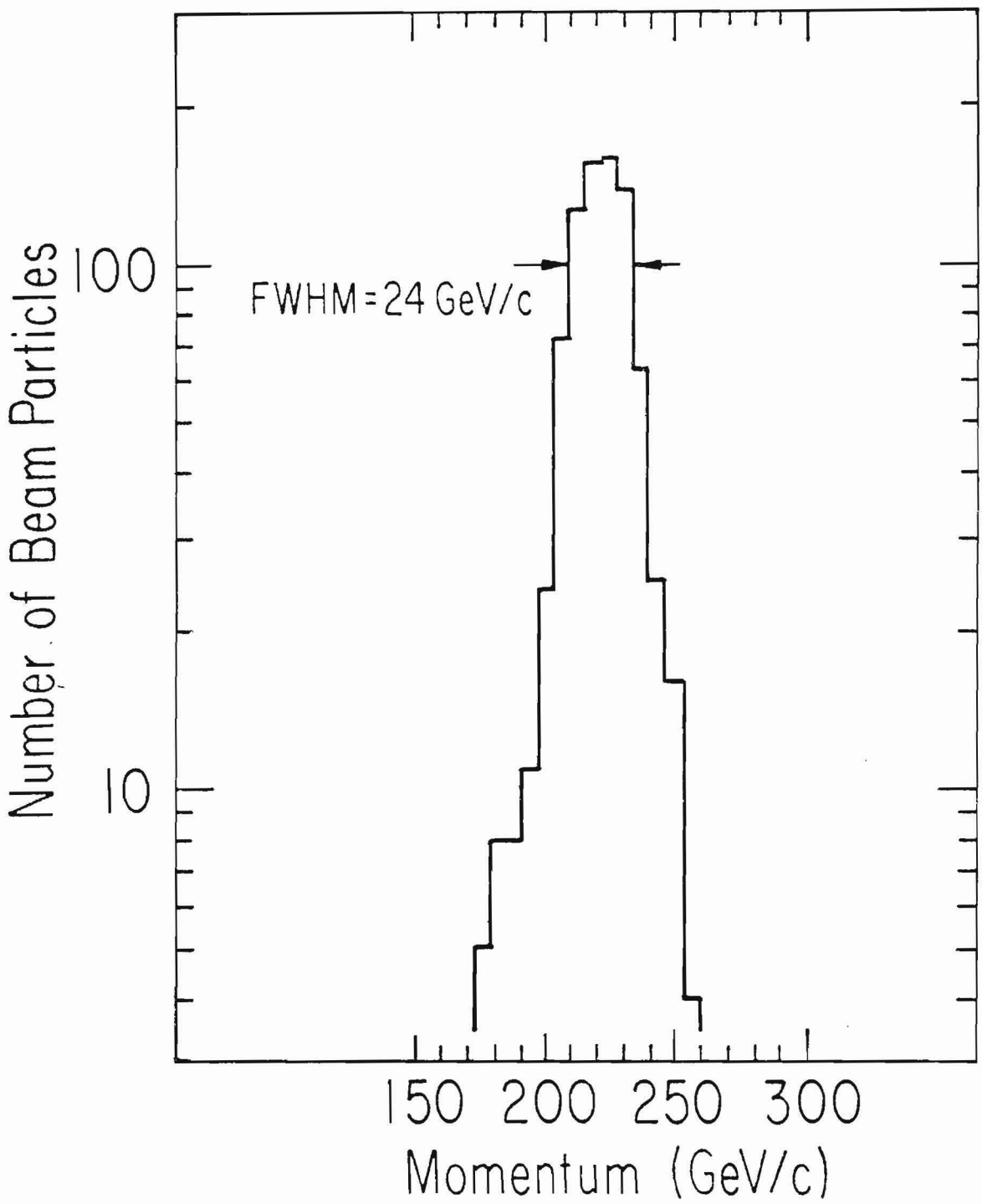
Number of Beam Particles
100
10
FWHM = 24 GeV/c
150 200 250 300
Momentum (GeV/c)

Fig. 15.--Plot of the number of good events divided by the number of beam particles as a function of run number. The vertical scale is arbitrary; the different beam particle and target types are offset for clarity.

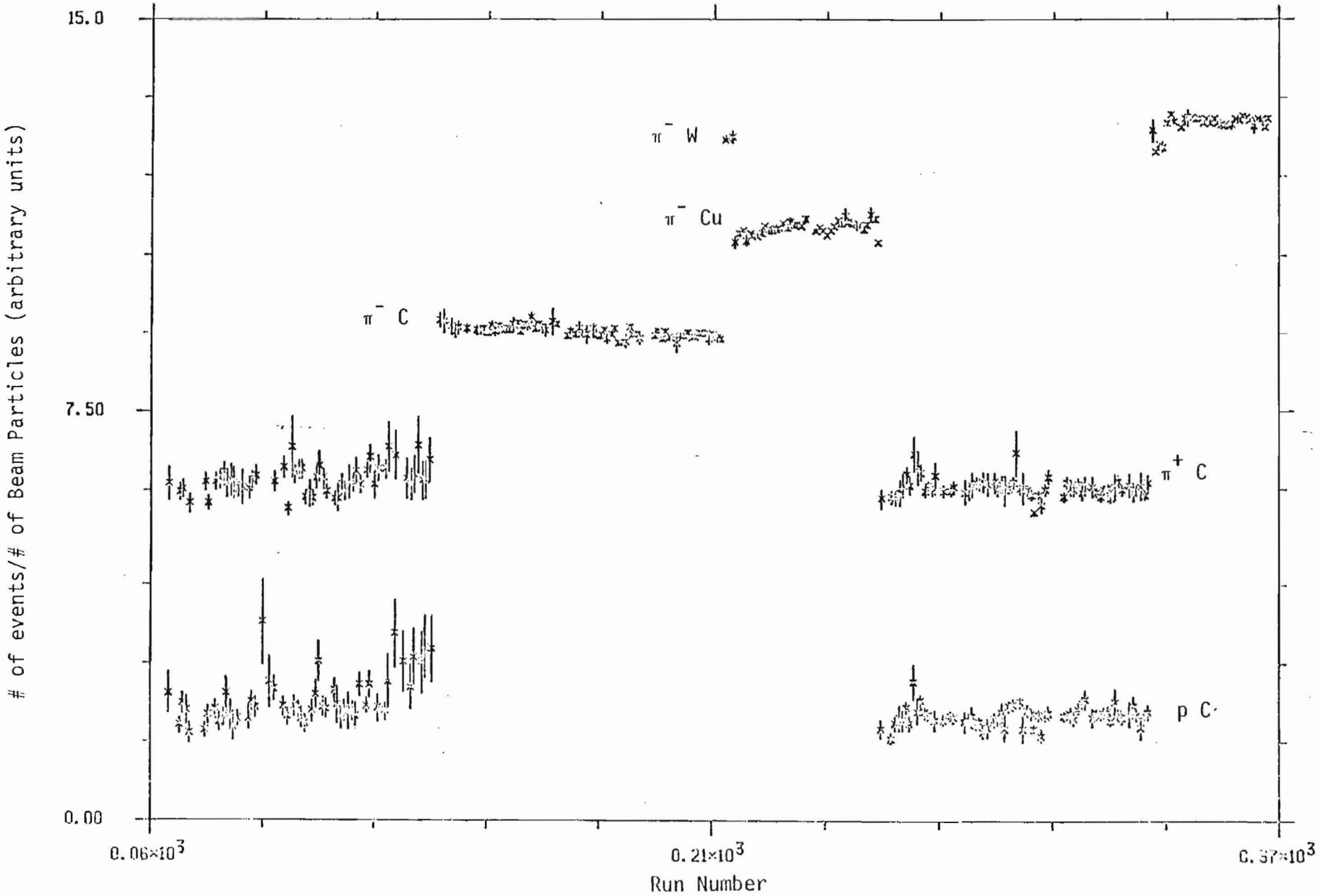
15.0
7.50
0.00
# of events/# of Beam Particles (arbitrary units)
π⁻ W
π⁻ Cu
π⁻ C
π⁺ C
p C
0.06×10³
0.21×10³
0.37×10³
Run Number

Fig. 16.--Momentum distributions for events with M >2 GeV/c^2 which satisfy the software trigger requirement. (a) Muons with the same charge as the beam; (b) Muons with charge opposite to the beam.

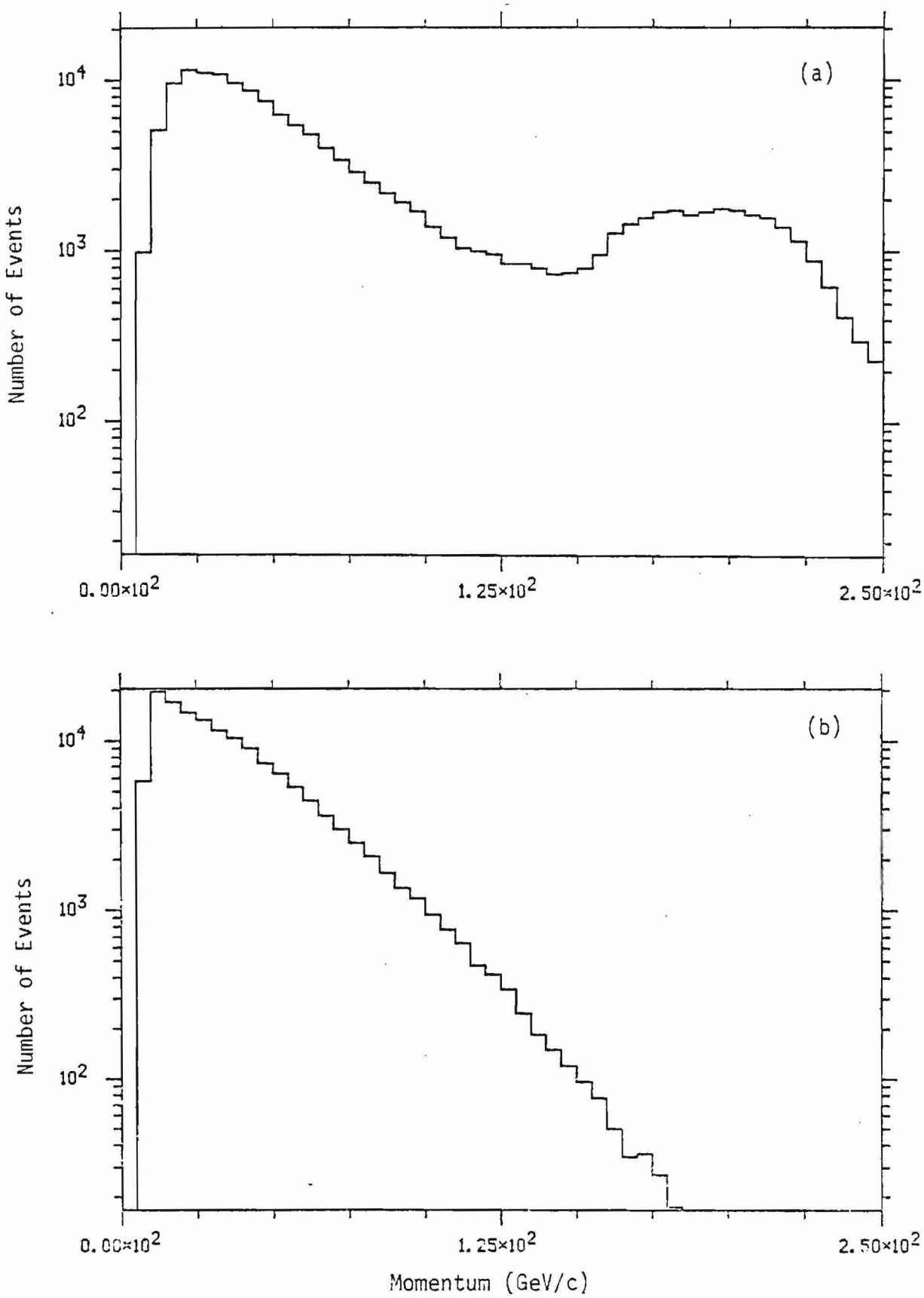
(a)
Number of Events
10^4
10^3
10^2
0.00×10^2
1.25×10^2
2.50×10^2
(b)
Number of Events
10^4
10^3
10^2
0.00×10^2
1.25×10^2
2.50×10^2
Momentum (GeV/c)

Fig. 17.--Momentum distributions (for events with $m > 2$ GeV/c^2 which satisfy the software trigger requirement) after beam momentum limits are imposed. (a) Muons with the same charge as the beam; (b) Muons with charge opposite to the beam.

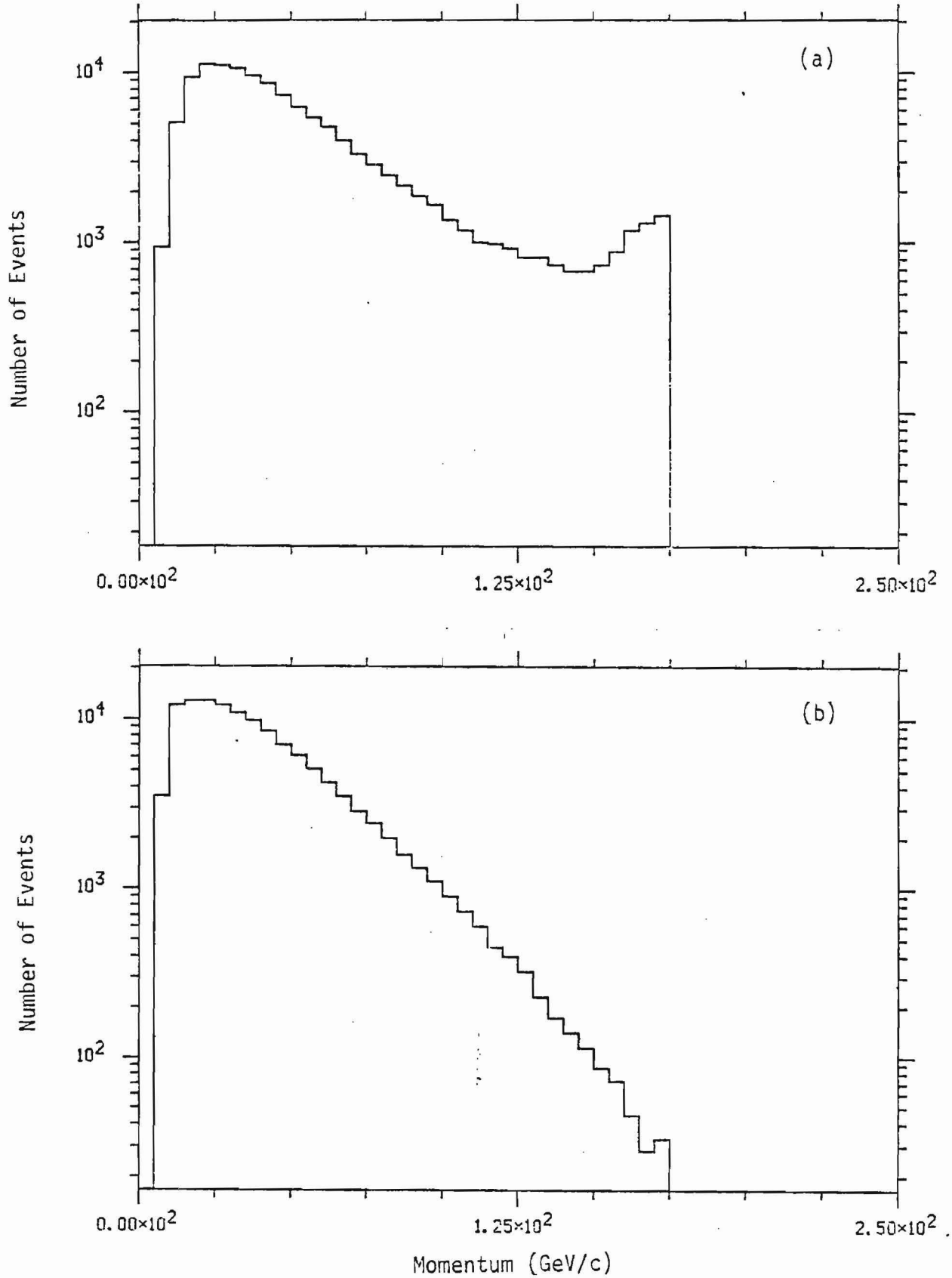
(a)
(b)
Number of Events
10^4
10^3
10^2
0.00×10^2
1.25×10^2
2.50×10^2
Momentum (GeV/c)

Fig. 18.--Probability distribution associated with χ^2 for the hypothesis that both muons come from a common vertex in the target. In the lower plot, the scale has been expanded to show the region 0.0-0.25 in more detail.

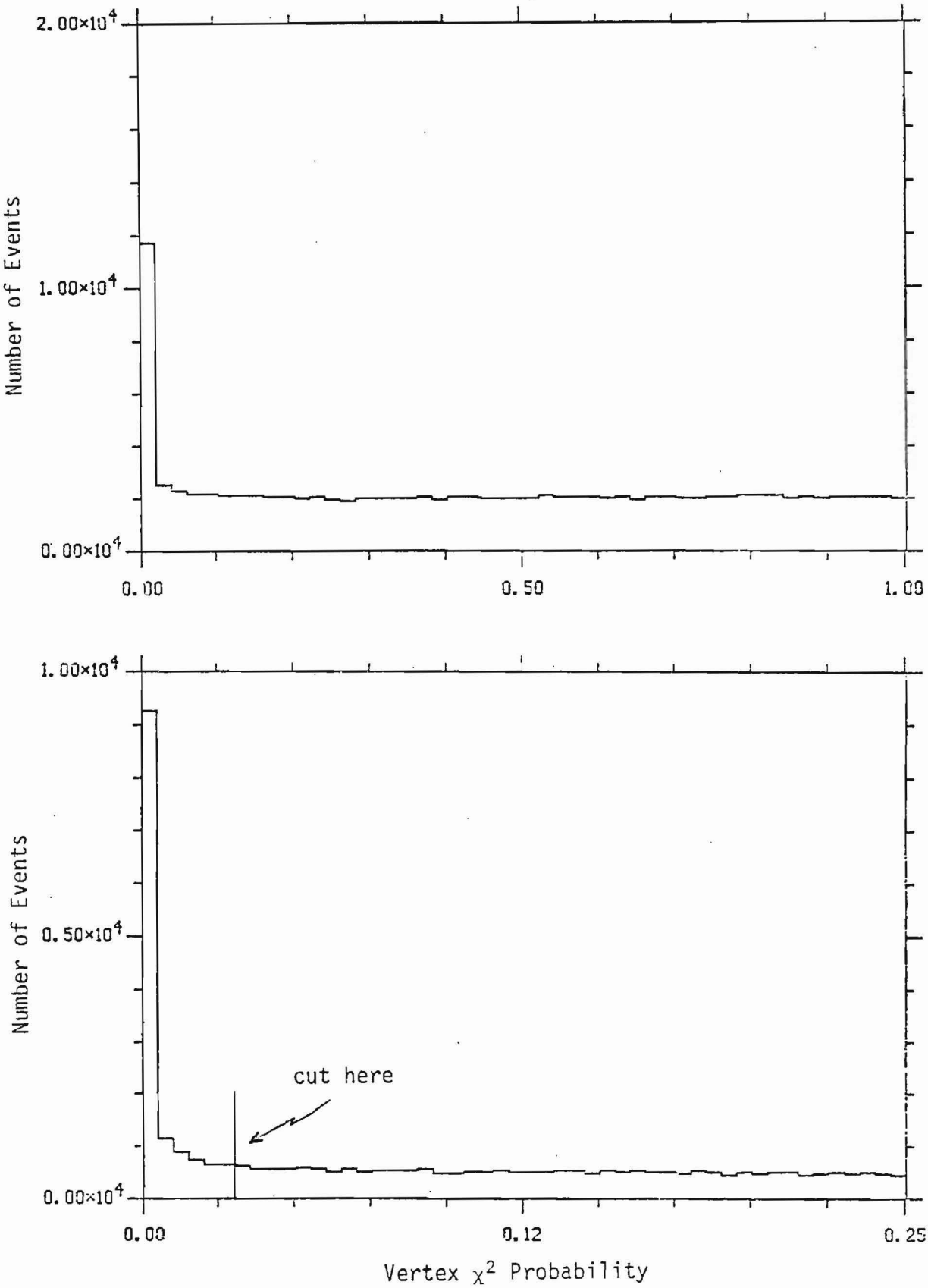
2.00×10^4
1.00×10^4
0.00×10^4
Number of Events
0.00
0.50
1.00
1.00×10^4
0.50×10^4
0.00×10^4
Number of Events
cut here
0.00
0.12
0.25
Vertex χ^2 Probability

Fig. 19.--Scatter plot of the reconstructed x vertex vs. y vertex with cut indicated. The origin is the center of the beam spot.

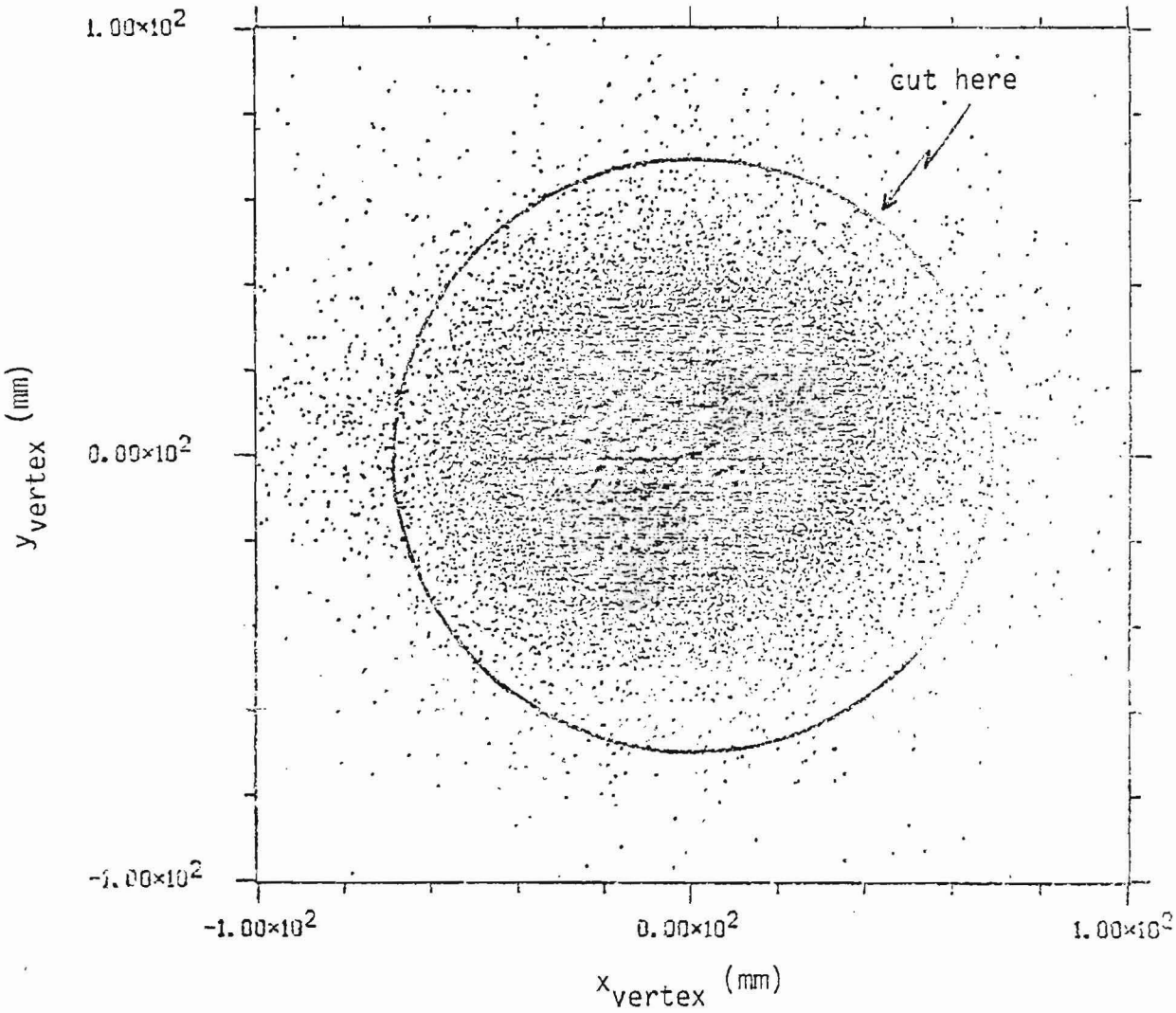
1.00×10^2
0.00×10^2
-1.00×10^2
-1.00×10^2
0.00×10^2
1.00×10^2
cut here
y_vertex (mm)
x_vertex (mm)

Fig. 20.--Scatter plot of reconstructed vertex position vs. momentum. Rvertex is measured from the center of the beam spot. (a) Muons with the same charge as the beam; (b) Muons with charge opposite to the beam.

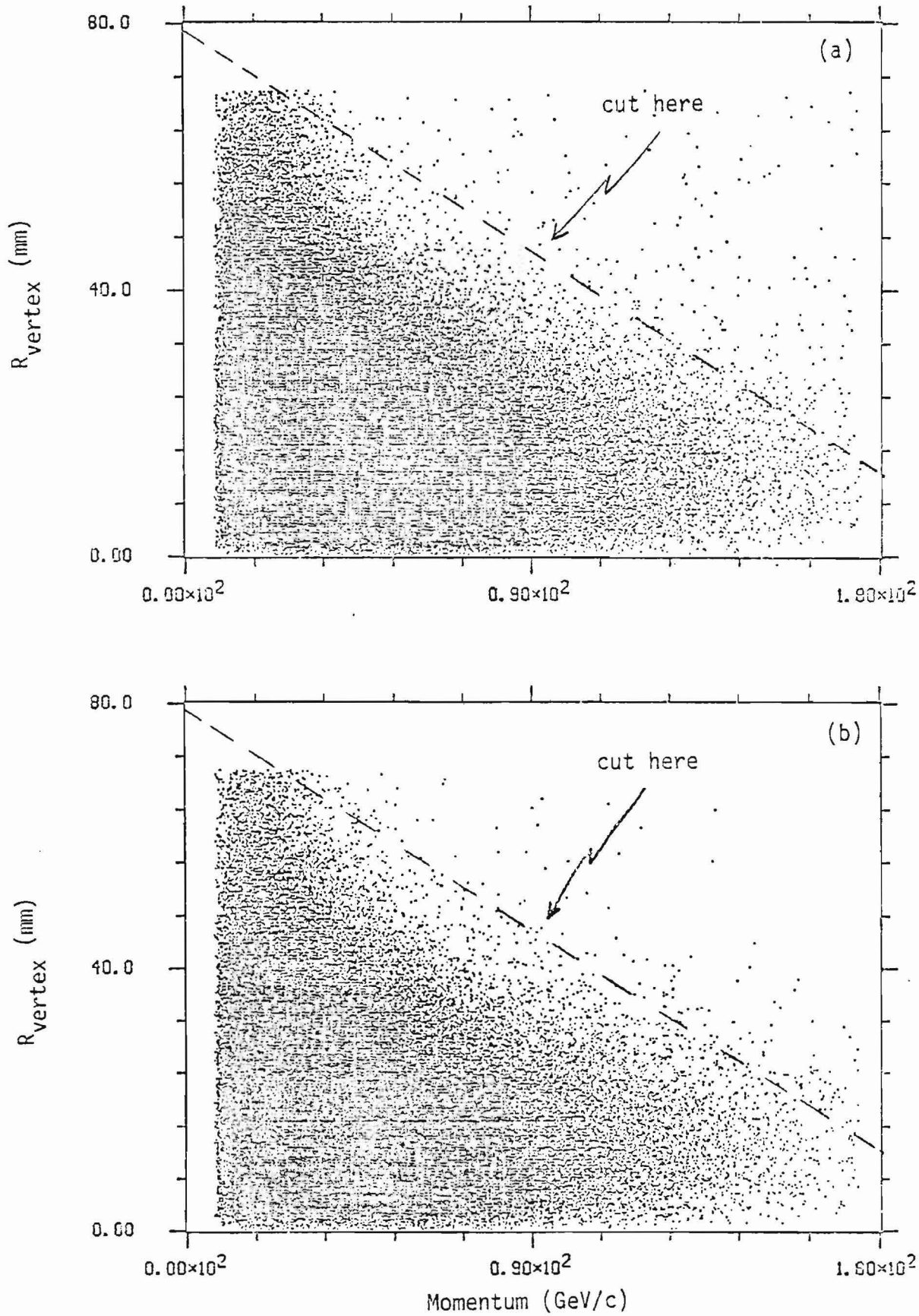
80.0
40.0
0.00
R_{vertex} (mm)
(a)
cut here
0.00×10^2
0.90×10^2
1.80×10^2
80.0
40.0
0.00
R_{vertex} (mm)
(b)
cut here
0.00×10^2
0.90×10^2
1.80×10^2
Momentum (GeV/c)

Fig. 21.--Momentum distribution after all event selection criteria have been applied. (a) Muons with the same charge as the beam; (b) Muons with charge opposite to the beam.

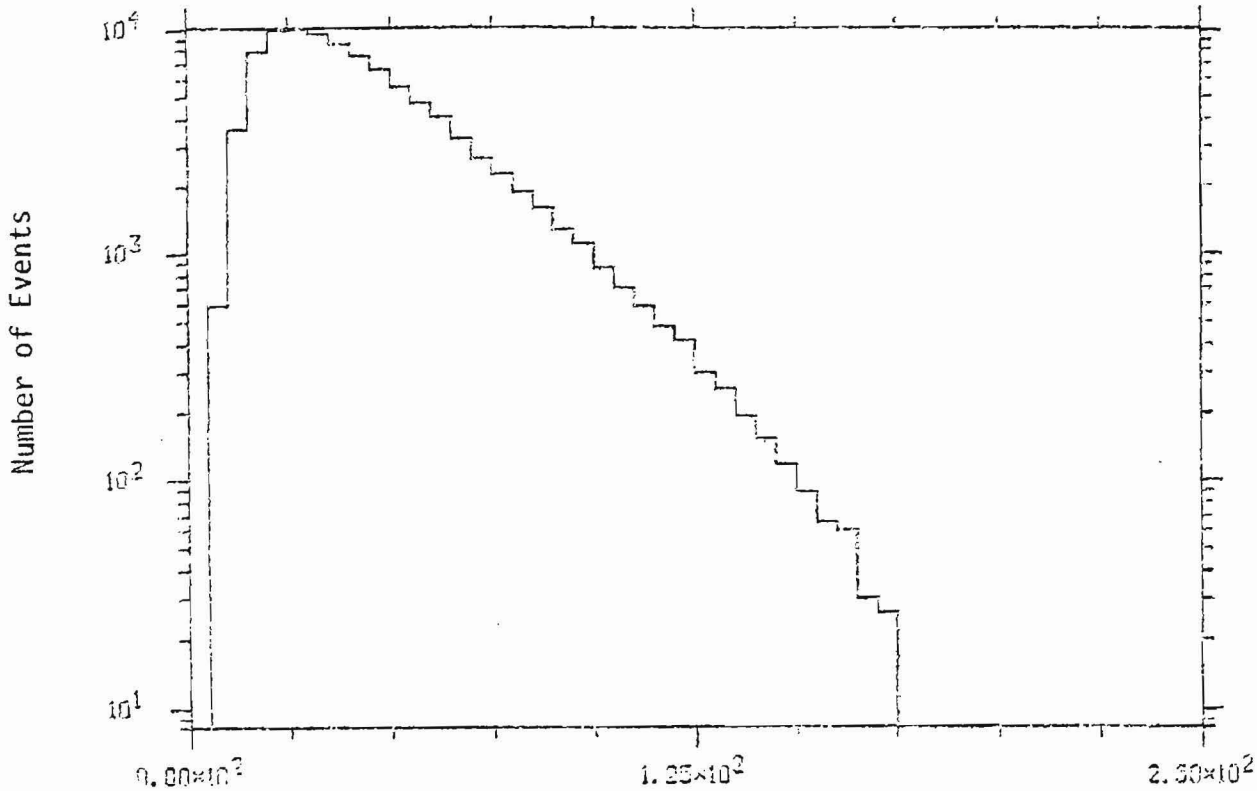
Number of Events
10^4
10^3
10^2
10^1
0.00×10^2
1.25×10^2
2.50×10^2

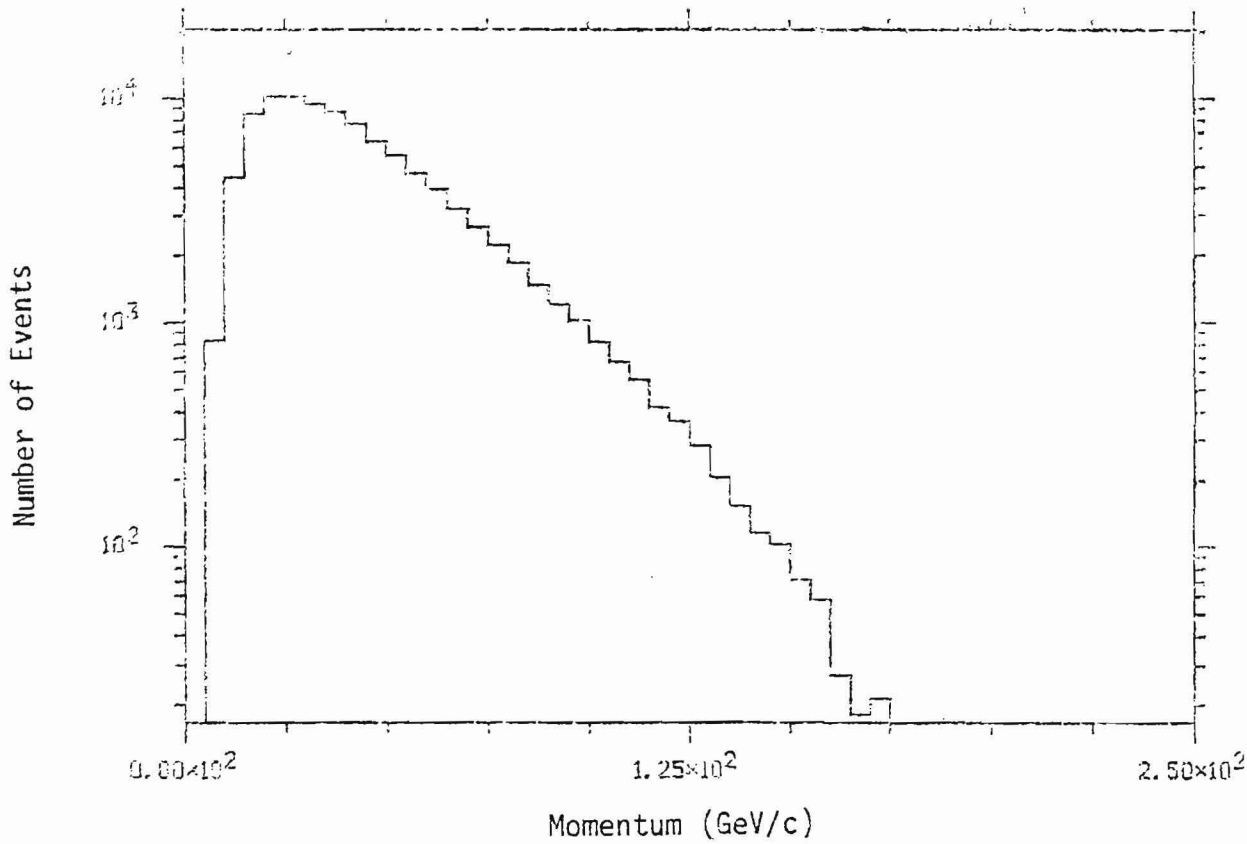
Number of Events
10^4
10^3
10^2
0.00×10^2
1.25×10^2
2.50×10^2
Momentum (GeV/c)

Fig. 22.--Mass distribution for π^- induced μ pair events. The top plot is opposite sign μ pairs. The lower plot shows the like sign μ pair background.

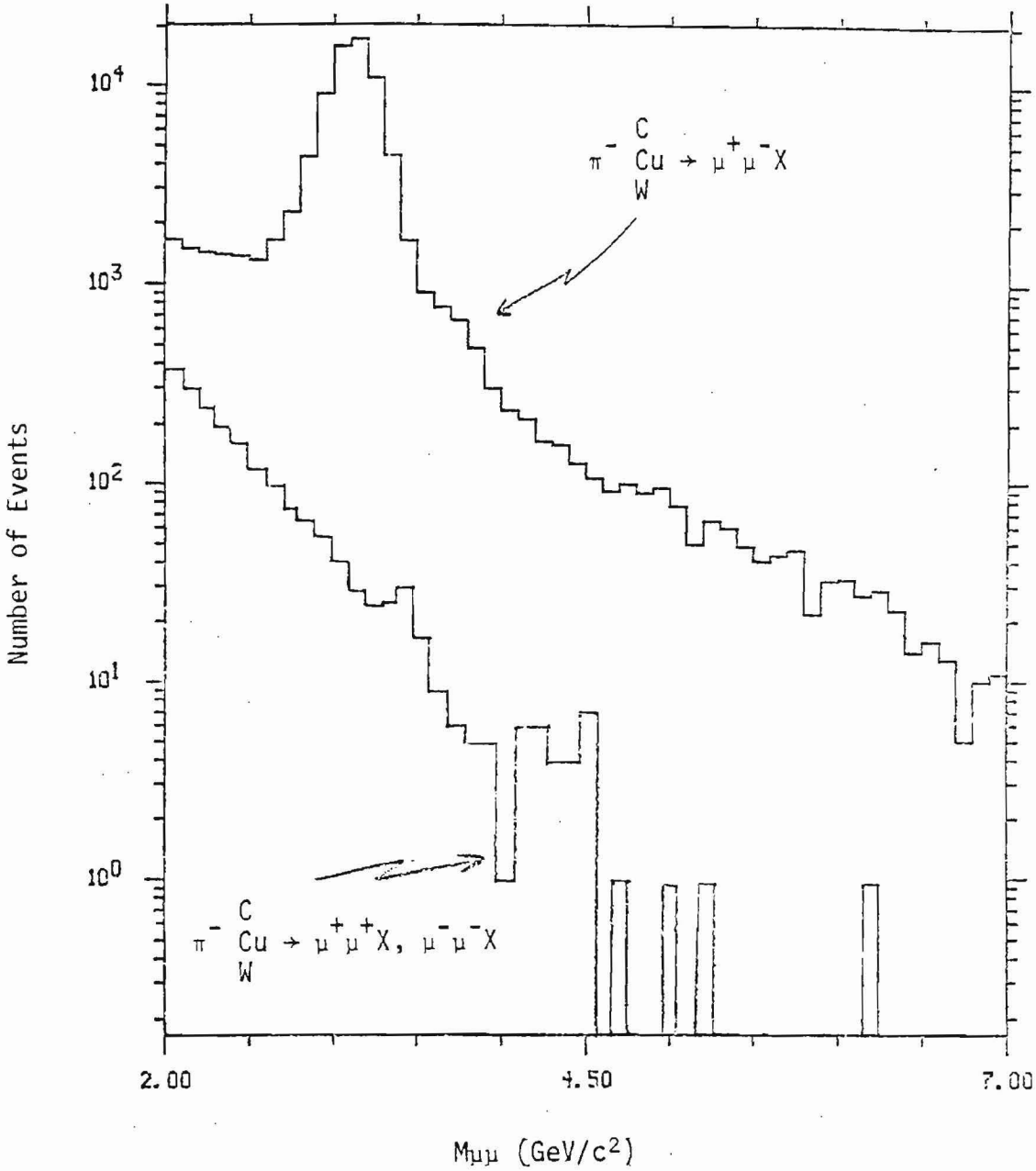
10^4
10^3
10^2
10^1
10^0
Number of Events
π^- C Cu W $\rightarrow \mu^+\mu^- X$
π^- C Cu W $\rightarrow \mu^+\mu^+ X$, $\mu^-\mu^- X$
2.00
4.50
7.00
$M_{\mu\mu}$ (GeV/c^2)

Fig. 23.--The detector efficiency. (a) as a function of mass (x_F = 0.3, p_T = 1.0 GeV/c); (b) as a function of x_F (M = 5.0 GeV/c^2, p_T = 1.0 GeV/c); (c) as a function of p_T (M = 5.0 GeV/c^2, x_F = 0.3).

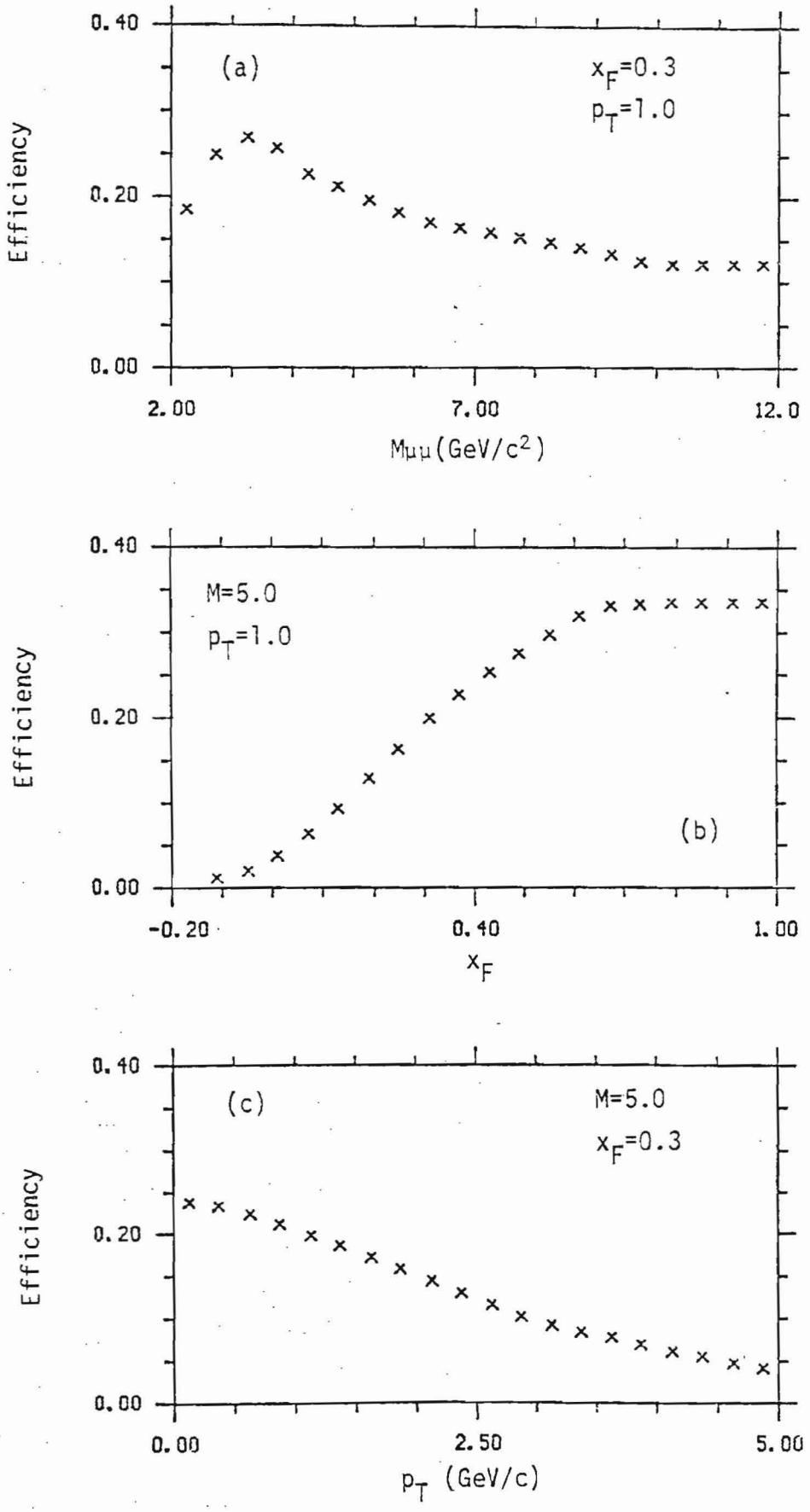
0.40
0.20
0.00
Efficiency
(a)
x_F=0.3
p_T=1.0
2.00
7.00
12.0
Mμμ(GeV/c²)
0.40
0.20
0.00
Efficiency
M=5.0
p_T=1.0
(b)
-0.20
0.40
1.00
x_F
0.40
0.20
0.00
Efficiency
(c)
M=5.0
x_F=0.3
0.00
2.50
5.00
p_T (GeV/c)

Fig. 24.--Detector efficiency vs. cos θ^* for events with mass greater than 3.5 GeV/c^2. The four plots correspond to four choices for the reference direction from which θ^* is measured. These choices are explained in Chapter IV. Also, see Fig. 64.

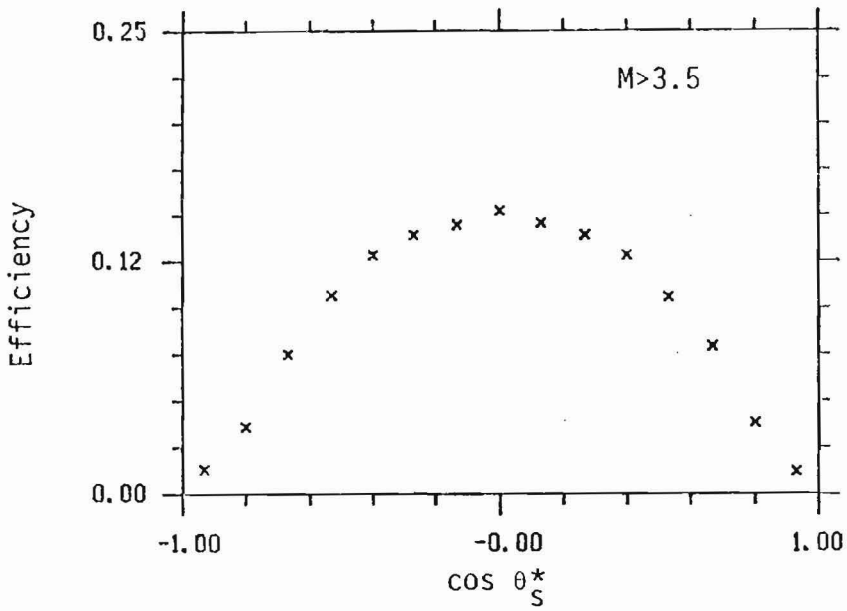
M>3.5
Efficiency
0.25
0.12
0.00
-1.00
-0.00
1.00
cos θ*s

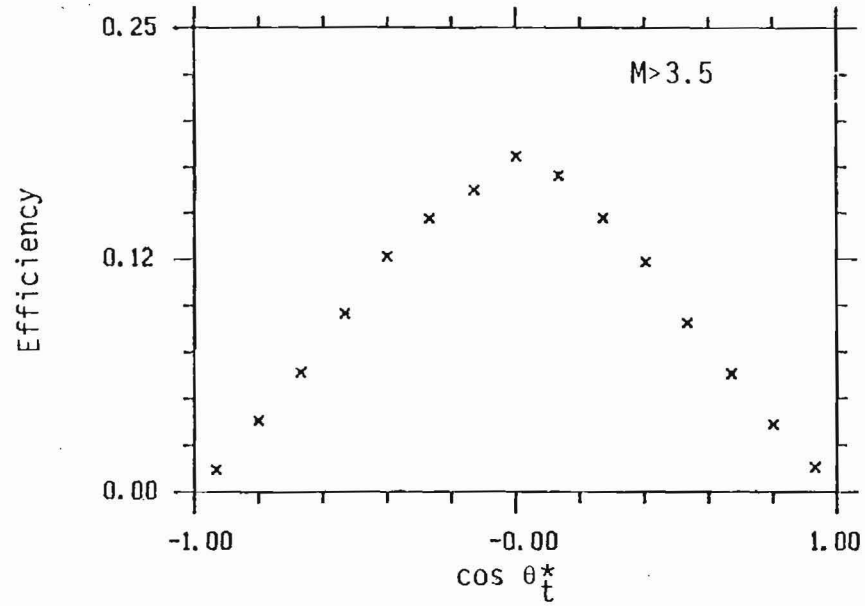
M>3.5
Efficiency
0.25
0.12
0.00
-1.00
-0.00
1.00
cos θ*t

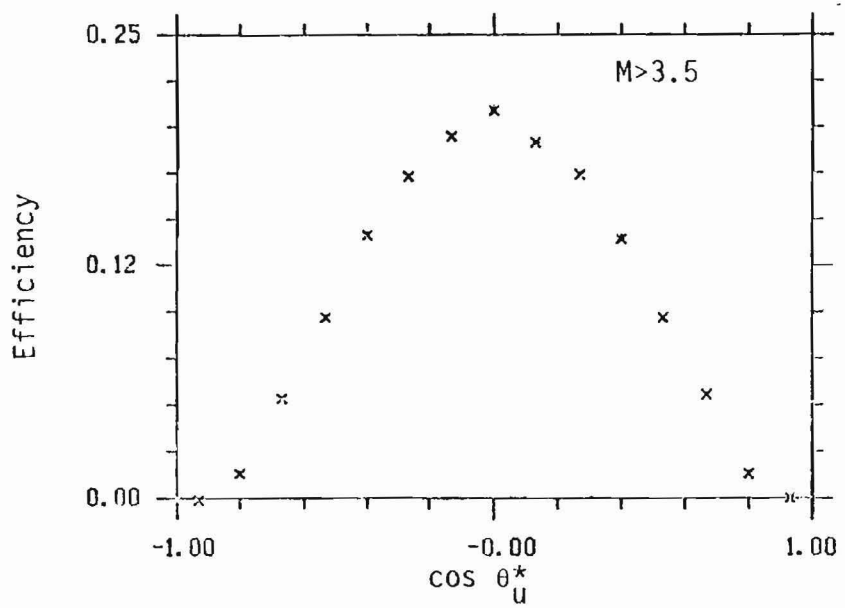
M>3.5
Efficiency
0.25
0.12
0.00
-1.00
-0.00
1.00
cos θ*u

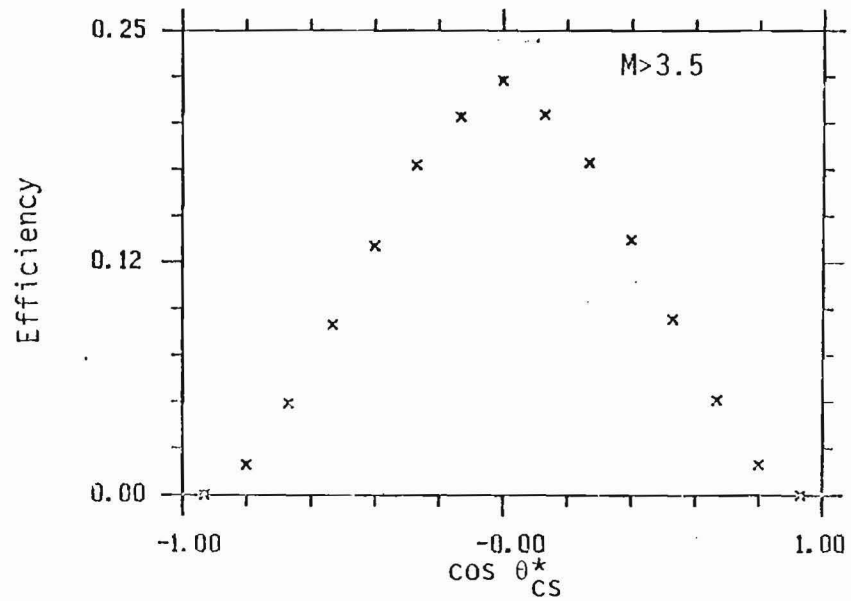
M>3.5
Efficiency
0.25
0.12
0.00
-1.00
-0.00
1.00
cos θ*cs

Fig. 25.--Detector efficiency vs. ϕ^* for events with mass greater than 3.5 GeV/c^2.

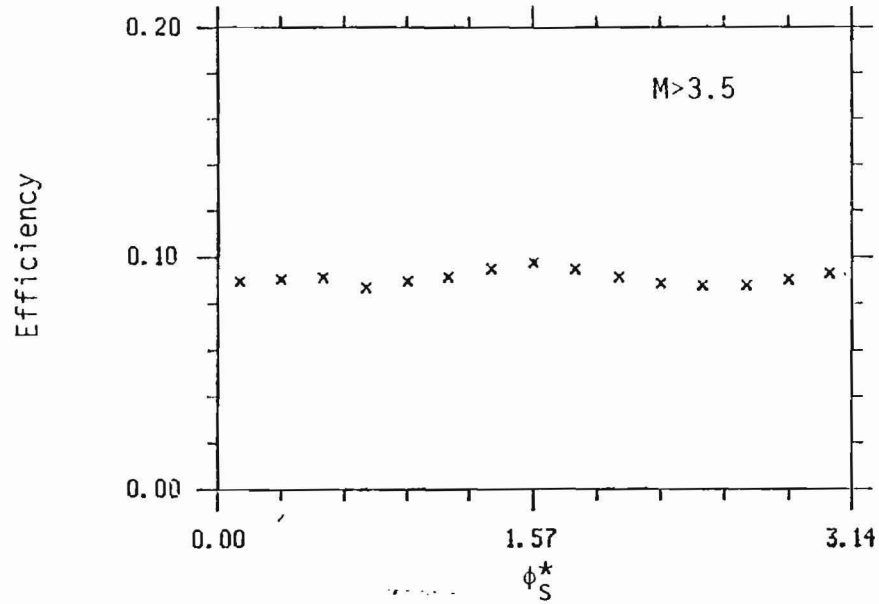
0.20
0.10
0.00
Efficiency
M>3.5
0.00
1.57
3.14
ϕ_s^*

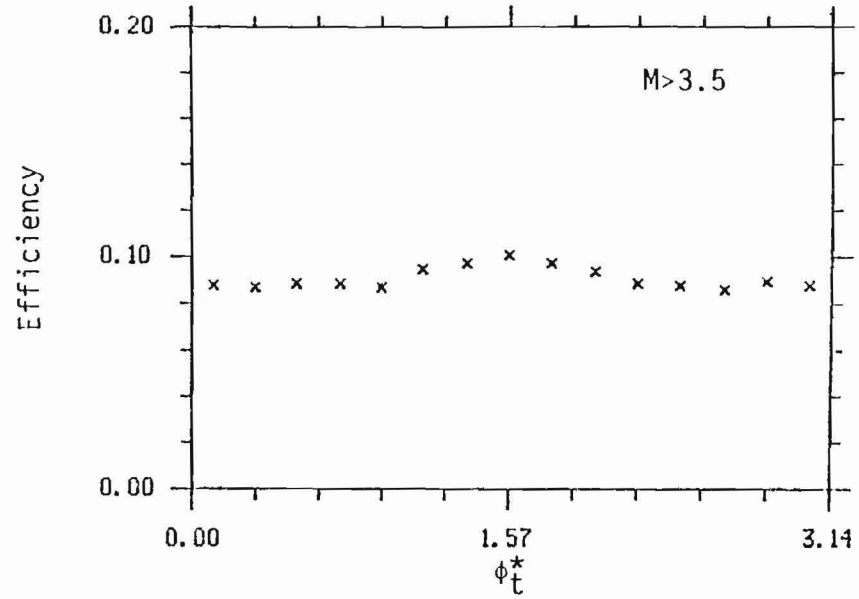
0.20
0.10
0.00
Efficiency
M>3.5
0.00
1.57
3.14
ϕ_t^*

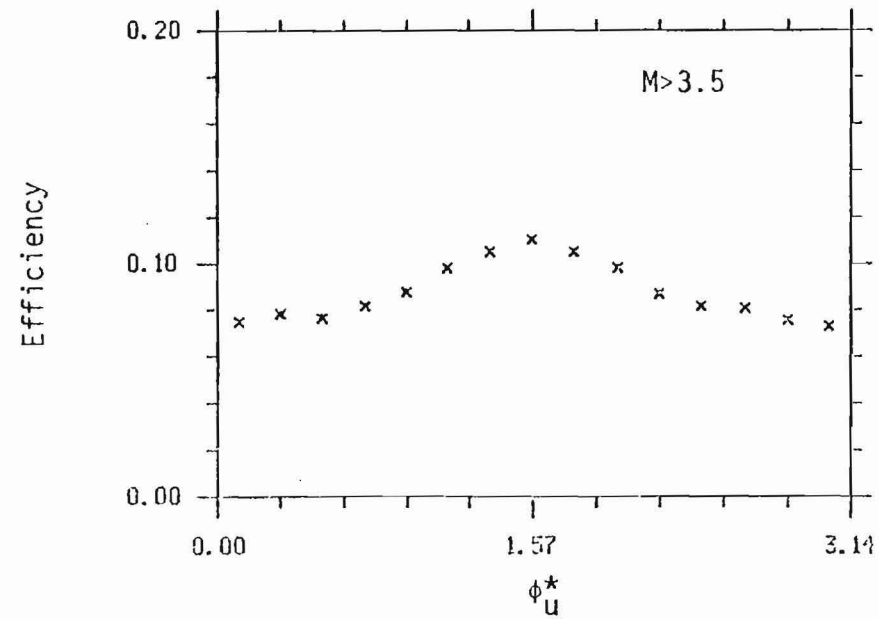
0.20
0.10
0.00
Efficiency
M>3.5
0.00
1.57
3.14
ϕ_u^*

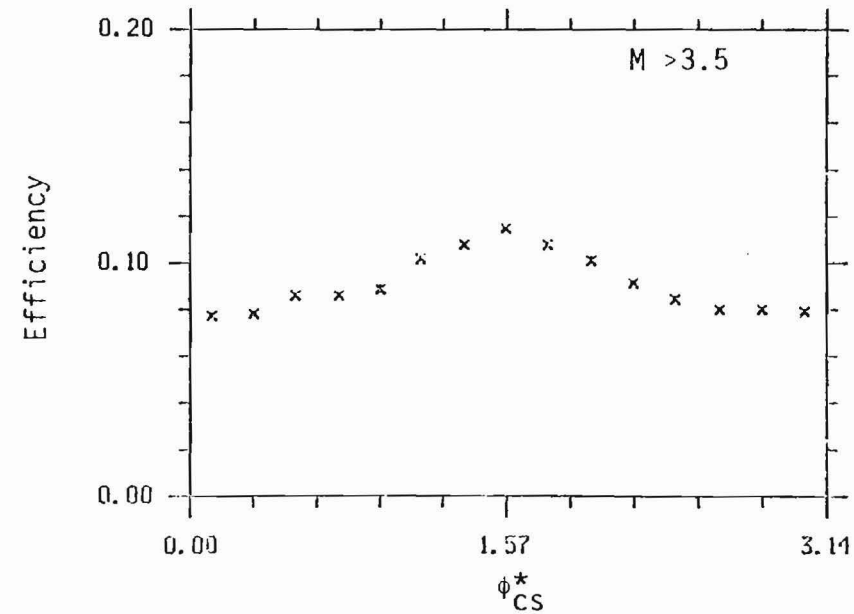
0.20
0.10
0.00
Efficiency
M >3.5
0.00
1.57
3.14
ϕ_{cs}^*

Fig. 26.--Effect of resolution smearing on the Feynman x spectrum. The solid line is a Monte Carlo generated x_F spectrum at the J/ψ mass. The x's are obtained by binning the successes, as described in the text, according to the value of x_F reconstructed and weighting by the appropriate efficiency.

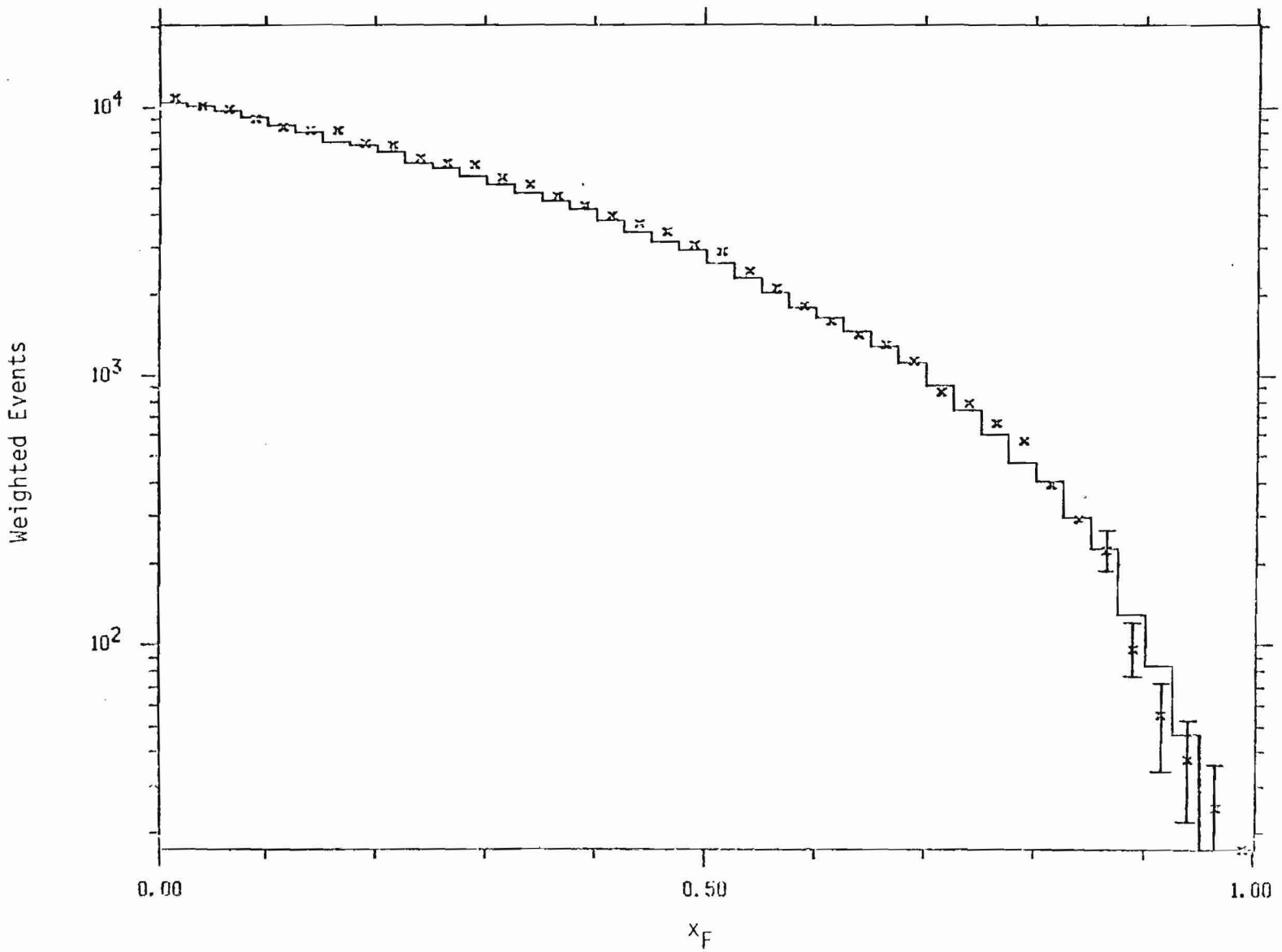
Weighted Events
10^4
10^3
10^2
0.00
0.50
1.00
x_F

Fig. 27.--Effect of resolution smearing on the transverse momentum spectrum.

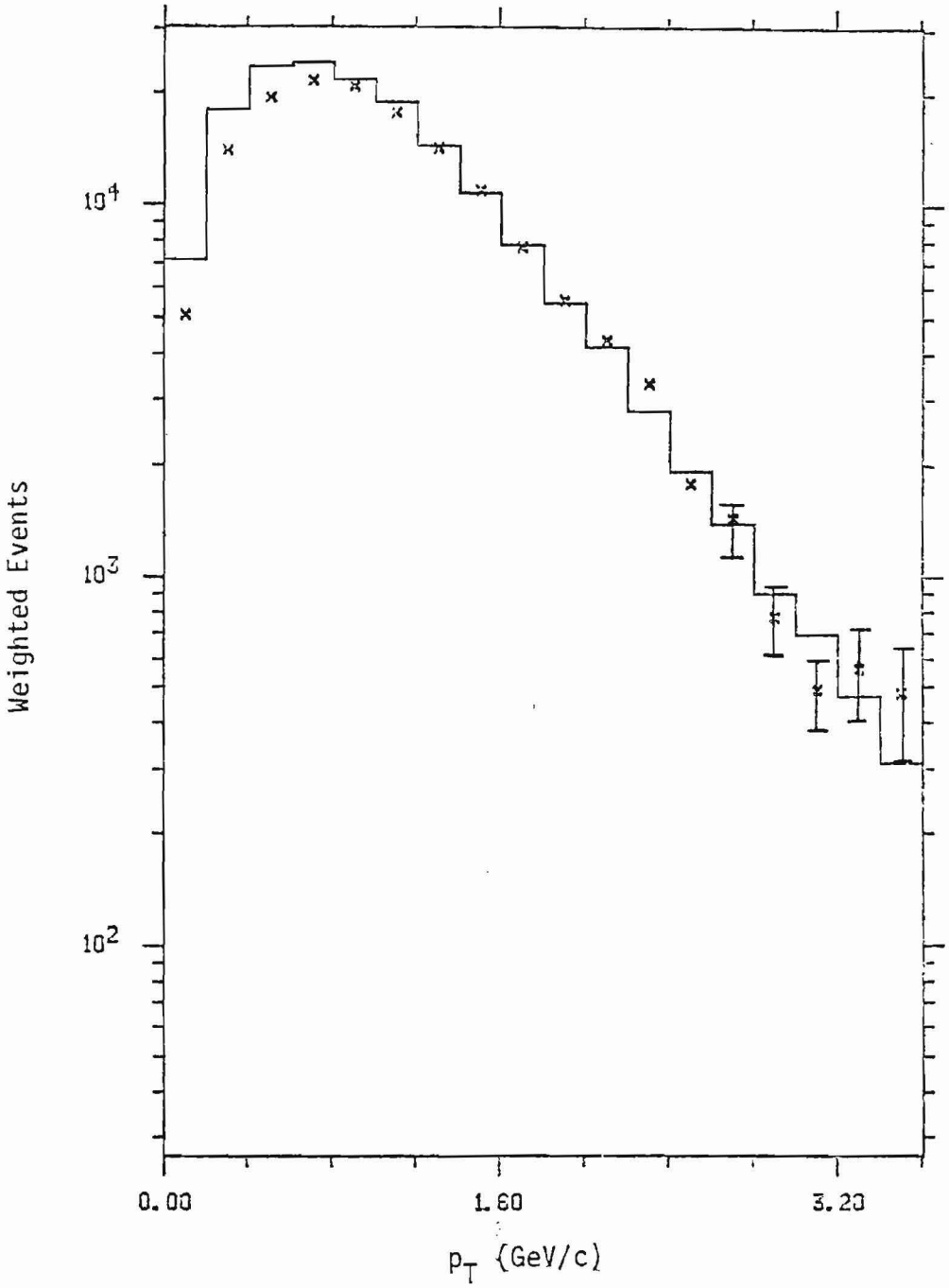
Weighted Events
10^4
10^3
10^2
0.00
1.60
3.20
p_T (GeV/c)

Fig. 28.--Mass spectrum for proton induced μ pairs (per carbon nucleus).

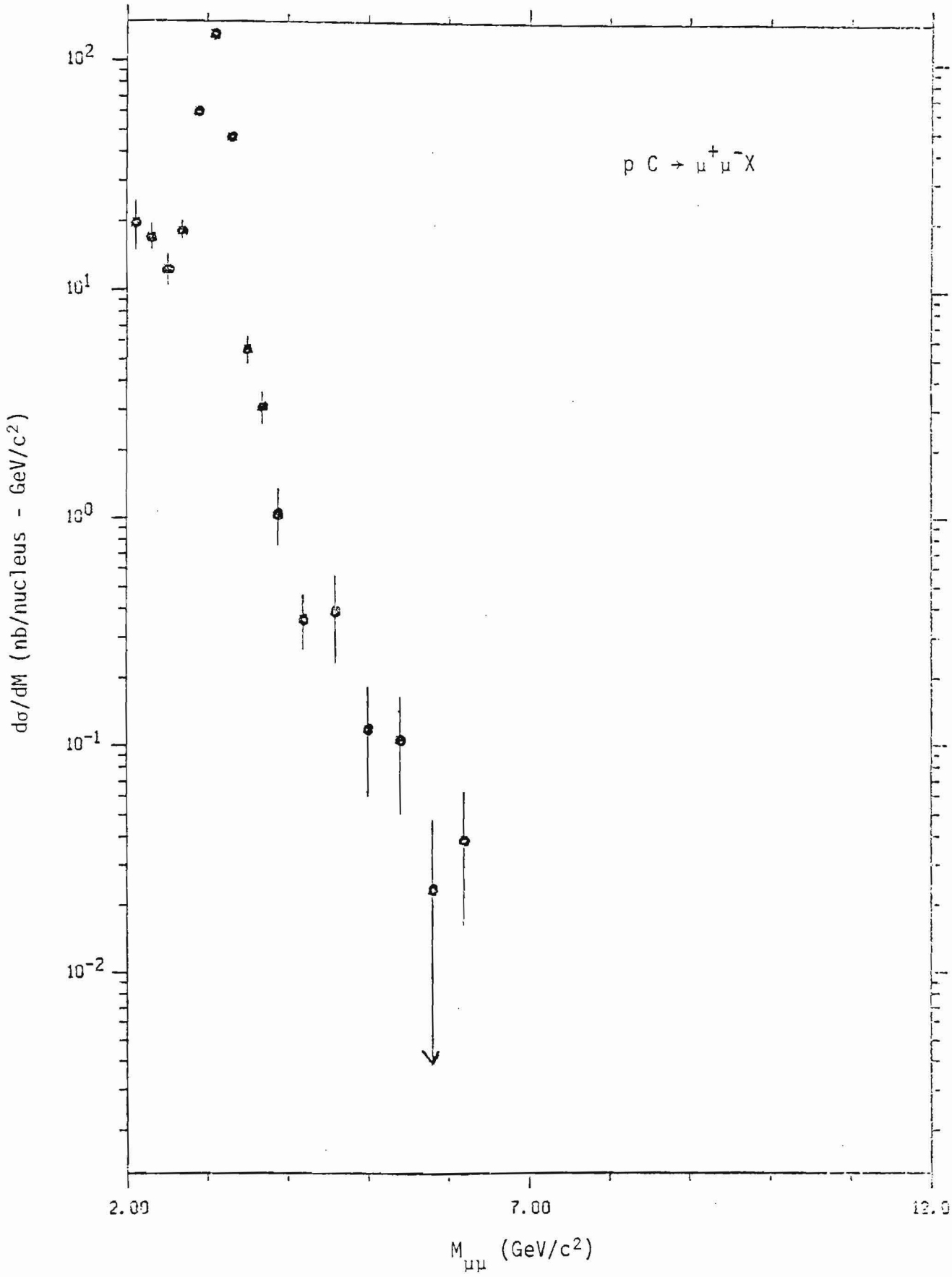
p C → μ+μ−X
dσ/dM (nb/nucleus - GeV/c2)
10^2
10^1
10^0
10^-1
10^-2
2.00
7.00
12.0
Mμμ (GeV/c2)

Fig. 29.--Mass spectrum for π^+ induced μ pairs (per carbon nucleus).

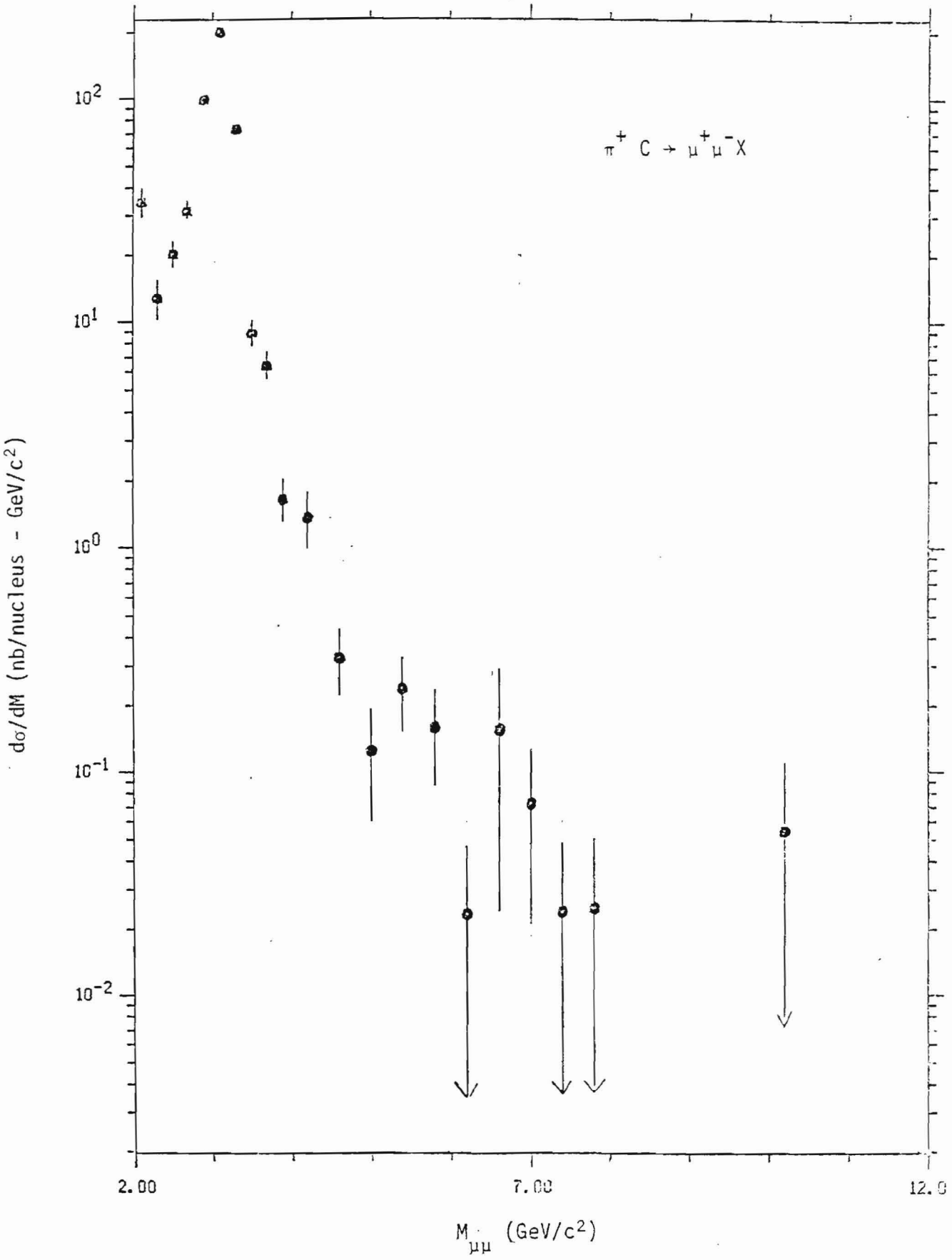
$\pi^+ C \rightarrow \mu^+\mu^- X$
10^2
10^1
10^0
10^{-1}
10^{-2}
$d\sigma/dM$ (nb/nucleus - GeV/c^2)
2.00
7.00
12.0
$M_{\mu\mu}$ (GeV/c^2)

Fig. 30.--Mass spectra for K^+ (a) and $\bar{p}$ (b) induced μ pairs (per carbon nucleus).

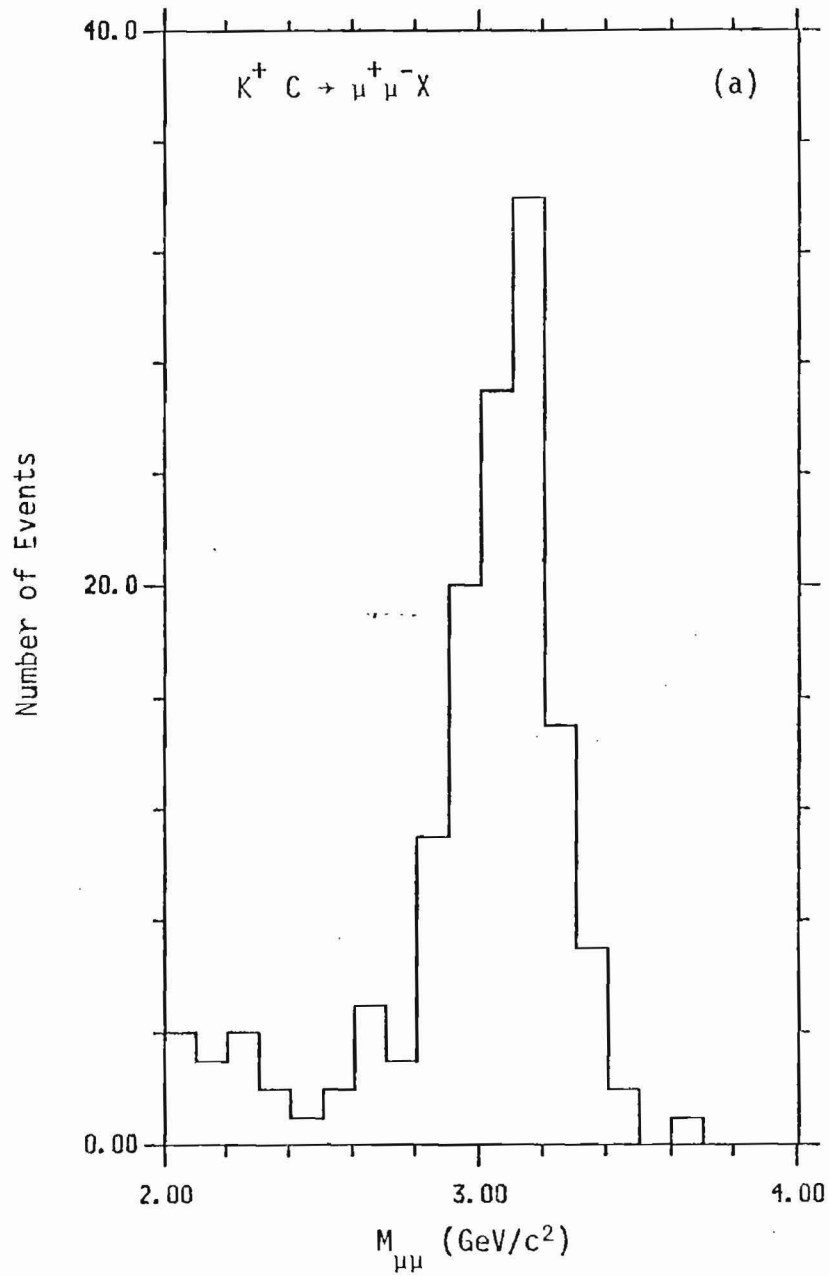
40.0
20.0
0.00
Number of Events
$K^+ C \rightarrow \mu^+\mu^- X$
(a)
2.00
3.00
4.00
$M_{\mu\mu}$ (GeV/c^2)

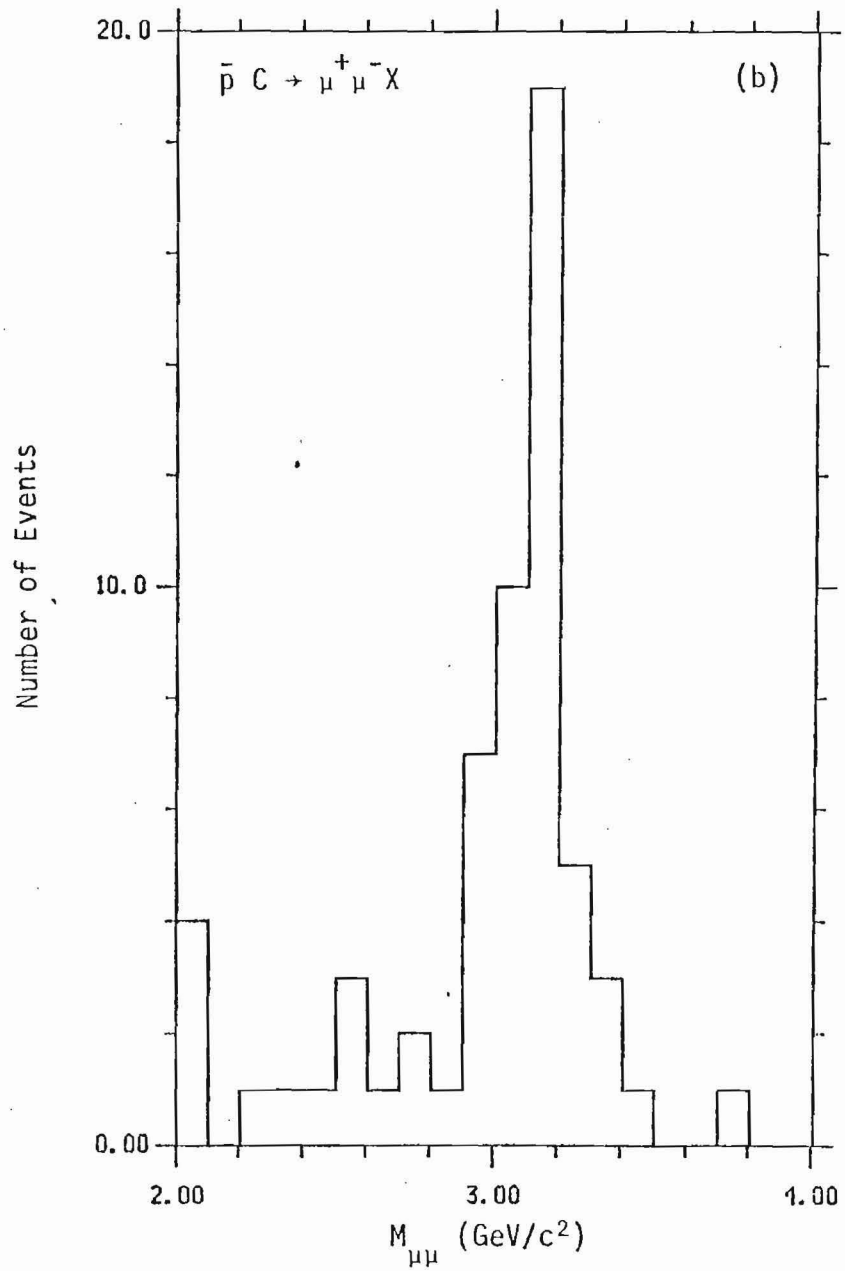
20.0
10.0
0.00
Number of Events
$\bar{p} C \rightarrow \mu^+\mu^- X$
(b)
2.00
3.00
4.00
$M_{\mu\mu}$ (GeV/c^2)

Fig. 31.--Mass spectrum for π^- induced μ pairs (per carbon nucleus).

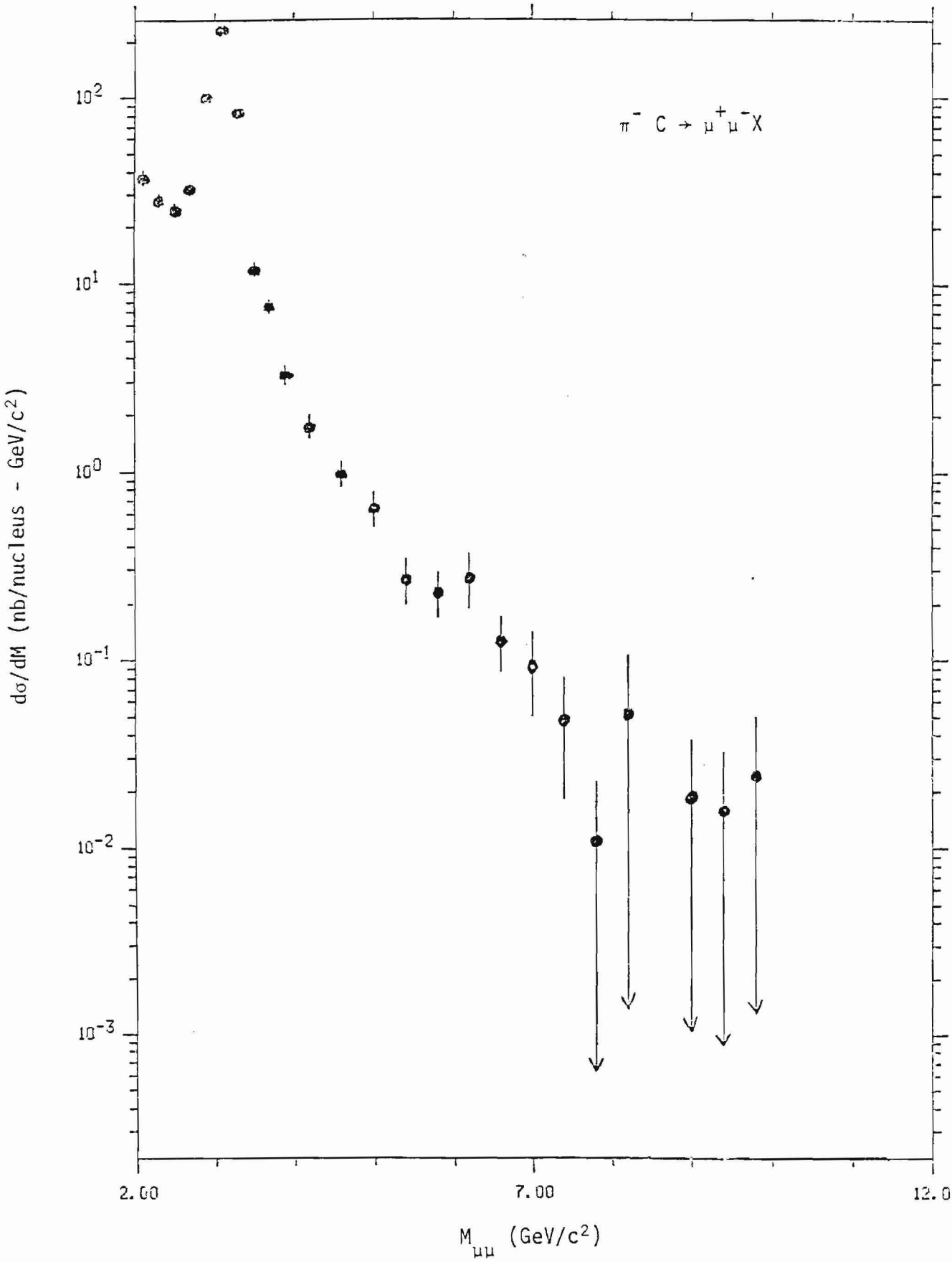
$\pi^- C \rightarrow \mu^+\mu^- X$
10^2
10^1
10^0
10^{-1}
10^{-2}
10^{-3}
$d\sigma/dM$ (nb/nucleus - GeV/c^2)
2.00
7.00
12.0
$M_{\mu\mu}$ (GeV/c^2)

Fig. 32.--Mass spectrum for π^- induced μ pairs (per copper nucleus).

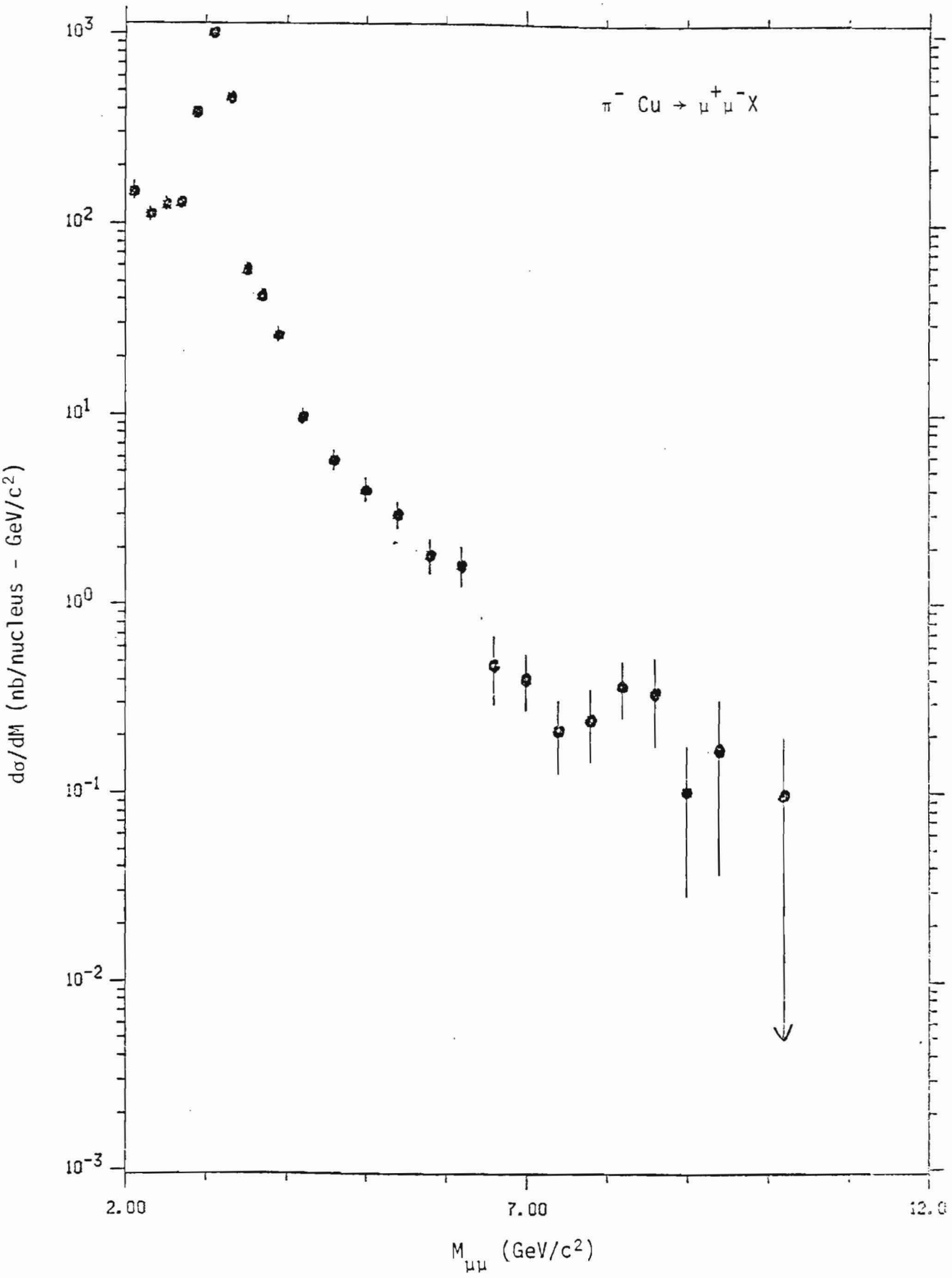
$\pi^- Cu \rightarrow \mu^+\mu^- X$
10^3
10^2
10^1
10^0
10^{-1}
10^{-2}
10^{-3}
$d\sigma/dM$ (nb/nucleus - GeV/c^2)
2.00
7.00
12.0
$M_{\mu\mu}$ (GeV/c^2)

Fig. 33.--Mass spectrum for π^- induced μ pairs (per tungsten nucleus).

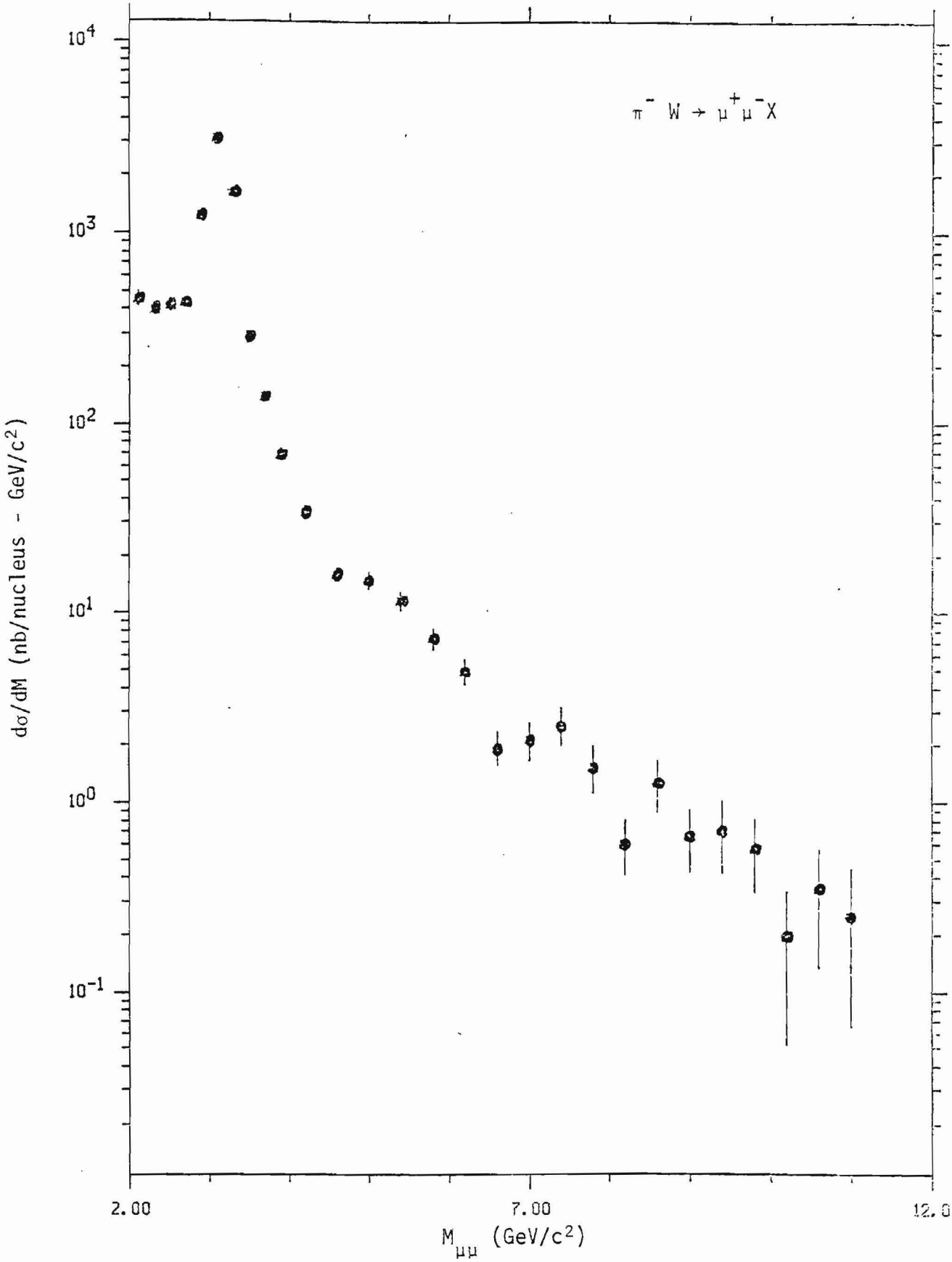
$\pi^- W \rightarrow \mu^+\mu^- X$
10^4
10^3
10^2
10^1
10^0
10^{-1}
$d\sigma/dM$ (nb/nucleus - GeV/c^2)
2.00
7.00
12.0
$M_{\mu\mu}$ (GeV/c^2)

Fig. 34.--Mass spectrum for π^- induced μ pairs (per nucleon). The extrapolation to cross section per nucleon used the measured A dependence. Only data with masses between 4.0 and 8.0 GeV/c^2 were used to determine the power law fit.

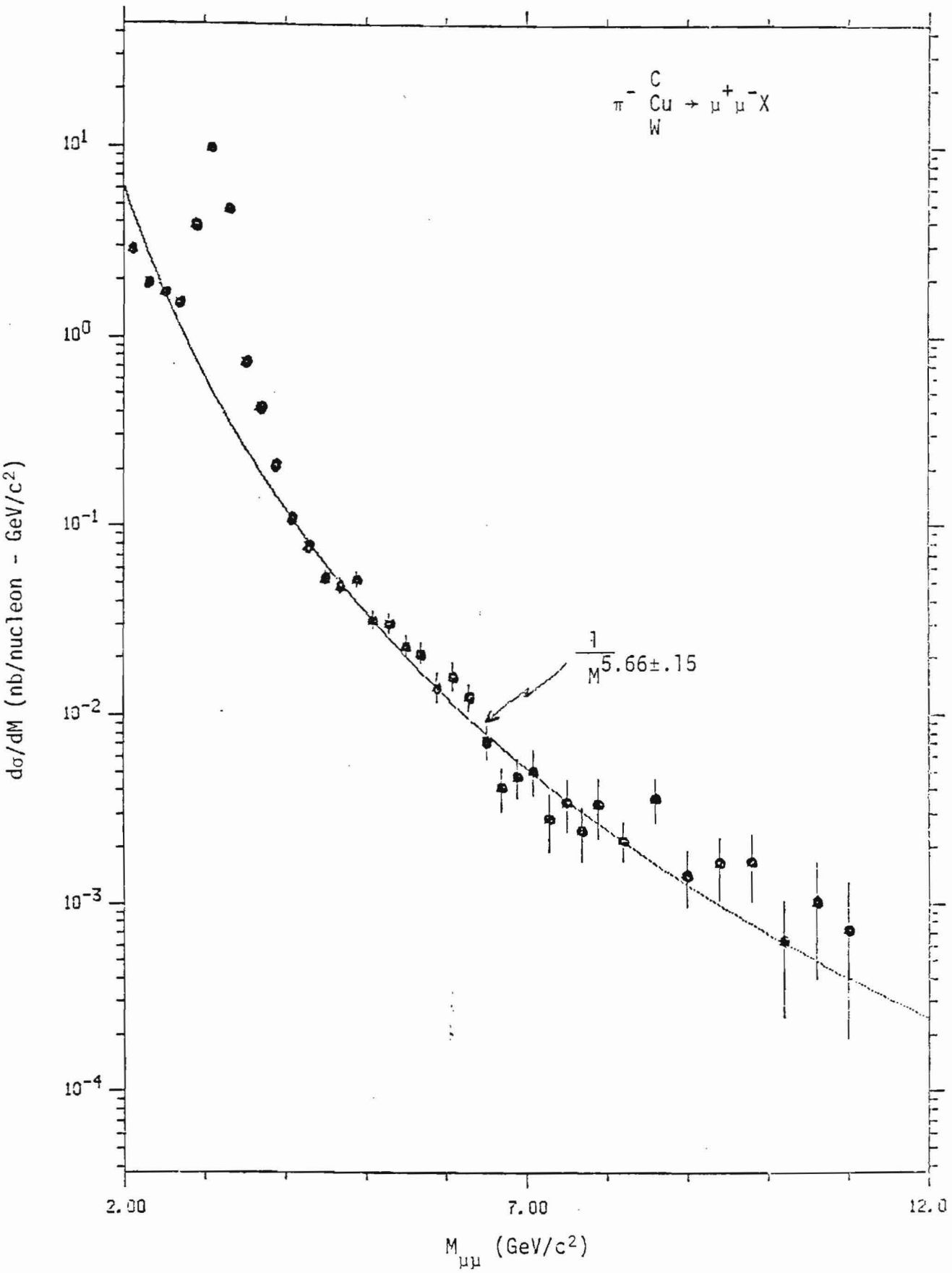
$\pi^- \begin{matrix} C \\ Cu \\ W \end{matrix} \rightarrow \mu^+\mu^- X$
$\frac{1}{M^{5.66\pm.15}}$
10^1
10^0
10^{-1}
10^{-2}
10^{-3}
10^{-4}
$d\sigma/dM$ (nb/nucleon - GeV/c^2)
2.00
7.00
12.0
$M_{\mu\mu}$ (GeV/c^2)

Fig. 35.--Mass spectrum for π^- induced μ pairs with masses between 2.5 and 4.5 GeV/c^2. The curve is a fit from a Monte Carlo determination of the J/ψ line shape.

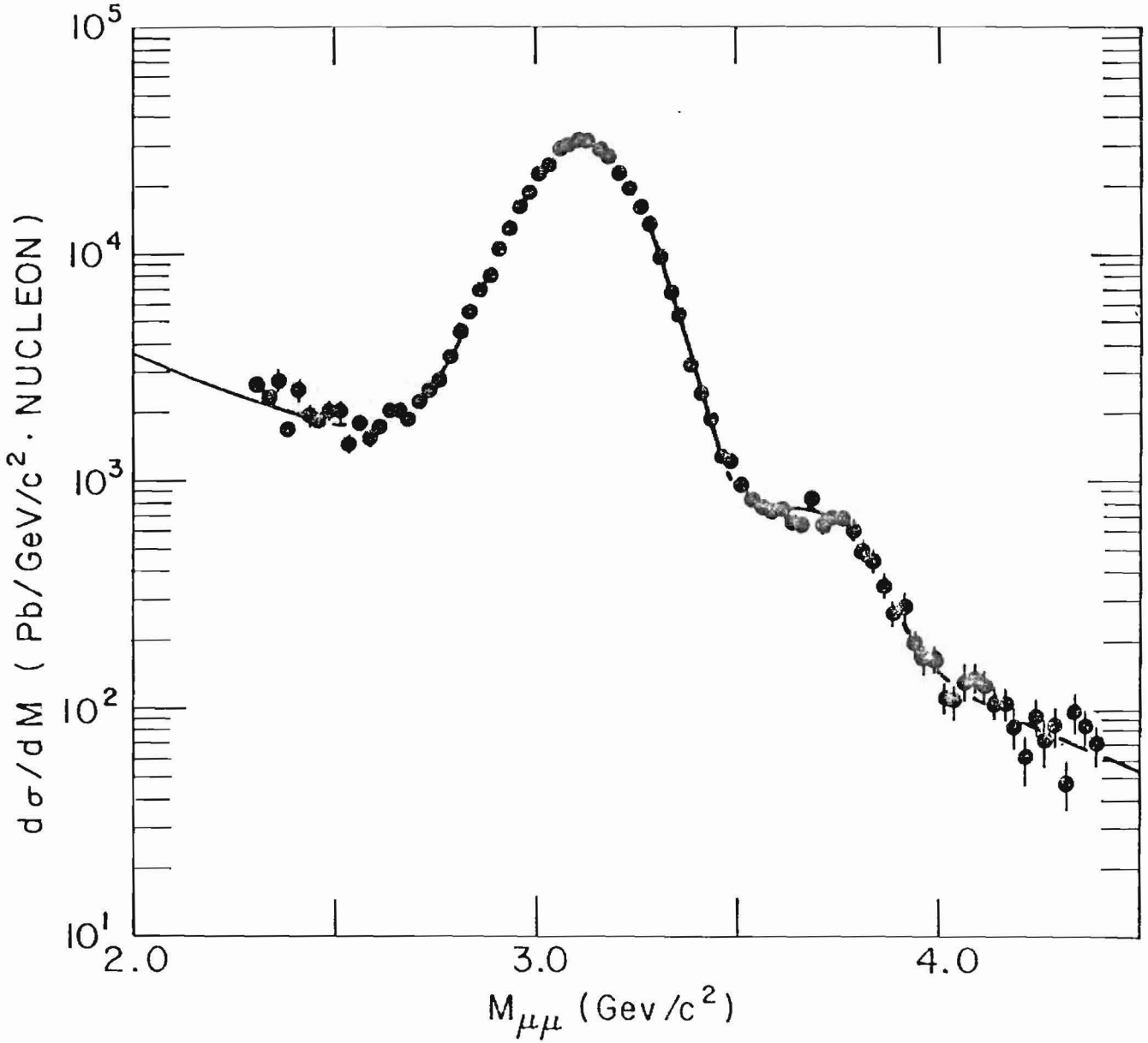
10^5
10^4
10^3
10^2
10^1
$d\sigma/dM$ (Pb/GeV/c^2 · NUCLEON)
2.0
3.0
4.0
$M_{\mu\mu}$ (Gev/c^2)

Fig. 36.--$Ed\sigma/dx_F$ per nucleon for π^- induced μ pairs with $p_T < 1.0$ GeV/c. (a) $2.0<M<2.7$ GeV/c^2; (b) J/ψ; (c) $3.5<M<4.0$ GeV/c^2.

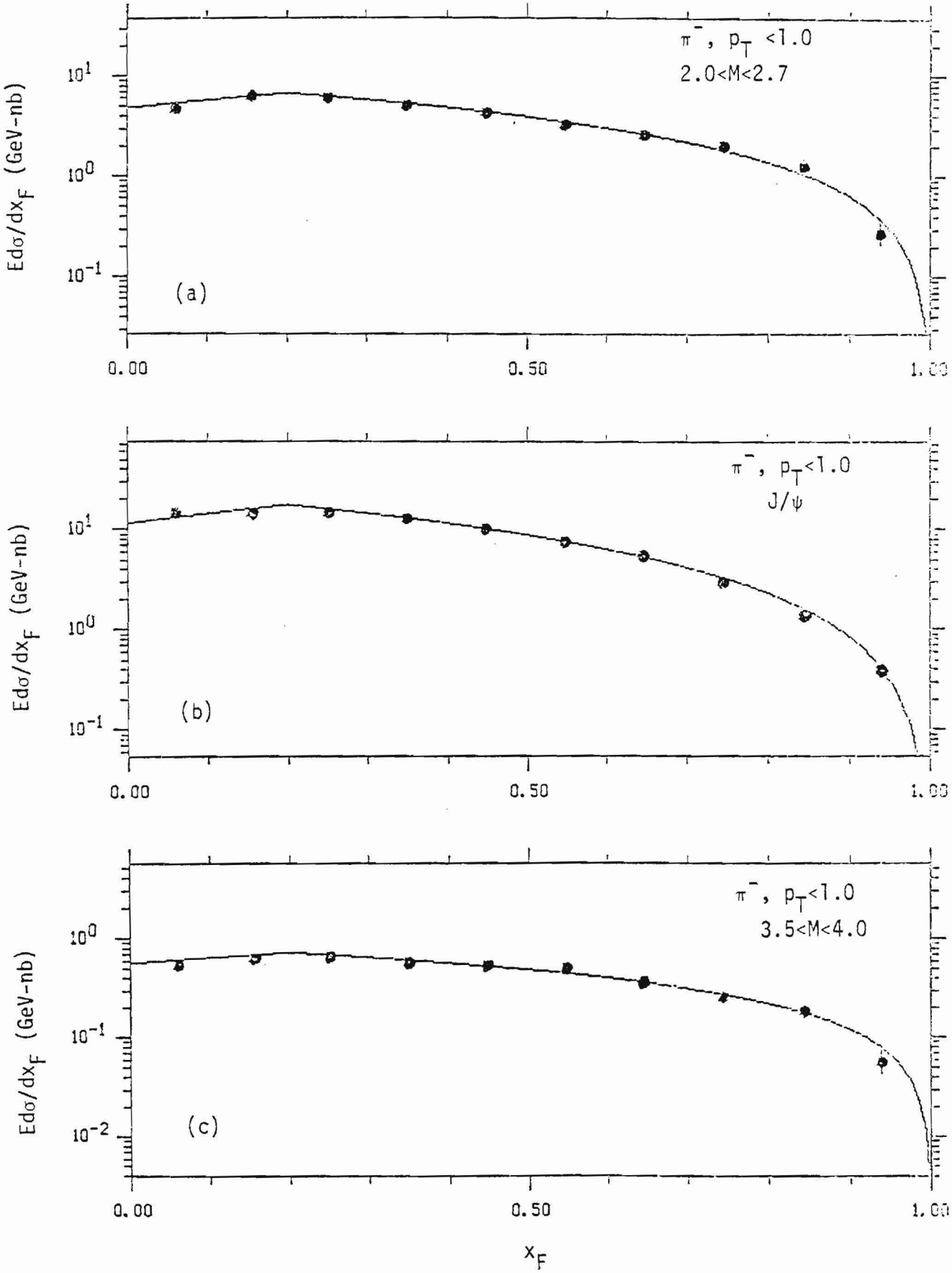
π⁻, p_T <1.0
2.0<M<2.7
(a)
π⁻, p_T<1.0
J/ψ
(b)
π⁻, p_T<1.0
3.5<M<4.0
(c)
Edσ/dx_F (GeV-nb)
10¹
10⁰
10⁻¹
10⁻²
0.00
0.50
1.00
x_F

Fig. 37.--$Ed\sigma/dx_F$ per nucleon for π^- induced μ pairs. (a) $4.0 < M < 6.0$ GeV/c^2, $p_T < 1.0$ GeV/c; (b) $6.0 < M < 8.0$ GeV/c^2, $p_T < 1.0$ GeV/c; (c) $M > 8.0$ GeV/c^2, all p_T.

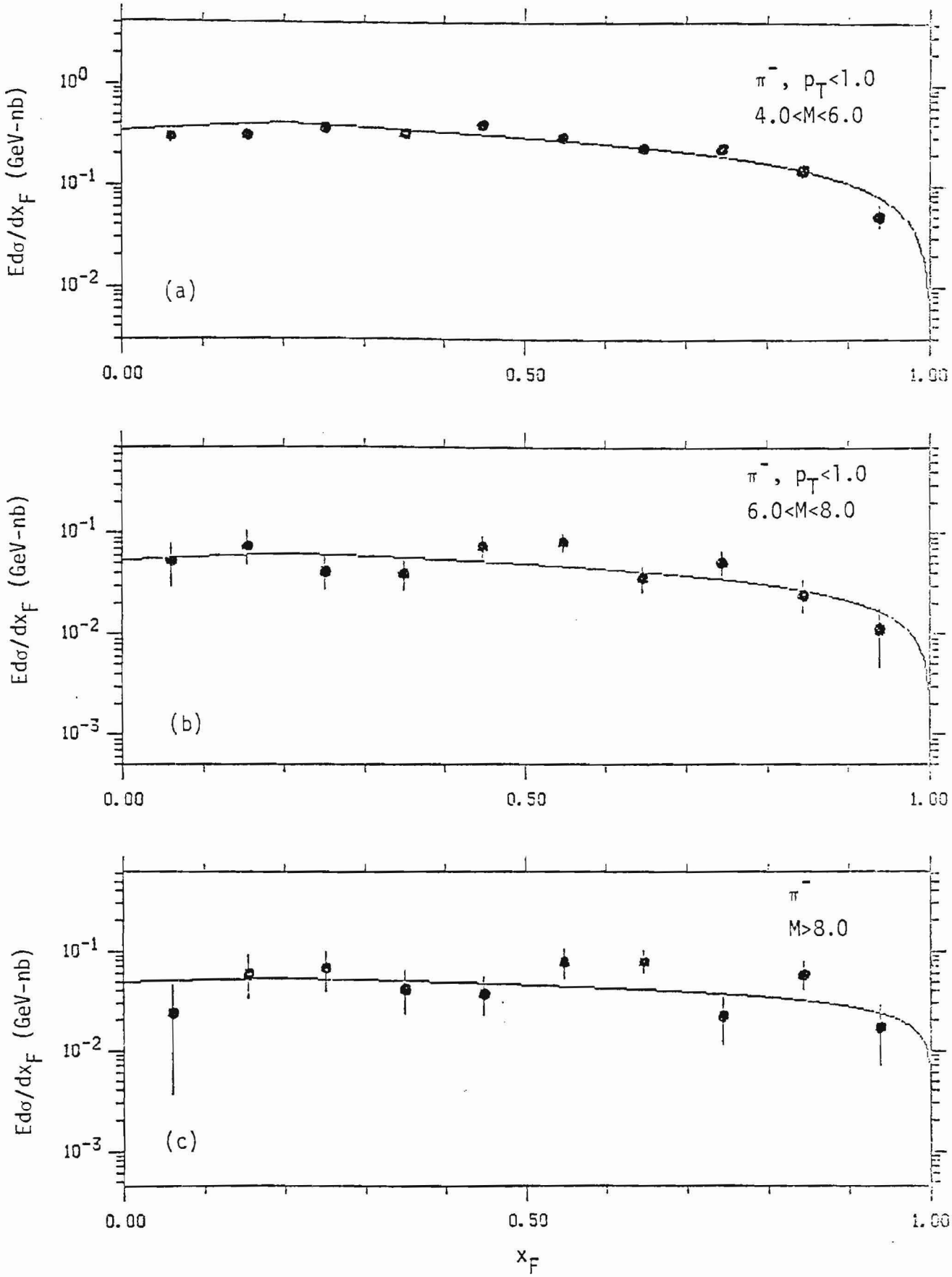
π^-, p_T<1.0
4.0<M<6.0
(a)
π^-, p_T<1.0
6.0<M<8.0
(b)
π^-
M>8.0
(c)
$Ed\sigma/dx_F$ (GeV-nb)
10^0
10^{-1}
10^{-2}
10^{-3}
0.00
0.50
1.00
x_F

Fig. 38.--$Ed\sigma/dx_F$ per nucleon for π^- induced μ pairs with $p_T > 1$ GeV/c. (a) $2.0 < M < 2.7$ GeV/c^2; (b) J/ψ; (c) $3.5 < M < 4.0$ GeV/c^2.

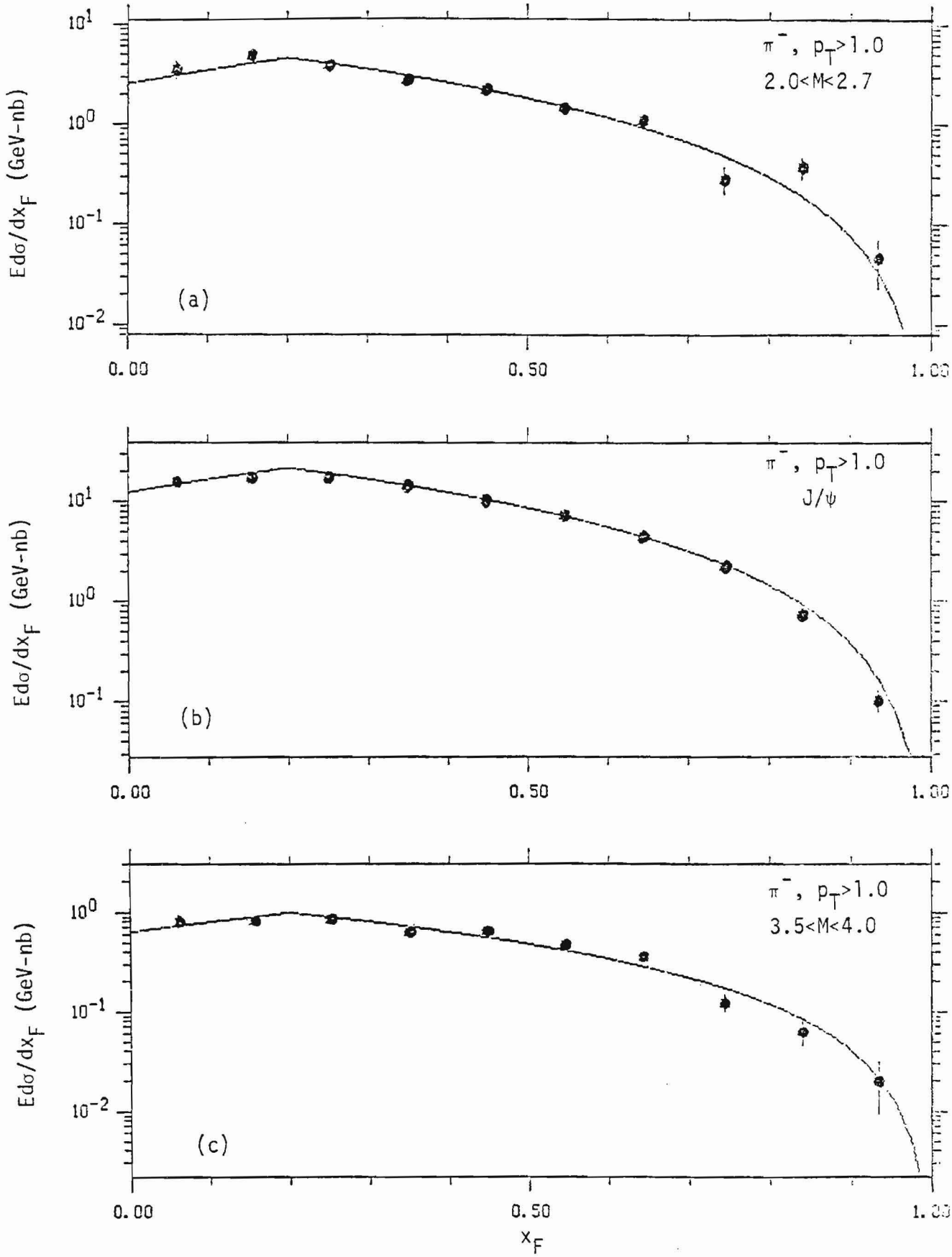
π^-, p_T>1.0
2.0<M<2.7
(a)
π^-, p_T>1.0
J/ψ
(b)
π^-, p_T>1.0
3.5<M<4.0
(c)
Edσ/dx$_F$ (GeV-nb)
10^1
10^0
10^{-1}
10^{-2}
0.00
0.50
1.00
x$_F$

Fig. 39.--$Ed\sigma/dx_F$ per nucleon for π^- induced μ pairs with $p_T > 1$ GeV/c. (a) $4.0 < M < 6.0$ GeV/c^2; (b) $6.0 < M < 8.0$ GeV/c^2.

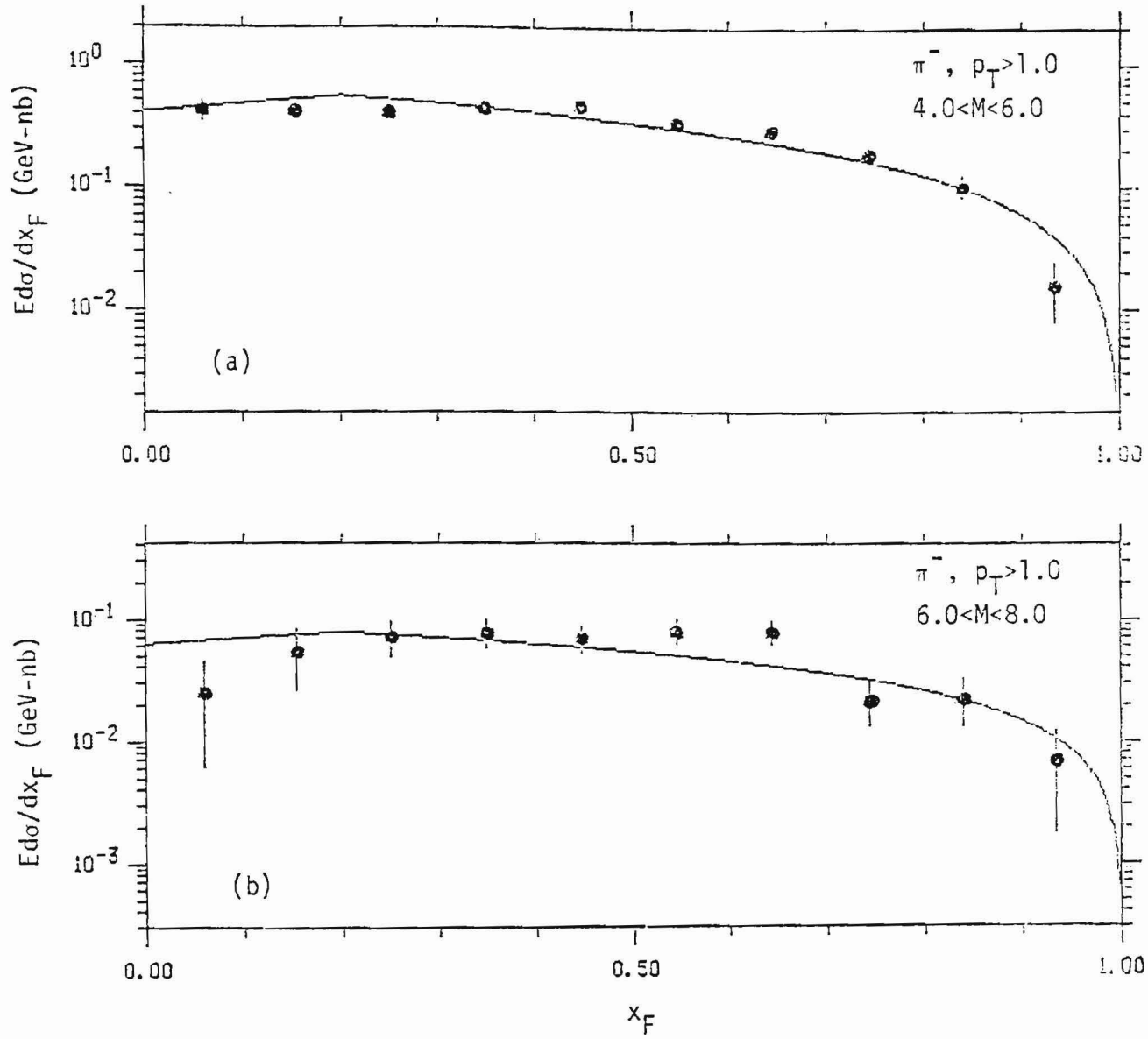
π^-, p_T>1.0
4.0<M<6.0
(a)
$E d\sigma/dx_F$ (GeV-nb)
10^0
10^{-1}
10^{-2}
0.00
0.50
1.00
π^-, p_T>1.0
6.0<M<8.0
(b)
$E d\sigma/dx_F$ (GeV-nb)
10^{-1}
10^{-2}
10^{-3}
0.00
0.50
1.00
x_F

Fig. 40.--$Ed\sigma/dx_F$ per nucleon for π^+ induced μ pairs. (a) $2.0 < M < 2.7$ GeV/c^2; (b) J/ψ.

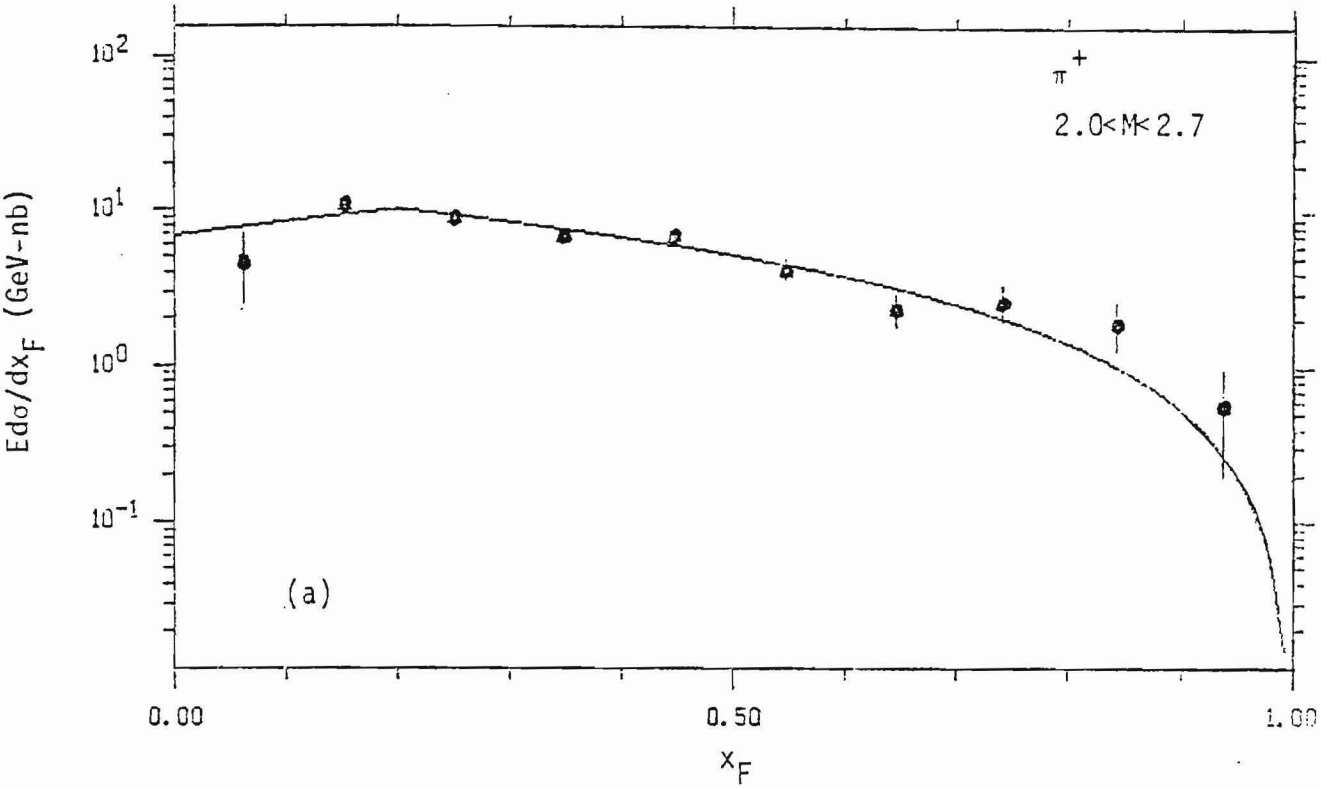
10^2
10^1
10^0
10^{-1}
$E d\sigma/dx_F$ (GeV-nb)
π^+
2.0<M<2.7
(a)
0.00
0.50
1.00
x_F

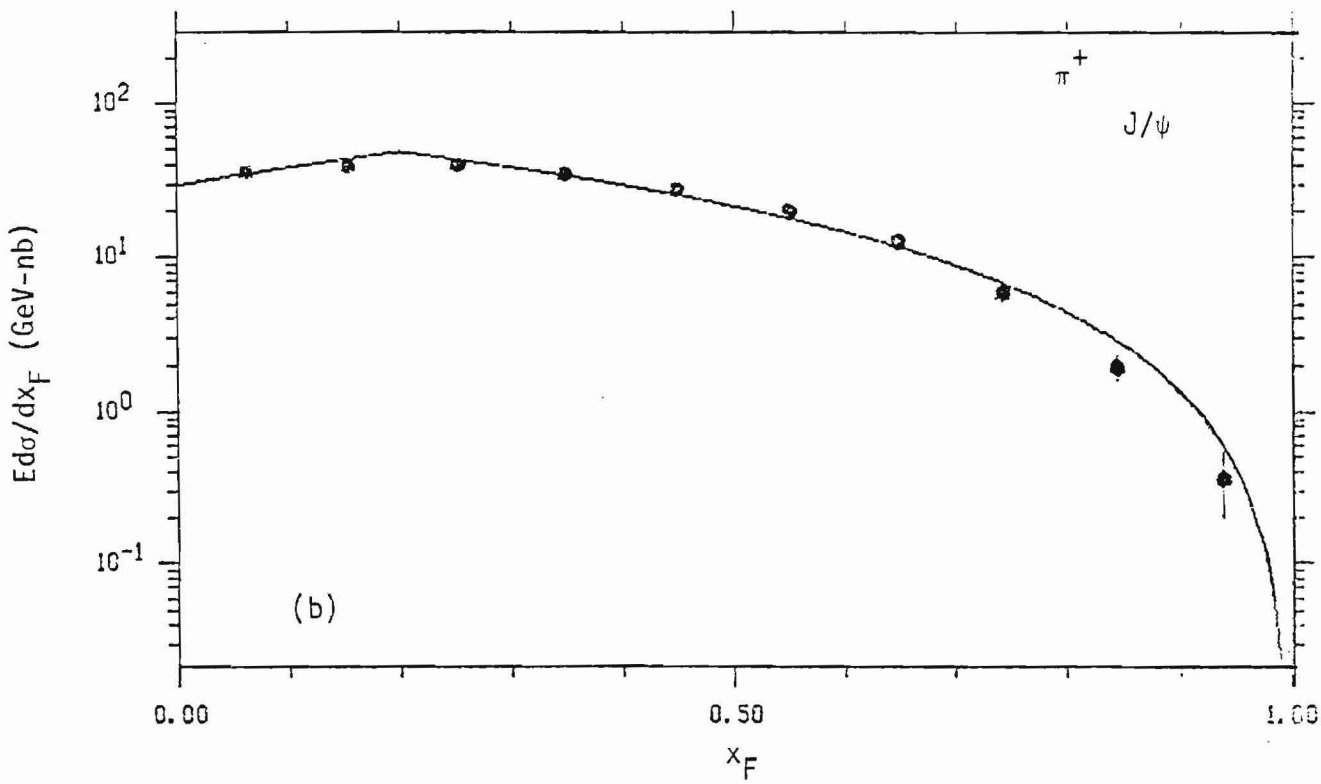
10^2
10^1
10^0
10^{-1}
$E d\sigma/dx_F$ (GeV-nb)
π^+
J/ψ
(b)
0.00
0.50
1.00
x_F

Fig. 41.--$Ed\sigma/dx_F$ per nucleon for π^+ induced μ pairs. (a) $3.5 < M < 4.0$ GeV/c^2; (b) $M > 4.0$ GeV/c^2.

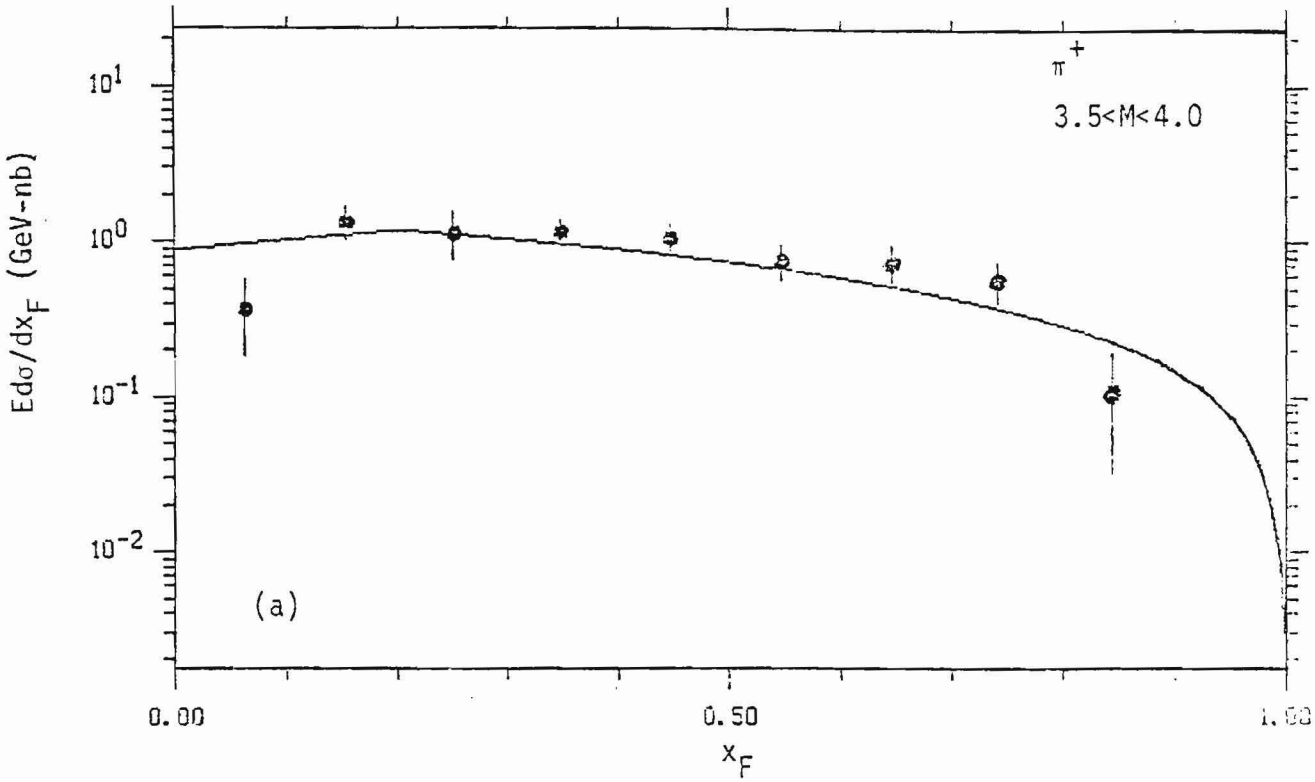
π^+
3.5<M<4.0
(a)
$Ed\sigma/dx_F$ (GeV-nb)
10^1
10^0
10^{-1}
10^{-2}
0.00
0.50
1.00
x_F

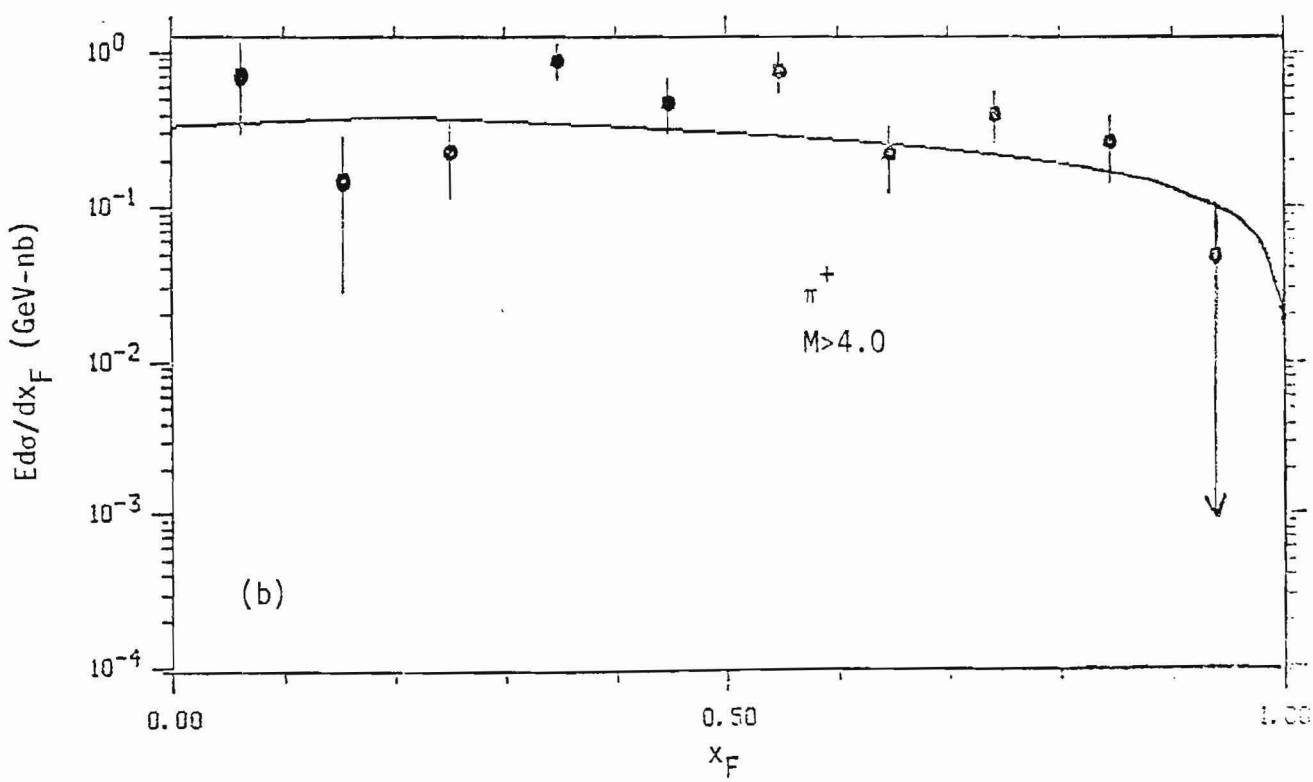
π^+
M>4.0
(b)
$Ed\sigma/dx_F$ (GeV-nb)
10^0
10^{-1}
10^{-2}
10^{-3}
10^{-4}
0.00
0.50
1.00
x_F

Fig. 42.--$Ed\sigma/dx_F$ per nucleon for proton induced μ pairs. (a) $2.0 < M < 2.7$ GeV/c^2; (b) J/ψ.

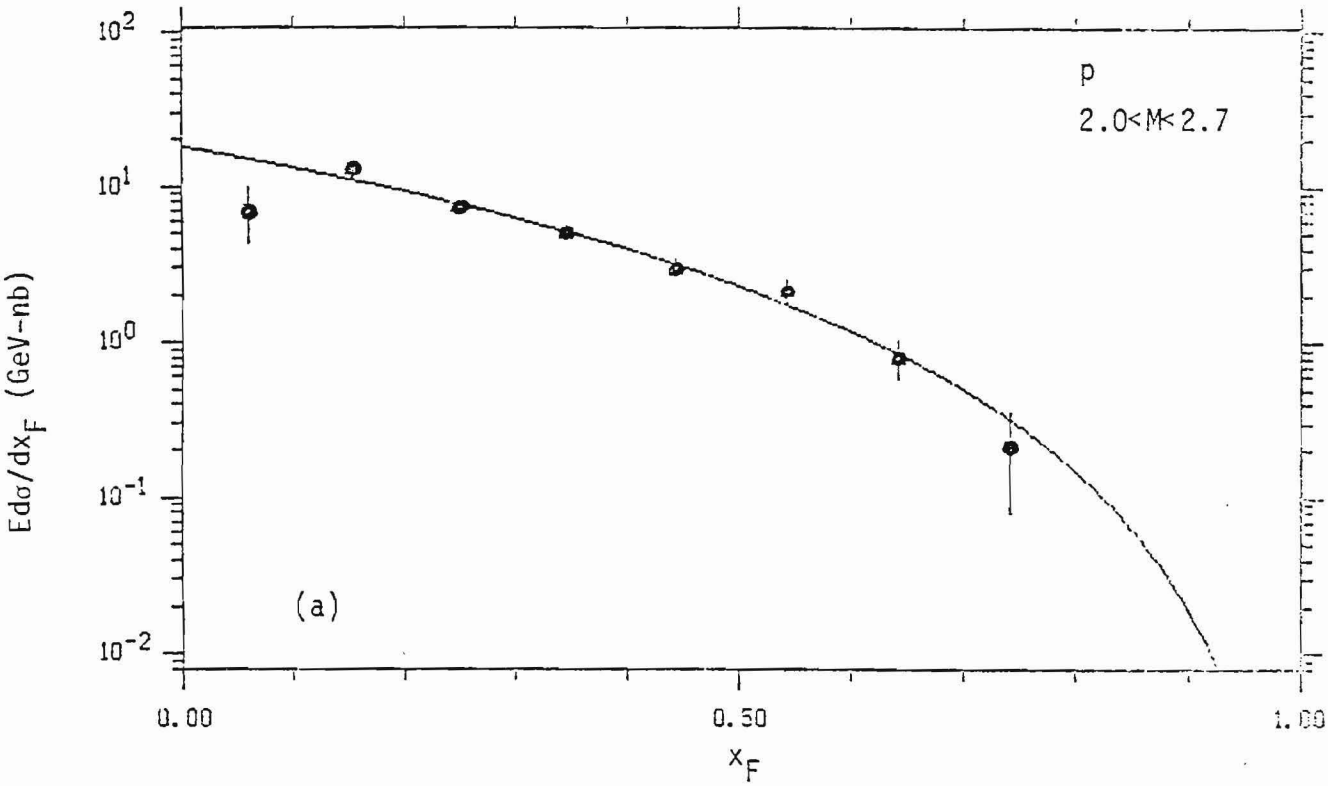
p
2.0<M<2.7
(a)
$Ed\sigma/dx_F$ (GeV-nb)
x_F
0.00
0.50
1.00
10^2
10^1
10^0
10^{-1}
10^{-2}

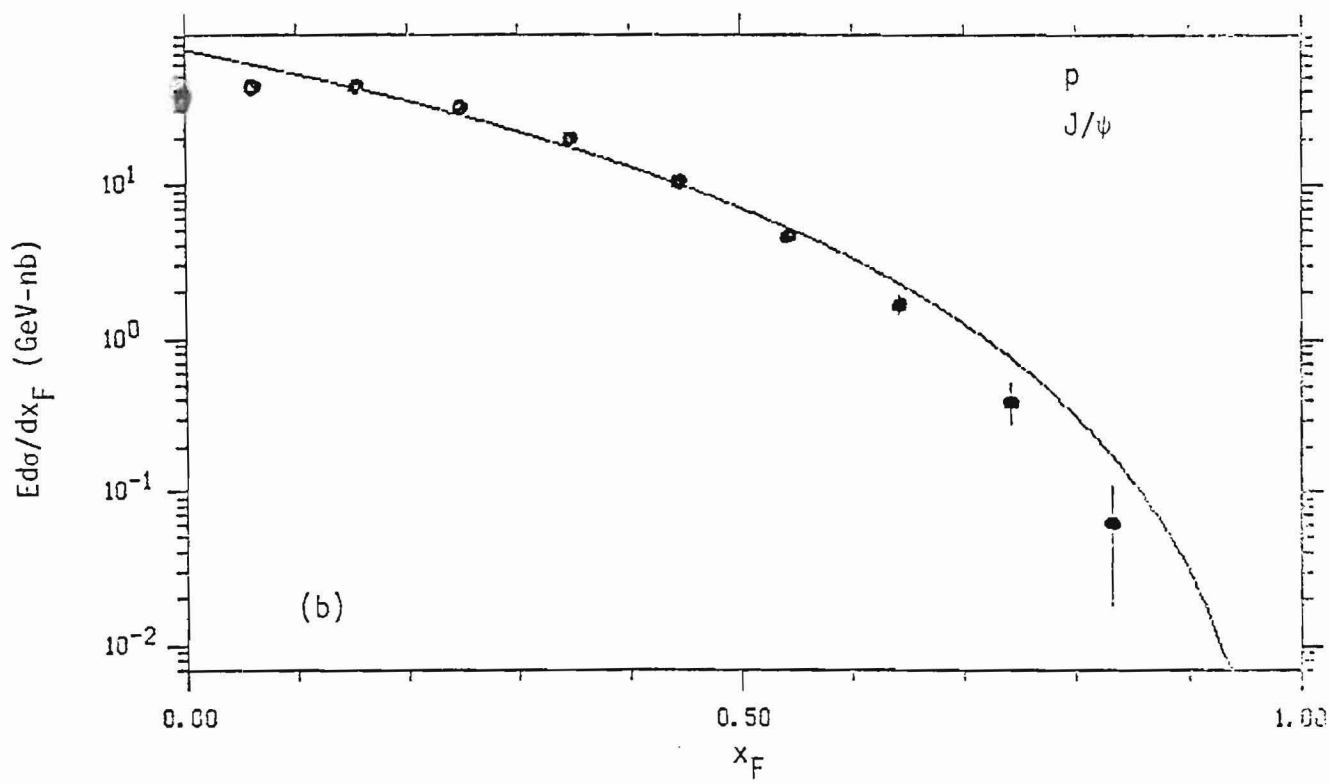
p
J/ψ
(b)
$Ed\sigma/dx_F$ (GeV-nb)
x_F
0.00
0.50
1.00
10^1
10^0
10^{-1}
10^{-2}

Fig. 43.--$Ed\sigma/dx_F$ per nucleon for proton induced μ pairs. (a) $3.5 < M < 4.0$ GeV/c^2; (b) $M > 4.0$ GeV/c^2.

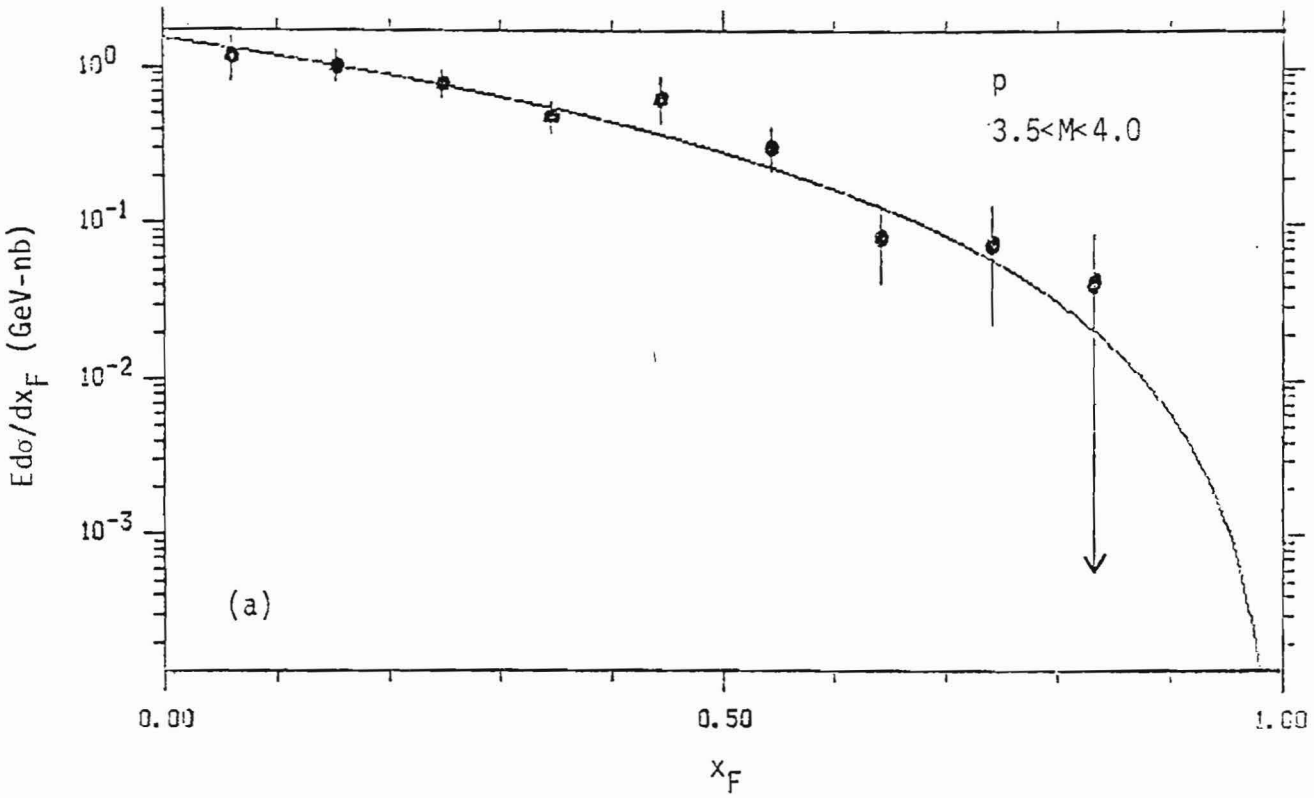
p
3.5<M<4.0
(a)
10^0
10^{-1}
10^{-2}
10^{-3}
$E d\sigma/dx_F$ (GeV-nb)
0.00
0.50
1.00
x_F

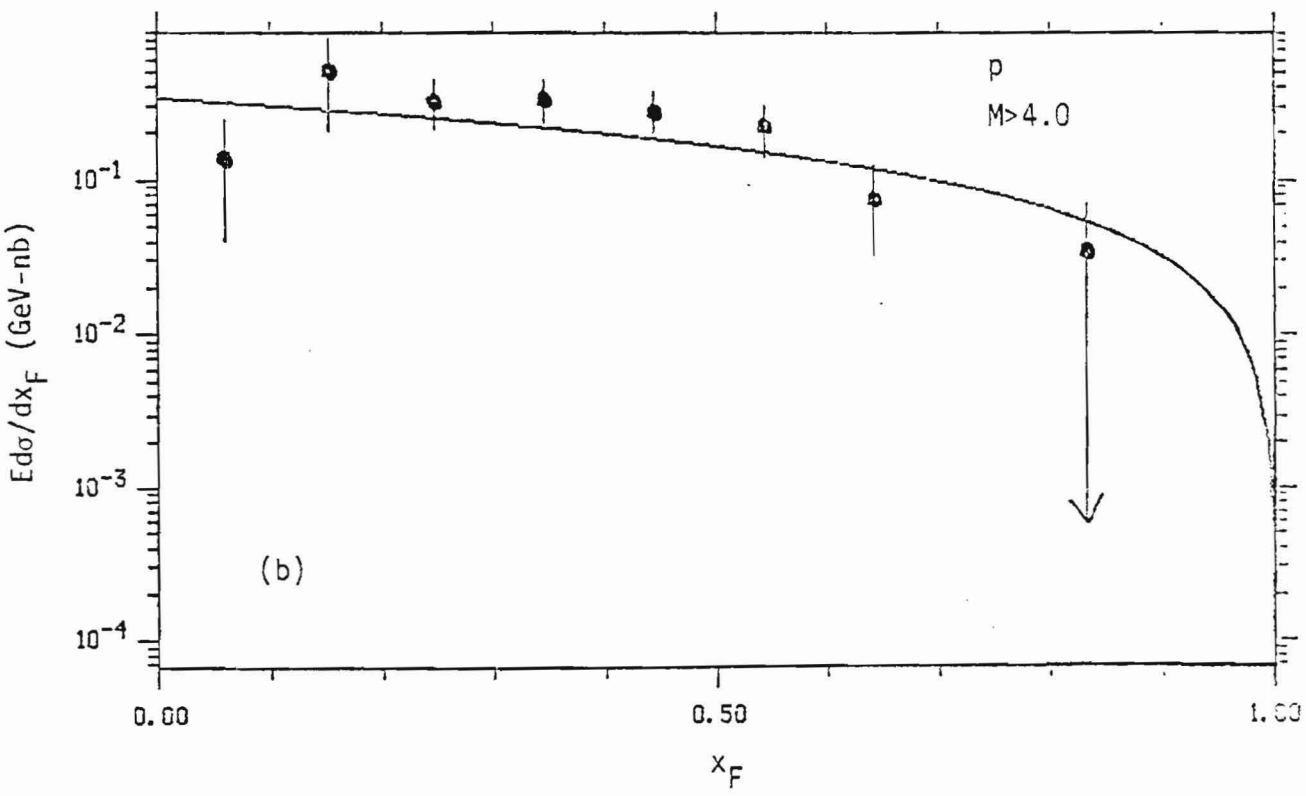
p
M>4.0
(b)
10^{-1}
10^{-2}
10^{-3}
10^{-4}
$E d\sigma/dx_F$ (GeV-nb)
0.00
0.50
1.00
x_F

Fig.44.--$Ed\sigma/dx_F$ per nucleon for K^+ (a) and $\bar{p}$ (b) induced J/ψ events. For K^+, the extrapolation to cross section per nucleon used the measured A dependence for pion induced μ pairs. For $\bar{p}$, the extrapolation to cross section per nucleon used the measured A dependence for proton induced μ pairs.

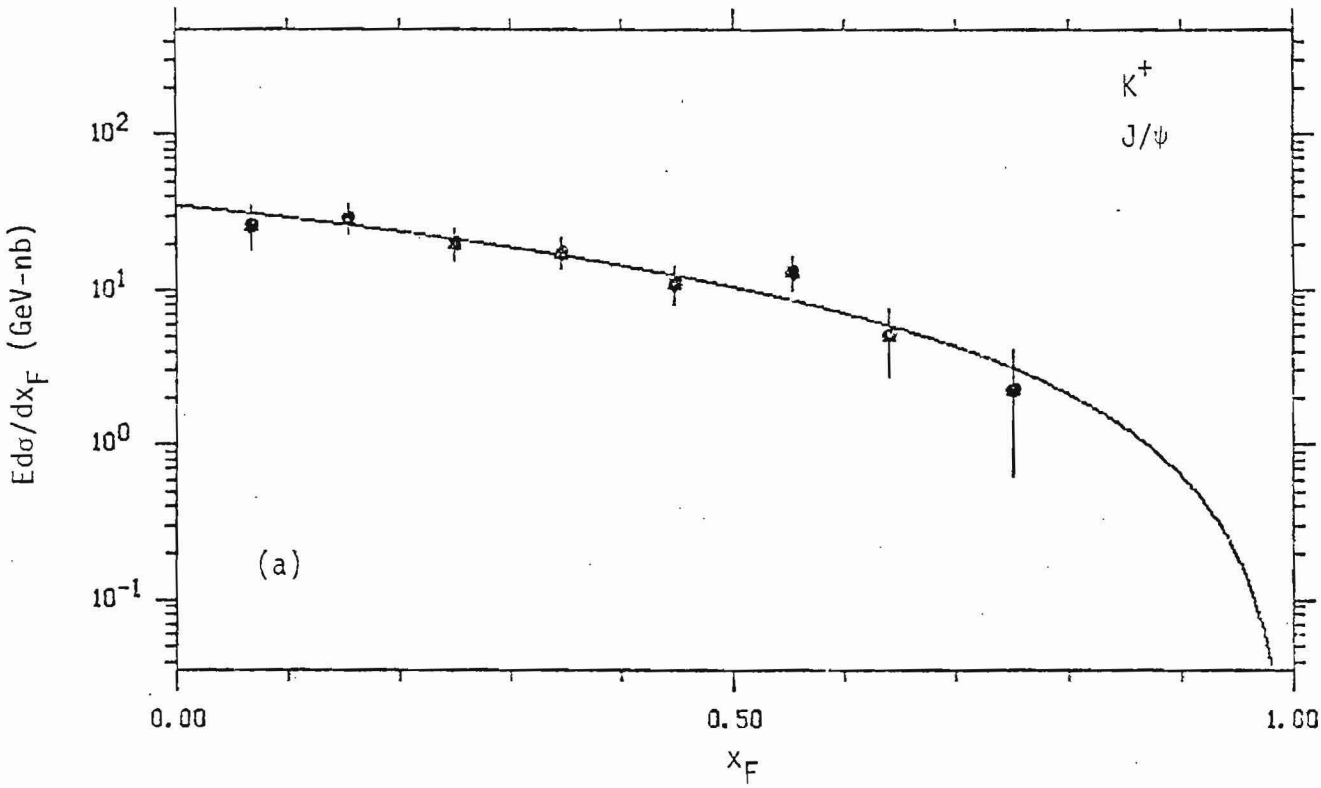
K^+
J/ψ
(a)
10^2
10^1
10^0
10^{-1}
$Ed\sigma/dx_F$ (GeV-nb)
0.00
0.50
1.00
x_F

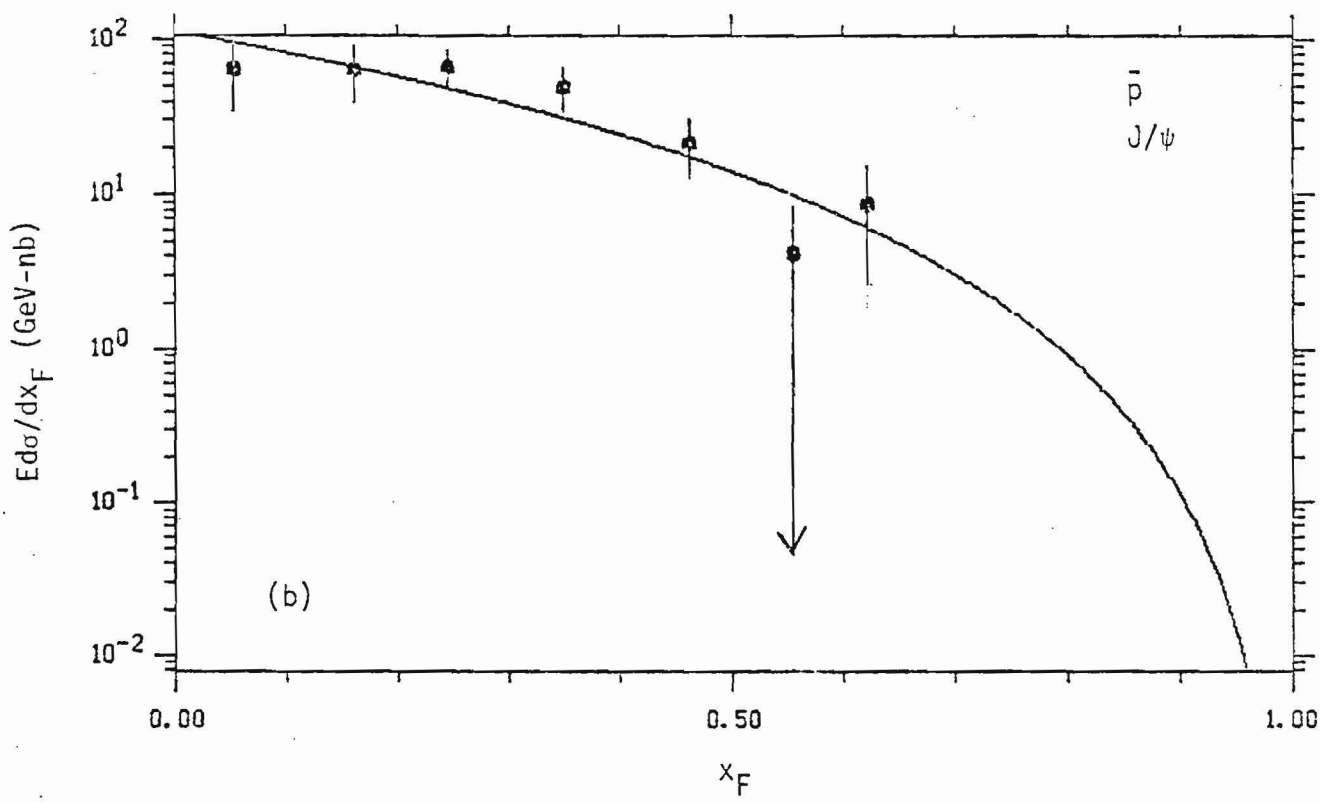
$\bar{p}$
J/ψ
(b)
10^2
10^1
10^0
10^{-1}
10^{-2}
$Ed\sigma/dx_F$ (GeV-nb)
0.00
0.50
1.00
x_F

Fig. 45.--$1/p_T\ d\sigma/dp_T$ (per nucleon) for π^- induced μ pairs with $x_F < 0.3$. (a) $2.0 < M < 2.7$ GeV/c^2; (b) J/ψ; (c) $3.5 < M < 4.0$ GeV/c^2.

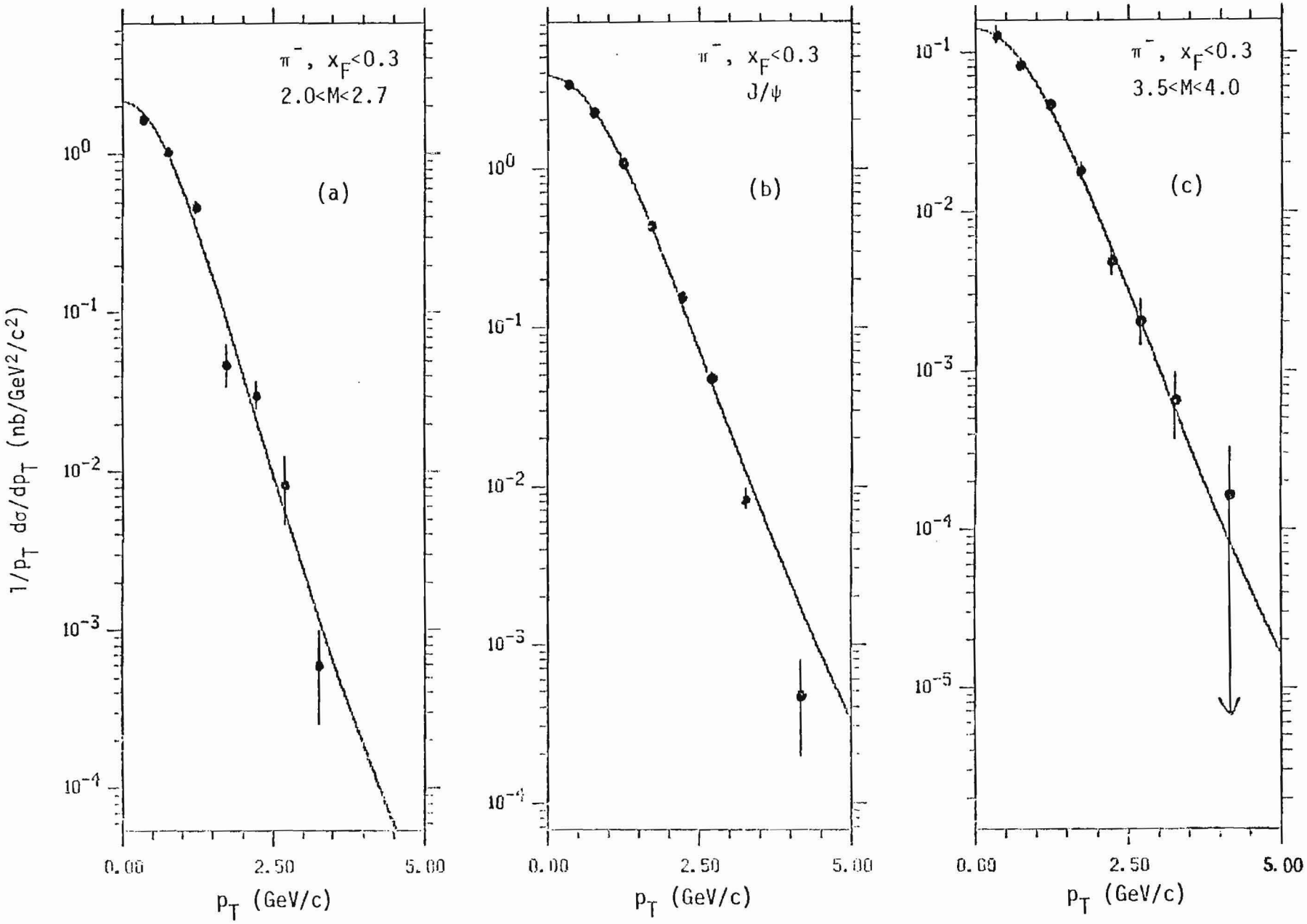
π⁻, x_F<0.3
2.0<M<2.7
(a)
π⁻, x_F<0.3
J/ψ
(b)
π⁻, x_F<0.3
3.5<M<4.0
(c)
1/p_T dσ/dp_T (nb/GeV²/c²)
p_T (GeV/c)
0.00
2.50
5.00

Fig. 46.--$1/p_T \, d\sigma/dp_T$ (per nucleon) for π^- induced μ pairs. (a) $4.0 < M < 6.0$ GeV/c^2, $x_F < 0.3$; (b) $6.0 < M < 8.0$ GeV/c^2, $x_F < 0.3$; (c) $M > 8.0$ GeV/c^2, all x_F.

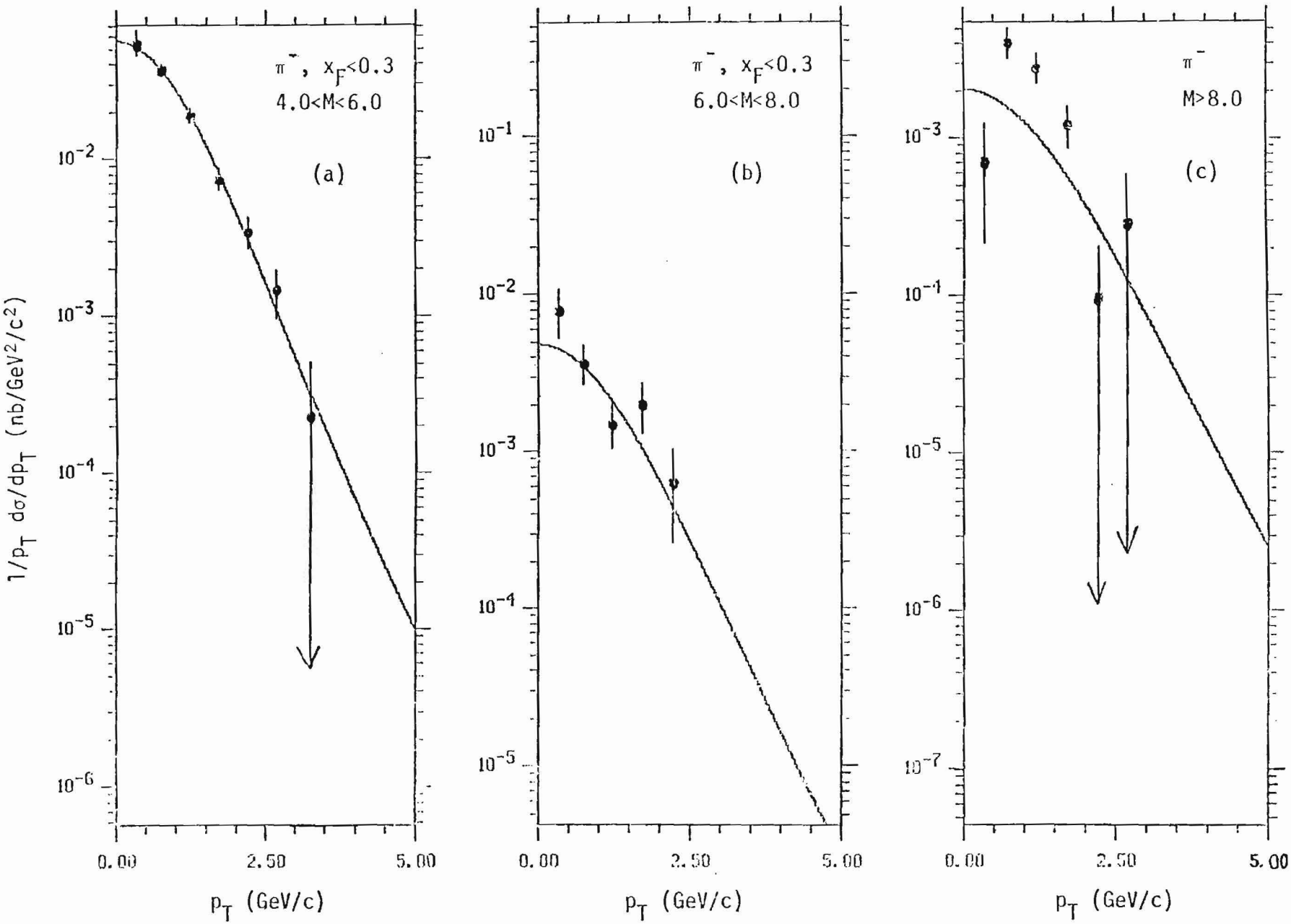
π^-, $x_F<0.3$
$4.0<M<6.0$
(a)
π^-, $x_F<0.3$
$6.0<M<8.0$
(b)
π^-
$M>8.0$
(c)
$1/p_T\ d\sigma/dp_T$ (nb/GeV^2/c^2)
10^{-1}
10^{-2}
10^{-3}
10^{-4}
10^{-5}
10^{-6}
10^{-7}
0.00
2.50
5.00
p_T (GeV/c)

Fig. 47.--$1/p_T \, d\sigma/dp_T$ (per nucleon) for π^- induced μ pairs with $x_F > 0.3$. (a) $2.0 < M < 2.7$ GeV/c^2; (b) J/ψ; (c) $3.5 < M < 4.0$ GeV/c^2.

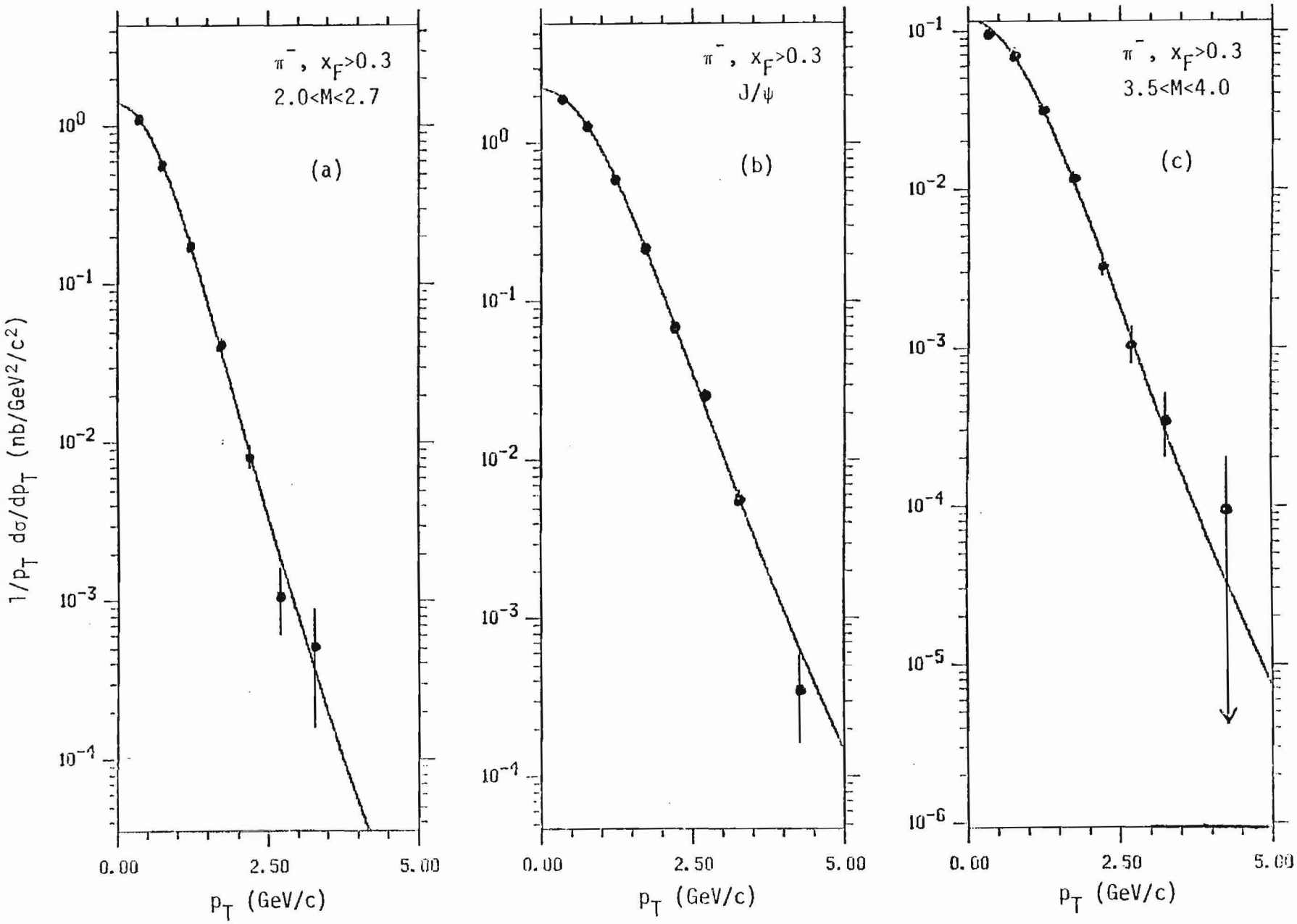
π^-, x_F>0.3
2.0<M<2.7
(a)
π^-, x_F>0.3
J/ψ
(b)
π^-, x_F>0.3
3.5<M<4.0
(c)
$1/p_T\ d\sigma/dp_T$ (nb/GeV²/c²)
p_T (GeV/c)
0.00
2.50
5.00
10^0
10^{-1}
10^{-2}
10^{-3}
10^{-4}
10^{-5}
10^{-6}

Fig. 48.--$1/p_T\ d\sigma/dp_T$ (per nucleon) for π^- induced μ pairs with $x_F > 0.3$. (a) $4.0 < M < 6.0$ GeV/c^2; (b) $6.0 < M < 8.0$ GeV/c^2.

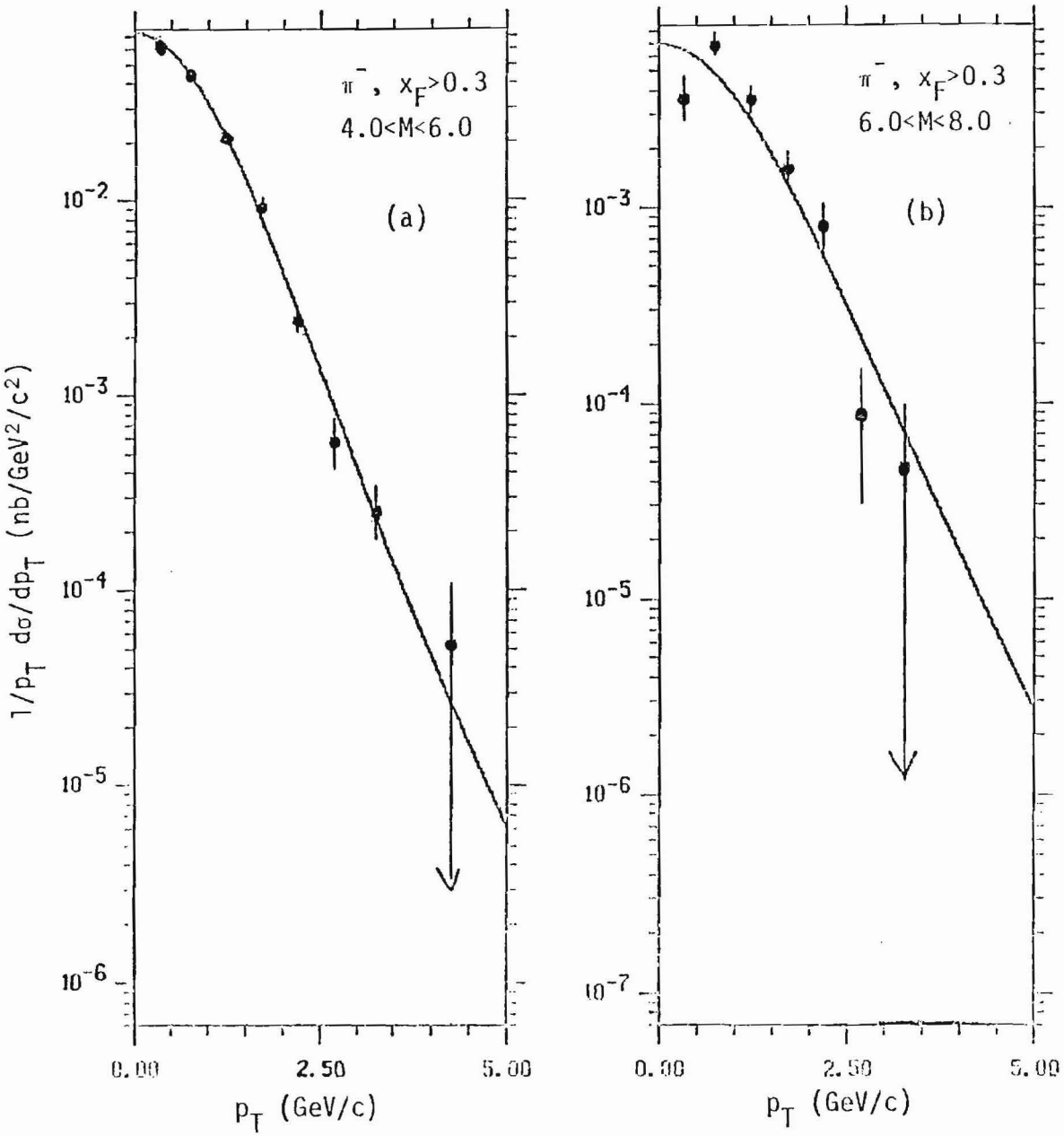
π^-, x_F>0.3
4.0<M<6.0
(a)
π^-, x_F>0.3
6.0<M<8.0
(b)
$1/p_T\ d\sigma/dp_T$ (nb/GeV^2/c^2)
10^{-2}
10^{-3}
10^{-4}
10^{-5}
10^{-6}
10^{-7}
0.00
2.50
5.00
p_T (GeV/c)

Fig. 49.--$1/p_T \, d\sigma/dp_T$ (per nucleon) for π^+ induced μ pairs. (a) $2.0 < M < 2.7$ GeV/c^2; (b) J/ψ.

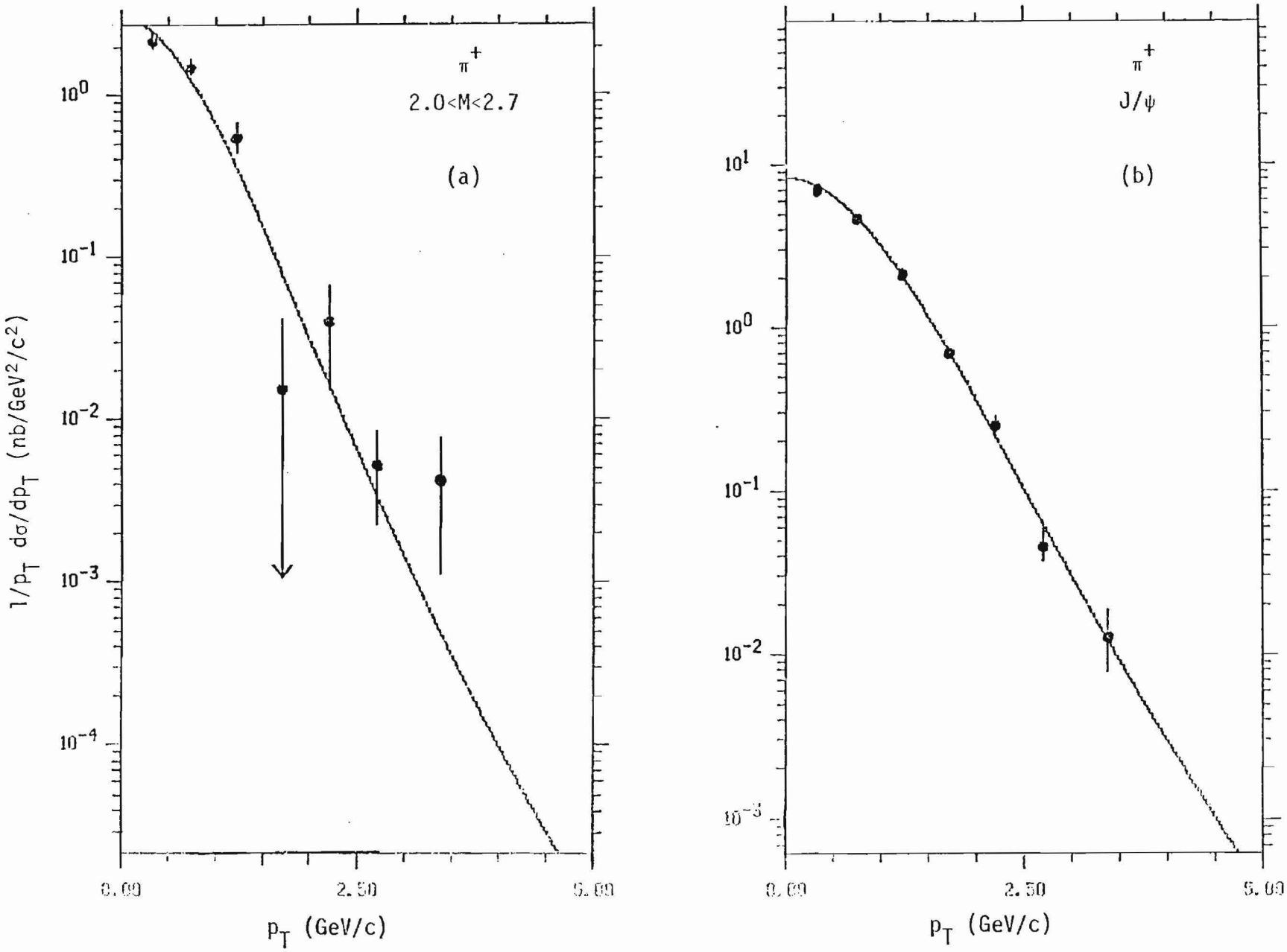
π^+
2.0<M<2.7
(a)
10^0
10^{-1}
10^{-2}
10^{-3}
10^{-4}
$1/p_T\ d\sigma/dp_T$ (nb/GeV^2/c^2)
0.00
2.50
5.00
p_T (GeV/c)
π^+
J/ψ
(b)
10^1
10^0
10^{-1}
10^{-2}
10^{-3}
0.00
2.50
5.00
p_T (GeV/c)

Fig. 50.--$1/p_T \, d\sigma/dp_T$ (per nucleon) for π^+ induced μ pairs. (a) $3.5 < M < 4.0$ GeV/c^2; (b) $M > 4.0$ GeV/c^2.

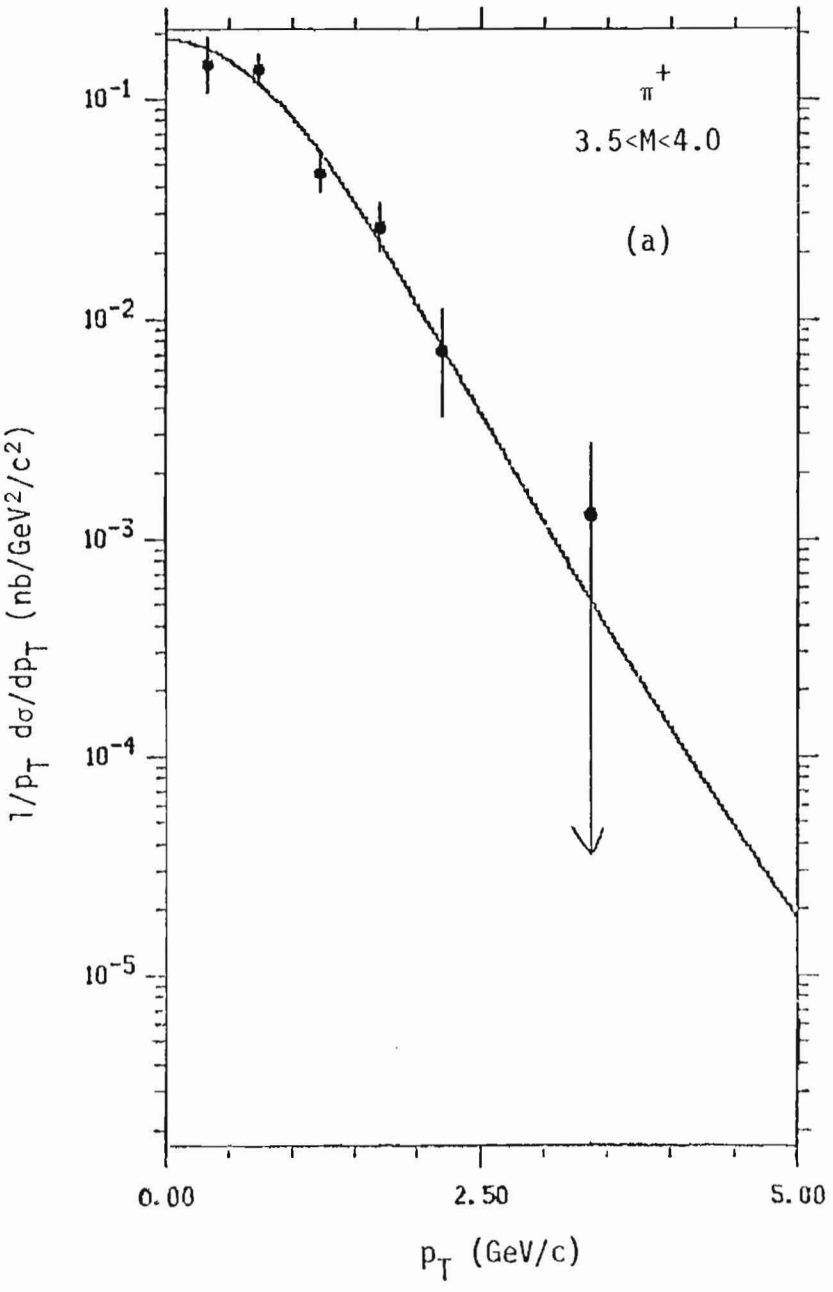
π^+
3.5<M<4.0
(a)
10^{-1}
10^{-2}
10^{-3}
10^{-4}
10^{-5}
$1/p_T\ d\sigma/dp_T$ (nb/GeV^2/c^2)
0.00
2.50
5.00
p_T (GeV/c)

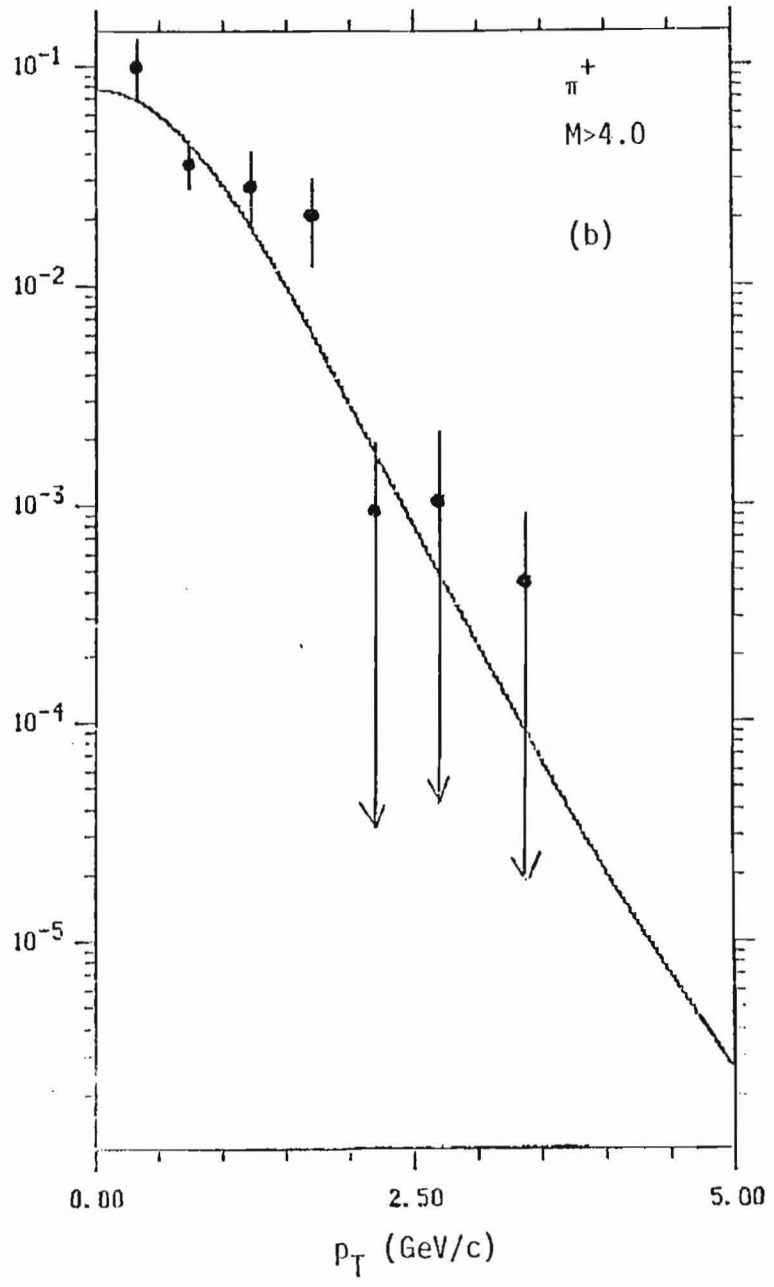
π^+
M>4.0
(b)
10^{-1}
10^{-2}
10^{-3}
10^{-4}
10^{-5}
0.00
2.50
5.00
p_T (GeV/c)

Fig. 51.--$1/p_T\ d\sigma/dp_T$ (per nucleon) for proton induced μ pairs. (a) $2.0 < M < 2.7$ GeV/c^2; (b) J/ψ.

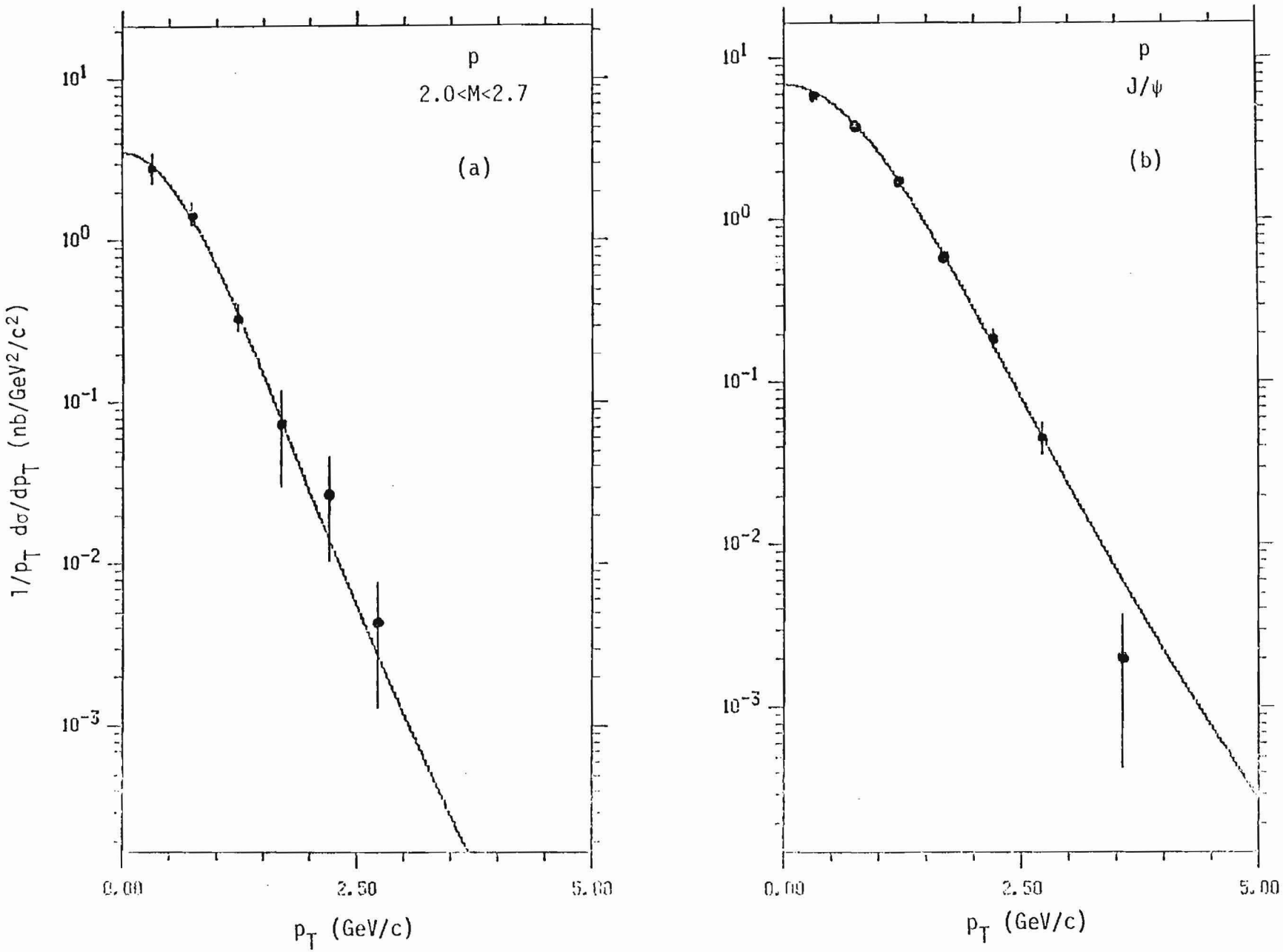
p
2.0<M<2.7
(a)
p
J/ψ
(b)
$1/p_T\ d\sigma/dp_T$ (nb/GeV²/c²)
10^1
10^0
10^{-1}
10^{-2}
10^{-3}
0.00
2.50
5.00
p_T (GeV/c)

Fig. 52.—$1/p_T \, d\sigma/dp_T$ (per nucleon) for proton induced μ pairs. (a) $3.5 < M < 4.0$ GeV/c^2; (b) $M > 4.0$ GeV/c^2.

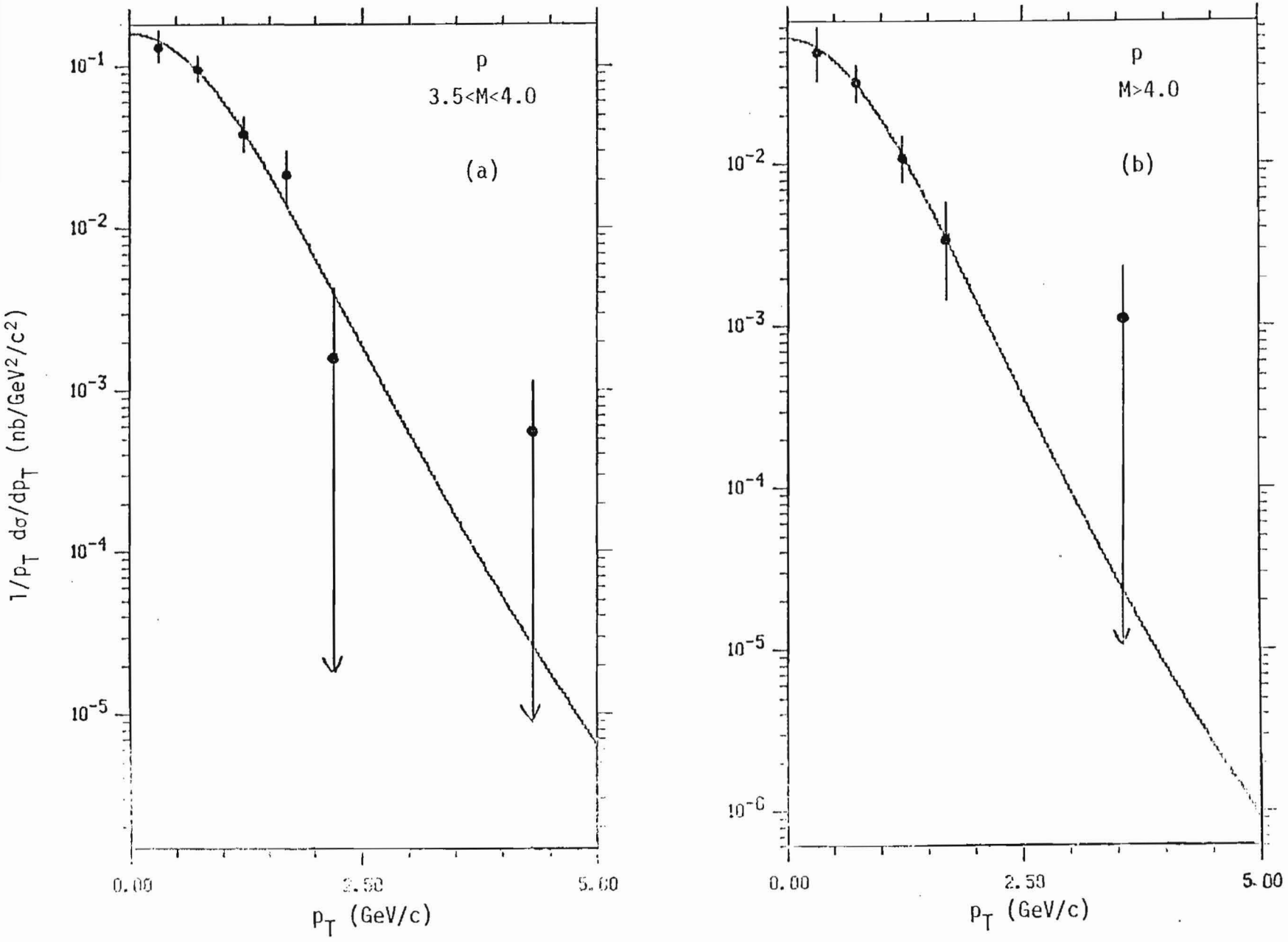
p
3.5<M<4.0
(a)
p
M>4.0
(b)
$1/p_T\ d\sigma/dp_T$ (nb/GeV^2/c^2)
10^{-1}
10^{-2}
10^{-3}
10^{-4}
10^{-5}
10^{-6}
0.00
2.50
5.00
p_T (GeV/c)

Fig.53.--$1/p_T \; d\sigma/dp_T$ (per nucleon) for K^+ (a) and $\bar{p}$ (b) induced J/ψ events.

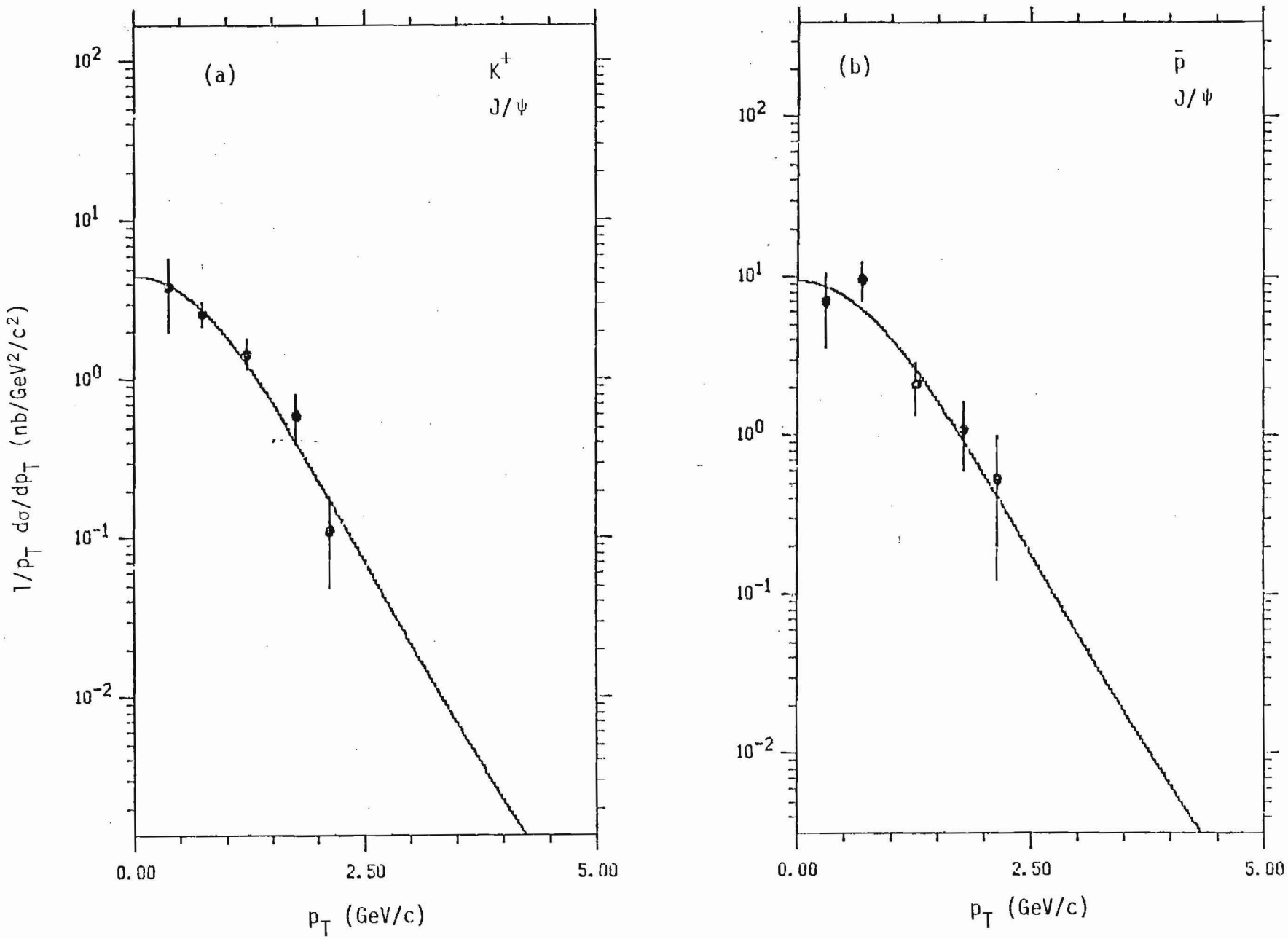
(a)
K^+
J/ψ
(b)
$\bar{p}$
J/ψ
$1/p_T\ d\sigma/dp_T$ (nb/GeV^2/c^2)
10^2
10^1
10^0
10^{-1}
10^{-2}
0.00
2.50
5.00
p_T (GeV/c)

Fig. 54.--Mean transverse momentum vs. mass for pion and proton induced μ pairs.

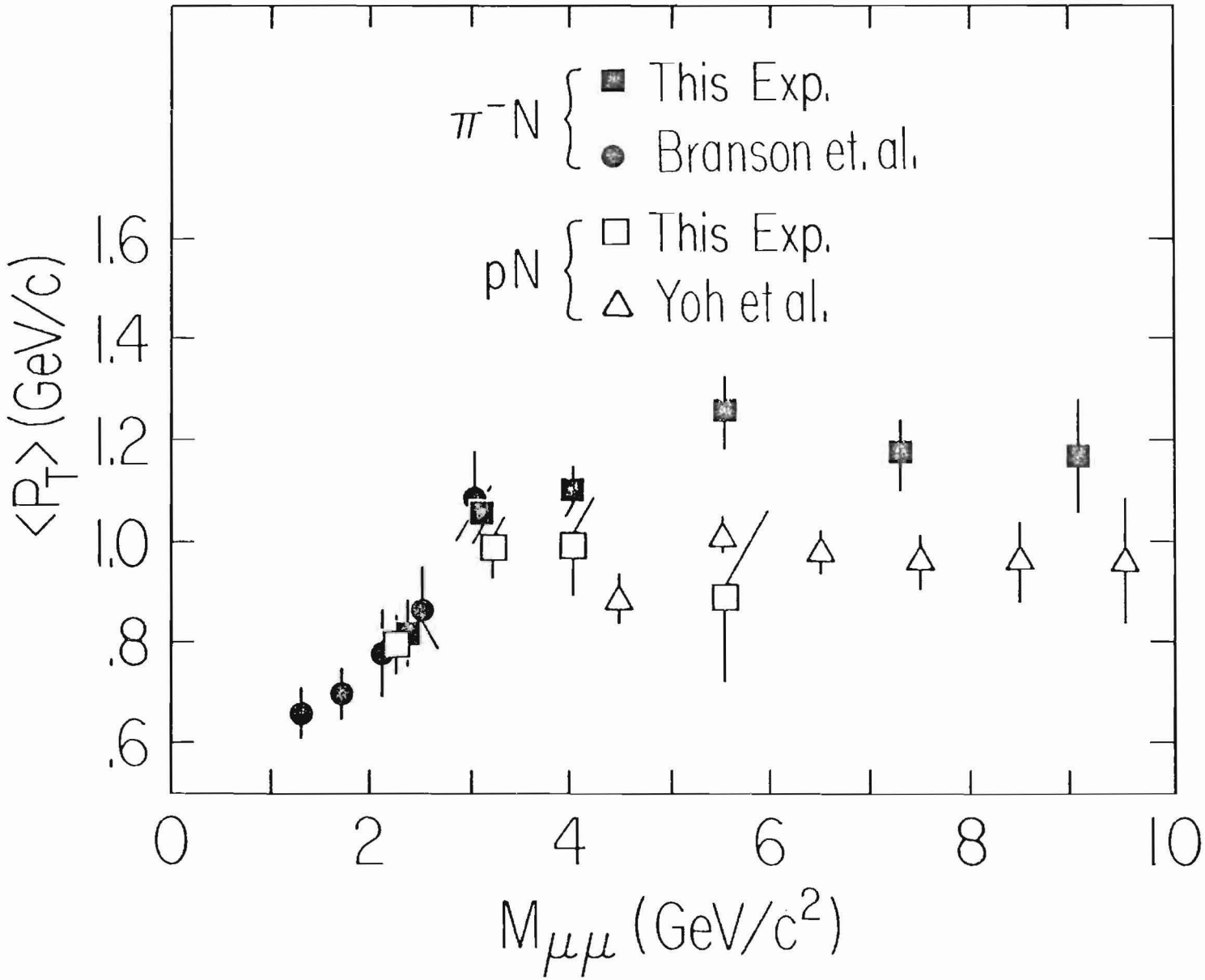
$\pi^- N$
This Exp.
Branson et. al.
pN
This Exp.
Yoh et al.
$\langle P_T \rangle$ (GeV/c)
1.6
1.4
1.2
1.0
.8
.6
0
2
4
6
8
10
$M_{\mu\mu}$ (GeV/c^2)

Fig. 55.--Mean transverse momentum vs. x_F for pion induced μ pairs.

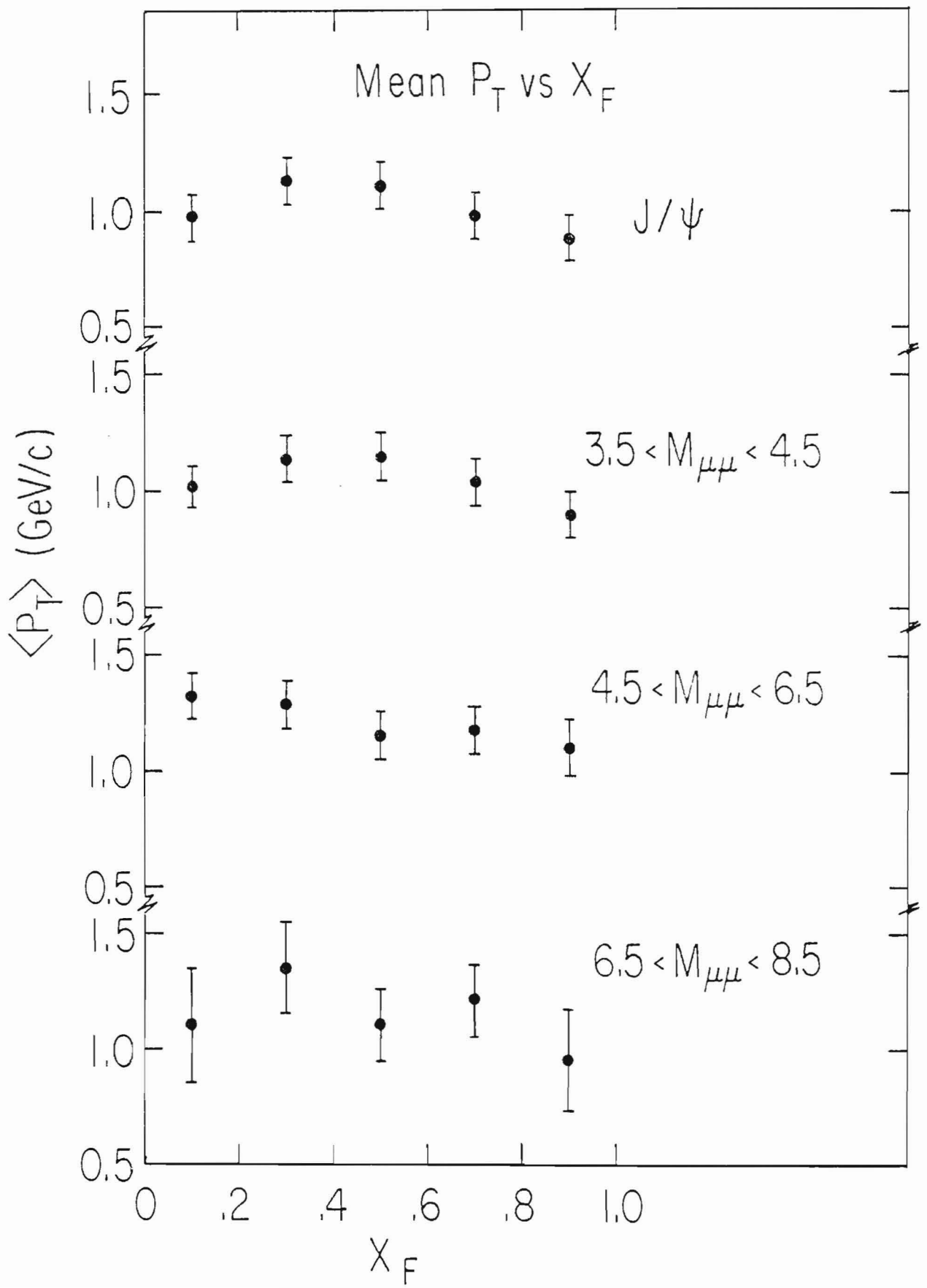
Mean P_T vs X_F
J/ψ
$3.5 < M_{\mu\mu} < 4.5$
$4.5 < M_{\mu\mu} < 6.5$
$6.5 < M_{\mu\mu} < 8.5$
$\langle P_T \rangle$ (GeV/c)
X_F
0.5
1.0
1.5
0
.2
.4
.6
.8
1.0

Fig. 56.--Total μ pair cross section (σ) vs. atomic mass number (A) for five mass intervals.

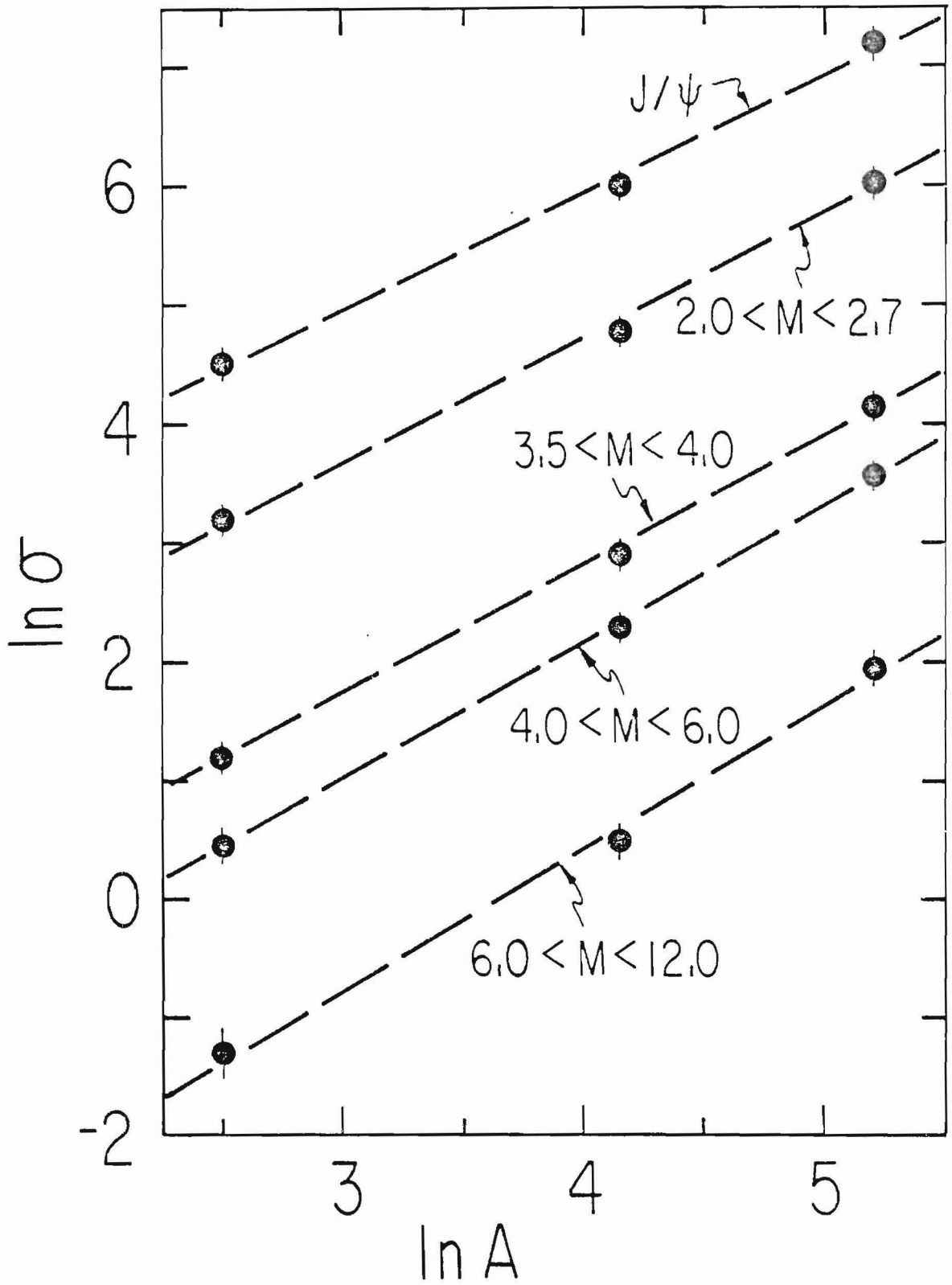
J/ψ
2.0 < M < 2.7
3.5 < M < 4.0
4.0 < M < 6.0
6.0 < M < 12.0
ln σ
ln A
6
4
2
0
-2
3
4
5

Fig. 57.--Atomic mass number dependence power α vs. mass for π^- induced μ pairs.

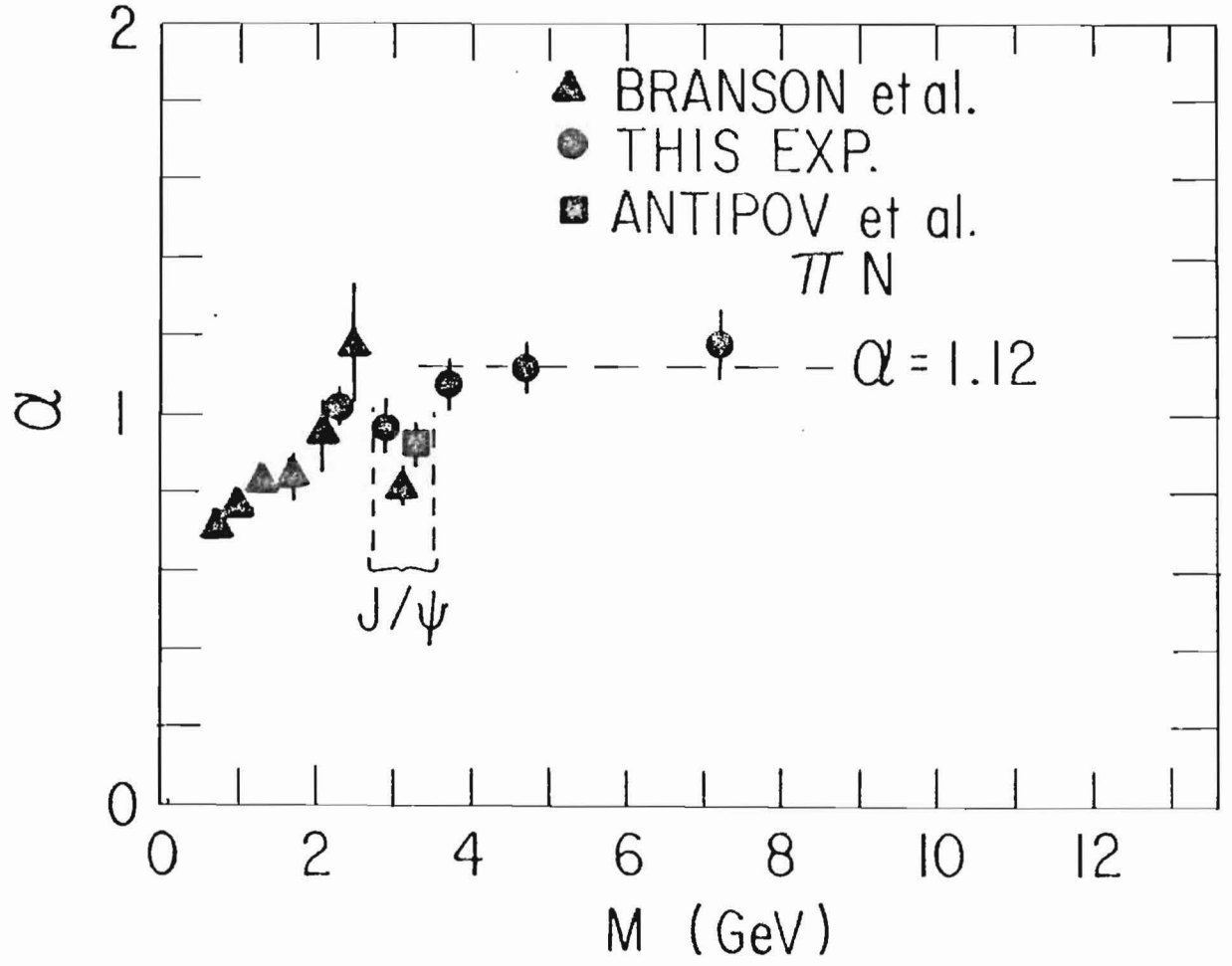
BRANSON et al.
THIS EXP.
ANTIPOV et al.
π N
α = 1.12
J/ψ
α
M (GeV)
0
1
2
0
2
4
6
8
10
12

Fig.58.--Atomic mass number dependence power α vs. mass for proton induced μ pairs.

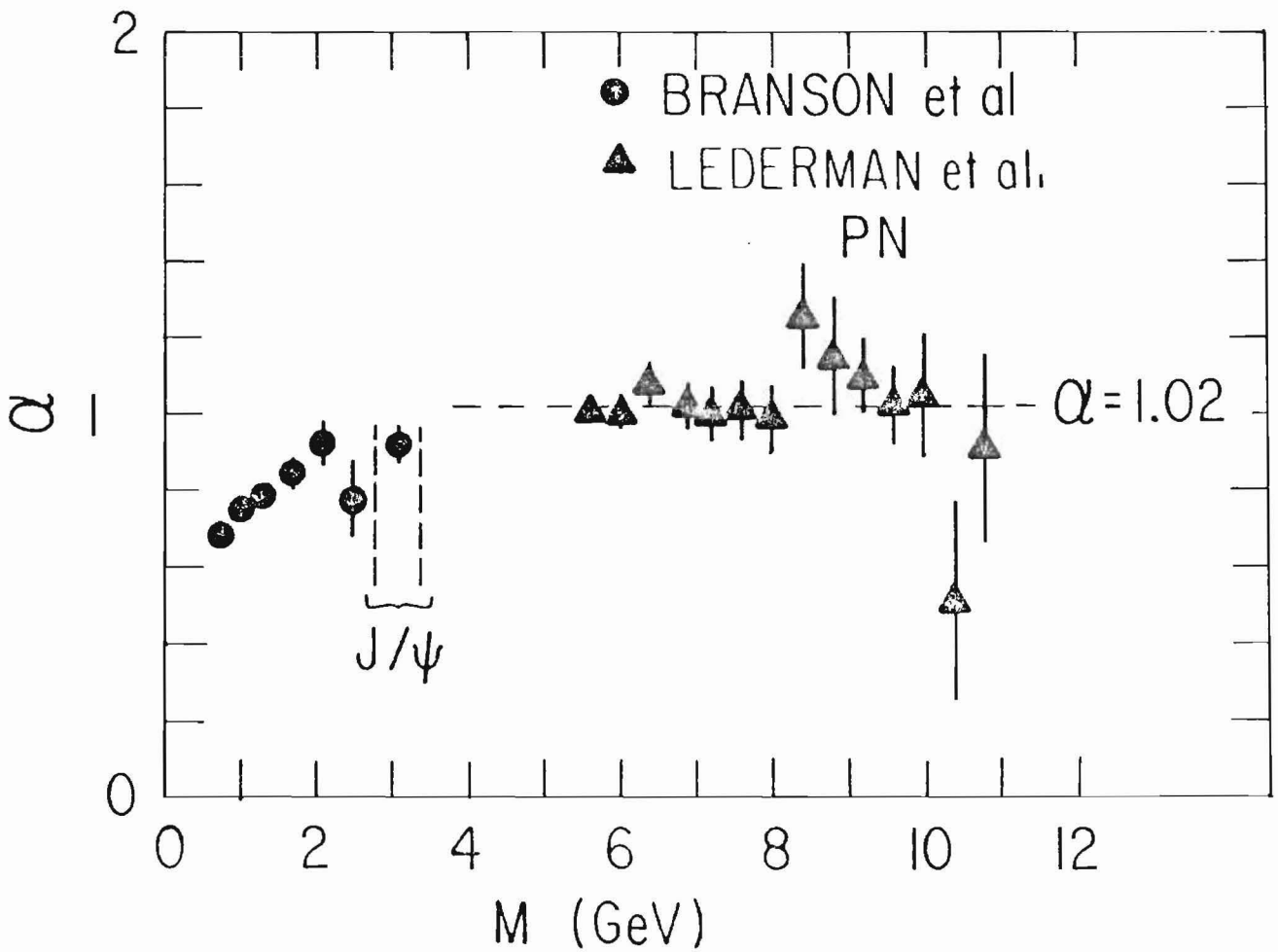
BRANSON et al
LEDERMAN et al.
PN
α
α = 1.02
J/ψ
2
1
0
0
2
4
6
8
10
12
M (GeV)

Fig. 59.--Atomic mass number dependence power α vs. p_T for π^- induced μ pairs.

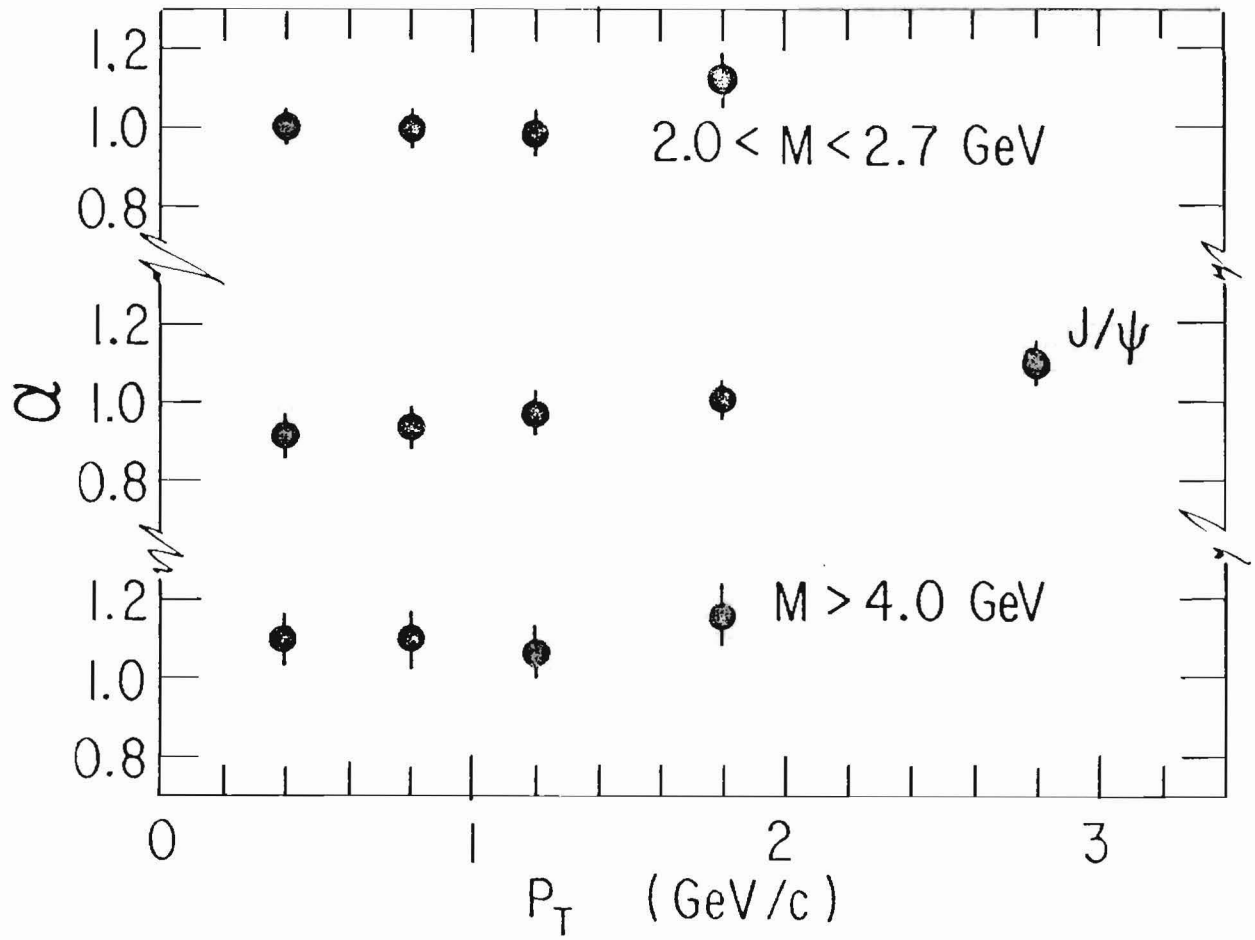
1.2
1.0
0.8
2.0 < M < 2.7 GeV
1.2
1.0
0.8
J/ψ
α
1.2
1.0
0.8
M > 4.0 GeV
0
1
2
3
P_T (GeV/c)

Fig. 60.--Atomic mass number dependence power α vs. x_F for π^- induced μ pairs.

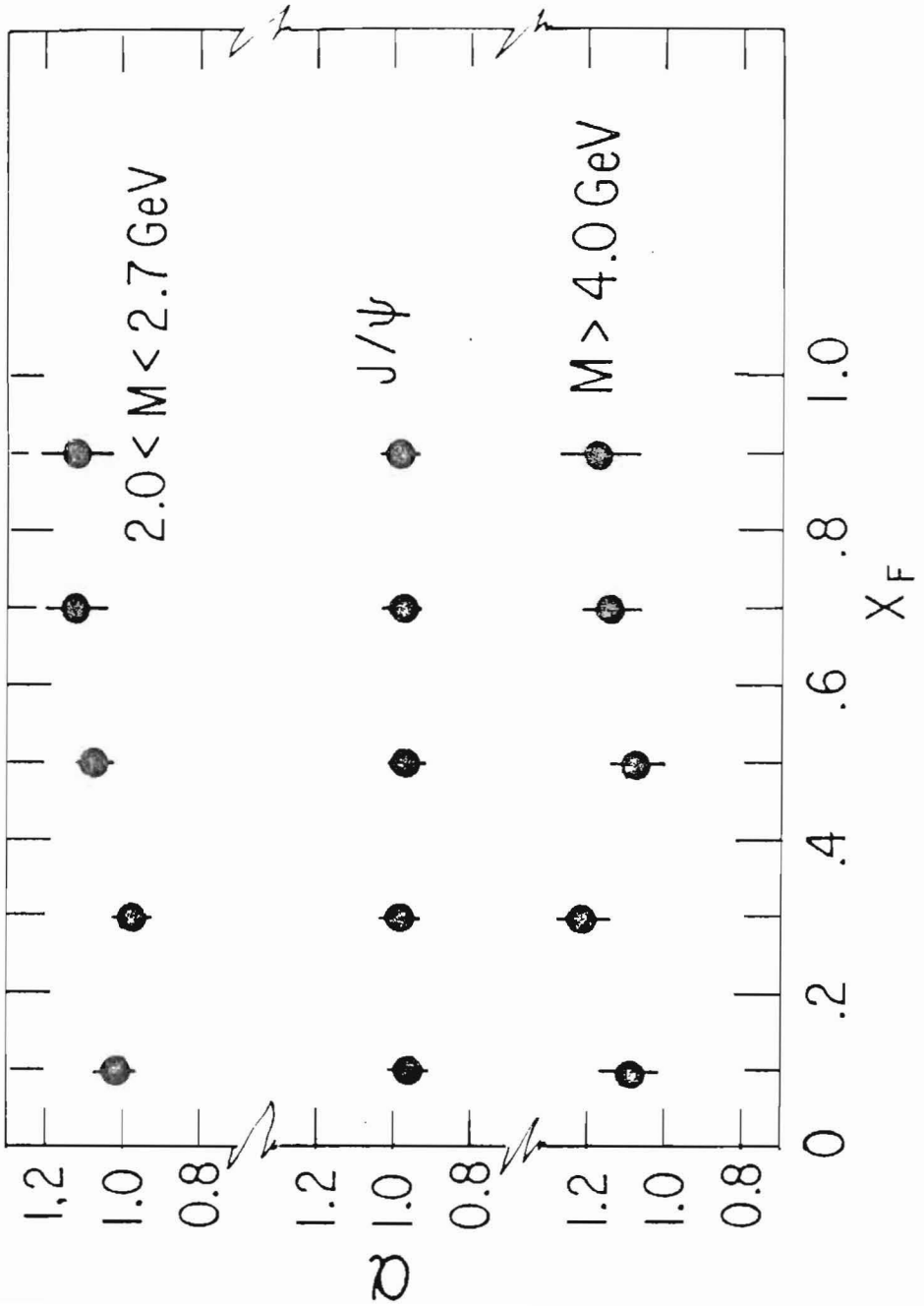
2.0 < M < 2.7 GeV
J/ψ
M > 4.0 GeV
1.2
1.0
0.8
1.2
1.0
0.8
1.2
1.0
0.8
α
0
.2
.4
.6
.8
1.0
X_F

Fig. 61.--Ratio of π^- induced μ pair cross section to proton induced μ pair cross section at $y_{c.m.} = 0.2$ as a function of mass. The proton data at 225 GeV/c were calculated from the scaling observed in the 200, 300 and 400 GeV/c data of Ref. 25.

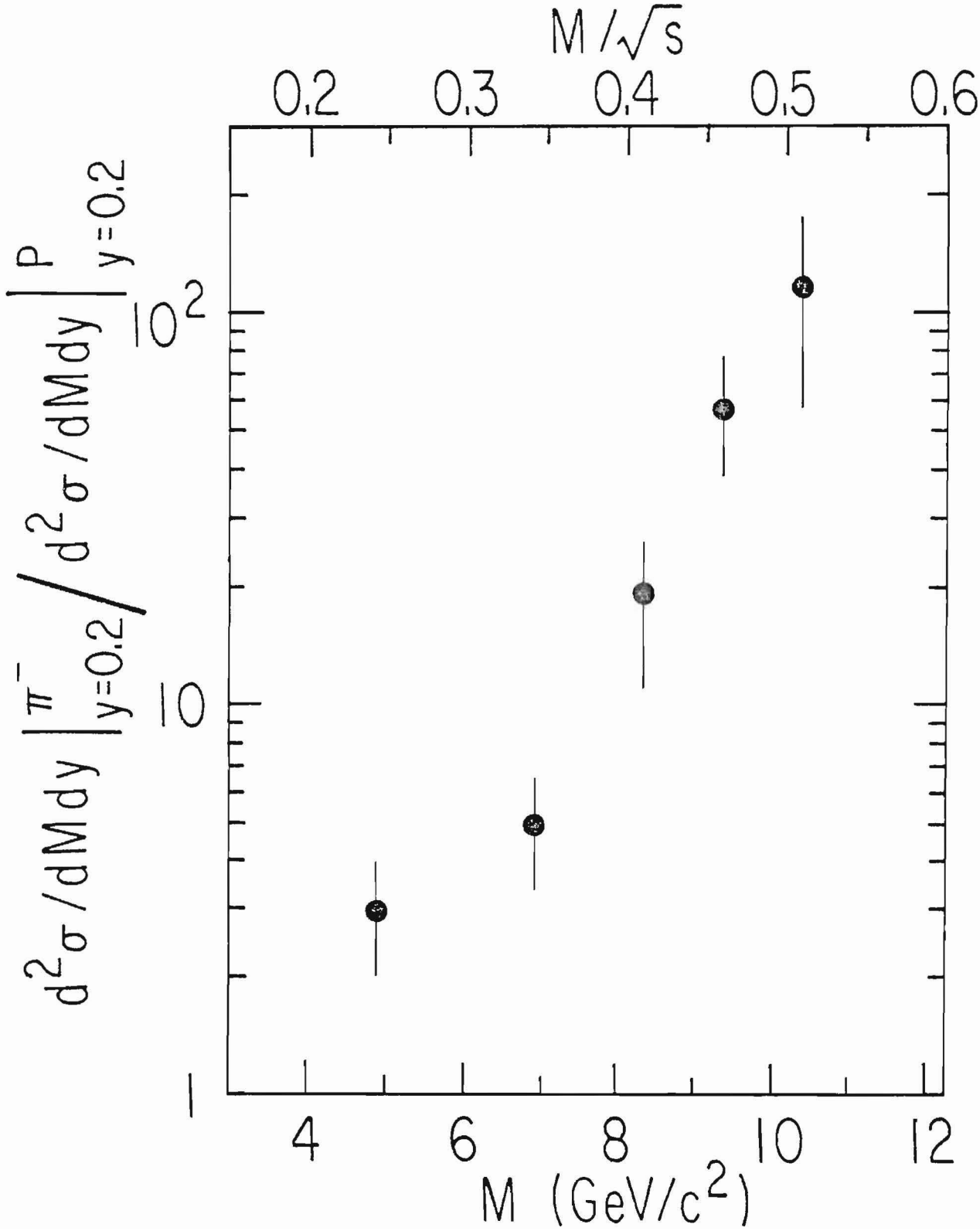
M/√s
0.2
0.3
0.4
0.5
0.6
d²σ/dMdy |π⁻ y=0.2 / d²σ/dMdy |P y=0.2
10²
10
1
4
6
8
10
12
M (GeV/c²)

Fig. 62.--The ratio of π^+ induced μ pair production to π^- induced μ pair production as a function of mass.

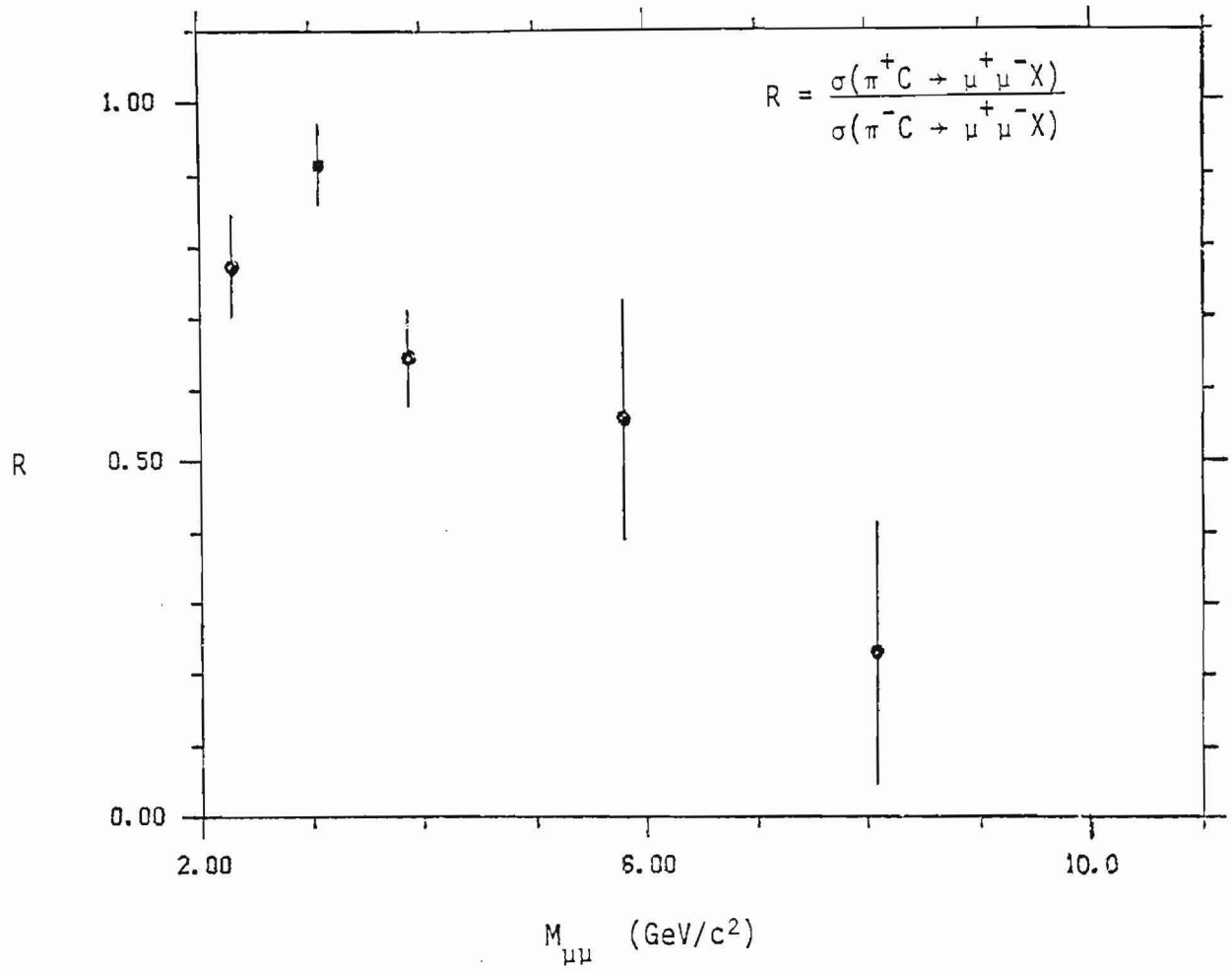
$R = \frac{\sigma(\pi^+ C \to \mu^+\mu^- X)}{\sigma(\pi^- C \to \mu^+\mu^- X)}$
1.00
0.50
0.00
R
2.00
6.00
10.0
$M_{\mu\mu}$ (GeV/c^2)

Fig. 63.--Polar angular distribution for μ pair events in three mass regions. The Collins-Soper direction, used for a reference axis, is defined in the text.

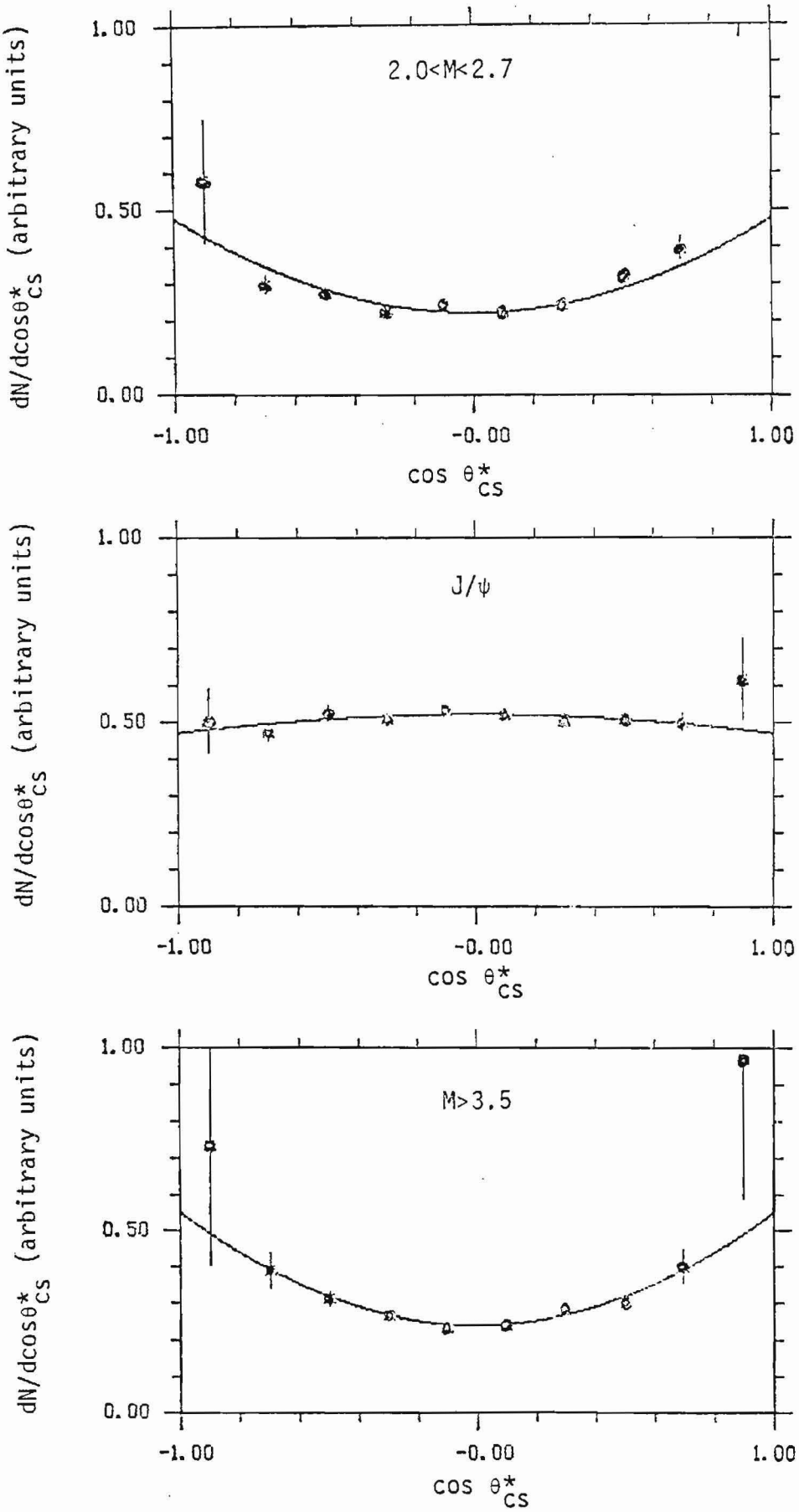
2.0<M<2.7
J/ψ
M>3.5
1.00
0.50
0.00
-1.00
-0.00
1.00
dN/dcosθ*cs (arbitrary units)
cos θ*cs

Fig. 64.--Reference directions for measuring the angle θ^* in the μ pair rest frame.

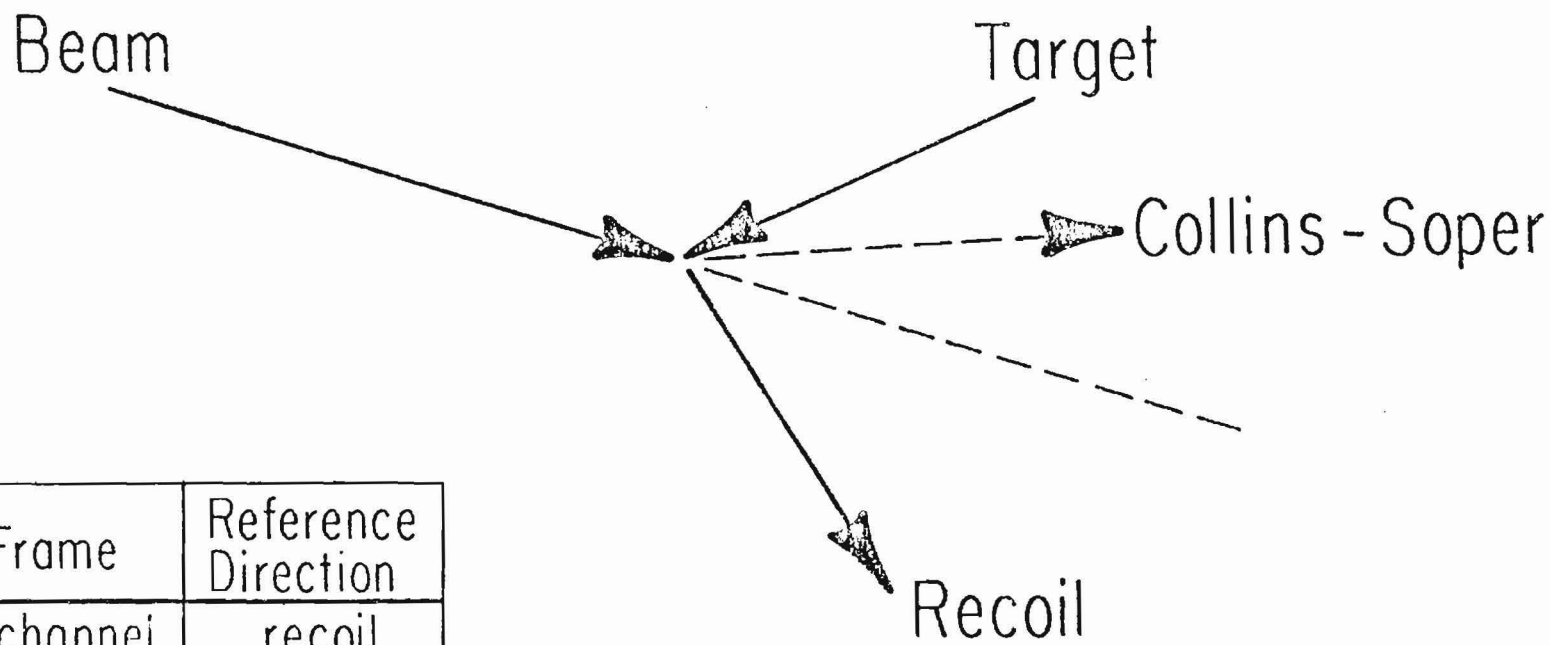

Frame	Reference Direction
s-channel	recoil
t-channel	beam
u-channel	target
Collins-Soper	$\hat{P}_B - \hat{P}_T$

Mu-Pair C.M. System

Fig. 65.--Polar angle distributions for μ pairs with masses between 2.0 and 2.7 GeV/c^2 for the s, t, and u channel systems.

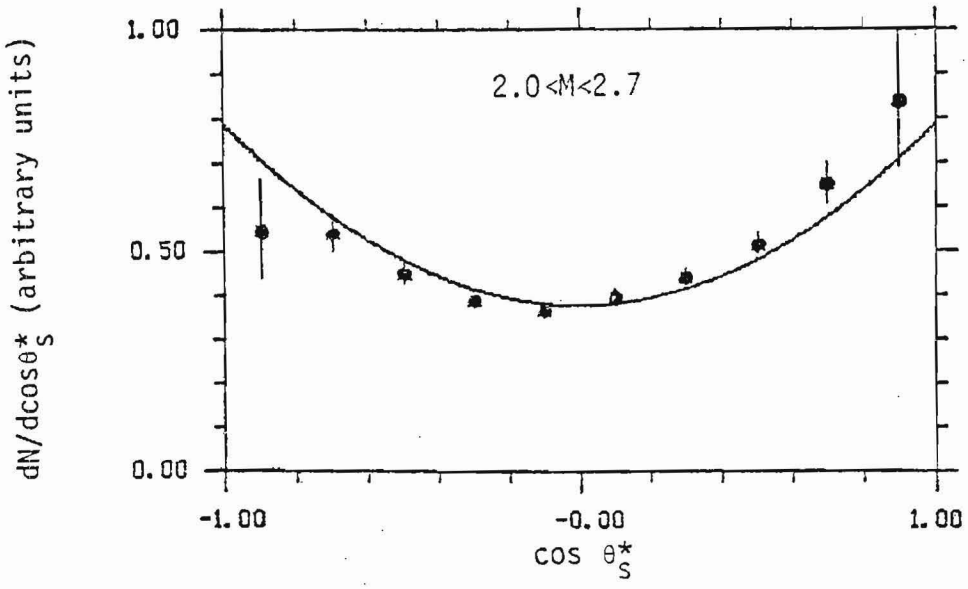
1.00
0.50
0.00
2.0<M<2.7
dN/dcosθ*s (arbitrary units)
-1.00
-0.00
1.00
cos θ*s

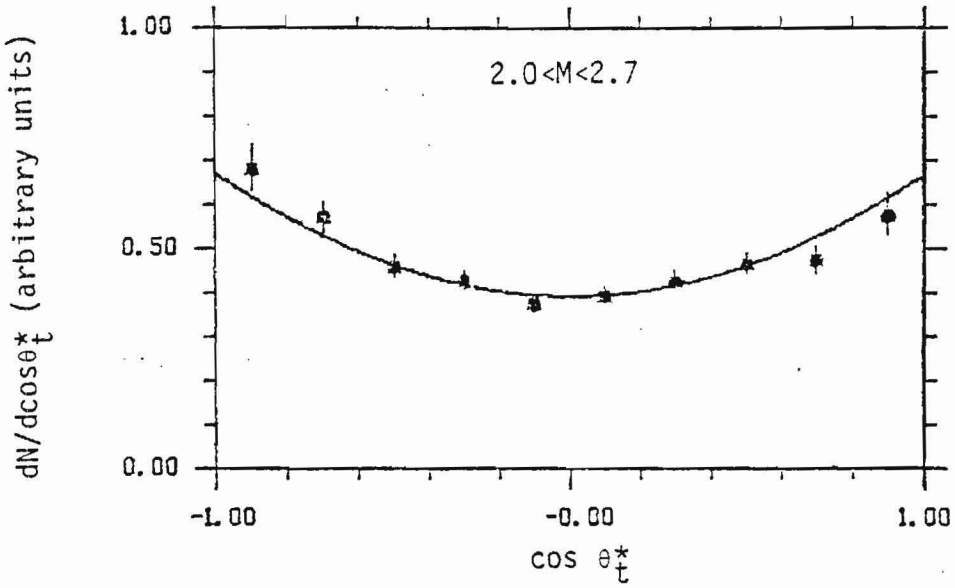
1.00
0.50
0.00
2.0<M<2.7
dN/dcosθ*t (arbitrary units)
-1.00
-0.00
1.00
cos θ*t

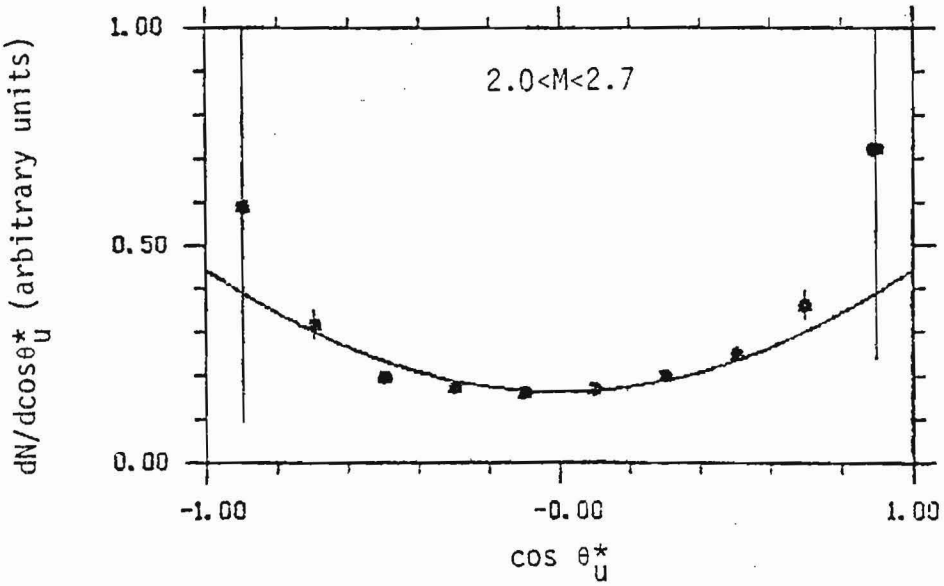
1.00
0.50
0.00
2.0<M<2.7
dN/dcosθ*u (arbitrary units)
-1.00
-0.00
1.00
cos θ*u

Fig. 66.--Polar angle distributions for μ pairs at the J/ψ mass for the s, t, and u channel systems.

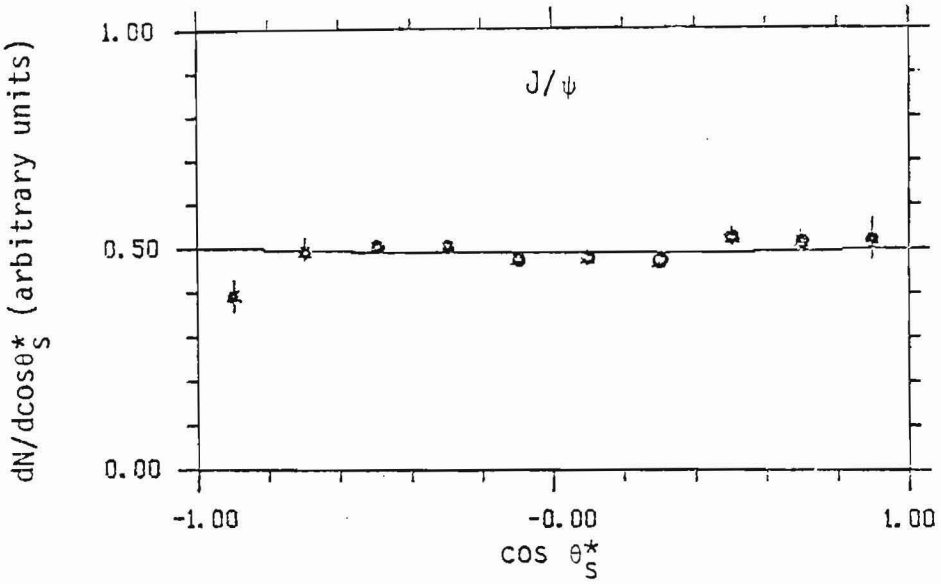
1.00
0.50
0.00
J/ψ
dN/dcosθ*s (arbitrary units)
-1.00
-0.00
1.00
cos θ*s

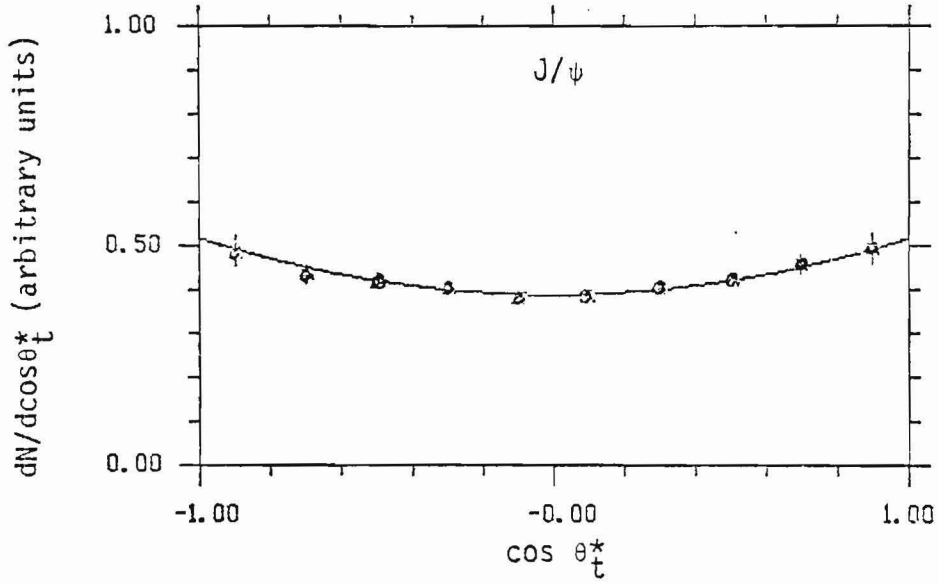
1.00
0.50
0.00
J/ψ
dN/dcosθ*t (arbitrary units)
-1.00
-0.00
1.00
cos θ*t

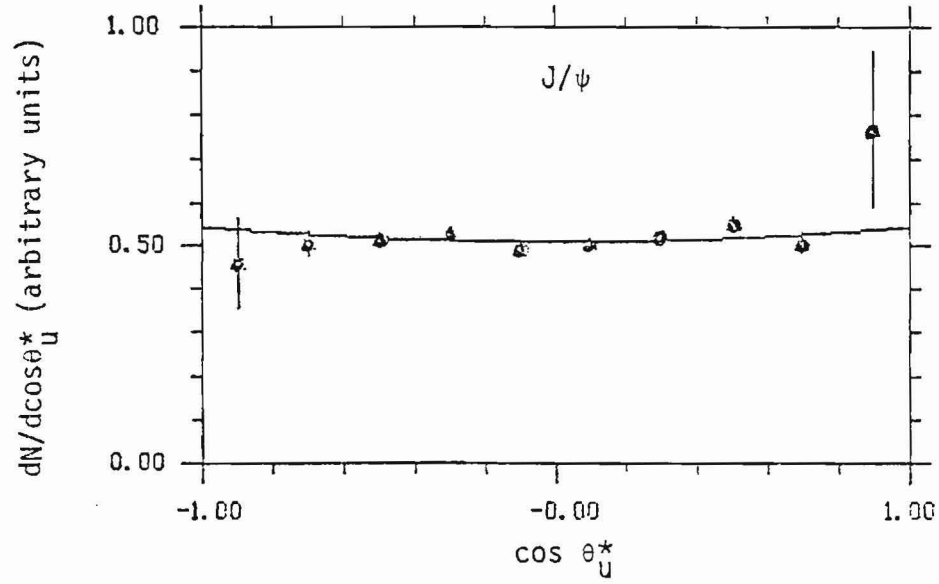
1.00
0.50
0.00
J/ψ
dN/dcosθ*u (arbitrary units)
-1.00
-0.00
1.00
cos θ*u

Fig. 67.--Polar angle distributions for μ pairs with $M>3.5$ GeV/c^2 for the s, t, and u channel systems.

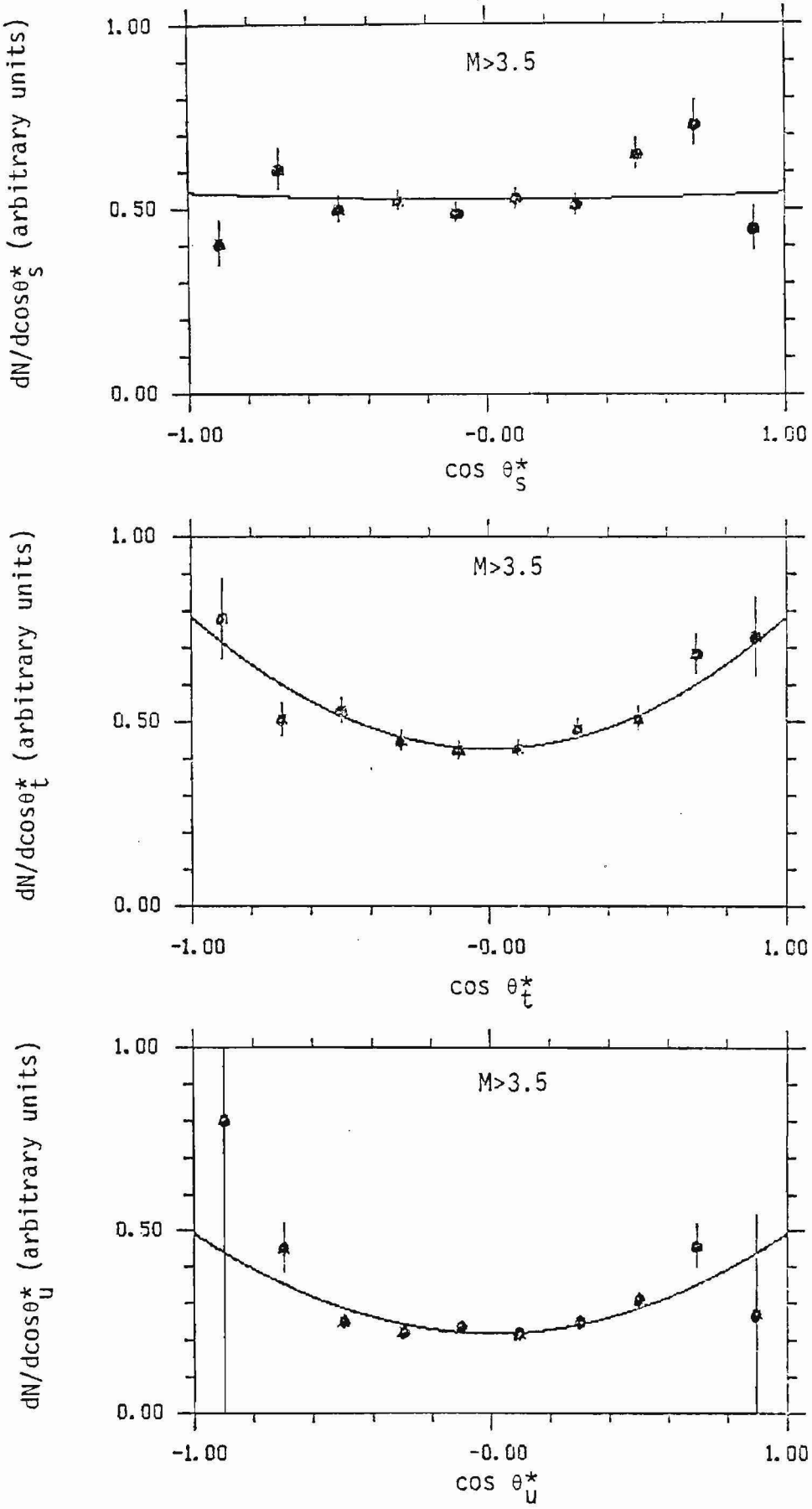
M>3.5
1.00
0.50
0.00
-1.00
-0.00
1.00
dN/dcosθ*s (arbitrary units)
cos θ*s
M>3.5
1.00
0.50
0.00
-1.00
-0.00
1.00
dN/dcosθ*t (arbitrary units)
cos θ*t
M>3.5
1.00
0.50
0.00
-1.00
-0.00
1.00
dN/dcosθ*u (arbitrary units)
cos θ*u

Fig. 68.--Polar angle distributions for μ pairs with $M>3.5$ GeV/c^2 and p_T <1 GeV/c for the four choices of reference axis shown in Fig. 64.

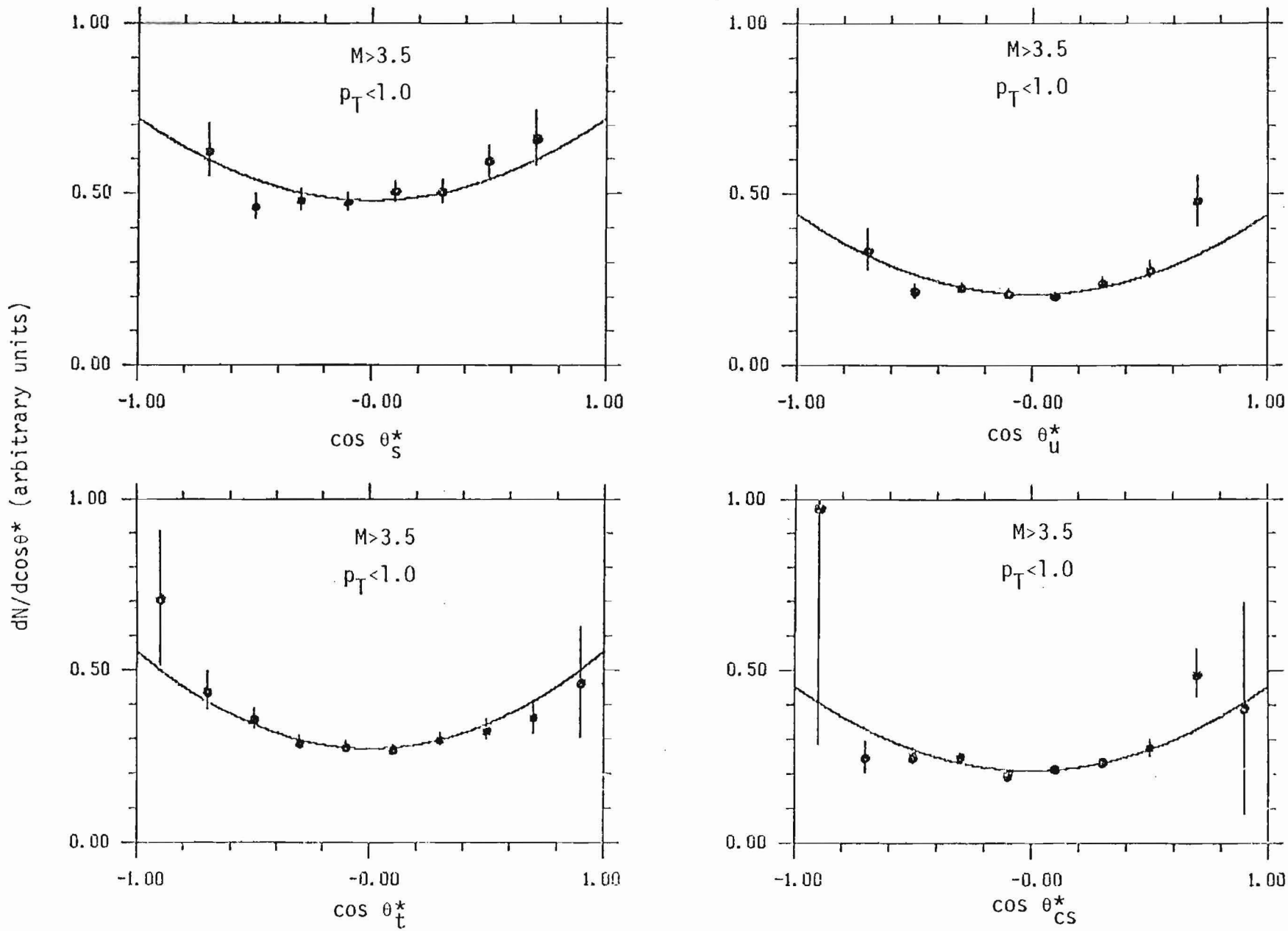
dN/dcosθ* (arbitrary units)
M>3.5
p_T<1.0
cos θ^*_s
cos θ^*_u
cos θ^*_t
cos θ^*_{cs}
1.00
0.50
0.00
-1.00
-0.00
1.00

Fig. 69.--Polar angle distributions for μ pairs with $M>3.5$ GeV/c^2 and p_T >1 GeV/c for the four choices of reference axis shown in Fig. 64.

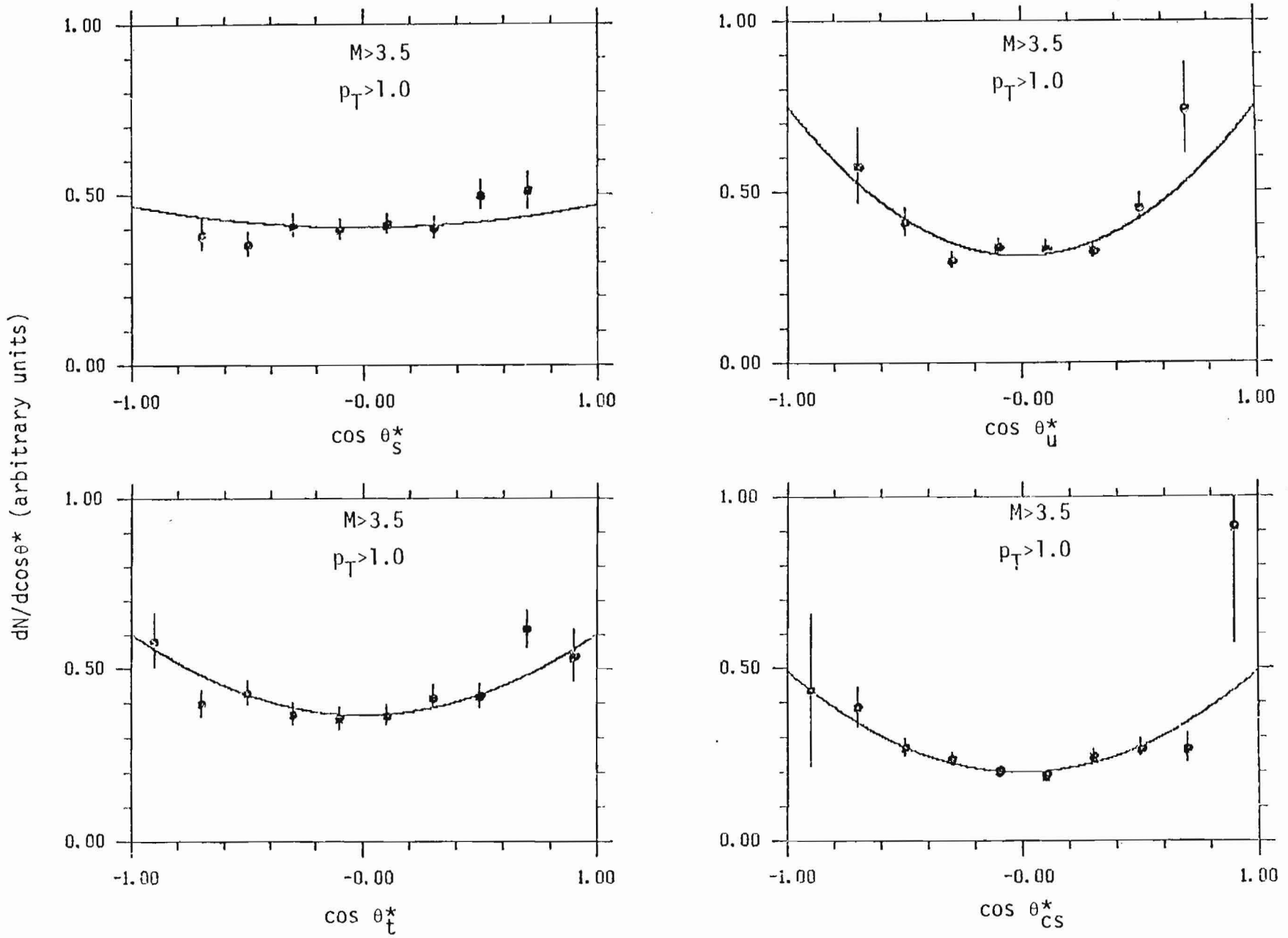
dN/dcosθ* (arbitrary units)
M>3.5
p_T>1.0
cos θ^*_s
cos θ^*_u
cos θ^*_t
cos θ^*_{cs}
1.00
0.50
0.00
-1.00
-0.00
1.00

Fig. 70.--Azimuthal angle distributions for μ pair events in three mass regions. The Collins-Soper direction, defined in the text, was used as a reference axis.

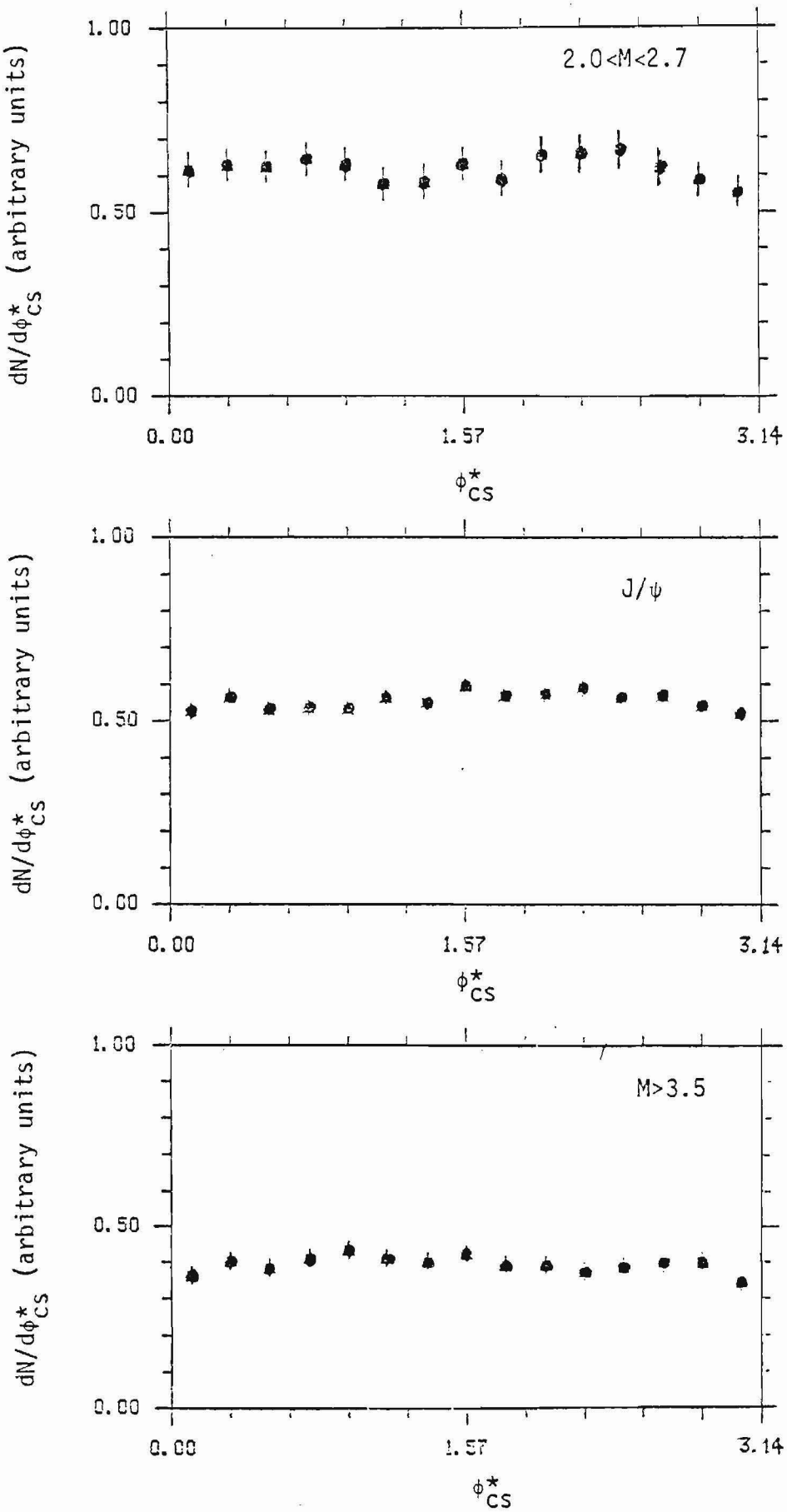
1.00
0.50
0.00
2.0<M<2.7
dN/dφ*cs (arbitrary units)
0.00
1.57
3.14
φ*cs
1.00
0.50
0.00
J/ψ
dN/dφ*cs (arbitrary units)
0.00
1.57
3.14
φ*cs
1.00
0.50
0.00
M>3.5
dN/dφ*cs (arbitrary units)
0.00
1.57
3.14
φ*cs

Fig. 71.--Azimuthal angle distributions of μ pairs with masses between 2.0 and 2.7 GeV/c^2 for the s, t, and u channel systems.

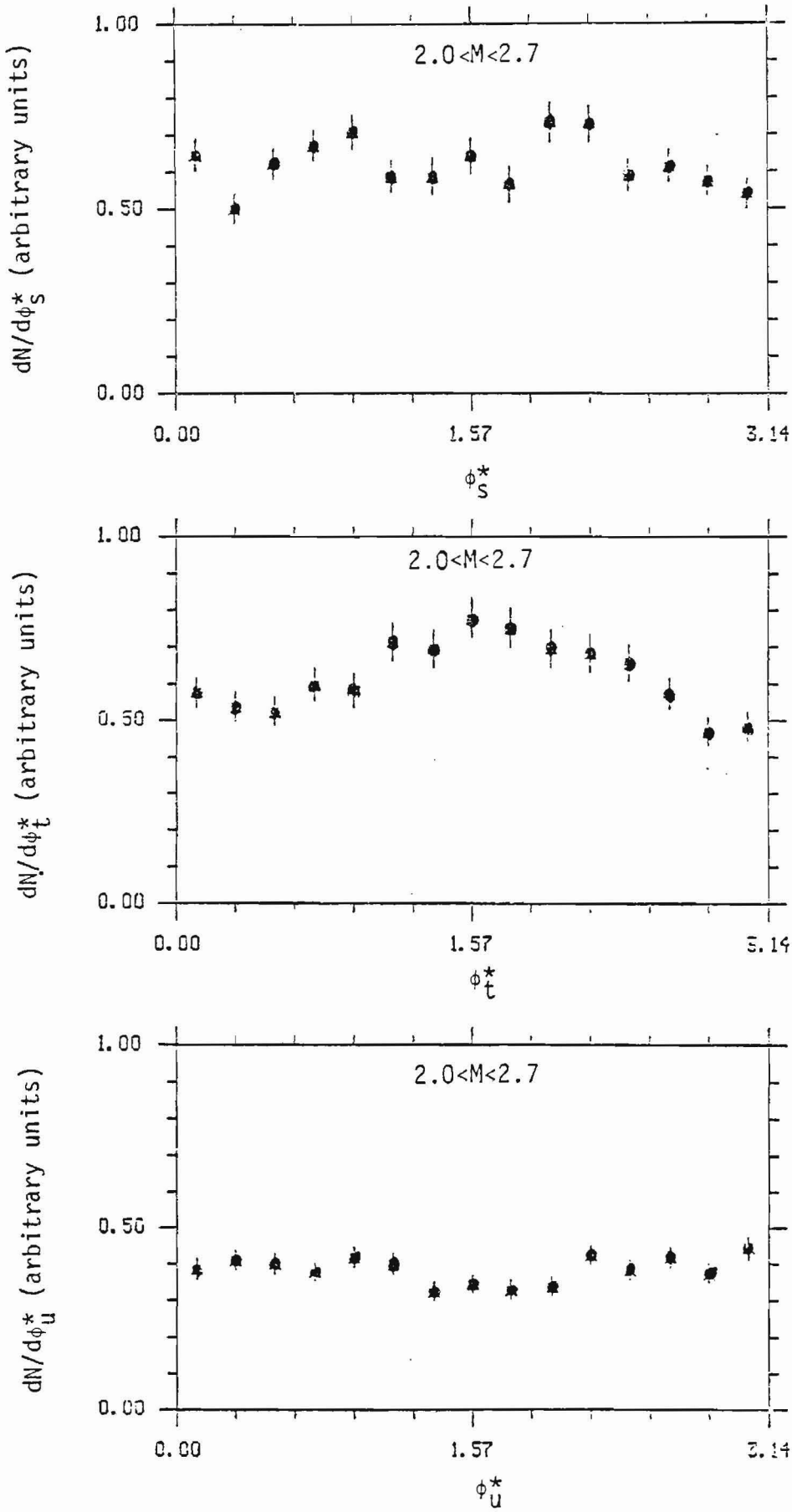
1.00
0.50
0.00
2.0<M<2.7
dN/dφ*s (arbitrary units)
0.00
1.57
3.14
φ*s
1.00
0.50
0.00
2.0<M<2.7
dN/dφ*t (arbitrary units)
0.00
1.57
3.14
φ*t
1.00
0.50
0.00
2.0<M<2.7
dN/dφ*u (arbitrary units)
0.00
1.57
3.14
φ*u

Fig. 72.--Azimuthal angle distributions for μ pairs at the J/ψ mass for the s, t, and u channel systems.

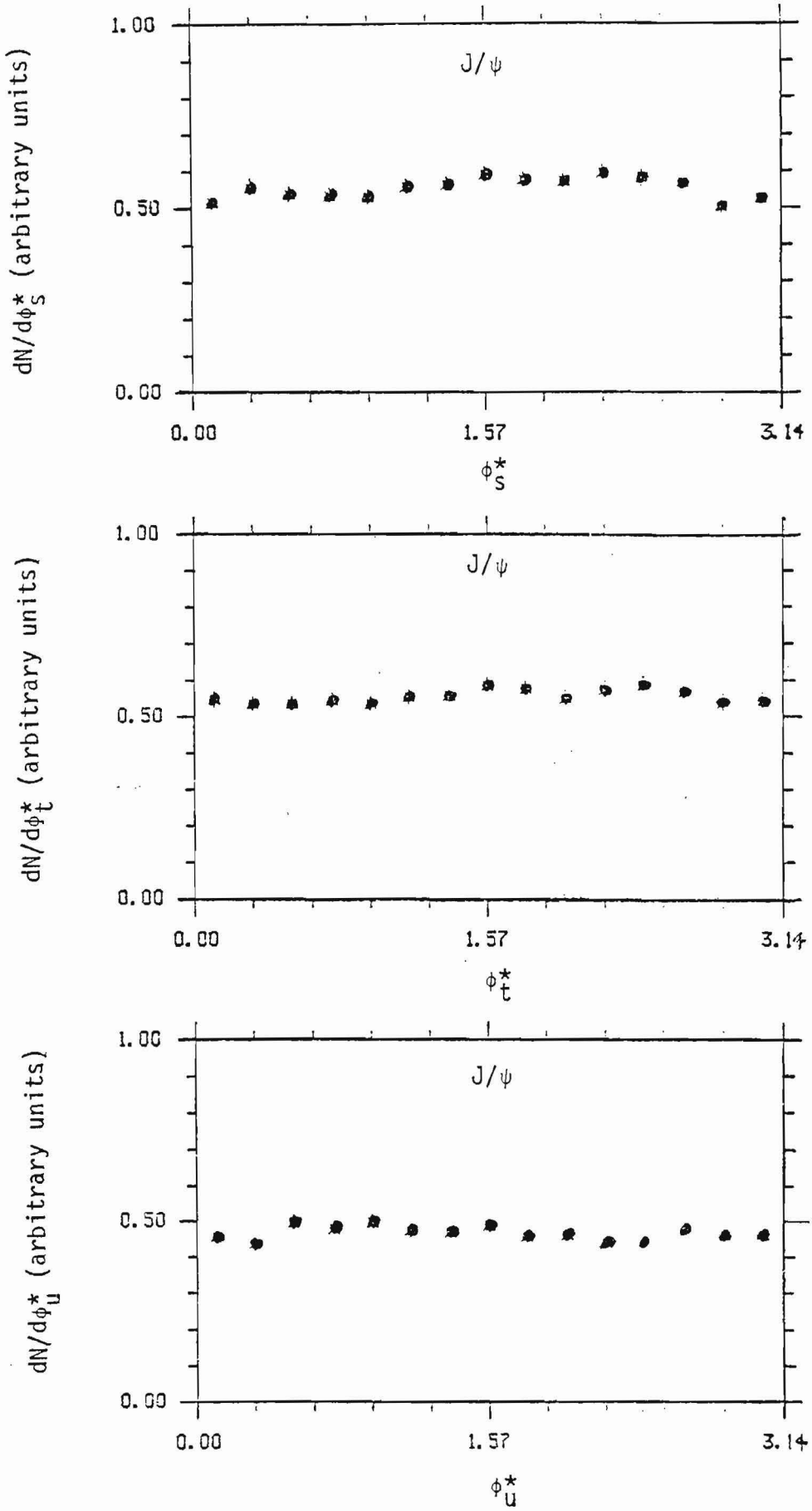
1.00
0.50
0.00
J/ψ
dN/dφ*s (arbitrary units)
0.00
1.57
3.14
φ*s
1.00
0.50
0.00
J/ψ
dN/dφ*t (arbitrary units)
0.00
1.57
3.14
φ*t
1.00
0.50
0.00
J/ψ
dN/dφ*u (arbitrary units)
0.00
1.57
3.14
φ*u

Fig. 73.--Azimuthal angle distributions for μ pairs with $M > 3.5$ GeV/c^2 for the s, t, and u channel systems.

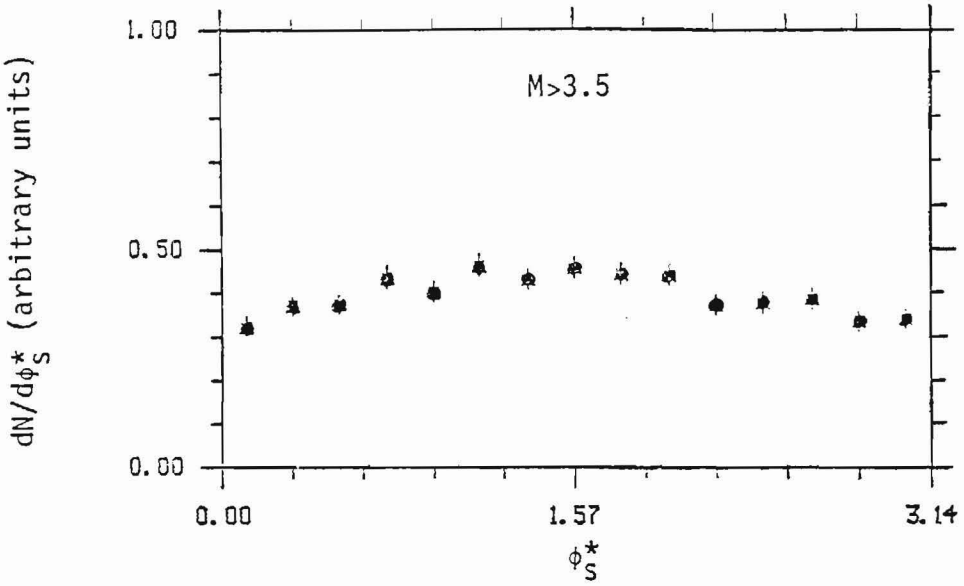
1.00
0.50
0.00
M>3.5
dN/dφ*s (arbitrary units)
0.00
1.57
3.14
φ*s

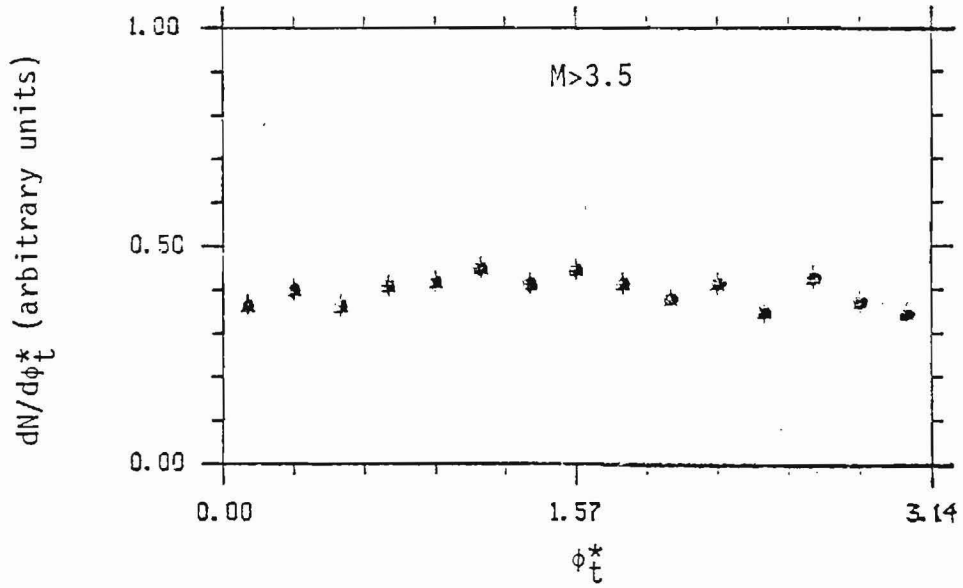
1.00
0.50
0.00
M>3.5
dN/dφ*t (arbitrary units)
0.00
1.57
3.14
φ*t

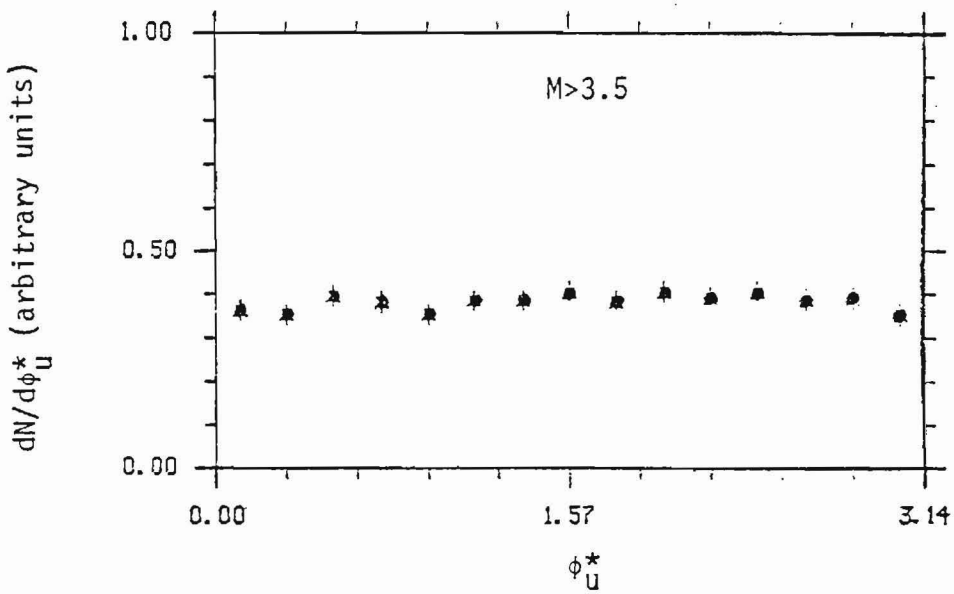
1.00
0.50
0.00
M>3.5
dN/dφ*u (arbitrary units)
0.00
1.57
3.14
φ*u

Fig. 74.--$M^3 d\sigma/dM$ vs. M^2/s for $pN \rightarrow \mu^+\mu^- X$. Data from Ref. 25 and Ref. 37 are converted from the measured $d^2\sigma/dMdy$ ($y=0$) to $d\sigma/dM$ ($x_F>0$) by using the antiquark distribution of Ref. 43 and valence quark distributions from deep inelastic lepton scattering. The resulting x_F distribution agrees well with the spectrum observed in this experiment.

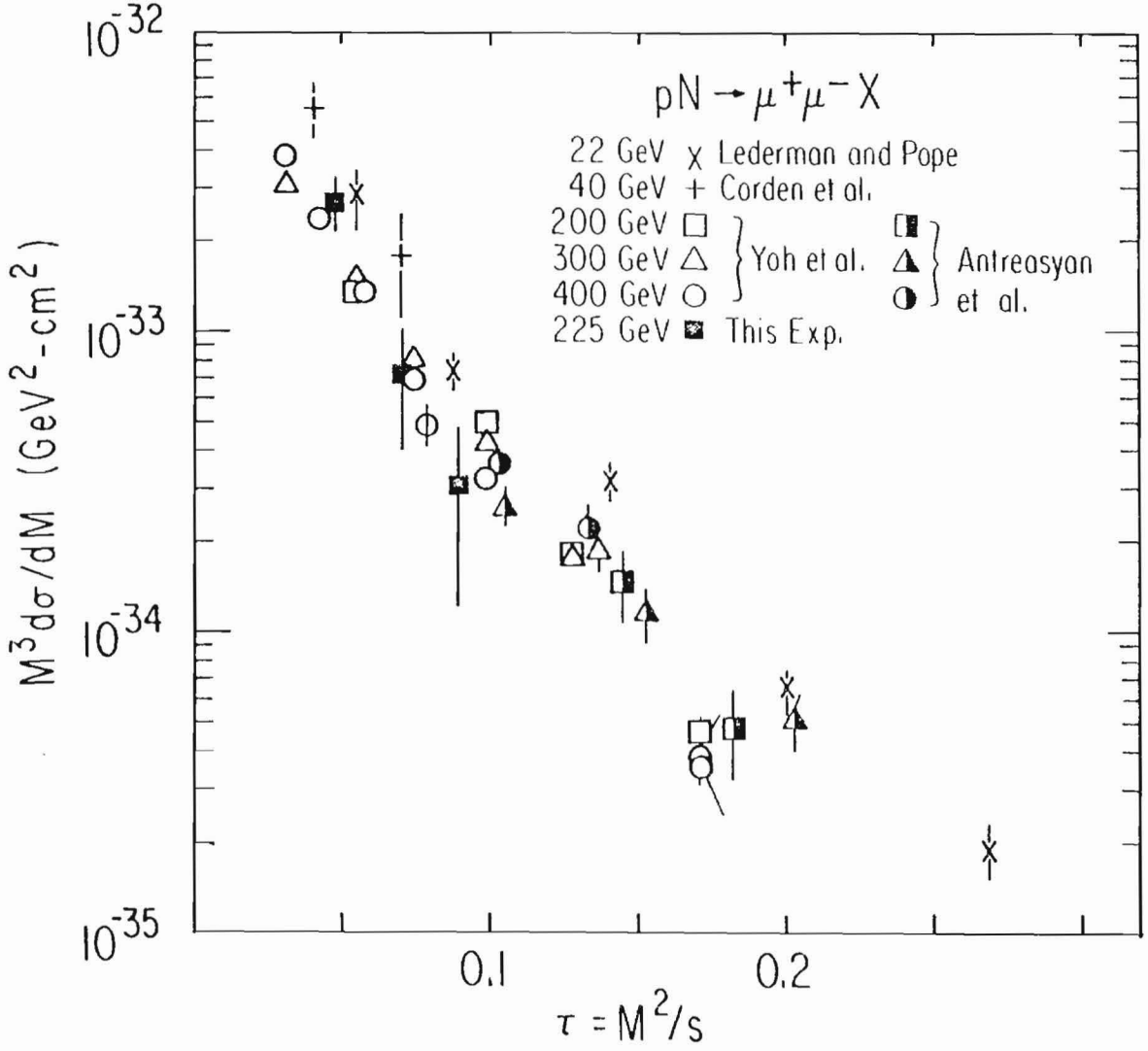
pN → μ+μ− X
22 GeV Lederman and Pope
40 GeV Corden et al.
200 GeV
300 GeV
400 GeV
Yoh et al.
Antreasyan et al.
225 GeV This Exp.
M³dσ/dM (GeV²-cm²)
10⁻³²
10⁻³³
10⁻³⁴
10⁻³⁵
0.1
0.2
τ = M²/s

Fig. 75.--$M^3 d\sigma/dM$ vs. M^2/s for $\pi^- N \rightarrow \mu^+ \mu^- X$.

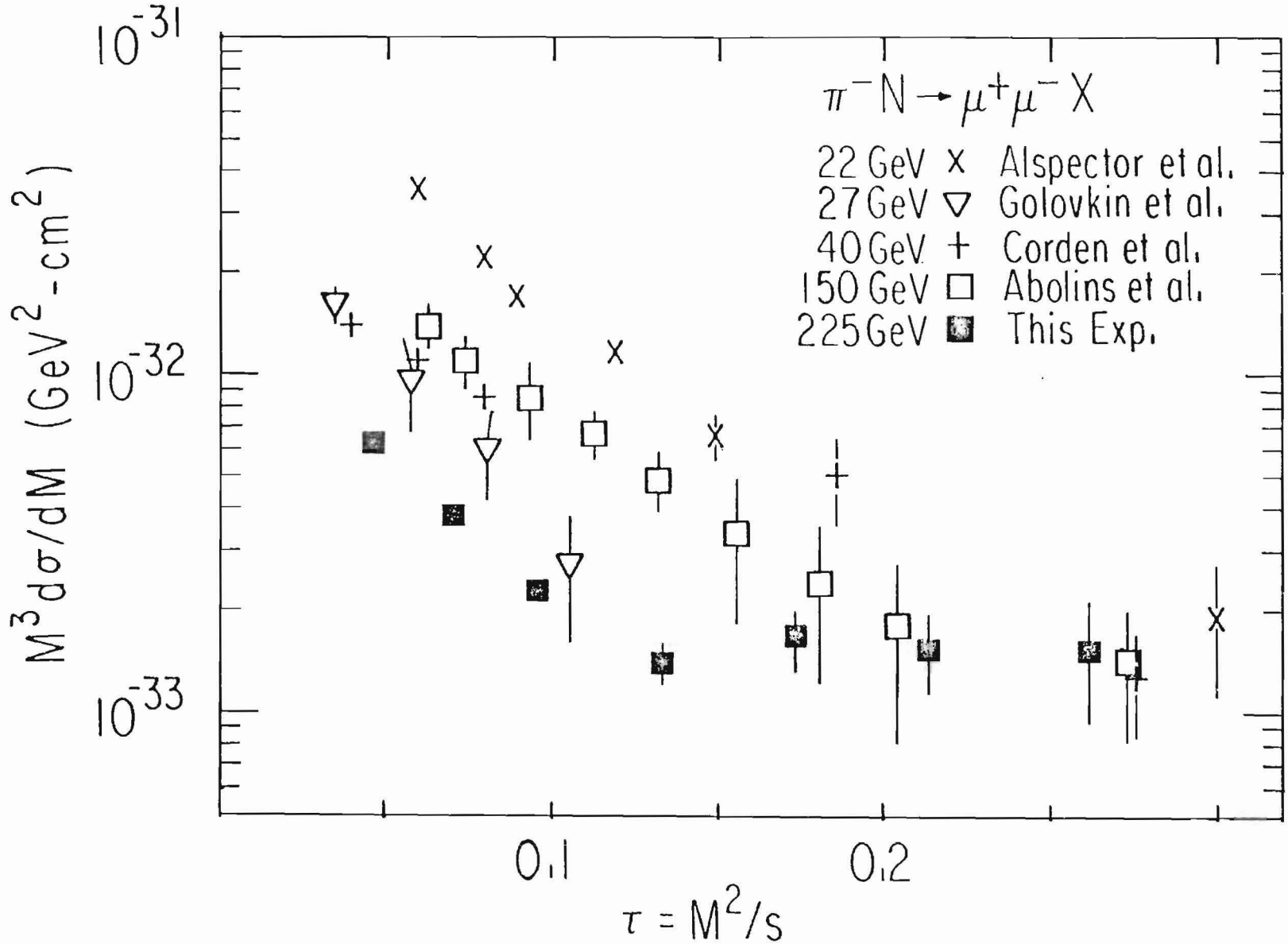
$\pi^- N \rightarrow \mu^+\mu^- X$
22 GeV × Alspector et al.
27 GeV ▽ Golovkin et al.
40 GeV + Corden et al.
150 GeV □ Abolins et al.
225 GeV ■ This Exp.
10^{-31}
10^{-32}
10^{-33}
$M^3 d\sigma/dM$ (GeV^2-cm^2)
0.1
0.2
$\tau = M^2/s$

Fig. 76.--The ratio $R = \sigma(\pi^+ N \to \mu^+\mu^- X)/\sigma(\pi^- N \to \mu^+\mu^- X)$ vs. $M/\sqrt{s}$ for continuum μ pairs. The carbon target data from this experiment are shown. Data are included from the experiment of Ref. 35 which detected μ pairs produced by 40 GeV pions on a copper target.

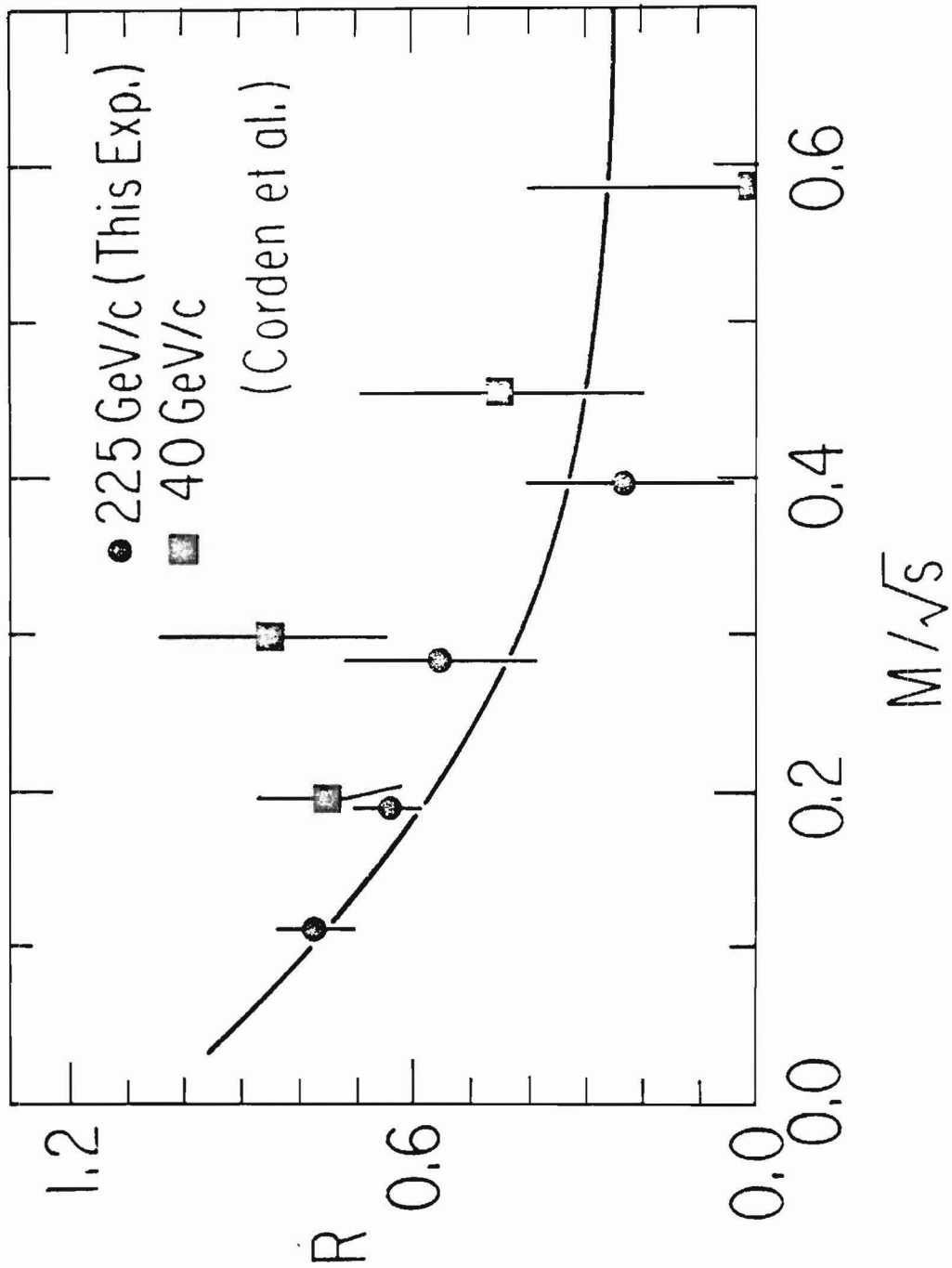
225 GeV/c (This Exp.)
40 GeV/c
(Corden et al.)
R
1.2
0.6
0.0
0.0
0.2
0.4
0.6
M/√s

Fig. 77.--Distribution of events in the x_1, x_2 plane. Lines of constant x_F ($x_F=x_1-x_2$) and curves of constant mass ($x_1x_2=M^2/s$) are also shown.

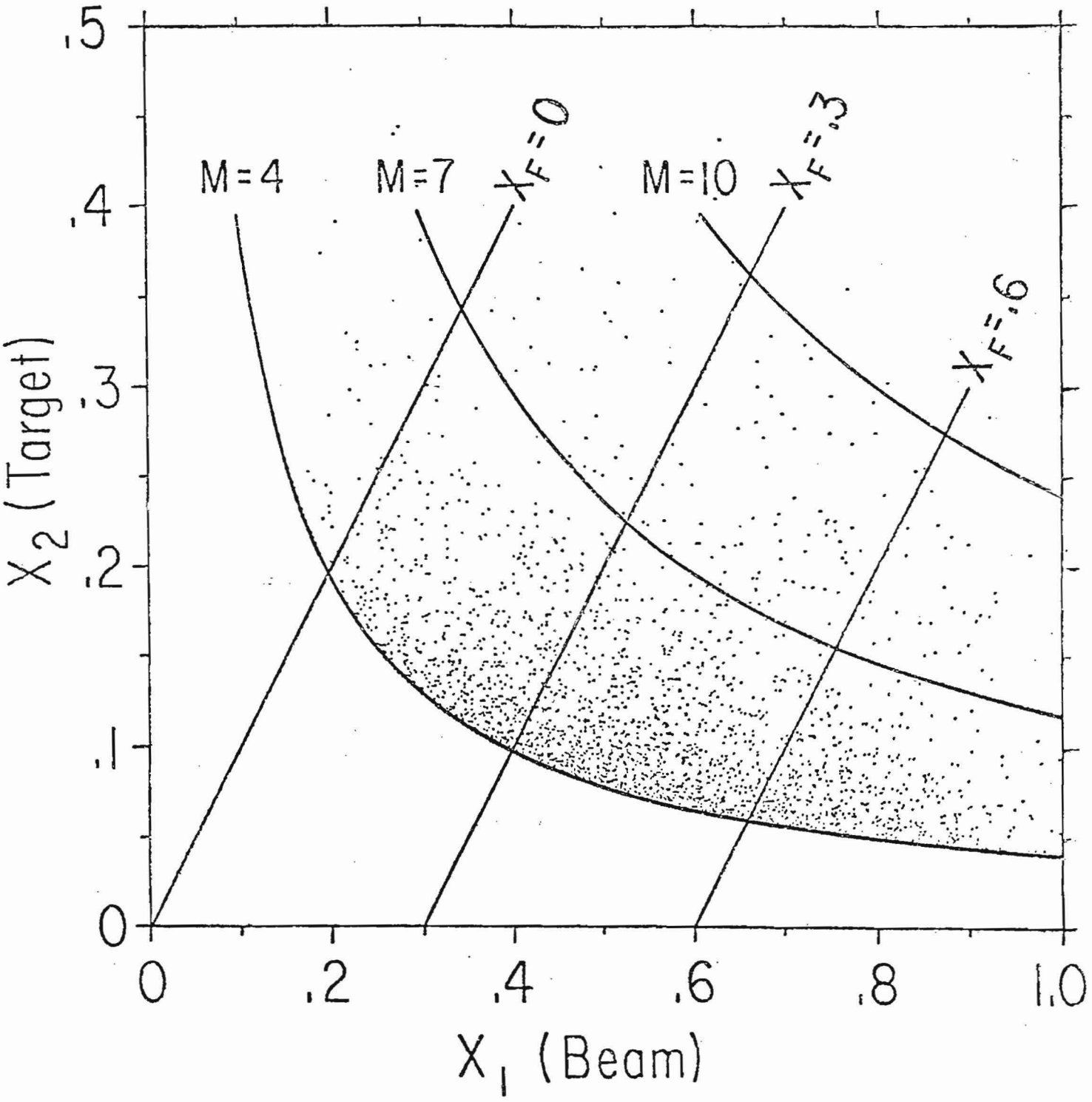
M=4
M=7
M=10
$X_F=0$
$X_F=.3$
$X_F=.6$
.5
.4
.3
.2
.1
0
X_2 (Target)
0
.2
.4
.6
.8
1.0
X_1 (Beam)

Fig. 78.--The nucleon structure function $g^N(x_2) = \frac{4}{9}x_2u^N(x_2) + \frac{1}{9}x_2\bar{d}^N(x_2)$ averaged over protons and neutrons in the C, Cu and W targets. Curve A was used to normalize the data points as described in the text. Curve B is from Buras and Gaemers (Ref. 40). Curve C is from G. C. Fox (Ref. 41).

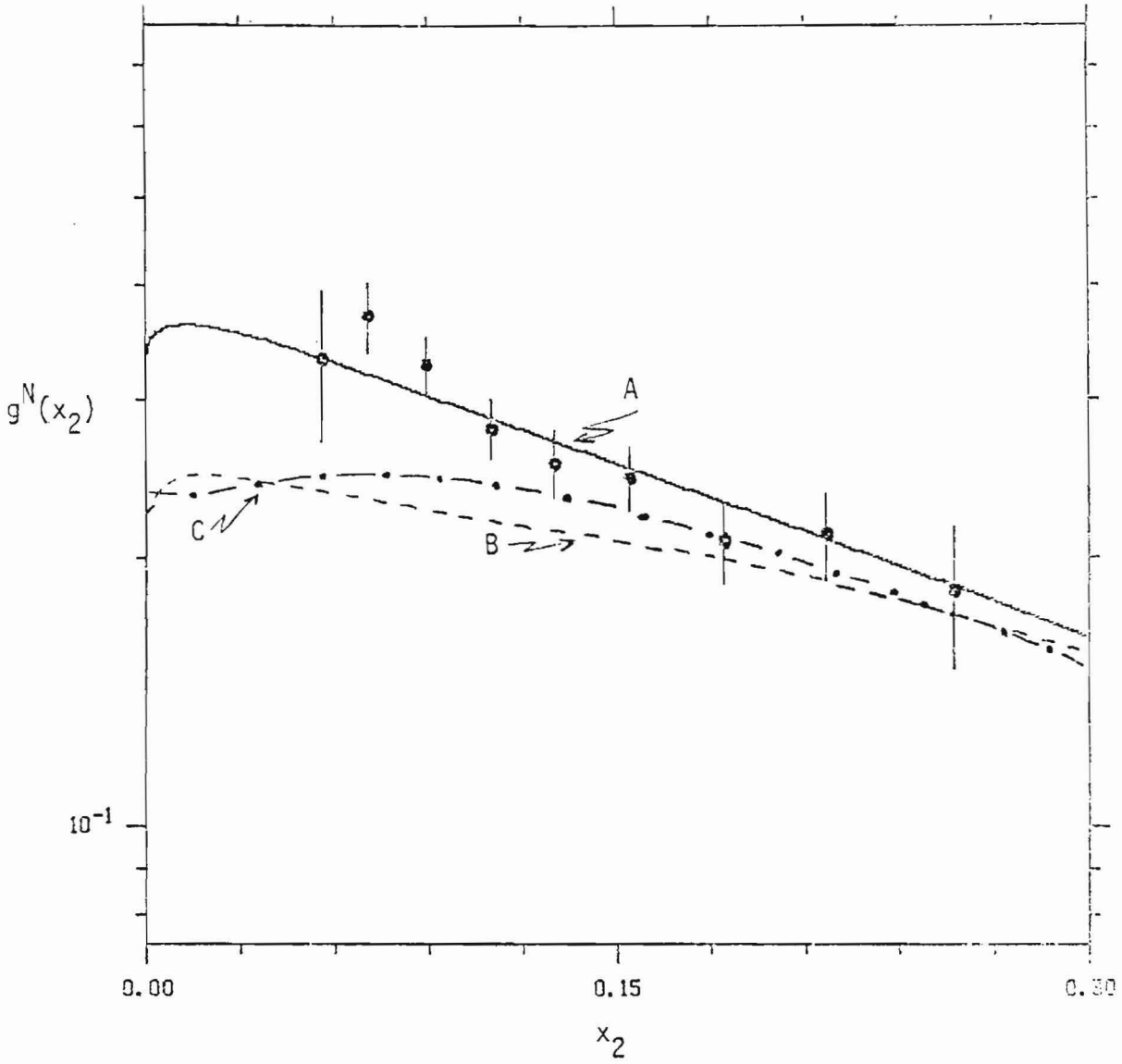
$g^N(x_2)$
10^{-1}
A
B
C
0.00
0.15
0.30
x_2

Fig. 79.--νW_2 vs. x for lepton-deuterium scattering at high q^2. The data points are from SLAC and FERMILAB. The curves were calculated using the valence quark distribution functions of Ref. 40. The solid line used the sea distribution of Ref. 43 and the dashed line used the sea distribution of Ref. 40.

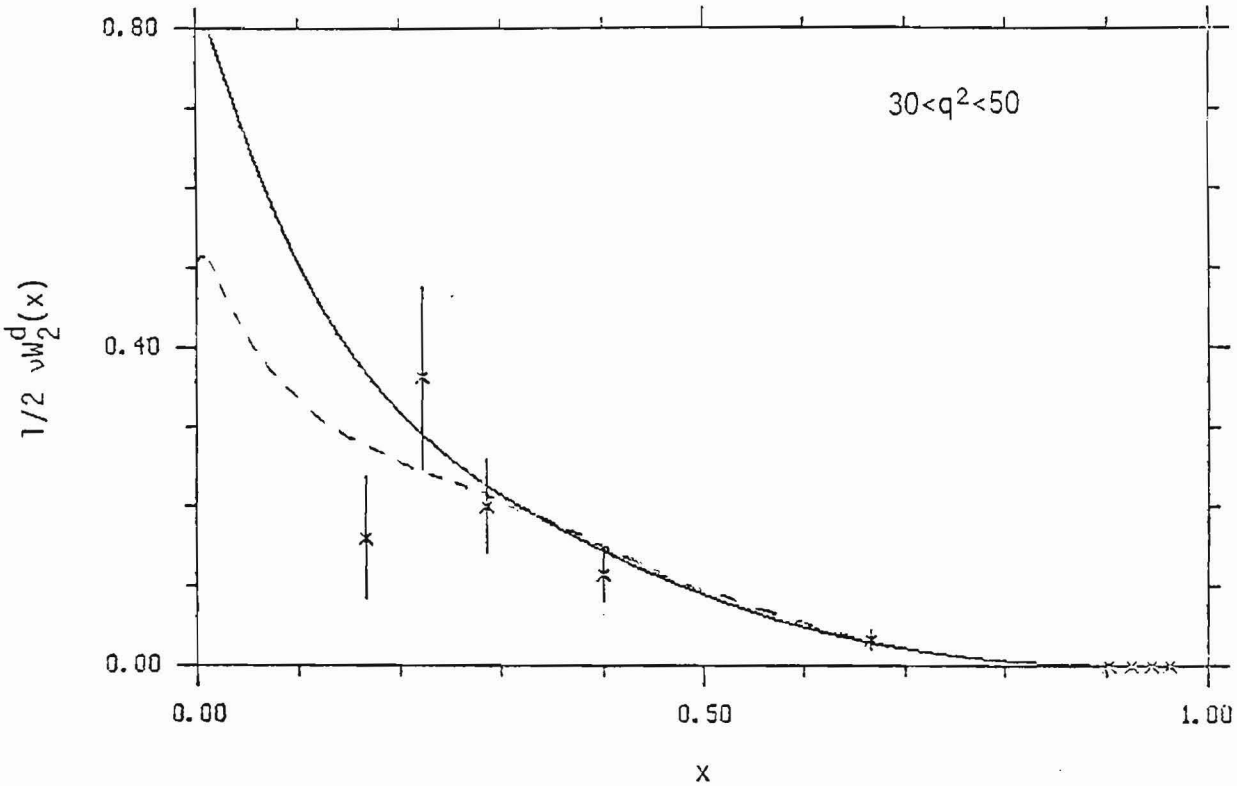
0.80
0.40
0.00
0.00
0.50
1.00
x
1/2 $\nu W_2^d(x)$
$30<q^2<50$

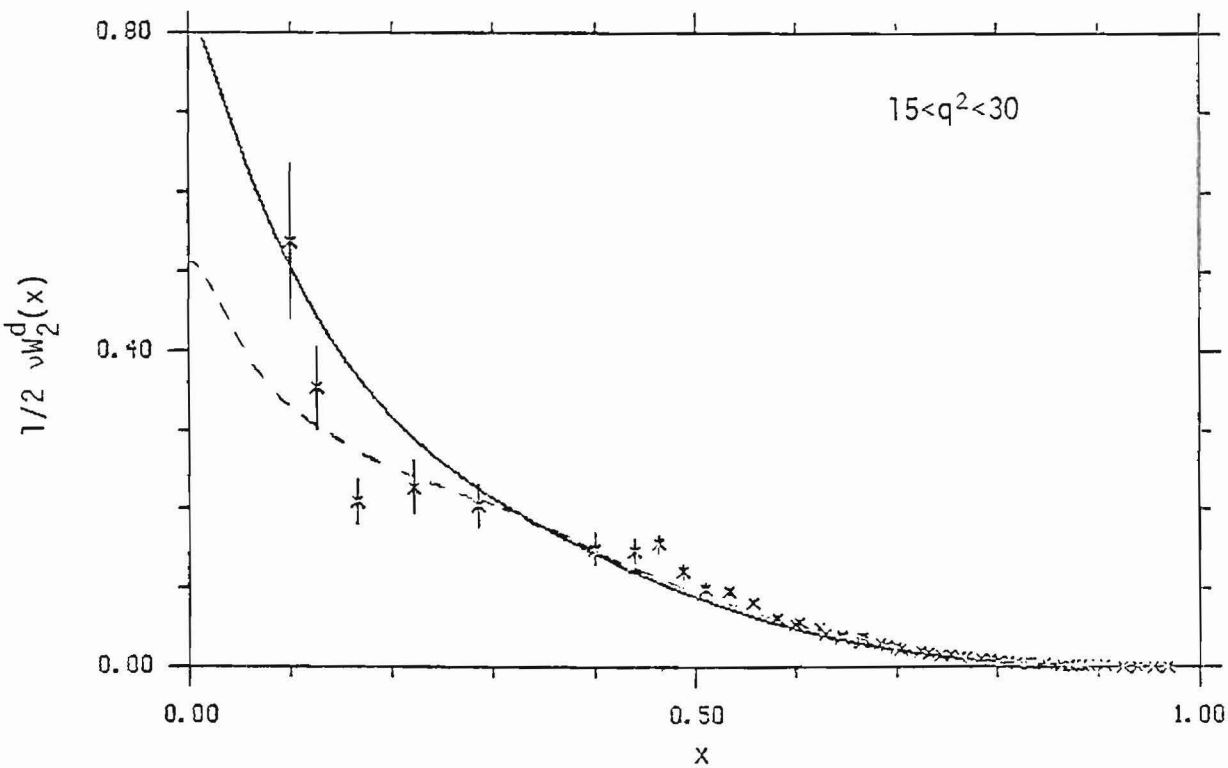
0.80
0.40
0.00
0.00
0.50
1.00
x
1/2 $\nu W_2^d(x)$
$15<q^2<30$

Fig. 80.--The momentum distribution for a valence quark in the charged pion: $f^{\pi}(x_1) = x_1 \bar{u}^{\pi}(x_1)$.

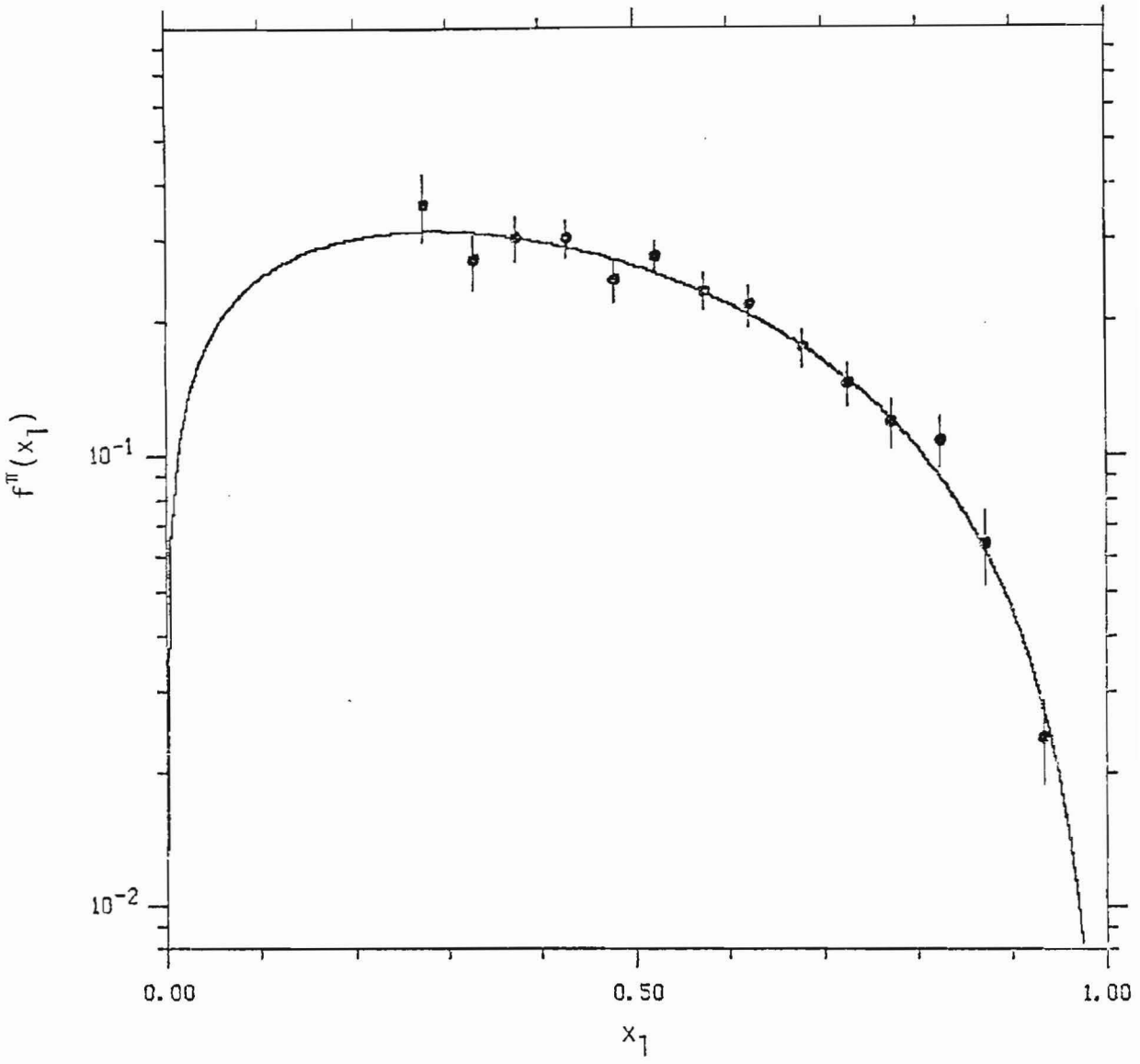
$f^{\pi}(x_1)$
10^{-1}
10^{-2}
0.00
0.50
1.00
x_1

Fig. 81.--The pion valence quark probability function $\bar{u}^{\pi}(x_1)$. A factor 1/3 for color was included in the analysis to determine the upper set of points. For the lower set of points, this factor was not included.

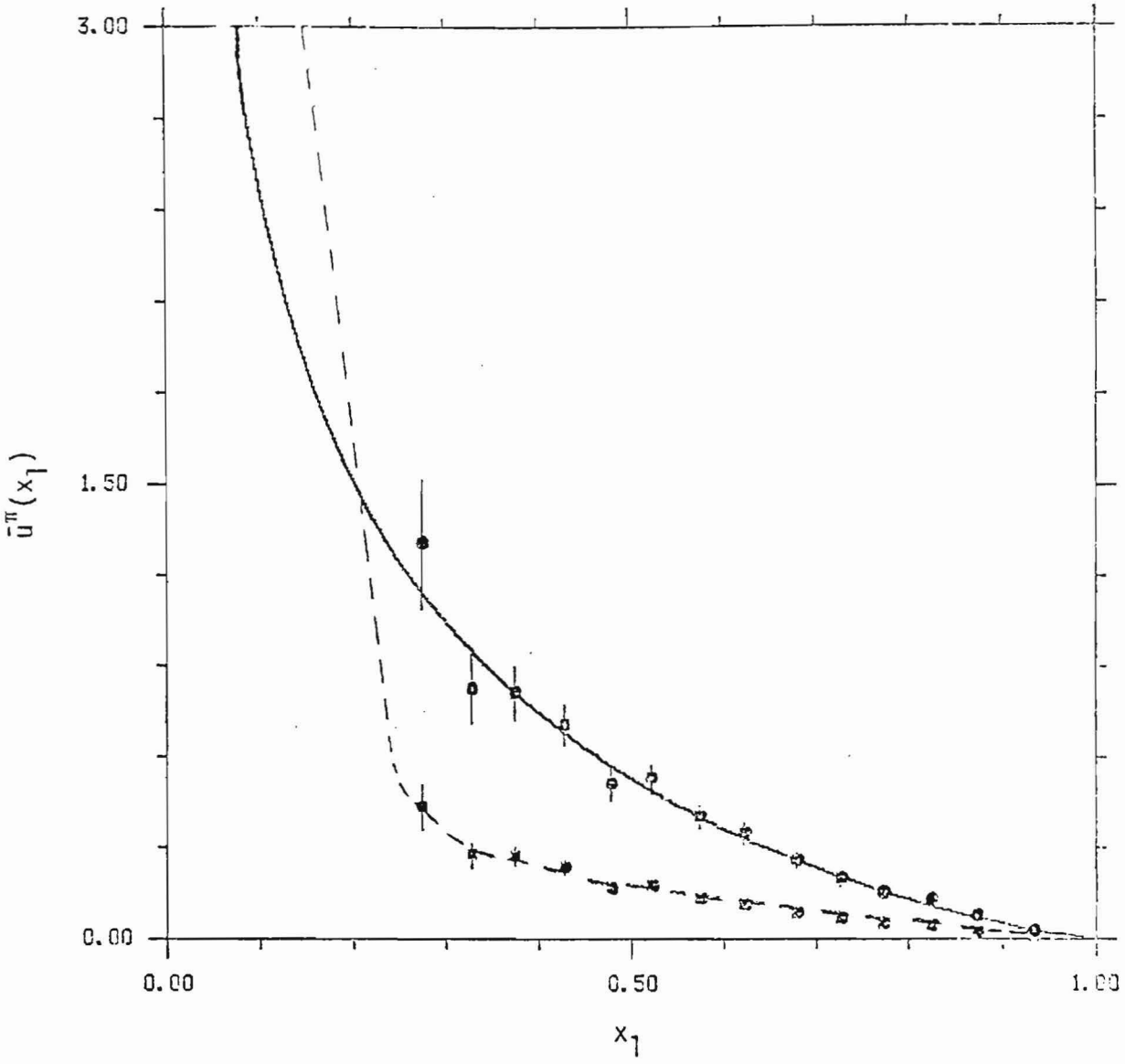
3.00
1.50
0.00
0.00
0.50
1.00
$\bar{u}^{\pi}(x_1)$
x_1

Fig. 82.--Mass spectrum for π^- induced μ pairs with masses between 4.0 and 8.75 GeV/c^2. The curve is calculated from the structure functions of Figures 78 and 80.

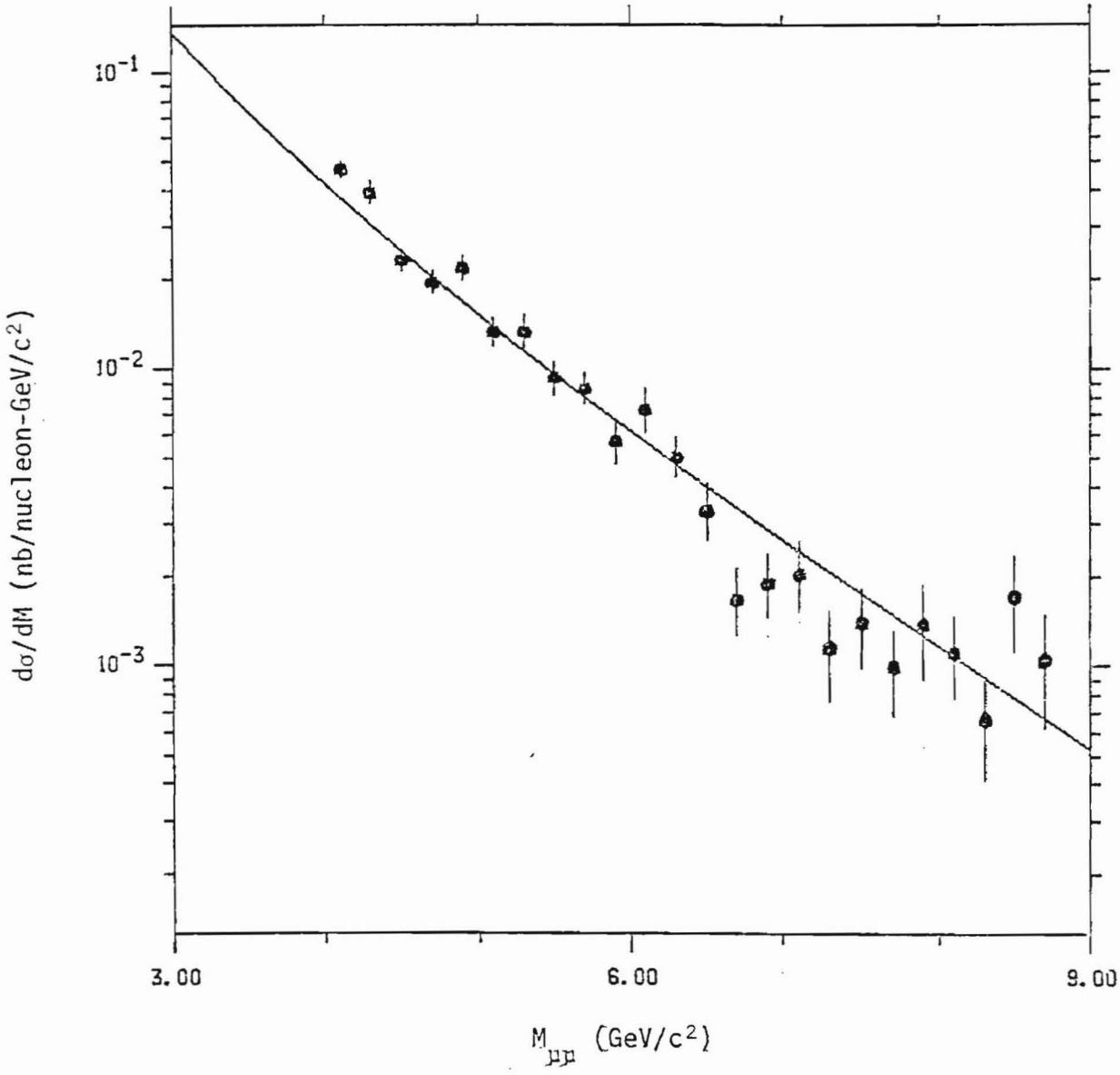
10^{-1}
10^{-2}
10^{-3}
$d\sigma/dM$ (nb/nucleon-GeV/c^2)
3.00
6.00
9.00
$M_{\mu\mu}$ (GeV/c^2)

Fig. 83.--Feynman x distributions for π^- induced μ pairs with masses between 4.0 and 8.75 GeV/c^2. The curves are calculated from the structure functions of Figures 78 and 80.

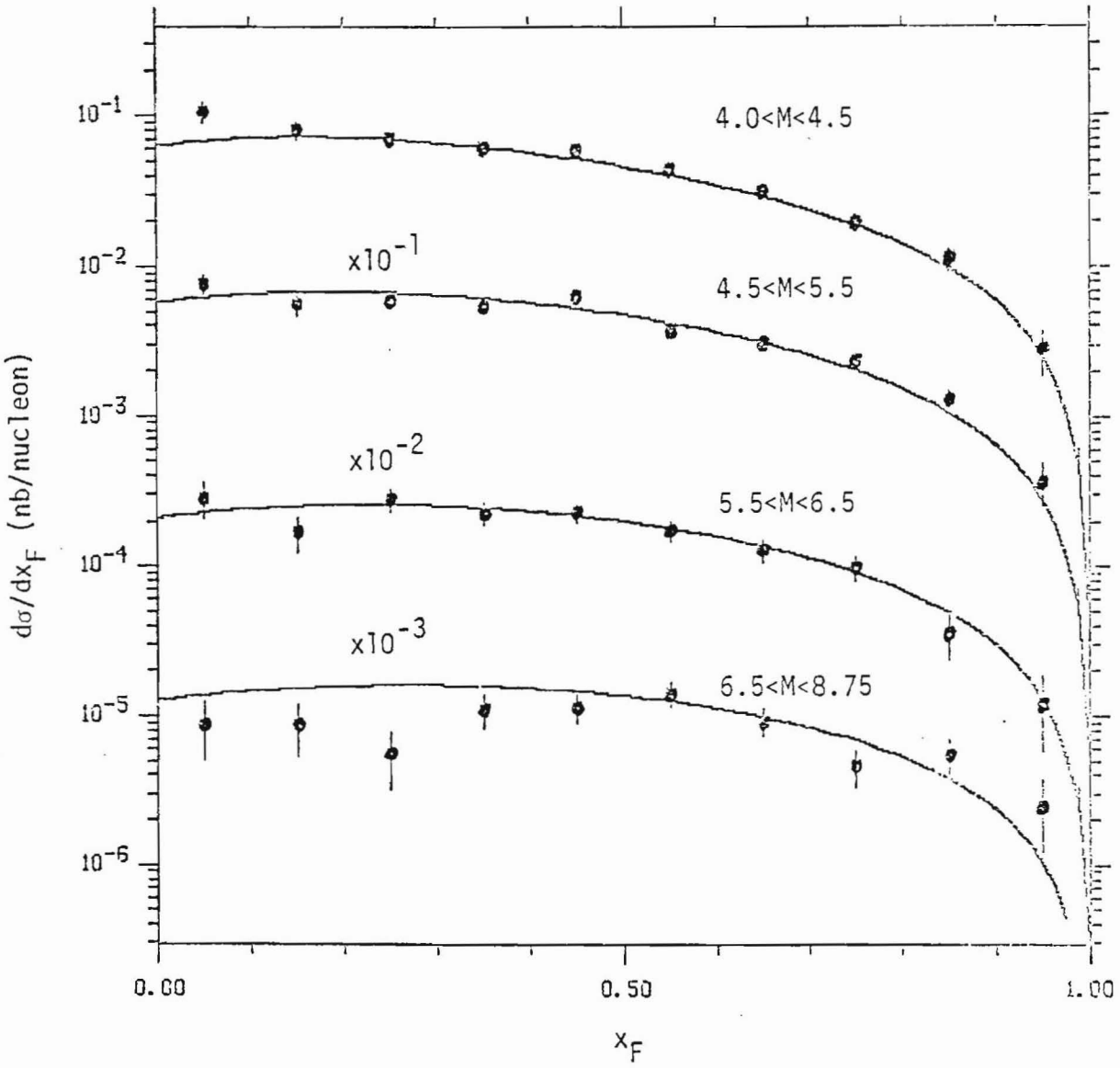
4.0<M<4.5
x10^-1
4.5<M<5.5
x10^-2
5.5<M<6.5
x10^-3
6.5<M<8.75
10^-1
10^-2
10^-3
10^-4
10^-5
10^-6
dσ/dx_F (nb/nucleon)
0.00
0.50
1.00
x_F

Fig. 84.--Mass spectrum for π^- induced μ pairs with masses between 0.3 and 8.75 GeV/c^2 and x_F>0.1. The lower mass data points (M <2 GeV/c^2) are from Ref. 51.

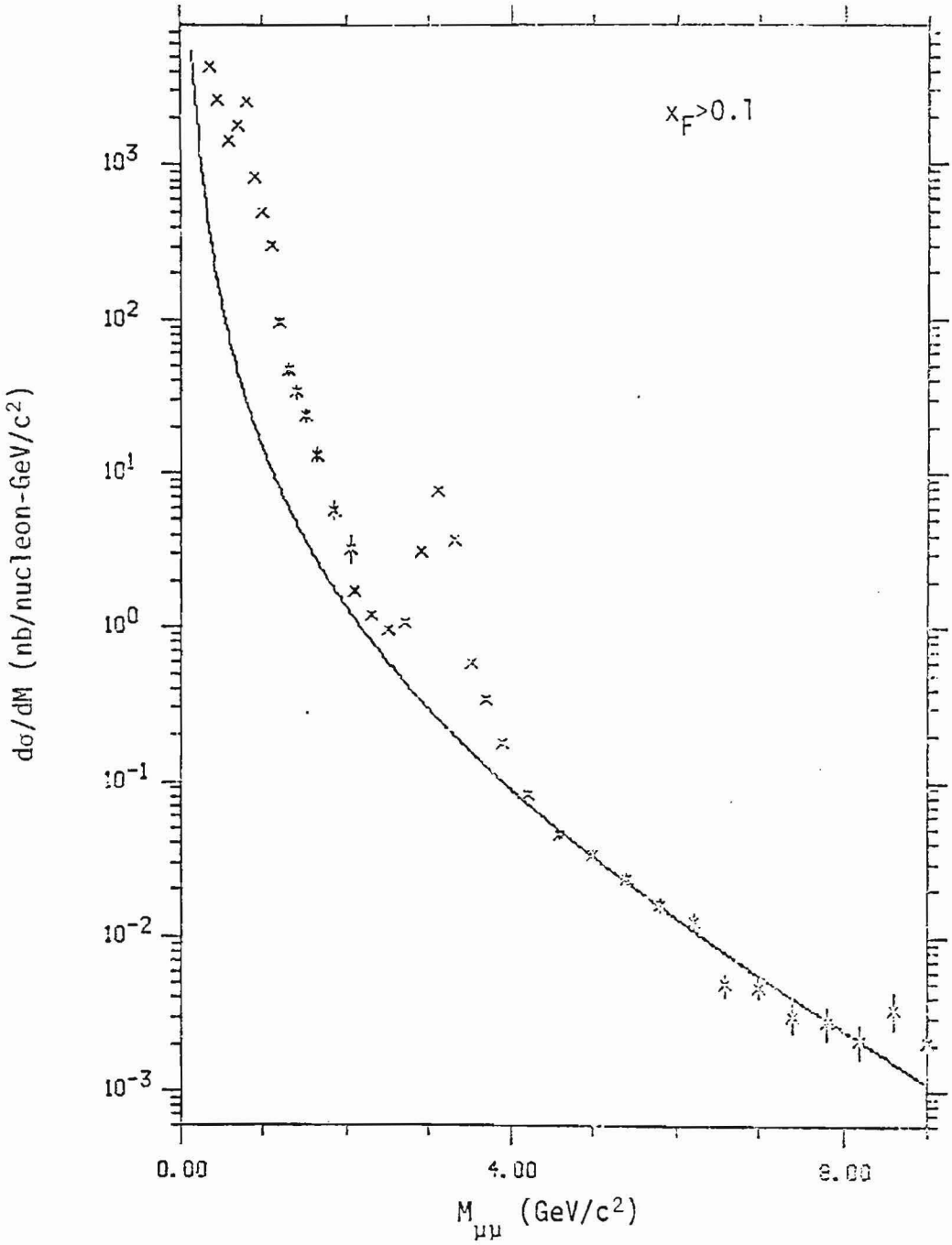
$x_F>0.1$
10^3
10^2
10^1
10^0
10^{-1}
10^{-2}
10^{-3}
$d\sigma/dM$ (nb/nucleon-GeV/c^2)
0.00
4.00
8.00
$M_{\mu\mu}$ (GeV/c^2)

Fig. 85.--The ratio $R = \sigma(\pi^+C \rightarrow \mu^+\mu^-X)/\sigma(\pi^-C \rightarrow \mu^+\mu^-X)$ as a function of mass. The curves are described in the text. The solid curve used the nucleon sea quark distribution of Ref. 43 and the dashed curve used the nucleon sea quark distribution of Ref. 40.

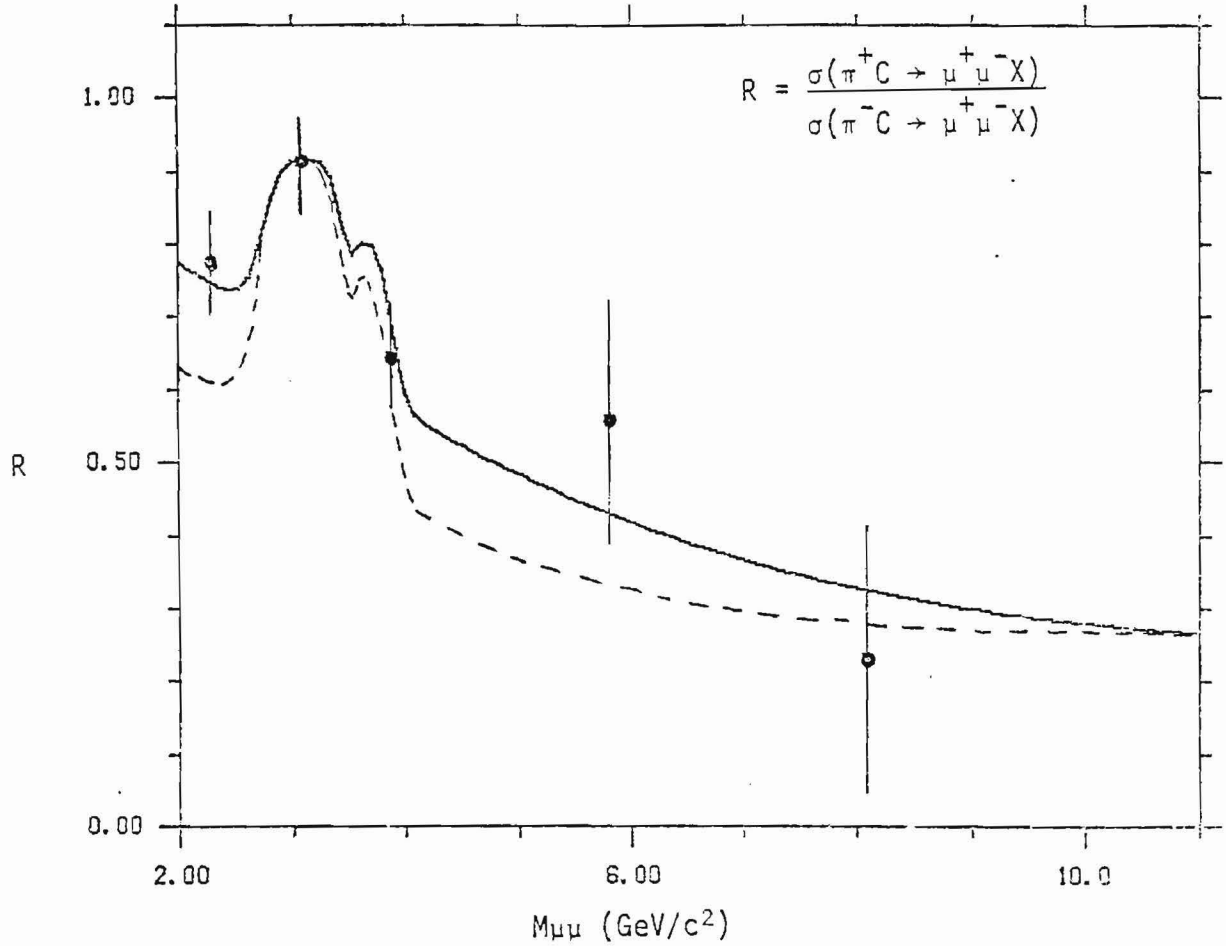
$R = \frac{\sigma(\pi^+ C \to \mu^+\mu^- X)}{\sigma(\pi^- C \to \mu^+\mu^- X)}$
1.00
0.50
0.00
R
2.00
6.00
10.0
Mμμ (GeV/c²)

Fig. 86.--Diagrams for deep inelastic lepton nucleon scattering.

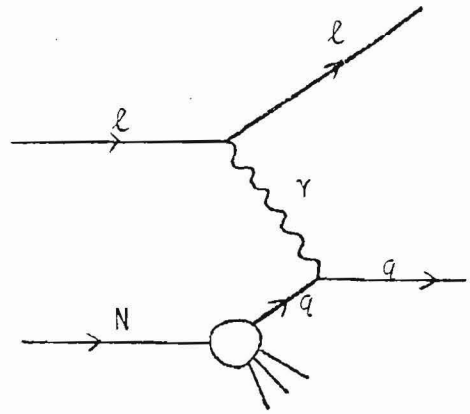
ℓ
ℓ
γ
q
q
N

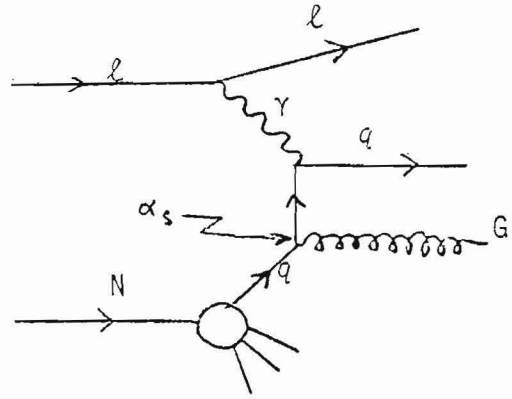
ℓ
ℓ
γ
q
α_s
G
q
N

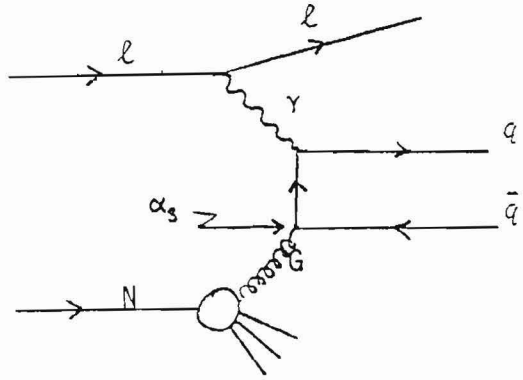
ℓ
ℓ
γ
q
α_s
$\bar{q}$
G
N

Fig. 87.--Diagrams for QCD corrections to the Drell-Yan mechanism.

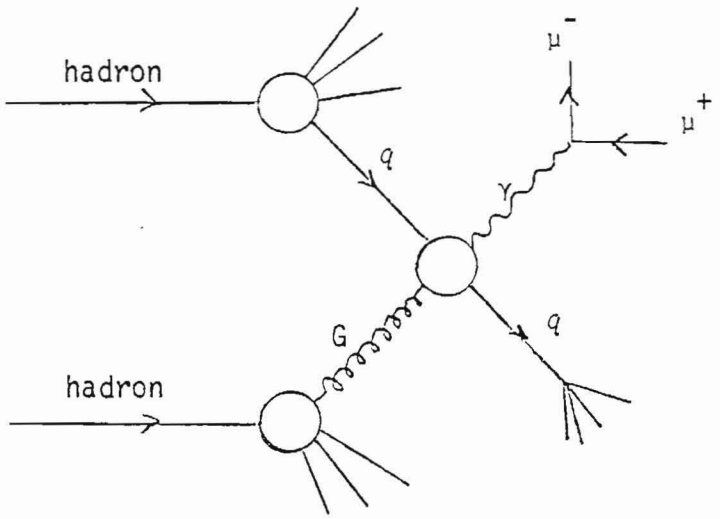
hadron
hadron
q
q
G
γ
μ⁻
μ⁺

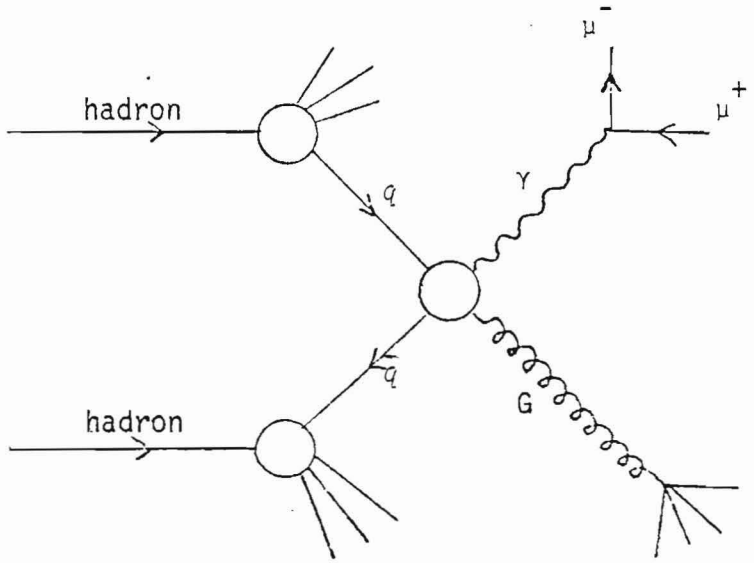
hadron
hadron
q
q
G
γ
μ⁻
μ⁺